University of Salford

School of Computing, Science & Engineering

PhD Thesis

Heuristic Modelling of Multijunction Solar Cells Using a Parallel Genetic Algorithm

University of Salford MANCHESTER

Slobodan Čičić

2018

CONTENTS

1 INTRODUCTION 1
  1.1 What's So Good About Solar Cells? 1
  1.2 A Brief History of Solar Cells 5
  1.3 Where Are We Now and Where Are We Going? 7
2 HISTORICAL BACKGROUND OF SOLAR CELLS ANALYSIS 11
3 BASIC SEMICONDUCTOR THEORY 21
  3.1 Basic Crystal Structure 22
  3.2 Carriers in Semiconductors 24
  3.3 $\mathbf{k} \cdot \mathbf{p}$ Method 32
  3.4 Absorption and Generation in Semiconductors 35
4 SOLAR CELL PARAMETERS AS A FUNCTION OF ENERGY GAP 42
5 BASIC SOLAR CELL THEORY 47
6 MULTI-JUNCTION SOLAR CELLS 60
  6.1 Multi-junction Solar Cell Device Structure 64
  6.2 Multi-junction Solar Cell Device Fabrication Methods 65
  6.3 Multi-junction Solar Cell Device Realization Approaches 68
    6.3.1 Monolithic Lattice-Matched MJSCs 68
    6.3.2 Metamorphic MJSCs 69
    6.3.3 Diluted Nitrogen MJSCs 70
    6.3.4 Mechanically Stacked and Wafer-Bonded MJSCs 70
    6.3.5 III-V on Silicon MJSCs 72
  6.4 Generalization of Equations for Multi-junction Solar Cells 73

7 LOSSES IN SOLAR CELLS 77
7.1 Diffusion Dark Current 77
7.2 Radiative Recombination in III-V Semiconductors 78
7.3 Shockley-Read-Hall Recombination 82
7.4 Band-to-band Auger Recombination in III-V Semiconductors 87

8 HEURISTIC MODELING OF MULTI-JUNCTION SOLAR CELLS 100
8.1 Genetic Algorithms 100
8.2 Shema Theorem 105
8.3 A Matematical Model of the Simple Genetic Algorithm 109
8.4 Genetic Algorithm Implementation Using Parallel Computing 113

9 RESULTS AND DISCUSSION 122
9.1 Overall Saturation Current 126
9.2 Unconstrained Multi-junction Solar Cells 128
9.3 Series Constrained Multi-junction Solar Cells 136
9.4 Comparison between theoretical model and experimental results 141
9.5 Photon Energy Converters 148

10 CONCLUSIONS 157

11 FUTURE WORK 161

LIST OF FIGURES

Figure 1.1 World ecological footprint per each year with different sources of footprint. [7] . . . 2
Figure 1.2 Primary energy world consumption [3] . . . 2
Figure 1.3 Biocapacity per person and Ecological Footprint per person in: (a) United States of America, (b) Canada, (c) China, (d) Norway. [13] . . . 3
Figure 1.4 Price history of silicon solar cells [1] . . . 6
Figure 1.5 Global market share by PV technology. [20] . . . 7
Figure 1.6 Best research-cell efficiencies. [2] . . . 8
Figure 3.1 Material classification based on conductivity: insulators (yellow), semiconductors (orange) and conductors (purple). . . . 21
Figure 3.2 Materials in Periodic Table: insulators (yellow), semiconductors (orange) and conductors (purple). . . . 22
Figure 3.3 Crystal lattice and unit cell. [4] . . . 22
Figure 3.4 Crystal lattice structures common for semiconductors: diamond (left) where all atoms are from column IV, and zincblende (right) where atoms are from columns III (e.g. red) and V (e.g. black). 23
Figure 3.5 Covalent bonding in diamond lattice with dark gray circles as atoms and black circles as electrons. . . . 25
Figure 3.6 Schematic of energy-band diagram for gallium-arsenide with different lattice orientations. [16] . . . 26
Figure 3.7 Fermi-Dirac distribution function for GaAs at different temperatures, conduction band level is presented on the graph, while valence band level is taken as the reference, i.e. $E_V = 0$ . . . 27

Figure 3.8 Schematic representation of impurities in a crystal lattice consisting of Column IV elements (dark gray) with n-type impurity (blue) and p-type impurity (red) 30
Figure 3.9 Fermi-Dirac distribution function in GaAs doped in various impurity concentrations at 300K temperature; indices "p" and "n" denote p-type and n-type impurities, respectively. 32
Figure 3.10 Light intensity attenuation as a function of penetration depth with initial intensity I_0. 36
Figure 4.1 Measured and calculated values of (a) effective masses and (b) effective densities of states and intrinsic carrier concentration [201] 44
Figure 4.2 Calculated absorption coefficients for various alloys and comparison with translated absorption coefficient for GaAs along the x-axis. 45
Figure 5.1 PN junction with holes (red) and electron (blue) concentration profile, charge concentration distribution Q, electric field **E** and potentials. [21] 49
Figure 5.2 Equivalent circuit of an ideal solar cell 56
Figure 5.3 JV curve of an ideal solar cell 57
Figure 6.1 Schematic representation of a triple-junction solar cell. [119] . . 61
Figure 6.2 Absorption of different parts of solar spectrum in each subcell in a triple-junction solar cell; colors coincide with Fig. 6.1. . . . 62
Figure 6.3 Semiconductors with respect to their lattice constant and energy gap (left) and solar irradiance as a function of photon energy (right). [24] 66
Figure 6.4 Absorption of different parts of solar spectrum in 4-junction solar cell. 74
Figure 6.5 Absorption coefficients in the 1st subcells (a), the 2nd subcells (b) and the 3rd subcells (c). 74

Figure 7.1 Schematic diagram for Shockley-Read-Hall recombination. [197] 82
Figure 7.2 Auger CHCC recombination. [28] 90
Figure 7.3 Auger recombination in p-type materials. [28] 91
Figure 8.1 Genetic algorithm flow chart 102
Figure 8.2 Schematic representation genetic algorithm 102
Figure 8.3 Schematic representation of one-point and two-point crossover and mutation 103
Figure 8.4 Illustration of the optimization progress for the 5-junction solar cell, where signs represent fitnesses of each individual while line represent fitness of the fittest individual in each generation during the optimization process. 117
Figure 8.5 Illustration of the optimization procedure for 5-junction solar cell: individuals distribution during the optimization procedure. 118
Figure 8.6 Distribution of individuals during the optimization process of single-junction device using genetic algorithm for different values of crossingover and mutation probability. 119
Figure 8.7 Distribution of individuals during the optimization process of 15-junction device using genetic algorithm for different values of crossingover and mutation probability. 120
Figure 9.1 Shockley-Queisser limit for: 6000K blackbody radiation (red), 6000K blackbody radiation scaled to be comparable with AM1.5 spectrum (black), real global (green) and direct (blue) irradiation 123
Figure 9.2 Saturation current density as a function of energy gap in a pn junction in case of: (i) overall losses accounted, (ii) only radiative recombination, (iii) only Auger recombination, and (iv) only diffusion dark current. 127

Figure 9.3 Maximum efficiency of unconstrained MJSC as a function of the number of subcells (lines, left axes) and the optimal arrangement of the E_g (signs, right axes): (i) for radiative recombination, (ii) for radiative recombination and diffusion dark current, (iii) for the radiative recombination, diffusion dark current and Auger recombination (iv) detailed balance limit [49]. 129
Figure 9.4 Optimization progress for individual SCs in unconstrained 4JSC under ASTMG173 Global tilt spectrum; signs represent fitnesses of each individual; lines represent fitness of the fittest individual in each generation during the optimization process. 130
Figure 9.5 Overall optimization progress for unconstrained 4JSC under ASTMG173 Global tilt spectrum 131
Figure 9.6 ASTM G173-03 Global tilted solar spectra and attenuated portion of this spectra absorbed by each of 4 subcells in unconstrained 4JSC 132
Figure 9.7 JV characteristics for individual subcells in unconstrained 4JSC 133
Figure 9.8 JV characteristics for individual subcells in unconstrained 4JSC when subcells are connected in series, i.e. when working as a two-terminal device 134
Figure 9.9 Solar cell output power as a function of difference (ΔJ) between short-circuit (J_{sc}) and optimal current (J_{opt}) in case of low, moderate and high losses levels. 134
Figure 9.10 Short circuit current as a function of energy gap under 6000K blackbody radiation (red), 6000K blackbody radiation scaled to be comparable with AM1.5 air mass (black), real global (green) and direct (blue) irradiation. 137

Figure 9.11 Maximum efficiency of series constrained MJSC as a function of the number of junctions (lines, left axes) and the optimal arrangement of the E_g (signs, right axes): (i) for radiative recombination, (ii) for radiative recombination and diffusion dark current, and (iii) for the radiative recombination, diffusion dark current and Auger recombination [201]. 138
Figure 9.12 Optimal JV curve for: (a) 2-junction solar cell, (b) 3-junction solar cell [201]. 141
Figure 9.13 Optimal JV curve for 4-junction solar cell [201]. 142
Figure 9.14 Predicted JV curve of our optimization based on extracted experimental parameters of record setting devices [201]: (a) Alta Devices® 2-junction solar cell [116], (b) Sharp® 3-junction solar cell [181]. 143
Figure 9.15 ASTM $G173-03$ Global tilted solar spectra and attenuated portion of this spectra absorbed by each of 3 subcells in 3-junction SC: (a) optimization based on our model [201] and (b) optimization based on extracted experimental parameters of record setting device [181]. 144
Figure 9.16 Illustration of the optimization procedure for series constrained 2JSC under ASTMG173 Global tilt spectrum: (a) signs represent fitnesses of each individual while line represent fitness of the fittest individual in each generation during the optimization process, (b) individuals distribution during the optimization procedure 147
Figure 9.17 Schematic representation of LPC VEHSA device 149
Figure 9.18 Maximum efficiency of LPC VEHSA device as a function of number of subcells, with $10\mu m$ thickness, $5W/cm^2$ laser irradiation and recombinations taken into account in different combinations 151

Figure 9.19 Maximum efficiency of LPC VEHSA device as a function of number of subcells ($10\mu m$ thickness; $10W/cm^2$ laser irradiation) and experimental data obtained in [71] . . . 152
Figure 9.20 Optimal currents, optimal and open-circuit voltages in LPC VEHSA devices as a function of number of subcells, with $10\mu m$ thickness, $5W/cm^2$ laser irradiation and all types of losses taken into account . . . 153
Figure 9.21 Current-voltage characteristics of LPC VEHSA device as a function of number of subcells, with $10\mu m$ thickness, $5W/cm^2$ laser irradiation and all types of losses taken into account . . . 153
Figure 9.22 Optimal and open-circuit voltages compared with energy gap (with $10\mu m$ thickness, $5W/cm^2$ laser irradiation and all losses taken into account) for each subcell in 15-subcell PEC VEHSA device . . . 155
Figure 9.23 Estimated topmost subcell thickness compared with results from the optimization (with $10\mu m$ thickness, $5W/cm^2$ laser irradiation and all losses taken into account) . . . 155

LIST OF TABLES

Table 9.1 Optimal parameters of an unconstrained MJSC in case when all types of losses are taken into account 135

Table 9.2 Maximum efficiencies of an unconstrained MJSC in with different combinations of losses 136

Table 9.3 Optimal parameters of a series constrained MJSC in case when all types of losses are taken into account [201] 139

Table 9.4 Maximum efficiencies of a series constrained MJSC in with different combinations of losses [201] 140

Table 9.5 Comparison of 2-junction, 3-junction and 4-junction SCs with experimental results [96, 201] 141

Table 9.6 Parameters of 15-subcell LPC 10 μm tick with 5 W/cm^2 laser power with Shockley-Read-Hall, radiative and Auger recombination taken into account 154

ACKNOWLEDGEMENTS

I would like to thank to all the people who supported and encouraged me during all this time.

First and foremost, I would like to thank my family and friends for supporting me in my work and encouraging me to follow my dream.

Next, I would like to thank all my professors from my elementary schools, Electrical Engineering High School "Nikola Tesla" in Belgrade, Serbia and School of Electrical Engineering, University of Belgrade, Serbia.

I would also like to thank my supervisor Professor Stanko Tomić and co-supervisor Professor Ian Morrison who's guidance helped me to grow as a researcher.

As well, thanks to Jacek, Mark, Tom, Simon, Alex, Dean, Malik, Adnan, Rabia, Hamid, Murtala, Bwebum, Jamie and Holi, students in the School of Computing, Science and Engineering at the University of Salford, for their help and invaluable discussions on both physics and everyday life. Thank you for providing me an invaluable insight in different cultures.

I would also like to thank all members of "la Suerte" dancing school for making my life very interesting during the last few years.

Maybe the most important, I would like to thank to all members of staff at the University, particularly to Catriona Nardone and her colleagues for supporting me with all the paperwork, lifting a huge weight off my shoulders and making all this possible. As every researcher will agree on, this weight is even heavier than all the problems in physics and mathematics combined.

And finally, special thanks to the NEDO Agency, Japan, for financial support under grant: "Research and Development on Innovative Solar Cells: Post-Silicon solar

cells for ultra-high efficiencies" and the contribution of COST Action MP1406 (MultiscaleSolar).

For all those to whom science is a way of life, and not "just" a job.

ABSTRACT

In order to fabricate solar cells with the highest possible values of efficiencies, material type, layer thickness and doping have to be properly selected. It can be achieved if light absorption and carrier generation are maximized and losses minimized. The same parameters that increase carrier generation, can increase certain types of losses. Parameters which reduce one type of losses, tend to increase the other types. Structural complexity of these devices combined with already mentioned conflicting requirements create vast parameter space which is highly uneven and contains a huge number of local minima and maxima. It makes it difficult for the most of search methods to locate the global maximum. Therefore, heuristic optimization is crucial for solving problems as complex as this one.

To find the optimal combination of these parameters, genetic algorithm is used with drift-diffusion model and all material parameters calculated as a function of energy gap. This way we have very realistic material parameter set which, together with detailed losses modeling, provide reliable results. To test the model, findings were compared with the record setting devices. Results were in agreement, which makes the model trustworthy. Two types of devices were optimized: multi-junction solar cells (MJSC) and photon energy converters (PEC). In case of MJSCs, parameters which were optimized are thicknesses, impurity concentrations, energy gaps and optimal current. And in case of PECs, thicknesses, impurity concentrations and optimal current were optimized. The optimization was repeated with different types of losses accounted in order to see how each one of them affects the overall efficiency. From the results of optimization it was possible to see what are the main drawbacks in the device efficiency and how to overcome them.

Calculations were carried out with ASTM G173 − 03 Global tilted solar spectrum in case of MJSCs and laser with intensity of $5\text{W}/\text{cm}^2$ and wavelength of $855n$m in case of PECs. The absorption was calculated from `kppw` code.

The maximum efficiencies achieved for the unconstrained device are 30.158%, 41.479%, 45.669%, 50.775% and 53.653% for MJSC devices with one, two, three, four and five subcells, respectively, when all types of losses are taken into account. In case of the series constrained device, the results are 31.080%, 42.467%, 48.276%, 50.777%, 53.653%, 54.917% and 55.317% for devices with up to seven subcells, respectively, when all types of losses are taken into account, as well. The values for the PECs are 69.431%, 68.838%, 66.676% and 65.698% for one, five, ten and fifteen subcells, respectively. This time all losses are accounted as well. If the model is applied to the record setting devices, the results are 32.34% for 2JSC and 38.1%, while actual, measured, values are $31.6 \pm 1.5\%$ and $37.9 \pm 1.2\%$, respectively, which is an outstanding match.

Detailed device parameters obtained through the optimization process are presented. Examination of those results leads to possible recipe how to fabricate the highest possible efficiency devices. It was concluded that the radiative recombination is the most dominant type of losses in III-V semiconductors and can be suppressed by increasing the material's energy gap. Diffusion dark current can be suppressed by increasing the energy gap as well, while the doping levels shoud be increased. On the other hand, Auger recombination can be reduced by decreasing the doping, while the increase of energy gap reduces Auger much more than the other two. This leads to significant drop in efficiency when the algorythm tries to suppress the Auger, in comparison when only the two other types of losses are accounted. Nevertheless, the suppression of all losses leads to more efficient devices. This analysis can be a guide the future experiments and indicate how much more efficiency can be achieved with these devices, which materials to target and how to correctly balance between various contradicting requirements imposed by the nature of semiconductor materials.

1

INTRODUCTION

For millennia humankind depended on resources found in nature. It was primarily wood and food. And then, a few thousand years ago, we discovered agriculture. It helped our species expand dramatically. Since bare existence was not an issue any more, art and religion started to develop. After that, science too. Science was a real breakthrough. We started to understand the environment and how to exploit it even further. So, our progress accelerated. It drew increase in energy consumption. Especially in the last two centuries. Fossil fuels fueled our progress. We had huge amounts of energy available and we have not been spending it rationally. That is the cause of pollution. Another important fact about fossil fuels is that they are not renewable. It means that we are running out of it. And we will run out of it in next few decades. In order to sustain our progress, we need a new energy source. It will probably be fusion. Until we create a sun on Earth, we can exploit energy of the Sun we already have via solar cells.

1.1 WHAT'S SO GOOD ABOUT SOLAR CELLS?

We have been using oil and coal as energy sources for two centuries now. During that time, we have depended on nature less and less, and our progress exploded. As a consequence, our influence on Earth and ecosystems became almost fatal. We are exploiting Earth by far more than we should.

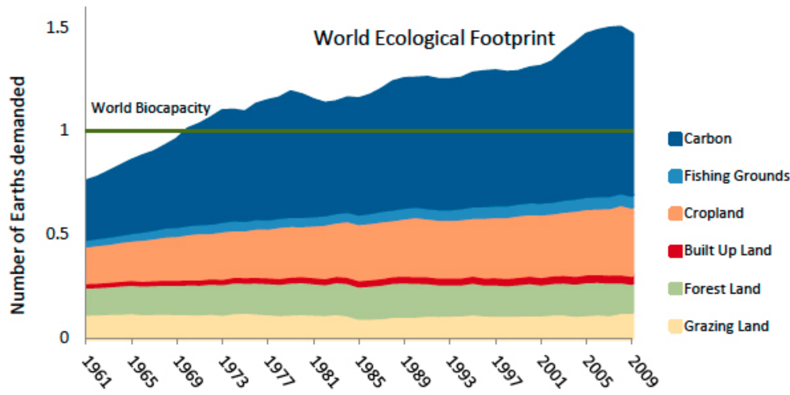

Figure 1.1: World ecological footprint per each year with different sources of footprint. [7]

The term earth's biocapacity refers to the resources that planet is able to provide and ecological footprint refers to our demands per year. When the ecological footprint exceeds Earth's biocapacity, it is called Earth Overshoot Day [11, 6]. In 2018th the Earth Overshoot Day was on the 1st August [5]! Just for comparison, in 2016th it was on the 5th August and in 2017th it was on the 3rd August [5]! From Fig. 1.1 it is evident that the most negative influence on the planet comes from carbon emission. In 2016th we produced 33,432 million tonnes of carbon dioxide [3].

If we just reduced the carbon emission by 50%, our ecological footprint would be within planet's limits (Fig. 1.1). Identifying the main sources of carbon emission can help us find a way to reduce it (Fig. 1.2).

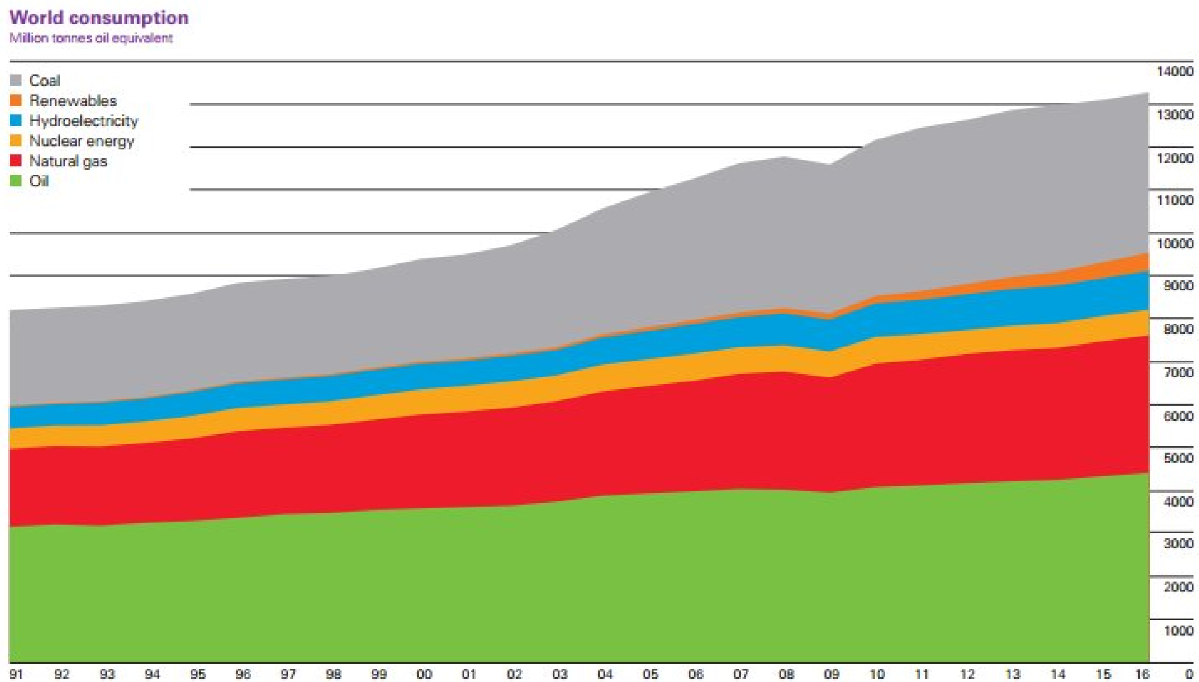

Figure 1.2: Primary energy world consumption [3]

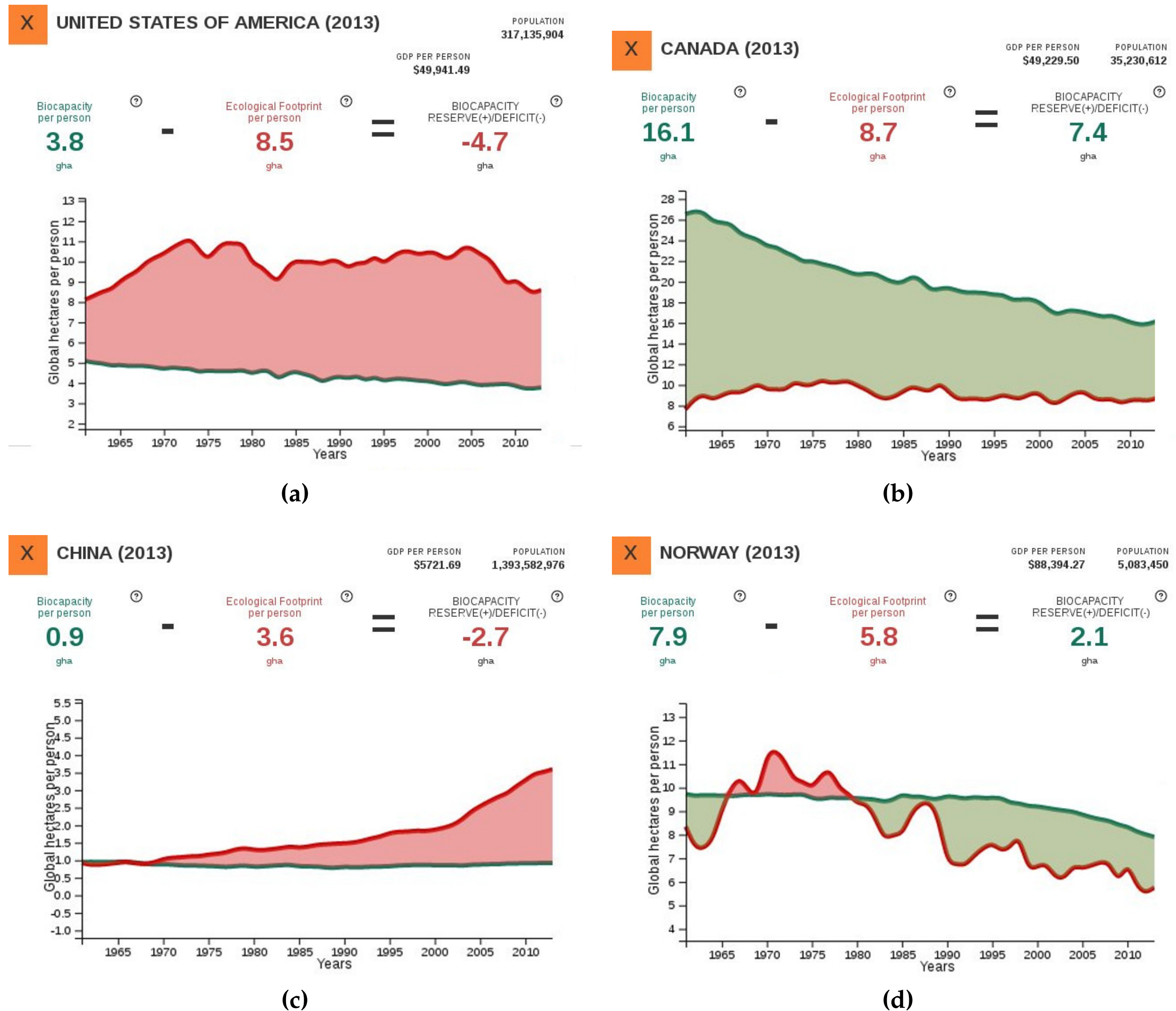

Figure 1.3: Biocapacity per person and Ecological Footprint per person in: (a) United States of America, (b) Canada, (c) China, (d) Norway. [13]

Developed countries have the most influence on ecology (Fig. 1.3). Energy consuming way of life makes them overexploit the planet. One example is United States of America (Fig. 1.3a). Other types of developed countries, like Canada (Fig. 1.3b), have huge ecological footprint per capita as well, whereas due to small population and large amount of resources they are significantly below their biocapacity.

Next, developing countries, like China (Fig. 1.3c) have still low ecological footprint per capita in comparison to the developed ones, but, due to large environment exploitation, their biocapacity per capita is even lower. Most countries start overexploiting the land as their standards are growing. Unlike them, Norway (Fig. 1.3d) is the example of how economic growth does not necessarily jeopardize the environ-

ment. In the last four decades, their biocapacity decreased slightly, while they have halved their ecological footprint per capita.

Most of carbon emission comes from energy production, traffics, farming, industry, and globalization.

As individuals, we can do many small things which would reduce carbon emission. We can buy products produced in any country in the world with one click of a mouse, without thinking how is it going to be delivered or if the production process is environmentally friendly. Only transportation accounts for 15% of all energy carbon emission in energy production [8], while overall energy production carbon emission is responsible for 72% of overall carbon emission [17]. Industrial processes are responsible for 6% of overall carbon emission [17], while energy consumed in manufacturing sector accounts for 12.4% of carbon emission [17]. For instance, we can eat less meat, or eat meat which is produced with lower carbon emission [10]. Farming is responsible for a huge amount of greenhouse gases [9]. Only livestock farming contributes to about 9% of total anthropogenic carbon dioxide emissions [9], but 37% of methane [9] and 65% of nitrous oxide emissions [9].

What we can do is buy locally produced food, which would reduce carbon emission from food transportation. When it comes to traffic, we can use bicycles, use public transportation or buy electric cars and charge them from solar panels.

As individuals, we can not do as much when it comes to energy production. It is up to scientists to invent the way and for governments to support them in the process. The best way we can help our planet is by producing more energy from renewable energy sources. In 2016th $13,276.3$ million tonnes oil equivalent (Mtoe) energy has been consumed [3], which is equal to around $154,403.37$TWh, since 1Mtoe=11.63TWh. Energy sources are graphically presented on Fig. 1.2. Only 419.5 Mtoe was produced from renewable energy sources [3], which is 14.1% more in comparison to the year before. Out of $24,816.4$ TWh generated electricity [3] in 2016th, only 333.1TWh came from solar [3]. It is 1.34% electricity generated from solar [3]. Compared to 256.2TWh produced [3] in 2015th, makes significant increase which is very encouraging.

On the other hand, we receive between $1,575$EJ and $49,837$EJ of energy from the Sun every year [23], depending on different assumptions on annual clear sky irradiance, annual average sky clearance, and available land area. In other units, it is between $0.44 \cdot 10^6$TWh and $13.84 \cdot 10^6$TWh, which makes between 18 and 575 times more than all electricity we produce per year. At the same time, it means there is between $1,313$ and $41,560$ times more solar energy available on the land on planet Earth than energy we are converting to electricity.

Another reason we have to switch to solar energy as the main source of electricity is its ecological footprint. If we take into account all energy used to produce and maintain solar photovoltaic (PV) panels and greenhouse gases produced in the process and compare it to energy produced during lifetime, we will see that it emits slightly more than 20g/kWh [32]. In comparison, a combined-cycle gas-fired power plant emits $400 - 599$ g/kWh [83], an oil-fired power plant 893 g/kWh [83], a coal-fired power plant $915 - 994$ g/kWh [139] or with carbon capture and storage 200 g/kWh [139], and a geothermal high-temperature power plant $91 - 122$ g/kWh [83].

1.2 A BRIEF HISTORY OF SOLAR CELLS

The photovoltaic effect was first discovered by French physicist Alexandre-Edmond Becquerel in 1839. He, at the age of 19, made the first photovoltaic cell in his father's lab using an electrode in a conductive solution. Almost 35 years later, in 1873, Willoughby Smith found photoconductivity in selenium. Four years later, in 1877. W.G. Adams and R.E. Day were experimenting with solidified selenium and published a paper titled *The action of light in selenium*. Charles Fritts built the first solid-state solar cell in 1883 using a thin layer of gold to coat the semiconductor selenium and form junctions. That solar cell was 1% efficient. The next step in progress of the photovoltaic solar cells was made by Polish physicist Jan Czochralski. He, in 1918, developed a method to grow single crystals of metal, which was used for growing semiconductor crystals by Gordon Teal and John Little thirty years later. Vadim

Lashkaryov discovered a p-n junction in copper-dioxide and silver sulfide photocells in 1941. Five years later the first modern solar cell was born. Russell Ohl patented a solar cell while working on research that led to the discovery of transistor.

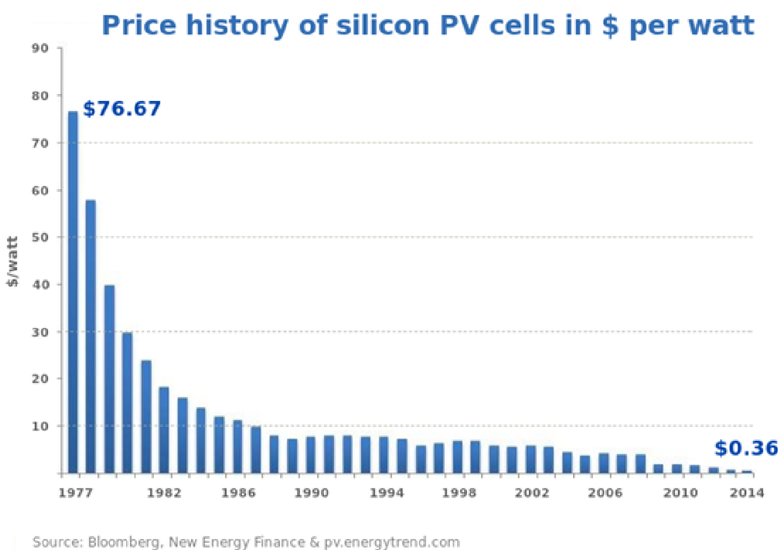

Figure 1.4: Price history of silicon solar cells [1]

In 1954 the first practical silicon solar cell was made in *Bell Labs*. The efficiency was 6%. A year later in *Hoffman Electronics Corporation* the first commercial solar cell was made with 2% efficiency (at price of almost 2000$/W), which increased to 14% by 1960. The first significantly efficient GaAs heterostructure solar cell was made in 1970 by Zhores Alferov. Solar cells gained their popularity in 1958 when Vanguard I, the first solar-powered satellite was launched. Soyuz 1, the first manned spacecraft was solar powered too. Those achievements were subsequently awarded the Nobel Price in physics to Zhores Alferov in the year 2000.

Elliot Berman founded *Solar Power Corporation* in 1969. They made an estimation for the next thirty years and concluded that energy prices will rise, which is good news for the, still pricy, solar panels. Together with *Exxon*, he brought prices from 100$/W to only 10$/W. In 2012 the price was only 0.62$/W [163]. In 1990s global warming and pollution became so obvious that many scientists, individuals, and organizations started pointing their attention to renewable energy sources. As a consequence, in the last few years more and more politicians have been supporting the idea of renewable energy.

From 2010 to 2016 the Compound Annual Growth Rate of Photovoltaics (PV) installations was 41% [14]. In 2014, China was the world's largest producer of PV modules with a share of 68% [14]. On the other hand, Europe holds the lead in total cumulative PV installations with 33% share [14], which is less than in the year before (40% [14]). The most common technology is Si-wafer [14] based and accounts for 94% [14] of the total production in 2016. Multi-crystalline silicon technology was about 70% [14] of the total production. The remaining 24% is mainly mono-crystalline silicon, which holds the second position in total. All thin film technologies combined add up to 6% [14].

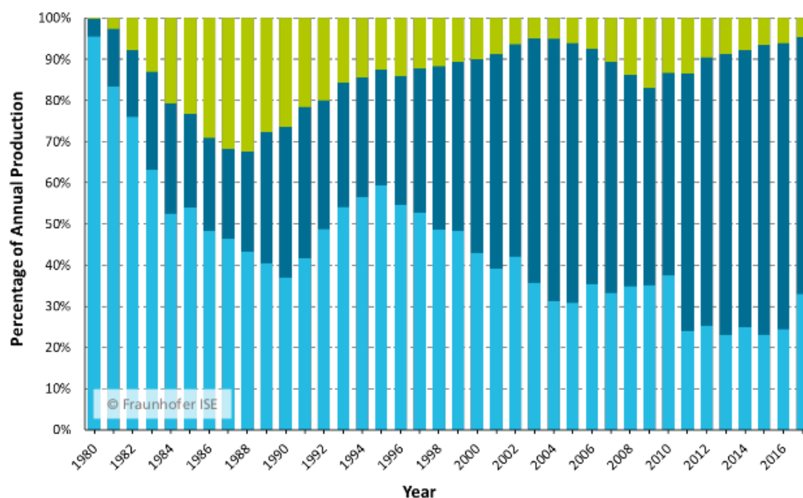

Figure 1.5: Global market share by PV technology. [20]

In terms of efficiency, mono-crystalline silicon solar cells are more efficient (26.7% [14, 96]) than multi-crystalline silicon (22.3% [14, 96]). Mono-crystalline silicon modules are the best performing modules with 24.4% efficiency [14]. The most efficient thin film solar cells are GaAs thin films (28.8% [96]), which are very expensive and thus not used in commercial applications. Significantly cheaper thin films, and commercially used, are CdTe with 21% efficiency [14, 96] and CIGS (copper indium gallium selenide) with 21.7% efficiency [14]. In PV modules there are many losses (e.g. resistance) that makes them less efficient. Therefore, mono-crystalline silicon modules efficiency goes up to 21% [14], multi-crystalline modules are around 17% [14] efficient and CdTe modules around 16% [14].

Efficiencies above 40% can be achieved using high concentration multi-junction solar cells. At the moment (1Q2018) the world record of 46% is held by a multi-junction solar cell developed by Soitec, CEA-Leti and Fraunhofer ISE [15, 14]. The cell consists of four junction III-V compounds with 508 suns concentration. Again, resistance, together with other losses, makes PV modules less efficient. The highest efficiency concentrated PV module, produced by Soitec, achieved 38.9% [14].

The Energy Payback Time is the time necessary for the photovoltaic system to produce as much energy as it was consumed in its production. It depends on the production technology itself, solar system type, geographical location of its installation, etc. At the moment, multi-crystalline silicon system in Southern Europe has Energy Payback Time of around 1 year [14]. For concentrated photovoltaic systems it is even less [14]. In general, in Southern Europe Energy Payback Time is up to 1.5 years [14], whereas in Northern Europe is up to 2.5 years [14].

Overview of different solar cell technologies and their development through history is presented in Fig. 1.6 by National Renewable Energy Laboratory (*NREL*).

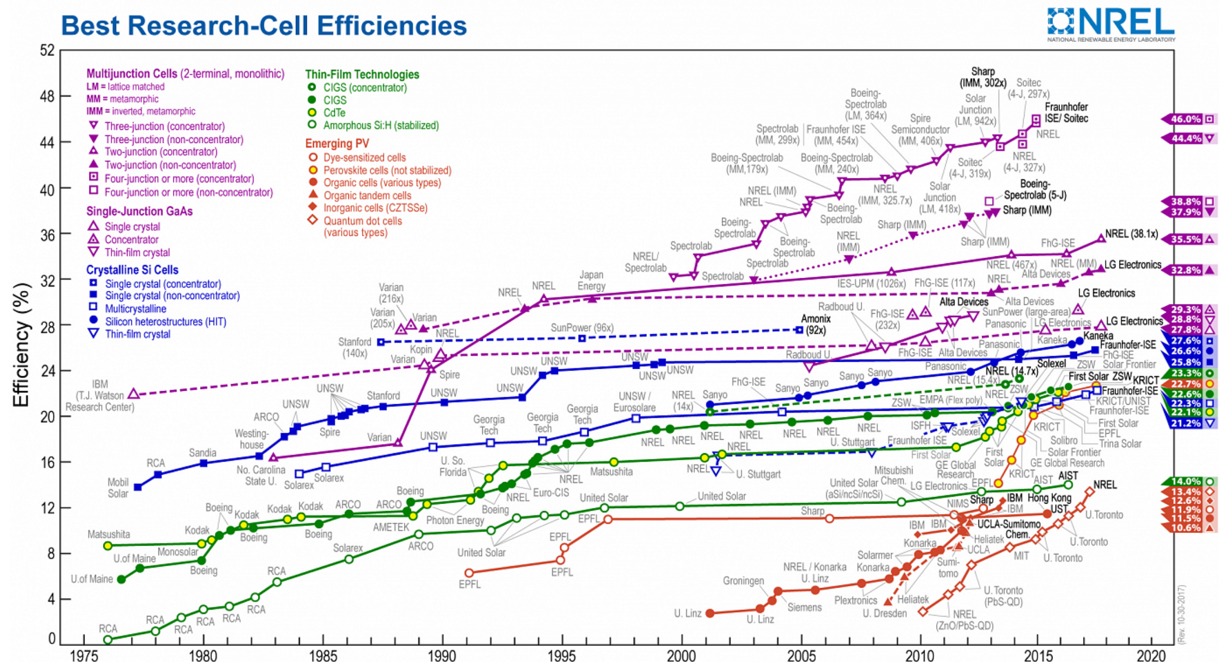

Figure 1.6: Best research-cell efficiencies. [2]

Besides the ones mentioned above, different technologies are emerging, as part of the 3rd generation PVs. They are based on new, promising, technologies or novel materials which could exceed current solar cell efficiencies.

In perovskite solar cells the active layer is usually a hybrid organic-inorganic lead or tin halide-based material. The absorbing materials are cheap and simple to manufacture and are believed to be very cheap to scale up. The advantages are broad absorption spectrum, fast charge separation, long transport distance of electrons and holes, long carrier separation lifetime, and more. These make them very promising materials for solar cells. One of the main disadvantages is the cost of electrodes, since the most common material used is gold. Another problem is the toxicity of some of the compounds used in perovskite solar cell fabrication. Next, there are problems with deterioration in presence of moisture and sensitivity to UV radiation. Thanks to all the advantages and despite all the disadvantages, at the moment ($1Q2018$) they are the most popular and they have promising future. Efficiencies rose from 3.8% [121] in 2009 to over 20.1% [58] in 2014. Now, the highest single junction solar cell efficiency is 20.9% [96, 217] And the highest mini-module efficiency is 16% [96, 19].

Dye-sensitized solar cells (DSSCs) were invented by Brian O'Regan and Michael Grätzel at UC Berkeley in 1988 [162]. Light absorption takes place in the sensitizer. Charge carrier separation is separated from absorption. Carriers are transported in the conduction band of the semiconductor. A photo-induced electron is being injected at the interface from the dye into the semiconductor. The advantage of sensitizers is absorption of photons with wide range of energies. Fabrication is possible with the conventional roll-printing technique. They are semi-flexible and semi-transparent as well. Next, they have good performance in low illumination condition, which makes them suitable for indoor use. Thanks to the low price, the price/performance ratio could be soon comparable to fossil fuel energy sources. Like perovskite, DSSCs are highly sensitive to UV and thermal degradation. Another problem is air infiltration. These downsides impede their application in real devices under real environmental

conditions. The efficiency of a single junction solar cell at the moment is 11.9% [96], while the maximum mini-module efficiency is 10.7% [96]

Quantum dot solar cells (QDSCs) use quantum dots as the absorbing photovoltaic material. They are based on the DSSCs. Band gaps in quantum dots are tunable over a wide range of energies by changing the dots' size, unlike the bulk materials where the band gap is fixed but different in different materials. Thanks to this property of quantum dots, they are very attractive for multi-junction solar cells which could have high number of layers and, potentially, cover the whole solar spectrum. They could have higher conversion efficiency due to hot carrier absorption. It would allow high voltages or high currents. The efficiency goes up to 15.3% for QDSCs [191].

Organic solar cells have thin films of organic semiconductors, which is the most common polymer. They are sensitized from a liquid solution, are flexible, and very lightweight. Production is possible by a simple roll-to-roll printing process, which can lead to inexpensive large-scale production. Molecular engineering allows different energy gaps to be created. Due to high absorption coefficient, they can be very thin, and, at the same time, very lightweight and low cost. Unlike other types of solar cell technologies, they are disposable and more environmentally friendly. On the other hand, they have low efficiency and low stability. For now, efficiencies are near 11.2% [151].

2

HISTORICAL BACKGROUND OF SOLAR CELLS ANALYSIS

Solar cells have been analyzed since they were invented in order to identify the bottlenecks in their performance. Various authors were emphasizing the potential of silicon solar cells. Among them were Chapin, Fuller and Pearson [54] in 1954. In the same year Pfann and var Roesbrook [168] expanded the model including analytic expressions optimizing or matching the load. Next, a year later researchers Prince [170] and Loferski [137] attempted to predict the dependence of efficiency upon energy gap.

The treatment of solar cells in above-mentioned publications was based on empirical values for material constants. Even though there was very good agreement with experiments, according to Shockley and Queisser [188] it was not theoretically justified. They considered the detailed balance as a better way to theoretically calculate the upper limit of efficiency. This limit is a consequence of the nature of atomic processes required by the basic laws of physics. In their analysis they assumed the Sun and the solar cell to be black bodies with temperatures 6000K and 300K, respectively.

In the detailed balance limit, the solar cell absorbs the photons radiated from the Sun and emits photons back through radiative recombination. The fundamental band-to-band absorption per unit volume, unit energy and unit time were accounted for. It is generally assumed that one photon creates one electron-hole pair. The only theoretically unavoidable loss type is radiative recombination, therefore it is assumed to be the only loss. It is calculated as the emission of photons per unit volume, unit energy and unit time. It is assumed that one electron-hole pair emits one photon in radiative recombination. The difference between the number of absorbed and emitted

photons is the overall number of absorbed photons. From absorbed photons short-circuit current can be calculated and from emitted photons the open-circuit voltage can be calculated. This way, the J-V curve can be obtained and all the properties of the solar cell. The first great result from solar cell analysis said that the highest efficiency of a single junction solar cell, fabricated with a material with 1.1eV energy gap, is 30%.

The theory was revisited by Mathers [146] generalizing the result to any type of solar spectrum. He obtained 31% solar cell efficiency under AM1 spectrum illumination. The model was further generalized by various other authors including multi-junction solar cells, luminescent coupling between subcells, then increasing number of subcells to infinite and various other aspects which were omitted previously. In 1980. de Vos and Pauwels [60, 27], calculated efficiency for solar cells with a different number of subcells under both 1 sun and maximum concentration of 45900 suns. Those efficiencies were 30.4% for 1 solar cell, 42.3% for 2 subcells and 49% for 3 subcells, all under 1 sun. When the maximum concentration was applied, efficiencies were 40% for 1 solar cell, 55% for 2 subcells and 63% for 3 subcells. When the number of subcells was increased to infinite, the efficiency obtained for 1 sun irradiation was 68.2%, whereas in case of maximum concentration it was 86.8%. An interesting result was presented here as well. When the luminescent coupling was omitted, the efficiency dropped from 42.3% to 42.2% for the device with 2 subcells. This means that the luminescent coupling has small influence on efficiency.

In the same year, Parrot [164] achieved very similar results in an edge illuminated multi-junction solar cell. A device with an infinite number of subcells had 64% efficiency under 1 sun illumination and 88% under 45900 suns.

Araujo and Marti [35, 145] considered a different approach. They tried to restrict the photons emitted from the cells in both energy and solid angle. In their study, they found that solar cell efficiency can not be maximized with respect to the solid angle through which the photons are absorbed from and emitted to the ambient. The power will increase if that angle decreases, which limits the luminescent emission from the

solar cell. If reduced too much, it will reduce the solid angle through which sun light reaches the device. Therefore, the solid angle restriction leads to the maximum efficiency provided that solid angle under which photons are emitted from the cell is equal to the solid angle through which photons are absorbed from the sun. In other words, in order to achieve the highest efficiencies, all the nonilluminated surfaces of the devices should be perfect reflectors. If this condition is met, the maximum efficiency of a solar cell is independent of concentration.

Furthermore, they found that for optimal devices the highest efficiency is when the absorptivity is maximal. In the case of non-optimum devices, where energy gaps are lower than the optimum ones, non-ideal absorptivity can lead to maximum efficiency. Next, the efficiency of non-optimum solar cell could be increased if the emission of photons with energies higher than the non-optimum energy gap and lower than the optimal one is prevented, as long as the voltage across the device is lower than the energy gap.

When the Sun was assumed a black body at 5759K, they achieved 86.3% for an infinite number of subcells. When the device consisted of only one solar cell, the efficiency was 40.7%. The maximum efficiency was independent on concentration. These limiting efficiencies could not be overpassed with some innovative ideas, including quantum wells or impurity photovoltaic effect, since the above-described limitations refer to them as well.

The Detailed Balance Theory was not useful only for calculating maximum solar cell efficiencies, but for better understanding the photovoltaic effect and the solar cell devices themselves. Each theoretical analysis introduced a new aspect in solar cells which was previously omitted. As the detailed balance, as a method for solar cell analysis, was being developed, it showed its usefulness in understanding the thermodynamics of solar cells.

Thermodynamics is another interesting approach. Unlike the detailed balance, this approach does not take any assumption about the nature of the converter. The limiting efficiency can be derived from thermodynamics through energy and entropy

balance, as in case of pure thermal converters, whereas in the detailed balance principle it is done through the absorption and emission of photons. The two methods are equivalent. Proof of the claim is in fact that Parrot [165] derived, using a pure thermodynamic approach, the same current-voltage relationship as Shockley and Queisser [188].

In the thermodynamic approach, the solar cell is considered as a converter between two large reservoirs. The first one, the pump, is the Sun and the second one, the sink, is the substrate with a heat sink. The converter receives photons from the pump characterized by energy and entropy. At the same time, it emits photons characterized by another value of energy and entropy. In the process, the converter is producing work and heat, with some internal energy and entropy. Here the solar cell is a quantum system which, upon absorption of photons, is brought to an excited state where its free energy increases. The free energy does work, i.e. creates electron-hole pairs.

It can be shown that at the maximum power point, the photovoltaic conversion is an endoreversible process [202], i.e. all the irreversibilities come from coupling with the environment. Concentration interpreted in thermodynamic terms means the larger share of recombination radiation is being returned from the sink to the converter and from the converter to the pump, increasing the reversibility of the system. Luminescence (radiative recombination) is the reverse process of photovoltaic conversion, therefore an increase of luminescence decreases the irreversibility [190]. Higher reversibility means higher radiative efficiency and less energy converted to heat through non-radiative recombination. It is seen through the increase of open-circuit voltage.

Following this approach, Landsberg and Baruch [130] expanded already existing models and added the case when the pump does not completely surround the converter and when the entropy generation and some other processes are not neglected. They took into account return fluxes from the sink to the converter and from the converter to the pump. Next, the solid angle of radiation from the pump (the sun) and radiation distributed over a wide range of energies is accounted as well.

The results of their study are the conversion efficiency, the entropy generation flux and a current-voltage curve in a generalized and a more applicable form. They generalized the current-voltage characteristic for solid angle effects and arbitrary photon distribution. Some of their results were relevant to thermophotovoltaic conversion as well.

This efficiency is often referred to as the Landsberg efficiency [131]. It implies that there is no irreversibility in the photovoltaic conversion since the entropy generation comes from the black body radiation of a converter. Because the blackbody radiation is taken into account, it is always lower than the Carnot efficiency.

If the converter is modeled as a semiconductor illuminated with monochromatic light, it would be equivalent to a two-level quantum system. Results obtained under these conditions are equal to those from detailed balance. Since solar cells are more two-band then two-level systems, the analogy still holds because the two-band system is actually an assembly of an infinite number of two-level systems [130].

In a subsequent publication, these authors together with Parrot and de Vos concluded that even though the model was still incomplete, it can predict the efficiency of silicon solar cell with more accuracy than before. In case of an endoreversible thermal system, the efficiency of a single photovoltaic converter under one sun illumination would be only 12%, which is incorrect since there already are fabricated devices with higher efficiency. The inconsistency comes from the way quantum converters absorb the solar spectrum. While in pure thermal converters all spectrum is used, in quantum systems only part of the spectrum is absorbed, but with higher efficiency. Therefore, the above mentioned two-level model [130, 39] is necessary.

The results showed that, for tandem cells, without concentration the maximum efficiency is 42.31%, while if illumination is concentrated 1000 times the efficiency rises to 50.67%. Another interesting result is that, even though important, the exact choice of bandgaps is not critical due to the broadness of maximum.

Limiting efficiency calculated using thermodynamic and detailed balance models were completed by Araujo and Marti [145]. They reviewed different approaches. The

range of predicted efficiencies was between 85.4% and 95% in previous publications. The authors pointed out values between 93.3% and 95% in efficiency obtained from the standard thermodynamic models. Using the detailed balance, which is more accurate,the predicted limiting efficiency was 86.8%. They published the efficiencies and optimal energy gaps for devices with various number of subcells, different spectrums and configurations as well.

The main aim of this publication was to determine the limiting efficiencies of multi-gap systems. They analyzed two cases: with and without radiative coupling. In the first case, the photons that leave each subcell can be absorbed by the surrounding cells. In the second case, subcell has a reflector placed at the rear which reduces the emission loss and, consequently, absorption in the surrounding cells. The system configured as in the second case has higher efficiency, although only slightly, in case of finite number of subcells.

For 4-junction solar cell, with one sun AM1.5 direct normal irradiance and no angular restriction, the limiting efficiency is 54% in case with reflectors at the back side and 53.6% in the case without reflectors. The difference is very small, as already mentioned. When the concentration is maximal, the efficiencies are 71% and 70.7% with and without reflectors, respectively. Results for blackbody radiation at 6000K are very similar and slightly lower than in case of AM1.5 direct normal irradiance.

When the number of subcells is infinite, the difference between cases with and without reflector vanishes. The limiting efficiencies are 85% and 86.8% for AM1.5 direct normal irradiance and blackbody radiation at 6000K, respectively.

Another interesting result is the sensitivity of the maximum efficiency with respect to the band gap. These values are more sensitive to energy gaps of lower subcells. When AM1.5 direct normal irradiance is applied, there is no dependence on back side reflectors, while at the blackbody irradiation the optimal energy gaps are slightly higher when there are no reflectors than in case with reflectors. Maximal light concentration shifts the optimal energy gaps down for $(0.1-0.2)$eV regardless of the spectrum, while the analysis with reflectors still holds. It should be pointed out that

device exhibits huge dependence on the lowest subcell's energy gap in case of AM1.5 direct normal irradiance due to valleys in the spectrum caused by absorption in the atmosphere.

Another analysis of multi-junction solar cells based on the detailed balance was published by Brown and Green [50] in 2002. They predicted 86.8% efficiency for the devices with infinite number of subcells in both series constrained and unconstrained configuration. They published values of efficiencies and optimal energy gaps under blackbody radiation as well as under AM1.5 in series constrained as well as in unconstrained configurations. In the subsequent publication, authors showed that in case of series constraining the device, the efficiency drop is less than 1.5% relative.

The most complete analysis of solar cells using the analytical approach to quantify intrinsic losses and their effect on the device behavior was done by Hirst and Ekins-Daukes [100] in 2010. They considered that physical mechanisms were not presented clearly enough in the previous studies. This approach to solar cell analysis and photovoltaic conversion was done by considering energy and entropy fluxes. Conclusions were that conversion of thermal energy into entropy free work causes Carnot factor to limit the solar cell efficiency. Boltzmann factor, a consequence of the mismatch between absorption and emission angles which introduces irreversibility, limits the efficiency as well. Next, carrier thermalization, since the carriers are not extracted from the solar cell but non-radiatively recombined, and emission, since the carriers are radiatively recombined, but still not extracted to do useful work, are other limiting factors. Furthermore, the photons with energies lower than the material's energy gap can not be absorbed, which is known as the "below E_g" loss. These intrinsic losses are practically unavoidable, but can be reduced with novel solar cell designs.

The first step in their analysis is determining absorbed and emitted fluxes. Generalized Planck equation can describe the total photon emission of a body at temperature T and chemical potential μ per energy interval dE per unit solid angle Ω

$$n(E,T,\mu,\Omega) = \frac{2\Omega}{c^2h^3}\frac{E^2}{e^{(\frac{E-\mu}{k_BT})}-1} \tag{2.1}$$

where c is the speed of light, h Planck constant and k_B Boltzmann constant. The Sun is a thermal emitter and, therefore, chemical potential is $\mu = 0$ and temperature is T_S, while the photovoltaic device is luminescent emitter at temperature T_A, so $\mu = qV$, where q is carrier charge and V voltage across the device. Now, photon emitted flux from the Sun and absorbed by the photovoltaic device is $n(E, T_S, 0, \Omega_{abs})$ and flux emitted from the photovoltaic device to the environment is $n(E, T_A, \mu, \Omega_{emit})$. Since the device can absorb and emit only photons with energy higher than its energy gap, the photocurrent generated in the device, according to the detailed balance approach, is:

$$J(V) = q\int_{E_g}^{\infty} n(E,T_S,0,\Omega_{abs})dE - q\int_{E_g}^{\infty} n(E,T_A,V,\Omega_{emit})dE \tag{2.2}$$

Since $\mu = qV$, Eq. 2.2 is actually current-voltage characteristics. In case of an short circuit $V = 0$ and therefore $J_{\text{sc}} = J(V = 0)$. In case of open circuit, current is $J = 0$ and voltage in that case can be calculated as:

$$V_{\text{oc}} = E_g\left(1-\frac{T_A}{T_S}\right) - \frac{k_BT_A}{q}ln\left(\frac{\Omega_{emit}}{\Omega_{abs}}\right) + \frac{k_BT_A}{q}ln\left(\frac{\gamma(E_g,T_S)}{\gamma(E_g,T_A)}\right) \tag{2.3}$$

where $\gamma(E,T) = 2k_BT/(c^2h^3)(E^2+2k_BTE+k_B^2T^2)$. The first term in Eq. 2.3 is Carnot factor in open-circuit voltage. In the extreme case when $T_A = 0$ and $T_S \to \infty$ it allows $qV_{\text{oc}} \to E_g$. The second term is called the Boltzmann factor which, as already

mentioned, is a consequence of the mismatch between absorption and emission angles which introduces irreversibility, and, therefore, reduces voltage. The third term describes the increase of free energy per carrier. It is a consequence of the mismatch between the temperatures of absorbed and emitted photons. Excited carriers transfer heat and entropy to the lattice during the cooling process. Reduction in entropy increases reversibility and, thus, voltage. It can happen only in degenerate absorber. In discrete absorbers, photons are absorbed only in a narrow energy range, hence there is no cooling process.
Since the Sun and the device are at different temperatures, there is Carnot loss P_{car}:

$$P_{car} = \frac{E_g}{q} \left(\frac{T_A}{T_S} \right) J_{opt} \tag{2.4}$$

The discrepancy between absorption and emission solid angles cause Boltzman losses P_{bol}:

$$P_{bol} = \frac{k_B T_A}{q} ln \left(\frac{\Omega_{emit}}{\Omega_{abs}} \right) J_{opt} \tag{2.5}$$

Semiconductor ideally absorbs only photons with energies equal to its energy gap E_g. Photons with higher energies are absorbed as well, whereas the excess energy is lost in thermalization, which causes thermalization losses P_{th}:

$$P_{th} = q \int_{E_g}^{\infty} (E - E_g) \; n(E, T_S, 0, \Omega_{abs}) dE \tag{2.6}$$

These types of losses reduce carrier energy and, therefore cause a voltage drop. Emission loss and below E_g loss reduce the number of absorbed photons and, thus, the

current. Emission loss is equal to number of carriers which are radiatively recombined and were not extracted as current P_{em}:

$$P_{em} = E_g \int_{E_g}^{\infty} n(E, T_A, qV_{opt}, \Omega_{emit}) dE \tag{2.7}$$

Since photons with energy lower than the device's energy gap, it is considered as a loss as well P_{bel}:

$$P_{bel} = \int_{0}^{E_g} E \; n(E, T_S, 0, \Omega_{abs}) dE \tag{2.8}$$

Carnot loss can be reduced by keeping the device operating at lower temperatures, e.g. using heat sink. Solar irradiation concentration reduces irreversibility, and, thus, voltage drop associated with Boltzmann losses. The same effect can be achieved by limiting the angular emission of photons from the device. Thermalization loss can be reduced by introducing discrete energy selective contacts. This way hot carriers would be extracted to do useful work instead of creating losses in the solar cell. Another way of reducing thermalization losses is by splitting solar spectrum. It can be done with multi-junction solar cells. Multi-junction solar cells increase low energy photons absorption as well.

Losses reduce either a voltage or current in the device. If we understand the origins of the efficiency reducing factors and if we are able to quantify them, we will be able to understand how photovoltaic devices operate, and therefore how to design them properly, in order to maximize the conversion efficiency. Models describing these processes are very complex, which make it very difficult to see which ones affect significantly the device operation and in what way. It makes heuristic algorithms, such as genetic algorithm, crucial for tasks like this.

3

BASIC SEMICONDUCTOR THEORY

There are three major groups in which solid materials can be classified in terms of conductivity: conductors, semiconductors, and insulators. Materials such as fused quartz, pure diamond, and glass have very low conductivity, lower than 10^{-8}S/cm (Fig. 3.1). Conductors like silver, copper, and aluminum, on the other hand, have very high conductivity, higher than 10^{6}S/cm (Fig. 3.1).

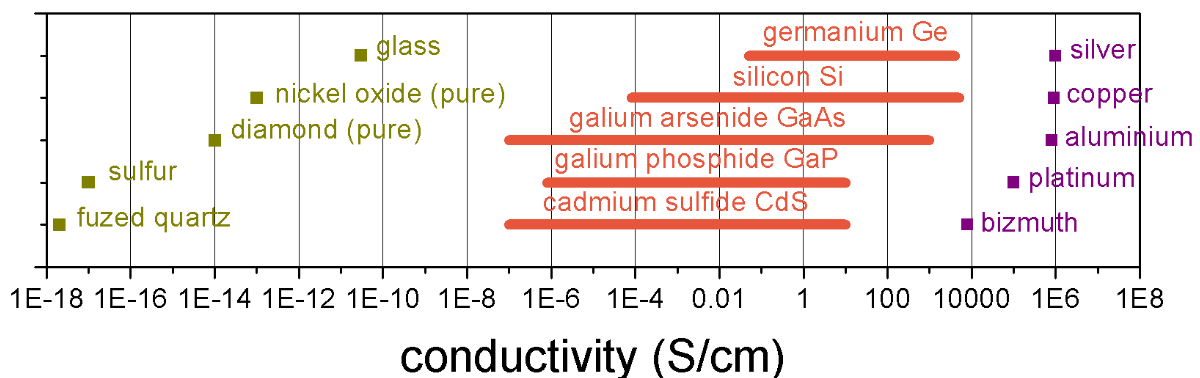

Figure 3.1: Material classification based on conductivity: insulators (yellow), semiconductors (orange) and conductors (purple).

Semiconductors are in between. There are no clear boundaries between these groups. Semiconductors have low conductivity and in that sense, they are similar to insulators, whereas their conductivity can be increased which makes them more similar to conductors. Their conductivity increases under the influence of heat, illumination, magnetic field... Their properties can be altered by introducing impurities as well. This makes them the most important materials for applications in electronics.

Figure 3.2: Materials in Periodic Table: insulators (yellow), semiconductors (orange) and conductors (purple).

Semiconductors can be composed of single atoms (element semiconductors) or alloys composed of multiple atoms. Element semiconductors are in Column IV in the Periodic table (Fig. 3.2). Typical representatives are silicon (Si) and germanium (Ge). Silicon is the most used semiconductor material because silicon devices exhibit good properties at room temperatures and it is one of the most abundant material on Earth (together with hydrogen, oxygen, and nitrogen), so the price is low in comparison with other semiconductors. Alloys can be composed of two (binary compounds), three (ternary compounds) or four atoms (quaternary compounds), or even more. Typical binary compounds are GaAs, AlAs, GaP... They are known as III-V materials since Al and Ga are from Column III in Periodic Table and P and As from Column V (Fig. 3.2). There are II-VI alloys as well, such as CdSe.

3.1 BASIC CRYSTAL STRUCTURE

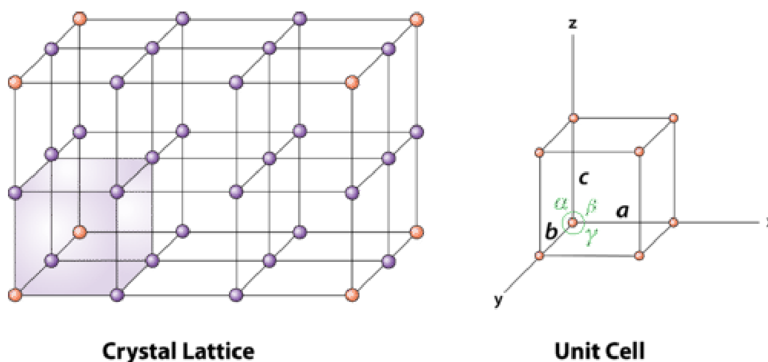

Figure 3.3: Crystal lattice and unit cell. [4]

Semiconductors are generally arranged in a periodic fashion, which is called crystal lattice (Fig. 3.3). They stay in a fixed position and can not move, except for vibrating. Since they are arranged in a crystal lattice, there is periodicity of a small number of atoms which is called unit cell or primi-

tive cell (Fig. 3.3). The relationship between this unit cell and the crystal lattice is described with three vectors **a**, **b** and **c**.

Vectors **a**, **b** and **c** are not necessarily perpendicular or the same length. Every point in the unit cell has its equivalent point in other cells, which can be represented with:

$$\mathbf{R} = m\mathbf{a} + n\mathbf{b} + p\mathbf{c} \tag{3.1}$$

where m,n and p are integer numbers.

Since the vectors do not need to be of equal length or perpendicular to each other, there are different shapes of the unit cell. There are only 7 crystal systems or shapes: cubic, tetragonal, orthorhombic, monoclinic, rhombohedral, hexagonal and triclinic, whereas there are 14 different crystal lattices (3 different cubic types, 2 different tetragonal types, 4 different orthorhombic types, 2 different monoclinic types, 1 rhombohedral, 1 hexagonal, 1 triclinic), called Bravais Lattices: simple cubic, face-centered cubic, body-centered cubic, simple tetragonal, body-centered tetragonal, hexagonal, simple ortorhombic, face-centered ortorhombic, body-centered ortorhombic, base-centered ortorhombic, rhombohedral, simple monoclinic, base-centered monoclinic and triclinic

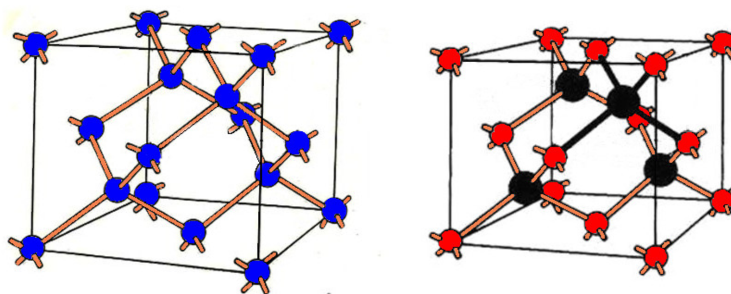

Figure 3.4: Crystal lattice structures common for semiconductors: diamond (left) where all atoms are from column IV, and zincblende (right) where atoms are from columns III (e.g. red) and V (e.g. black).

Element semiconductors crystallize in a diamond lattice structure (Fig. 3.4 left) . It is a form of a face-centered cubic lattice with actually two such sublattices interpenetrating each other with a displacement of $\frac{1}{4}$ along the body diagonal of the cube. Most

of III-V semiconductors have zincblende crystal lattice (Fig. 3.4 right) which is almost identical to the diamond crystal lattice. The difference is that in zincblende one sublattice consists only of column III atoms and the other only of column V atoms. Each atom is surrounded with four atoms from different column.

Since crystal lattices are not completely symmetric, crystal properties along different planes will not be identical. Therefore electrical, mechanical, thermal and other properties of devices fabricated of semiconductor materials will depend on crystal orientation. The crystal orientation planes can be defined using Miller indices (h, k, l). They can be obtained by finding the places where the plane intercepts three Cartesian coordinates. Next, reciprocal values of the distances of those places should be determined. Miller indices are the smallest three integer numbers with the same ratio. If the value of any index is 0, it means that the plane is parallel with the axis. If the plane intercepts the axis on a negative side, Miller indices are presented with a bar over, for example $(\bar{h}, k, l)$.

3.2 CARRIERS IN SEMICONDUCTORS

In both diamond and zincblende lattice atoms are surrounded by four nearest neighbors. Since in diamond lattice all atoms are the same, they have four valence electrons. In order to be in a stable condition, atoms need eight electrons in the outer orbit, therefore they borrow four electrons from their neighbors. It is called covalent bonding. In case of zincblende and III-V alloys, they have atoms with either three or five valence electrons. They share electrons as well in order to reach eight, which makes covalent bonding (Fig. 3.5). Besides dominant covalent bonding, there is a small contribution of an ionic attraction between Ga^{+} and As^{-}.

Since these bonds are strong, in absence of any external excitation, all electrons are in the valence band and there is no conduction. At higher temperatures, under illumination or any other excitation, a small number of electrons breaks the bond and jumps to conduction band where it can participate in current conduction. In that case,

those electrons leave empty spaces which are called holes. The Hole is just absence of electrons, but for simplicity will be observed as a particle. Consequently, it carries charge of the opposite sign than the one electron carries and move in the opposite direction.

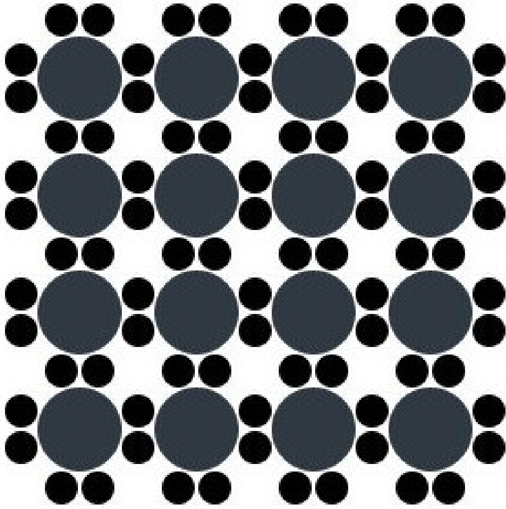

Figure 3.5: Covalent bonding in diamond lattice with dark gray circles as atoms and black circles as electrons.

Some of the electrons gain enough energy to completely break the bond and become completely free, whereas the most of them just loosen the bond while still moving in the periodic potential of the nuclei. In the first case, they have the free electron mass. In the second, the interaction with other particles has to be accounted. That is why the effective mass of electron and hole is introduced. This way, electrons and holes can be treated as a classical charged particles.

Depending on what kind of potential the particle is, its effective mass m^* can be determined from:

$$\frac{1}{m^*} \equiv \frac{1}{\hbar^2}\frac{d^2E(k)}{dk^2} \tag{3.2}$$

The relation between energy E and wave vector k for gallium-arsenide GaAs with different lattice orientation (Miller indices) is presented on a simplified version of energy band diagram Fig. 3.6.

Narrower parabolas for electrons than for holes (HH,LH and SO) indicate lower electron effective mass than hole effective masses.

Another interesting thing that can be seen on the diagram is that GaAs has a minimum of the conduction band in Γ valley and a maximum of the valence band for the same value of momentum. Therefore, excited electrons can directly transition to conduction band without changing in momentum. Semiconductors with similar prop-

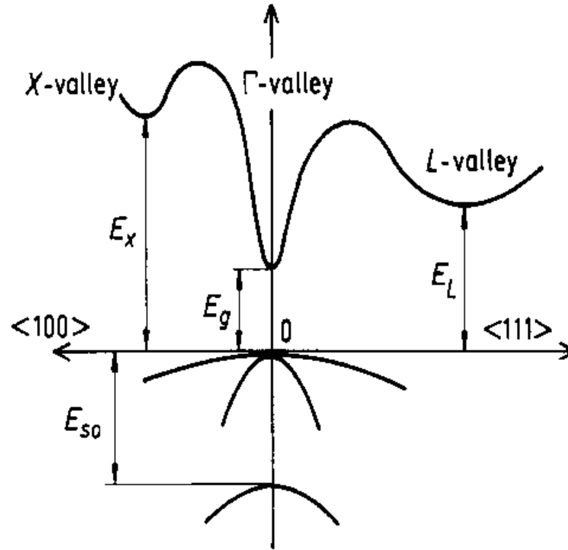

Figure 3.6: Schematic of energy-band diagram for gallium-arsenide with different lattice orientations. [16]

erties are called direct semiconductors. Indirect semiconductors require momentum change in order for the same transition to happen. Typical representatives are silicon and germanium.

As already explained, semiconductors are not such a good conductors since they have low concentration of electrons in the conduction band. Electron distribution of electrons in valence and conduction bands can be described with Fermi-Dirac statistics:

$$f_{FD}(E) = \frac{1}{1 + e^{\frac{E-E_F}{k_B T}}} \tag{3.3}$$

where E is particle energy, E_F Fermi energy, k_B Boltzmann constant and T temperature. The Fermi-Dirac distribution function (f_{FD}) shows what is the probability a particle will occupy a position at energy E. It is very dependent on temperature, which is obvious from Eq. 3.3 and Fig. 3.7.

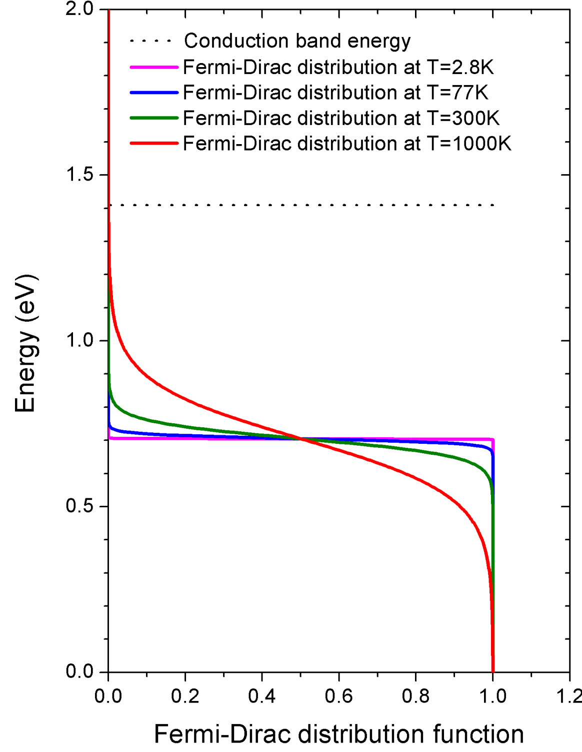

Figure 3.7: Fermi-Dirac distribution function for GaAs at different temperatures, conduction band level is presented on the graph, while valence band level is taken as the reference, i.e. $E_V = 0$

The exact number of electrons per unit volume in the conduction band can be determined as:

$$n = \int_{E_C}^{E_{top}} N(E) f_{FD}(E) dE \tag{3.4}$$

where E_C is the bottom energy of the conduction band, E_{top} is the top of the conduction band, $N(E)$ is the density of states at energy E. Essentially, at each energy there is number of available positions N which electrons can potentially occupy and f_{FD} describes the probability electrons will actually occupy those positions. Concentration of holes in the valence band can be obtained in similar fashion. After solving the

Eq. 3.4, concentration of electrons in conduction band and holes in the valence band is, respectively:

$$n = N_C e^{-\frac{E_C - E_F}{K_B T}} \tag{3.5}$$

$$p = N_V e^{-\frac{E_F - E_V}{K_B T}} \tag{3.6}$$

where E_C is the bottom of the conduction band, E_V is the top of the valence band, N_C and N_V effective densities of states in conduction and valence band, respectively, which can be calculated as:

$$N_C = 2M_C \left(\frac{2\pi m_C^* k_B T}{h^2} \right)^{3/2} \tag{3.7}$$

$$N_V = 2 \left(\frac{2\pi m_V^* k_B T}{h^2} \right)^{3/2} \tag{3.8}$$

where k_B is Boltzmann constant, T temperature, h Planck constant, m_C^* and m_V^* effective masses in conduction and valence band, respectively. Parameter M_C represents the number of equivalent energy minima in the conduction band. For Si $M_C = 6$, for Ge $M_C = 4$, for direct III-V materials $M_C = 1$ and for indirect III-V materials $M_C = 3$. Values of effective densities of states at $T = 300K$ for silicon are $N_C = 2.86 \cdot 10^{19}$ cm^{-3} and $N_V = 2.66 \cdot 10^{19}$cm^{-3}, while for gallium-arsenide $N_C = 4.7 \cdot 10^{17}$cm^{-3} and $N_V = 7 \cdot 10^{18}$cm^{-3}

If a semiconductor contains significantly more carriers generated via thermal excitation than the ones from impurities, it is called intrinsic semiconductor. In such case,

every electron which leaves the valence band leaves a hole behind, therefore, there is an equal number of electrons and holes, so $n = p = n_i$, or:

$$np = n_i^2 \tag{3.9}$$

This relation is called mass action law and stands in any case of thermal equilibrium. Combining equations Eq. 3.5, Eq. 3.6, Eq. 3.9 and $E_g = E_C - E_V$ we can obtain the number of carriers in an intrinsic semiconductor:

$$n_i = \sqrt{N_C N_V} e^{-\frac{E_g}{2k_B T}} \tag{3.10}$$

Values of number of carriers in an intrinsic semiconductor at $T = 300K$ for silicon are $n_i = 9.65 \cdot 10^9 \text{cm}^{-3}$ and for gallium-arsenide $n_i = 2.25 \cdot 10^6 \text{cm}^{-3}$. Obviously, $N_C >> n$ and $N_V >> p$. In this case, $E_C - E_F >> k_B T$ (Eq. 3.5) and $|E_V - E_F| >> k_B T$ (Eq. 3.6).

Next, combining equations Eq. 3.5 and Eq. 3.6 with the property of intrinsic semiconductors where $n = p$, we can obtain the Fermi level in an intrinsic semiconductor:

$$E_F = \frac{E_C + E_V}{2} + \frac{k_B T}{2} ln\left(\frac{N_V}{N_C}\right) \tag{3.11}$$

Since, in most of applications, materials have $E_g > 0.5\text{eV}$ and at room temperatures $k_B T \approx 0.025\text{eV}$, $(E_C + E_V)/2 >> k_B T/2 \cdot ln(N_V/N_C)$, therefore $E_F \approx E_g/2$. The same approximation was assumed in Fig. 3.7.

One of the ways to alter the properties in semiconductors, e.g. increase conductivity, is to introduce impurities. Now the semiconductor is called extrinsic. Impurities can introduce an electron or a hole in the semiconductor. Impurities which are from lower Column than the element semiconductor in the Periodic table will introduce holes. On the other hand, impurities will introduce electrons if they are from a higher Column

than the semiconductor in the Periodic table (Fig. 3.2). I case of alloys, if an atom is replaced by an impurity from a lower Column in Periodic table, the impurity will introduce holes. In the opposite case, the impurity will introduce electrons.

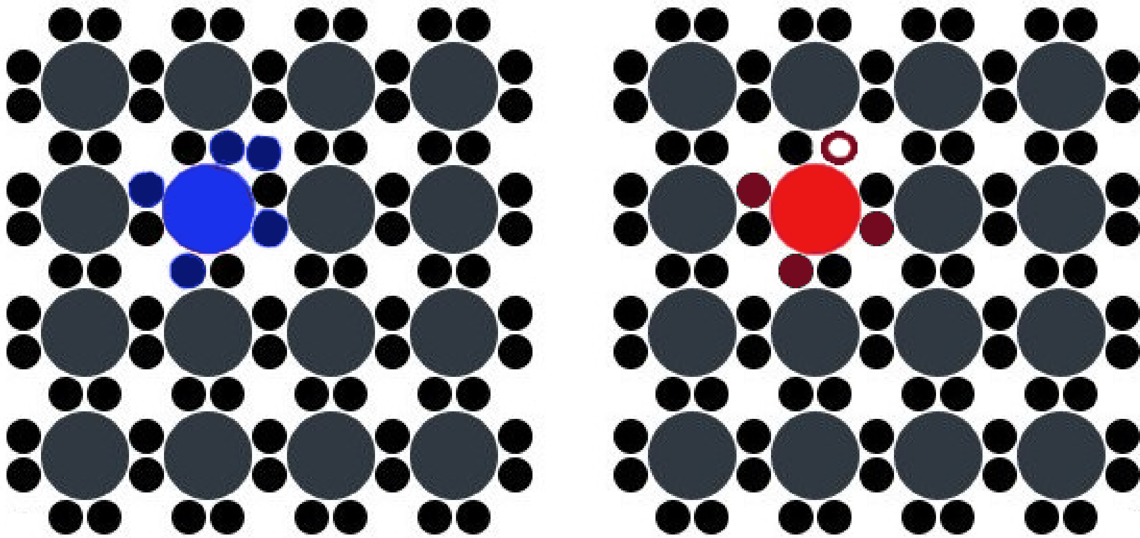

Figure 3.8: Schematic representation of impurities in a crystal lattice consisting of Column IV elements (dark gray) with n-type impurity (blue) and p-type impurity (red)

The easiest way to explain this is graphically (Fig. 3.8). In the first case, one atom from the Column IV (dark gray), e.g. silicon, is replaced by one atom from Column V (blue), e.g. phosphorus. Since atoms from Column V have one electron more (dark blue) than atoms from Column IV (black), four of its electrons will form covalent bonds with surrounding atoms. Meanwhile, the fifth electron, which has relatively small binding energy with the phosphorus atom, will be easily ionized and become a conducting electron in the conduction band. This is how an n-type semiconductor is created and why these impurity atoms are called donors. In the second case, one atom from the Column IV (dark gray), again silicon, is replaced by one atom from Column III (red), e.g. boron. Since boron has one electron less (dark red) than silicon atoms, three of its electrons will form covalent bonds with surrounding silicon atoms. Since there is no fourth electron, there will be a vacancy (dark red ring), which an electron from silicon can fill, leaving another vacancy, i.e. hole. This is how a p-type semiconductor is created and why these impurity atoms are called acceptors.

If the impurities have low ionization energies, we can assume all of them are ionized and, therefore $n = N_d$ and $p = N_a$, where N_d is donor concentration and N_a is acceptor concentration. At the same time, in order to alter the properties of the material significantly, $N_d >> n_i$ and $N_a >> n_i$. Since a semiconductor is usually doped by donors or acceptors, it can be either n-type or p-type material. Since the Eq. 3.9 stands in all cases of thermal equilibrium, it can be used to calculate the minority carrier concentration. In n-type material electrons are majority carriers, so $n_n = N_d$ and holes are minority $p_n = n_i^2/N_d$. Similarly in p-type semiconductor: $p_p = N_a$ and $n_p = n_i^2/N_a$. It is obvious that $n_n >> p_n$ and $n_p << p_p$.

The importance of the Fermi level has already been discussed. It was calculated (Eq. 3.11) with the condition $n = p$. In an extrinsic semiconductor it has to be re-evaluated. General expressions for carrier concentrations (Eq. 3.5 and Eq. 3.6) are still correct, therefore they can be used again, with corrections $n = N_d$ and $p = N_a$. Now, Fermi level in n-type and p-type semiconductor are, respectively:

$$E_F = E_C - k_B T \cdot ln\left(\frac{N_C}{N_d}\right) \tag{3.12}$$

$$E_F = E_V + k_B T \cdot ln\left(\frac{N_V}{N_a}\right) \tag{3.13}$$

Schematic representation doping affecting Fermi-Dirac distribution function is shown in Fig. 3.9. Doping significantly brings Fermi level to either conduction zone either to the valence zone. At higher impurity concentrations, semiconductors can conduct electricity even at room temperatures. At impurity levels around $N = 10^{14}\text{cm}^{-3}$ the conduction is still weak, while at higher impurity levels there is a significant number of carriers in the conduction zone. In an extreme case when impurity concentrations are equal to the effective density of states ($N_d = N_C$ and $N_a = N_V$) value of logarithm in Eqs. 3.12 and 3.13 would be equal to zero and, hence, Fermi level would coincide

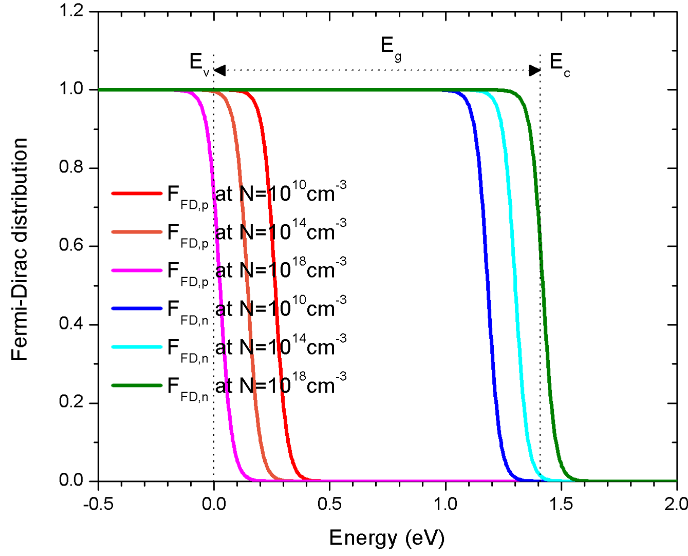

Figure 3.9: Fermi-Dirac distribution function in GaAs doped in various impurity concentrations at 300K temperature; indices "p" and "n" denote p-type and n-type impurities, respectively.

with the bottom of the conduction band in n-type semiconductors ($E_F = E_C$) and would coincide with the top of the valence band in p-type semiconductors ($E_F = E_V$). In this case the expressions Eqs. 3.12 and 3.13 are incorrect. Expressions Eq. 3.5 and 3.6 were derived from Eq. 3.5 under assumption $E - E_F >> 3k_BT$ in Eq. 3.3. Therefore, Eqs. 3.12 and 3.13 are correct only in case of non-degenerate semiconductor, so $E_C - E_F >> 3k_BT$ and $|E_V - E_F| >> 3k_BT$.

3.3 $\mathbf{k} \cdot \mathbf{p}$ METHOD

The $\mathbf{k} \cdot \mathbf{p}$ perturbation theory is commonly used to calculate optical properties and the band structure of semiconductors. It allows derivation of analytic equations for energy dispersion and effective masses. Thanks to the periodicity of the crystal lattice, if the solution of Schrödinger equation is known for one particle in the center of Brillouin zone, it is possible to obtain solutions for any particle at any point in the

Brillouin zone using material's energy gap and matrix element at the center of the zone. Schrödinger equation for a particle at any point of the zone can be written as:

$$H\Psi_n(\mathbf{r}) = E_n\Psi_n(\mathbf{r}) \tag{3.14}$$

where Ψ_n is the wave function of the particle at the discrete level at energy E_n, while H is the Hamiltonian operator. In case of semiconductors, the "particle" can be either hole or electron and the "discrete energy level" can be conduction band or one of the three valence bands: heavy hole, light hole or the spin-orbit split-off band. In general form, due to the periodicity of the lattice potential, the particle wave function can be expressed according to Bloch theorem:

$$\Psi_{n\mathbf{k}}(\mathbf{r}) = e^{i\mathbf{kr}}u_{n\mathbf{k}}(\mathbf{r}) \tag{3.15}$$

where $u_{n\mathbf{k}}(\mathbf{r})$ is Bloch periodic lattice functions for arbitrary direction and wave vector, while $e^{i\mathbf{kr}}$ is a plane wave.

In the center of the zone, where $\mathbf{k_0} = 0$, Hamiltonian can be expressed as:

$$H_0 = \frac{p^2}{2m} + V(\mathbf{r}) \tag{3.16}$$

where $\mathbf{p}$ is the particle momentum, m particle mass and $V(\mathbf{r})$ the periodic lattice potential. Particle away from the center will have different wave vector $\mathbf{k}$, therefore it can be introduced to Hamiltonian as a perturbation. Since the momentum of such particle is $\hbar\mathbf{k}$, the new Hamiltonian is:

$$H = \frac{(\mathbf{p} + \hbar\mathbf{k})^2}{2m} + V(\mathbf{r}) \tag{3.17}$$

Now, since $(\mathbf{p} + \hbar\mathbf{k})^2 = p^2 + 2\hbar\mathbf{k}\mathbf{p} + \hbar^2k^2$, we can say $H_1 = 2\hbar\mathbf{k}\mathbf{p}$ is the first order, and $H_2 = \hbar^2k^2$ second-order perturbation. Due to $\mathbf{kp}$ term in the first order perturbation, this method was named the "kp method" [111]. Provided that the energies and the matrix elements momentum between the wave functions in the center of Brillouin zone are known, band structure in the vicinity of the center can be calculated.

Taking into account both first and second order perturbations with Eqs. 3.16 and 3.17, we can obtain the Hamiltonian:

$$H = H_0 + \frac{\hbar}{m}\mathbf{k}\mathbf{p} + \frac{\hbar^2k^2}{2m} \tag{3.18}$$

Now, combining the previous expression with Eqs. 3.18 and 3.15, we can solve the Schrödinger equation 3.14 and calculate the eigen energy of a particle in a semiconductor:

$$\begin{aligned} E_{n,\mathbf{k}} = E_{n,\mathbf{k}=0} + \frac{\hbar^2}{2m}\sum_{i,j}\mathbf{k_i}\delta_{i,j}\mathbf{k_j} \\ + \frac{\hbar^2}{m^2}\sum_{i,j}\sum_{n\neq m}\mathbf{k_i}\frac{\langle u_{n,\mathbf{k}=0}|\mathbf{p_i}|u_{m,\mathbf{k}=0}\rangle\langle u_{m,\mathbf{k}=0}|\mathbf{p_j}|u_{n,\mathbf{k}=0}\rangle}{E_{n,\mathbf{k}=0} - E_{m,\mathbf{k}=0}}\mathbf{k_j} \end{aligned} \tag{3.19}$$

where discrete energy levels n and m can be conduction, heavy hole, light hole or the spin-orbit split-off band. The vector of momentum operators is $\mathbf{p} = -i\hbar\nabla$ and the matrix elements in Dirac notation are:

$$\langle u_{n,\mathbf{k}=0}|\mathbf{p_i}|u_{m,\mathbf{k}=0}\rangle = -i\hbar\int u_{n,\mathbf{k}=0}\nabla u_{m,\mathbf{k}=0}d\mathbf{r} \tag{3.20}$$

Next, since $\delta_{ii} = 1$ and $\delta_{i \neq j} = 0$ (Kronecker delta function), and taking into account symmetry of Bloch functions and the fact that p is an antisymmetric operator, Eq. 3.19 can be simplified:

$$E_{n,\mathbf{k}} = E_{n,0} + \frac{\hbar^2 k^2}{2m} + \frac{\hbar^2}{m^2} \sum_{n \neq m} \frac{|\langle u_{n,0}|\mathbf{kp}|u_{m,0}\rangle|^2}{E_{n,0} - E_{m,0}} \tag{3.21}$$

Similarly, Bloch function is:

$$u_{n,\mathbf{k}} = u_{n,0} + \frac{\hbar}{m} \sum_{n \neq m} \frac{|\langle u_{n,0}|\mathbf{kp}|u_{m,0}\rangle|^2}{E_{n,0} - E_{m,0}} u_{m,0} \tag{3.22}$$

3.4 ABSORPTION AND GENERATION IN SEMICONDUCTORS

Semiconductor devices are often used in applications such as light sources or light detectors. Therefore, their interaction with light is especially interesting. It is actually the interaction of light with carriers in semiconductors. Carriers in semiconductors can be described by two basic equations: continuity equation and Poisson equation. Continuity equation takes care of carrier number conservation and can be presented in a form for electrons and holes, respectively:

$$\frac{\partial n}{\partial t} = \frac{1}{q} \nabla J_n + G_n - U_n \tag{3.23}$$

$$\frac{\partial p}{\partial t} = -\frac{1}{q} \nabla J_p + G_p - U_p \tag{3.24}$$

where G and R are generation and recombination rates per volume unit in semiconductors. The Poisson equation, on the other hand, describes the relationship between carriers and potential:

$$\nabla^2\phi = \frac{q}{\varepsilon_0\varepsilon_r}(n-p) \tag{3.25}$$

where q is electron charge, ε_0 vacuum permittivity, ε_r relative permittivity, ϕ electrostatic potential.

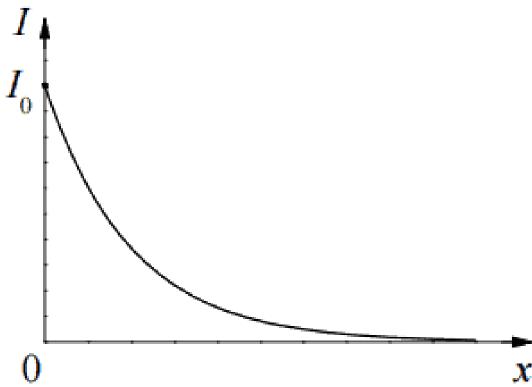

Figure 3.10: Light intensity attenuation as a function of penetration depth with initial intensity I_0.

The interaction of light with semiconductors can be described by generation and recombination (Eqs. 3.23, 3.25). Generation increases the number of carriers by absorption of light and recombination decreases by light emission. On a macroscopic level, light (photon) absorption can be described by absorption coefficient α. If a slab on one side is illuminated with light, the light intensity will be attenuated by traveling through the slab. The attenuation depends on the absorption coefficient and the path traveled through the slab. Represented graphically (Fig. 3.10) and mathematically (Eq. 3.26):

$$I(x) = I_0(x)e^{-\alpha L} \tag{3.26}$$

where $I(x)$ is light intensity in any point, $I_0 = I(x=0)$ is the intensity on the surface of the slab, L thickness of the slab.

The absorption coefficient α depends on the energy of incident photons as well as on material type. It is often approximated by the quadratic relation between absorption coefficient $\alpha \sim (E-E_g)^2$ in case of $E > E_g$, while assuming no absorption otherwise.

If each absorbed photon creates an electron-hole pair, generation per unit volume at coordinate x is:

$$G(x) = \int \Phi(E,x)\alpha(E,x)dEdx \tag{3.27}$$

where $\Phi(E,x)$ if photon flux at each energy and at each coordinate. Using $\Phi(E,x) = \Phi(E)e^{\alpha x}$, taking into account whole spectrum, generation rate in a slab of thickness L is:

$$G(x) = \int_0^\infty \int_0^L \alpha(E,x)\Phi(E)e^{\int_0^x \alpha(E,x')dx'}dEdx \tag{3.28}$$

In order to describe absorption coefficient on a microscopic level, we have to start with Fermi's Golden Rule:

$$W_{i\mapsto f} = \frac{2\pi}{\hbar}|\langle i|\hat{H}|f\rangle|^2\delta(E_f - E_i \mp E) \tag{3.29}$$

where $\hbar$ is Planck constant, $\delta(x)$ Dirac function, E_i energy of initial level $|i\rangle$, E_f energy of final level $|f\rangle$ and $E = E_f - E_i$ photon energy. Negative sign in delta function signifies absorption ($E_f > E_i$) and positive emission ($E_f < E_i$). Fermi Golden Rule is actually a probability of transitioning from one state to another under some influence described with perturbation Hamiltonian $\hat{H}$, when Hamiltonian of interaction is $H = H_0 + \hat{H}$ and H_0 is unperturbed Hamiltonian. Taking this into account, transition rate from lower to higher energy level (absorption) in a semiconductor is:

$$r_{i\mapsto f} \sim W_{i\mapsto f} f_i(1 - f_f)N_f \tag{3.30}$$

where N_f is the density of final states, f_i is probability there is a particle at the initial state, $(1 - f_f)$ is the probability there is an available final state and $W_{i \mapsto f}$ is the probability such transition can happen. If there are particles in the final position as well, there is a probability reverse transitions might happen:

$$r_{f \mapsto i} \sim W_{i \mapsto f} f_f (1 - f_i) N_i \tag{3.31}$$

where N_i is the density of initial states, f_f is probability there is a particle at final state, $(1 - f_i)$ is the probability there is an available initial state. According to quantum mechanics, the same matrix element is responsible for transitions in both directions, therefore, $W_{i \mapsto f}$ is the probability the transition from final to initial state can happen as well. Now, the net transition rate is the difference of transition rates from initial to final and reverse transition rate:

$$\begin{aligned} r(E) &= \frac{2\pi}{\hbar} \int \int |\langle i|\hat{H}|f\rangle|^2 \delta(E_f(\mathbf{k_i}) - E_i(\mathbf{k_i}) \mp E) \\ &\times \quad (f(E_i(\mathbf{k_i})) - f(E_f(\mathbf{k_f}))) N_i(\mathbf{k_i}) N_f(\mathbf{k_f}) d^3\mathbf{k_i} d^3\mathbf{k_f} \end{aligned} \tag{3.32}$$

In order to determine matrix element $\langle i|\hat{H}|f\rangle$, we have to introduce vector potential $\mathbf{A}(\mathbf{r}, t)$ and scalar potential $\Phi(\mathbf{r}, t)$. In case if Coulomb gauge is chosen:

$$\begin{aligned} \Phi &= 0 \\ \nabla \cdot \mathbf{A} &= 0 \end{aligned} \tag{3.33}$$

Now Hamiltonian of interaction can be written as:

$$H = \frac{(\hat{\mathbf{p}} + \frac{q}{c}\mathbf{A})^2}{2m_0} + V \tag{3.34}$$

where $\hat{\mathbf{p}}$ is momentum operator and V potential in which the transition occurs. Taking into account Coulomb gauge, the fact that $\hat{\mathbf{p}}$ does not commutate with $\mathbf{A}$ and neglecting the term containing $q^2\mathbf{A}^2$, Hamiltonian of interaction becomes:

$$H = \frac{\hat{\mathbf{p}}}{2m_0} + \frac{q}{2m_0 c}\mathbf{A}\hat{\mathbf{p}} + V \tag{3.35}$$

Since $H_0 = \hat{\mathbf{p}}^2/(2m_0) + V$, the perturbation Hamiltonian is:

$$\hat{H} = \frac{q}{2m_0 c}\mathbf{A}\hat{\mathbf{p}} \tag{3.36}$$

The advantage of $\hat{H}$ is that it can be easily combined with $\mathbf{k} \cdot \mathbf{p}$ theory (Eqs. 3.19 - 3.22) due to $\hat{\mathbf{p}}$. Using above mentioned expressions, in case of electric dipole approximation, matrix element $\langle i|\hat{H}|f\rangle$ can be determined the same way as in [219]:

$$\langle i|\hat{H}|f\rangle = i\frac{q}{m_0\omega}\frac{E_0}{2}M_{if} \tag{3.37}$$

where E_0 is electromagnetic field strength, ω angular frequency, the dipole matrix element $M_{if} = |\langle i|\hat{e} \cdot \hat{\mathbf{p}}|f\rangle|$ and $\hat{e}$ is polarization vector. Finally, introducing Eq. 3.37 into Eq. 3.32 we can obtain:

$$\begin{aligned} r(E) &= \frac{2\pi}{\hbar}\frac{q^2}{m_0^2\omega^2}\frac{E_0^2}{4}\int\int M_{if}^2 \delta(E_f(\mathbf{k_i}) - E_i(\mathbf{k_i}) \mp E) \\ &\times (f(E_i(\mathbf{k_i})) - f(E_f(\mathbf{k_f})))N_i(\mathbf{k_i})N_f(\mathbf{k_f})d^3\mathbf{k_i}d^3\mathbf{k_f} \end{aligned} \tag{3.38}$$

Since transition rate depends on electromagnetic field strength E_0, which is closely related to light intensity I, we can make use of Eq. 3.26 and express absorption in terms of intensity:

$$\alpha = -\frac{1}{I}\frac{dI}{dx} \tag{3.39}$$

The intensity of radiation in a semiconductor can be expressed as:

$$I = U_E c \tag{3.40}$$

where $c = c_0/n$ is the speed of light in the observed medium, c_0 speed of light in vacuum, n refraction index of a medium and U_E energy density of the radiation. Plane wave, traveling through the medium, transfers its energy at the same rate (if averaged per cycle) as it's loosing it's intensity with distance, so:

$$\frac{\partial U_E}{\partial t} = \frac{\partial I}{\partial x} \tag{3.41}$$

Combining Eqs. 3.39-3.41 and relation between energy density of the radiation U_E and electromagnetic field strength E_0, $U_E = n^2 E_0^2/(8\pi)$, absorption coefficient is:

$$\alpha = -\frac{8\pi}{E_0^2 n c_0}\frac{\partial U_E}{\partial t} \tag{3.42}$$

Finally, the connection between U_E and $r(E)$ in this case can be expressed with:

$$\frac{\partial U_E}{\partial t} = -E r(E) \tag{3.43}$$

With all relations in place, the expression for absorption coefficient is:

$$\begin{aligned} \alpha(E) &= \frac{4\pi^2}{\hbar}\frac{q^2}{nc_0 m_0^2 \omega^2}E\int\int M_{if}^2 \delta(E_f(\mathbf{k_i}) - E_i(\mathbf{k_i}) - E) \\ &\times (f(E_i(\mathbf{k_i})) - f(E_f(\mathbf{k_f})))N_i(\mathbf{k_i})N_f(\mathbf{k_f})d^3\mathbf{k_i}d^3\mathbf{k_f} \end{aligned} \tag{3.44}$$

Taking into account relation $E = \hbar\omega$, we can introduce $A_\alpha = 4\pi^2 q^2 \hbar/(nc_0 m_0 E)$. For low-intensity irradiation not too many electrons are being transferred to the conduction band, therefore it can be considered practically empty ($f_f \approx 0$) while the valence band can be considered full ($f_i \approx 1$). Consequently, absorption coefficient α can be written as:

$$\alpha(E) = \frac{A_\alpha}{m_0}E\int\int M_{if}^2 \delta(E_f(\mathbf{k_i}) - E_i(\mathbf{k_i}) - E)N_i(\mathbf{k_i})N_f(\mathbf{k_f})d^3\mathbf{k_i}d^3\mathbf{k_f} \tag{3.45}$$

This macroscopic expression for absorption coefficient is very general. Matrix element M_{if} includes different transitions and can be applied to both direct and indirect semiconductors. Since it contains the densities of initial and final states for different wave vectors $\mathbf{k}$, it is possible apply it to semiconductors with different crystal orientations.

4

SOLAR CELL PARAMETERS AS A FUNCTION OF ENERGY GAP

In III-V semiconductors most of the material parameters, like effective masses, effective densities of states or intrinsic carrier concentrations, depend directly on energy gap of the material. Other parameters can be derived from these basic parameters. These relations can be derived from $\mathbf{k} \cdot \mathbf{p}$ theory (Eqs. 3.19 - 3.22).

Expression 3.19 can be presented in terms of an effective mass m^* [178]:

$$E_{n,\mathbf{k}} = E_{n,\mathbf{k}=0} + \sum_{i,j} \frac{\hbar^2}{2m^*_{ij}} \mathbf{k_i k_j} \tag{4.1}$$

where effective mass is:

$$\frac{m}{m^*_{ij}} = \delta_{i,j} + \frac{\hbar}{m} \sum_{n \neq m} \frac{\langle u_{n,\mathbf{k}=0} | \mathbf{p_i} | u_{m,\mathbf{k}=0} \rangle \langle u_{m,\mathbf{k}=0} | \mathbf{p_j} | u_{n,\mathbf{k}=0} \rangle}{E_{n,\mathbf{k}=0} - E_{m,\mathbf{k}=0}} \tag{4.2}$$

Since we are interested in effective masses in semiconductors, mass m in previous expressions can be replaced with free electron mass m_0. Solving Eq. 4.2 at Γ point (Fig. 3.6) near $\mathbf{k} = 0$ only for conduction and valence bands and taking into account spin-orbit splitting, we can come to an expression for electron effective mass m_e [112]:

$$m^*_e = \frac{m_0}{1 + \frac{2P^2}{3m_0} \left(\frac{2}{E_g} + \frac{1}{E_g + \Delta} \right)} \tag{4.3}$$

where m_0 is the free electron mass, E_g the energy gap and Δ the spin-orbit splitting and P is the optical dipole matrix element between conduction and valence band states in Γ point. Magnitude of the optical dipole matrix element is approximately $P = \frac{2\pi\hbar}{a}$, where a is the lattice constant. The approximation stands for nearly free electron gas. For most of $III - V$ semiconductors $\frac{2P^2}{m_0} \approx (21 - 26)$eV, which is surprisingly constant. Measured values of m_e^* are compared with the values calculated using Eq. 4.3. Electron effective masses were calculated under assumption $\frac{2P^2}{m_0} = 20$eV. Taking these approximations into account, Eq. 4.3 becomes:

$$m_e^* = \frac{m_0}{1 + \frac{20eV}{3}\left(\frac{2}{E_g} + \frac{1}{E_g + \Delta}\right)} \tag{4.4}$$

Similarly, light hole m_{lh}^*, heavy hole m_{hh}^* and spin-orbit interaction m_{so}^* effective masses can be calculated from expressions:

$$m_{lh}^* = \frac{m_0}{1 + \frac{2}{3}\frac{20eV}{E_g}} \tag{4.5}$$

$$m_{hh}^* = \frac{m_0}{2} \tag{4.6}$$

$$m_{so}^* = \frac{m_0}{1 + \frac{1}{3}\frac{20eV}{E_g + \Delta}} \tag{4.7}$$

These models provide results (Fig. 4.1a) which are in agreement with experiments [205]. Lines represent values from models and dots experimental values. Further, effective

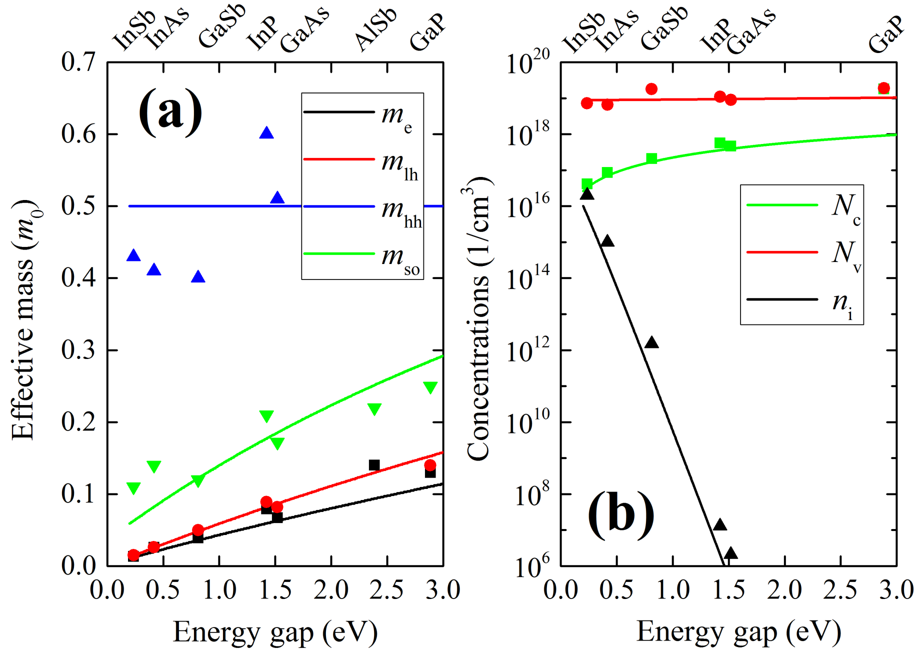

Figure 4.1: Measured and calculated values of (a) effective masses and (b) effective densities of states and intrinsic carrier concentration [201]

density of states in conduction N_C (Eq. 3.7) and valence N_V (Eq. 3.8) band can be calculated:

$$N_C = 2\left(\frac{2\pi m_e^* k_B T}{h^2}\right)^{3/2} \tag{4.8}$$

$$N_V = 2\left(\frac{2\pi m_h^* k_B T}{h^2}\right)^{3/2} \tag{4.9}$$

where $m_h^* = (m_{lh}^{*3/2} + m_{hh}^{*3/2})^{2/3}$. In this case, conduction band effective mass is equal to electron effective mass ($m_C^* = m_e^*$) and valence band effective mass is equal to reduced mass ($m_V^* = m_h^*$). Next, intrinsic carrier concentration n_i can be calculated as:

$$n_i = \sqrt{N_C N_V} e^{-E_g/2k_B T} \tag{4.10}$$

Agreement with experiments [18] still stands (Fig. 4.1b). Lines represent values from models and dots experimental values.

Another important parameter in semiconductor materials is refraction index $\bar{n}$. Since there is no simple way to analitically determine its relation to energy gap E_g, it has to be approximated. One of such relations is [123]:

$$\bar{n} = KE_g^C \tag{4.11}$$

where $K = 3.3668$ and $C = -0.32234$. Constants K and C were obtained from the regression fitting method used on the large set of experimental data on refractive index of semiconducting and oxide materials, and it is valid in the region $E_g \in [0.1 - 8.5]$ eV [123].

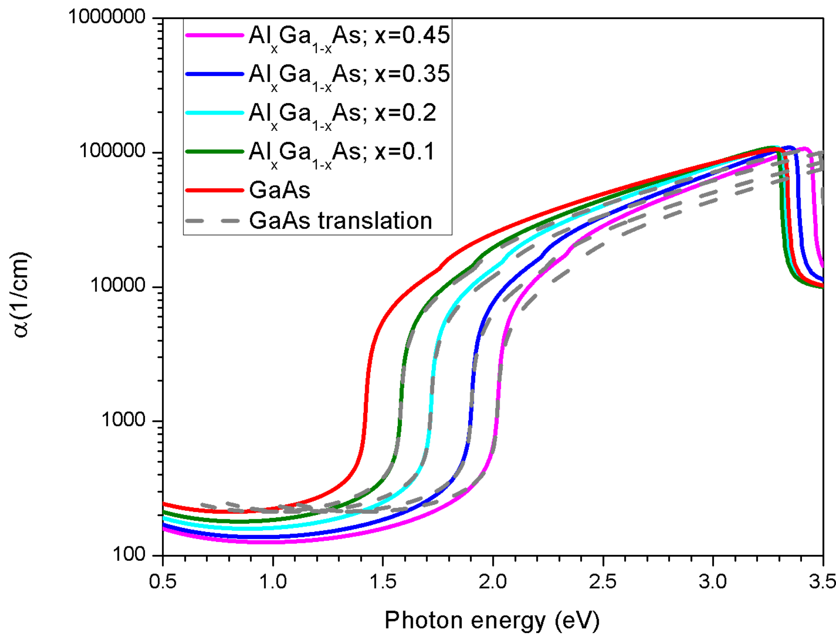

Figure 4.2: Calculated absorption coefficients for various alloys and comparison with translated absorption coefficient for GaAs along the x-axis.

Absorptions are calculated using parallel implementation of the multi-band $\mathbf{k} \cdot \mathbf{p}$ code `kppw` [198]. If the optimization procedure is such that it requires absorption coefficient values for large number of different materials, repeating these calculations

becomes very time consuming. Until now there were few methods of approximating absorptions with Heaviside step function ($E < E_g \Rightarrow \alpha = 0; E > E_g \Rightarrow \alpha = const.$) or using $E < E_g \Rightarrow \alpha = 0; E > E_g \Rightarrow \alpha \sim \sqrt{E > E_g}$. Since the photon absorption edge is not perfectly vertical, there is a small absorption even for photon energies below the energy gap, called Urbach tail [200]. In some more detailed analysis, Urbach tail is often taken into account as well. Unfortunately, these are all only approximations.

Since III-V materials with energy gaps in a smal range useful for solar cells have very similar shape of the absorption coefficients (Fig. 4.2), possible solution is to assume identical shape and calculate the absorption only for one material. The absorption can calculated for GaAs in the beginning of the optimization and translated along the x-axis. When absorptions obtained this way are compared with the actual absorption profiles of the real alloys, a very good matching can be observed for materials with energy gaps larger than GaAs (Fig. 4.2). It was assumed the same stands for materials with energy gaps lower then the one of GaAs.

5

BASIC SOLAR CELL THEORY

In semiconductor materials that exhibit quantum properties, the highest populated quantum states at absolute zero temperature, $T = 0$ K, is called the valence band (VB) and the lowest unpopulated is the conduction band (CB). In the region between those bands, there are no energy levels, and the motion of the electrons with such combinations of momentum and energy in $(\hbar\mathbf{k}, E)$ space is forbidden by the laws of quantum physics. The energy difference between the conduction and the valence bands is called energy gap (E_g) and it varies from material to material. For example, insulators have high energy gaps, of the order $E_g > 6$ eV, and higher, whereas metals do not have a band gap at all, because of CB and VB overlap. Semiconductor materials of interest here have E_g similar to the energy of visible light and infrared photons, i.e. between zero and 3 eV. At temperatures higher than absolute zero, a certain number of electrons will get energy higher than the E_g and will be promoted from the VB to CB. The number of those electrons is described by Fermi-Dirac statistics. The empty spaces left in the VB by such promotion are called holes. At this moment, the VB becomes predominantly populated and the CB predominantly unpopulated. In order to be promoted to the CB, the electrons need to receive energy in the excess of the energy of an E_g.

The energy required for electrons to be transferred from VB to CB can be received from the external light sources as well. The light is electromagnetic radiation given, according to laws of quantum mechanics, in chunks (quanta) of energy called "photons". The effect when the electron, promoted from the VB by external light, ends up

bound in empty spaces of the CB is called "photovoltaic effect". The Sun spectrum is not monochromatic, i.e. not all photons have the same energy. The variation of the number of photons from the Sun with temperature and photon wavelength could be initially approximated as a black-body radiation function. This means that the Sun emits radiation at various wavelengths from the infra-red to the ultra-violet part of the spectrum. Semiconductors optimally absorb only small portion of the Sun spectrum, i.e. photons with energies similar to material's E_g. It is transparent for the lower energy photons, while photons with higher energy than the E_g are being rapidly thermalized. When a photon with excess energy in comparison to the E_g is absorbed, this excess energy is usually wasted as heat.

One route to overcome the poor spectral matching by single gap materials, is to introduce materials with different E_g into the solar cell (SC) device. The device, consisting of several layers (subcells) of semiconductor material, each of which with different E_g is called multi-junction solar cell (MJSC). Such design is generally achieved by fabricating subcells with different E_g on top of each other. The topmost subcell is with the highest E_g, and this subcell will be directly exposed to the Sun. This subcell will absorb the photons with energy higher the its E_g. Such subcell is also transparent for the photons with energy lower than its E_g. Next subcell has slightly lower E_g, and so on. Such concept provides for the elimination of the high energy photons from being absorbed in subsequent layers and prevent them to contribute to the losses.

Energy gap is closely related to solar cell voltage and population of electrons and holes in the conduction band to current. Since the electric current is flow of electrons and holes in opposite directions, we need to direct them somehow. In solar cells it can be done using asymmetric structures, like metal-semiconductor junction, heterojunction or homojunction with asymmetric doping, which is most widely used. In asymmetrically doped homojunction we have two parts of the same semiconductor doped differently. Doping can be p-type and n-type. N-type doping increases the number of electrons (donors) and p-type increases the number of holes (acceptors) which contribute to the current. When these two are joint, a built-in potential is

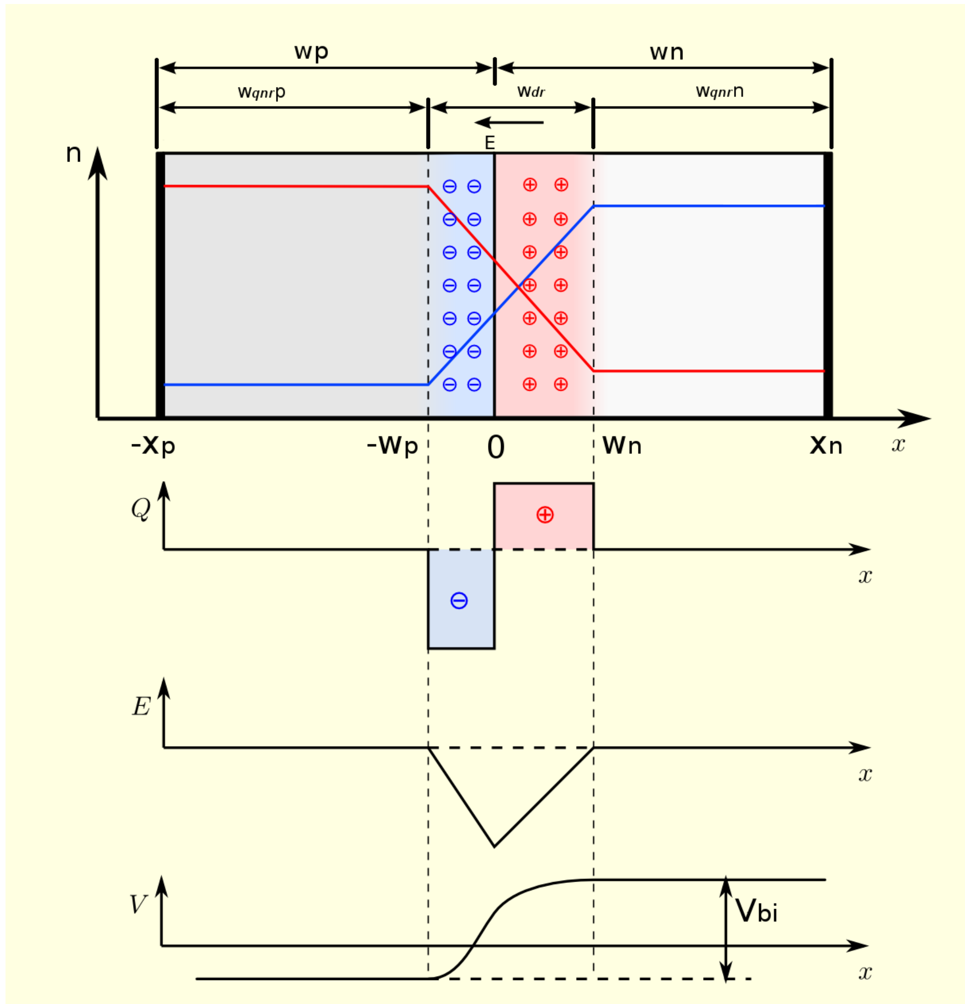

Figure 5.1: PN junction with holes (red) and electron (blue) concentration profile, charge concentration distribution Q, electric field **E** and potentials. [21]

formed. That potential forces electrons and holes to flow in opposite directions and creates the current.

Joining p-type and n-type materials will create a pn-junction (Fig. 5.1). The width of p-type material is w_p and width of n-type material is w_n. Since there are excess of holes in p-side and electrons in the n-side of the junction, diffusion will force them to move across the junction, leaving behind ionized atoms in the lattice, which can not move. Holes are leaving p-side, which makes the atoms left behind negatively charged. On the opposite side, when electrons leave the lattice, the atoms left behind become positively charged. Now, negatively charged atoms on the p-side and positively charged atoms on the n-side create an electric field (**E** on Fig. 5.1.) with the direction from positive n-side to negative p-side. This electric field is called built-in

field and it prevents electrons and holes from diffusing around and forcing the holes to go back to the p-side and electrons back to the n-side. Since the diffusion of the charges to the other side increases the intensity of the electric field, which, on the other hand, is preventing the diffusion, balance is finally reached creating a small depleted area around the place of the junction. This area is called the depletion region. On the Fig. 5.1 it is between $-W_p$ and W_n and its width is w_{dr}. Now, when almost all holes are on the p-side, the amount of positive and negative charges is almost the same, so this region is pretty much neutral. Hence, it is called quasi-neutral P region. On the Fig. 5.1 it is between $-X_p$ and $-W_p$ (width is w_{qnrP}). Similarly applies to n-side. On the Fig. 5.1 quasi-neutral N region is between W_n and X_n and its width is w_{qnrN}. Holes are majority carriers on the p-side and minority on the n-side, which is represented by the red line on the Fig. 5.1. Electrons are majority carriers on the n-side and that is represented by the blue line.

When the pn-junction is under excitation (for example illuminated solar cell) new electron-hole pairs are created across the device. The field **E** quickly forces holes to the p-side and the electrons on the n-side. Now, the concentration of carriers is significantly increased on each side. Since the carriers have opposite charge than the ionized atoms, they create an electric field with the opposite direction, lowering the built-in field. This is called direct polarization. Now, as the external excitation continues, majority carrier concentration on each side is increasing dramatically, which allows strong diffusion to the other side, where they become minority carriers. The electric field is creating drift current and returning them back, but following the enormous concentration of carriers, the diffusion current is significantly larger, which, finally, allows minority carriers to reach contacts and become useful current.

Generally, a p-n junction can be observed as three sections: quasi-neutral p region (left side on the Fig. 5.1), quasi-neutral n region (right side) and space-charge (or depletion) region (in the middle). It is called the depletion-region approximation. In reality, there are no boundaries, but we use it to make our life easier. Namely, to simplify maths. Since the left and right-hand side are quasi-neutral, we consider

that all voltage drop (built-in voltage) is across the depletion region. The following derivations are based on [153, 78, 104].

$$V_{bi} = \frac{k_B T}{q} \ln\left(\frac{N_d N_a}{n_i^2}\right) \tag{5.1}$$

where V_{bi} is the built-in voltage (Fig. 5.1), k_B the Boltzmann constant, T the temperature, q the electric charge, n_i the carrier concentration for intrinsic material, N_d the concentration of donors and N_a the concentration of acceptors.

$$Q = \begin{cases} qN_a & \text{for } x \in (-\mathrm{W_p}, 0) \\ qN_d & \text{for } x \in (0, \mathrm{W_n}) \end{cases} \tag{5.2}$$

$$\frac{d^2\varphi}{dx^2} = \begin{cases} \frac{q}{\varepsilon_0\varepsilon_r} N_a & \text{for } x \in (-\mathrm{W_p}, 0) \\ \frac{q}{\varepsilon_0\varepsilon_r} N_d & \text{for } x \in (0, \mathrm{W_n}) \end{cases} \tag{5.3}$$

$$\mathbf{E} = -\frac{d\varphi}{dx} \tag{5.4}$$

where Q is the charge concentration (Fig. 5.1), φ the electrostatic potential, $\varepsilon_0\varepsilon_r$ the permittivity, $\mathbf{E}$ the electric field (Fig. 5.1) and $\mathrm{W_p}$,$\mathrm{W_n}$ and x are the coordinates, as shown on the Fig. 5.1. Combining (5.2) with Poisson's equation (5.3) and Gauss equation (5.4), we can calculate electric field, potentials and, thus, the voltage across the depletion region. Quasi-neutral regions are considered neutral, so any electric field there is not taken into account.

$$\varphi = \begin{cases} \frac{qN_a}{2\varepsilon_0\varepsilon_r} (x + \mathrm{W_p})^2 + C_p & \text{for } x \in (-\mathrm{W_p}, 0) \\ \frac{qN_d}{2\varepsilon_0\varepsilon_r} (x + \mathrm{W_n})^2 + C_n & \text{for } x \in (0, \mathrm{W_n}) \end{cases} \tag{5.5}$$

constants C_p and C_n are the integration constants and can be calculated from boundary conditions. We can set the boundary conditions by deciding which electrode is going to be the reference point. Or, we can take p-n junction interface as a reference point. It makes no difference since we are interested in voltage and it is the difference between potentials.

$$V = \varphi \left(x = \mathrm{W_n} \right) - \varphi \left(x = \mathrm{W_p} \right) \tag{5.6}$$

Now, we can calculate width of the depletion region.

$$\mathrm{w_{dr,p}} = \sqrt{\frac{2\varepsilon_0\varepsilon_r}{q} \frac{N_a}{N_d \left(N_d + N_a \right)} V_{bi}} \tag{5.7}$$

$$\mathrm{w_{dr,n}} = \sqrt{\frac{2\varepsilon_0\varepsilon_r}{q} \frac{N_d}{N_a \left(N_d + N_a \right)} V_{bi}} \tag{5.8}$$

$$\mathrm{w_{dr}} = \mathrm{w_{dr,p}} + \mathrm{w_{dr,n}} = \sqrt{\frac{2\varepsilon_0\varepsilon_r}{q} \left(\frac{1}{N_d} + \frac{1}{N_a} \right) V_{bi}} \tag{5.9}$$

These results are for thermal equilibrium. When voltage (forward bias) V across the junction is applied, instead of V_{bi} we have $(V_{bi} - V)$. In case of reverse bias, it is $(V_{bi} + V)$.

Currents in quasi-neutral regions are minority carrier based. In quasi-neutral P region (left side on Fig. 5.1) electrons are minority carriers and the expression for current is $j_n(\lambda, x)$. In quasi-neutral N region (right side) minority carriers are holes and current is $j_p(\lambda, z)$.In depletion region current $j_{dr}(\lambda)$ is majority current and depends on a

number of absorbed photons. Expressions for currents are obtainable from transport equations:

$$j_n(\lambda, x) = qD_n \frac{dn}{dx} \tag{5.10}$$

$$j_p(\lambda, x) = -qD_p \frac{dp}{dx} \tag{5.11}$$

where n and p are minority electron and hole concentration and D_n and D_p diffusion coefficients for electrons and holes, respectively. Since it was assumed the regions are neutral, drift dependent parts of the current equations were neglected.

Spectrum can be taken from [22], or can be accounted as black body irradiance and calculated as:

$$I(\lambda, T) = \frac{2\pi hc^2}{\lambda^5 \left(e^{\frac{hc}{\lambda k_B T}} - 1 \right)} \tag{5.12}$$

where h is the Planck constant and c the speed of light. Irradiance $I(\lambda, T)$ unit is $\frac{W}{\mathrm{cm^2 s \mu m}}$. Incident power P_{inc} with unit $\frac{W}{\mathrm{cm^2}}$ can be obtained by integrating irradiance over the whole spectrum. In equations for calculating current, flux $\Phi(\lambda, T)$ with unit $\frac{\mathrm{photons}}{\mathrm{cm^2 s \mu m}}$ is required, so irradiance needs to be converted to flux:

$$\Phi \left[\frac{\mathrm{photons}}{\mathrm{cm^2 s \mu m}} \right] = I \left[\frac{\mathrm{W}}{\mathrm{cm^2 s \mu m}} \right] \frac{\lambda}{hc} \tag{5.13}$$

Using flux together with absorption $\alpha(\lambda)$, generation rate can be determined:

$$g(\lambda, x) = \alpha(\lambda)\Phi(\lambda, T)e^{-\alpha(\lambda)x} \tag{5.14}$$

Next step is solving continuity equations for carriers in quasi-neutral regions. Since we can neglect the electric field in the quasi-neutral regions and sunlight is not changing rapidly with time, continuity equations can be simplified. Differential equation in quasi-neutral P and N regions are, respectively:

$$\frac{d^2n}{dx^2} - \frac{n - n_0}{L_n^2} + \frac{g(\lambda, x)}{D_n} = 0 \tag{5.15}$$

$$\frac{d^2p}{dx^2} - \frac{p - p_0}{L_p^2} + \frac{g(\lambda, x)}{D_p} = 0 \tag{5.16}$$

Boundary conditions in quasi-neutral P and N regions are, respectively:

$$\begin{aligned} n - n_0 &= \tfrac{n_i^2}{N_a}\left(e^{\frac{qV}{k_BT}} - 1\right) \quad & x = -\mathrm{W_p} \\ D_n\tfrac{dn}{dx} &= S_n(n - n_0) \quad & x = -\mathrm{X_p} \end{aligned} \tag{5.17}$$

$$\begin{aligned} p - p_0 &= \tfrac{n_i^2}{N_d}\left(e^{\frac{qV}{k_BT}} - 1\right) \quad & x = \mathrm{W_n} \\ -D_p\tfrac{dp}{dx} &= S_p(p - p_0) \quad & x = \mathrm{X_n} \end{aligned} \tag{5.18}$$

In steady state, like solar illumination, and uniform doping current is constant through the device. That is why we will calculate currents at the edges of the deple-

tion region. After solving Eqs. (5.10 - 5.18) we obtain expressions for currents in both quasi-neutral and depletion regions [154, 78]:

$$j_n(\lambda,-\mathrm{W_p}) = \underbrace{\frac{q\Phi\alpha L_n}{\alpha^2L_n^2-1}\left[\frac{e^{-\alpha \mathrm{w_{qnrP}}}\left(\frac{S_nL_n}{D_n}\cosh\frac{\mathrm{w_{qnrP}}}{L_n}+\sinh\frac{\mathrm{w_{qnrP}}}{L_n}\right)-\left(\frac{S_nL_n}{D_n}-\alpha L_n\right)}{\frac{S_nL_n}{D_n}\sinh\frac{\mathrm{w_{qnrP}}}{L_n}+\cosh\frac{\mathrm{w_{qnrP}}}{L_n}}+\alpha L_n e^{-\alpha \mathrm{w_{qnrP}}}\right]}_{\text{light-dependent part}} \underbrace{-\frac{qD_nn_0}{L_n}\left(e^{\frac{qV}{k_BT}}-1\right)\left[\frac{\frac{S_nL_n}{D_n}\cosh\frac{\mathrm{w_{qnrP}}}{L_n}+\sinh\frac{\mathrm{w_{qnrP}}}{L_n}}{\frac{S_nL_n}{D_n}\sinh\frac{\mathrm{w_{qnrP}}}{L_n}+\cosh\frac{\mathrm{w_{qnrP}}}{L_n}}\right]}_{\text{voltage-dependent part}} \tag{5.19}$$

$$j_p(\lambda,\mathrm{W_n}) = \underbrace{\frac{q\Phi\alpha L_p}{\alpha^2L_p^2-1}e^{-\alpha \mathrm{w_{qnrN}}}\left[\frac{\left(\frac{S_pL_p}{D_p}\cosh\frac{\mathrm{w_{qnrN}}}{L_p}+\sinh\frac{\mathrm{w_{qnrN}}}{L_p}\right)-\left(\frac{S_pL_p}{D_p}-\alpha L_p\right)e^{-\alpha \mathrm{w_{qnrN}}}}{\frac{S_pL_p}{D_p}\sinh\frac{\mathrm{w_{qnrN}}}{L_p}+\cosh\frac{\mathrm{w_{qnrN}}}{L_p}}+\alpha L_p\right]}_{\text{light-dependent part}} \underbrace{-\frac{qD_pp_0}{L_p}\left(e^{\frac{qV}{k_BT}}-1\right)\left[\frac{\frac{S_pL_p}{D_p}\cosh\frac{\mathrm{w_{qnrN}}}{L_p}+\sinh\frac{\mathrm{w_{qnrN}}}{L_p}}{\frac{S_pL_p}{D_p}\sinh\frac{\mathrm{w_{qnrN}}}{L_p}+\cosh\frac{\mathrm{w_{qnrN}}}{L_p}}\right]}_{\text{voltage-dependent part}} \tag{5.20}$$

$$j_{dr}(\lambda) = q\Phi(\lambda)e^{-\alpha \mathrm{w_{qnrP}}}\left(1-e^{-\alpha \mathrm{w_{dr}}}\right) \tag{5.21}$$

The equivalent circuit of an ideal solar cell is shown on (Fig. 5.2). The idea of creating equivalent circuits and models is in a better understanding of device behavior on a macroscopic level. Current I_L is photogenerated current. It is equal to the total sum of currents from depletion region and both quasi-neutral regions without voltage-

dependent part in the equations (5.19 – 5.21). Current I_0 is a diode (dark) current in an ideal solar cell. When there is no sunlight ($\Phi = 0$) only non-zero parts of (5.19 – 5.20) are voltage-dependent.

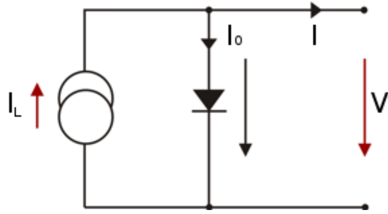

Figure 5.2: Equivalent circuit of an ideal solar cell

In quasi-neutral regions the current results from minority carrier diffusion. Illumination dependent part and voltage dependent part have opposite signs because the dark and illumination currents have the opposite direction. Illumination dependent part is usually a few orders of magnitude larger and that makes for a useful current. Since dark current has the opposite sign, it is effectively decreasing the useful current and is, therefore, accounted as a loss. It is voltage and thermally driven. It depends on material properties, impurities, dimensions etc. so the formulae depends on the particular case. Current I is a solar cell output current. Voltage V is the voltage across the output terminals. Since $I = J/A$, where A is surface size, terms I and J can be used interchangeably.

$$J = J_L - J_0 \tag{5.22}$$

$$J_0 = J_{\text{sat}} \left(e^{\frac{qV}{k_B T}} - 1 \right) \tag{5.23}$$

$$J = J_L - J_{\text{sat}} \left(e^{\frac{qV}{k_B T}} - 1 \right) \tag{5.24}$$

$$J_{\text{sat}} = J_{\text{DARK,0}} + J_{\text{RAD,0}} + J_{\text{SRH,0}} + J_{\text{AUG,0}} \tag{5.25}$$

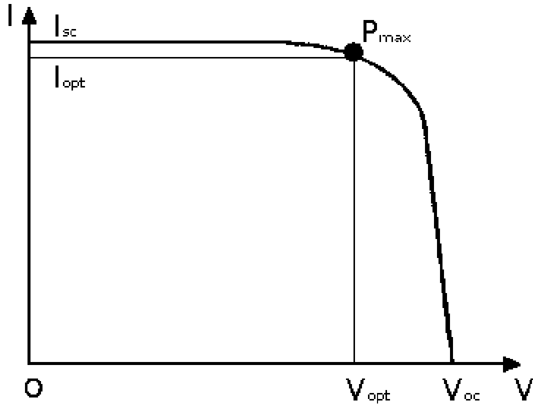

Figure 5.3: JV curve of an ideal solar cell

where J_{sat} is diode saturation current, $J_{\text{DARK},0}$ voltage-dependent part of short-circuit current, $J_{\text{RAD},0}$ radiative recombination current, $J_{\text{SRH},0}$ Shockley-Read-Hall recombination current and $J_{\text{AUG},0}$ Auger recombination current. In an analysis of equations (5.22 – 5.24) and an equivalent circuit (Fig. 5.2) there are two characteristic parameters: V_{oc} - open circuit voltage ($J = 0$) and J_{sc} - short circuit current ($V = 0$). Open circuit voltage is simply voltage across the device when no external load is connected. In case of short circuit current, the device is short-circuited and, hence, the voltage across the device is equal to zero. Current-voltage dependence (also known as JV curve) can be expressed in form of Eq. 5.24, and is presented on Fig. 5.3.

$$J_{\text{sc}} = J_{\text{L}} \tag{5.26}$$

$$V_{\text{oc}} = \frac{k_{\text{B}}T}{q} \ln\left(\frac{J_{\text{L}}}{J_{\text{sat}}} + 1\right) \tag{5.27}$$

$$FF = \frac{J_{opt}V_{opt}}{J_{\text{sc}}V_{\text{oc}}} \tag{5.28}$$

There are two important conclusions from this analysis. First, short circuit current is equal to photogenerated current. It is very useful since it allows us a direct measurement of current generated by sunlight. The other is the fact that voltage depends on current intensity. It means that the higher current, the higher voltage and, thus, the

output power. Furthermore, this means that concentrating sunlight could improve solar cell efficiency. The downside is an increase if temperature which affects efficiency negatively.

Short circuit current J_{sc} is the maximum possible current that can be drained from the solar cell (Fig. 5.3). On the other hand, open circuit voltage V_{oc} is the maximum voltage across the output terminals Fig. 5.3. Unfortunately, voltage is zero for short circuit current and the current is zero for open circuit voltage. Therefore, we have to find the optimal voltage V_{opt} and the optimal current J_{opt} for maximum output power, which can be seen on (Fig. 5.3). Optimal current is always lower than short circuit current and optimal voltage is always lower than open circuit voltage. Another important parameter of solar cells is fill factor FF. It is the quotient of maximum power available from solar and hypothetical output power as a product of open circuit voltage and short circuit current. Slopes on the JV curve (Fig. 5.3) depend on the device quality, so the FF can be observed as a quality measure. Furthermore, JV curve can tell us where is the bottleneck in the solar cell efficiency.

Now, based on preceding analysis we can write the final set of equations for optimization of solar cell performance [154, 78]:

$$j_n(\lambda, -\mathrm{W_p}) = \frac{q\Phi\alpha L_n}{\alpha^2 L_n^2 - 1}\left[\frac{e^{-\alpha \mathrm{w_{qnrP}}}\left(\frac{S_n L_n}{D_n}\cosh\frac{\mathrm{w_{qnrP}}}{L_n} + \sinh\frac{\mathrm{w_{qnrP}}}{L_n}\right) - \left(\frac{S_n L_n}{D_n} - \alpha L_n\right)}{\frac{S_n L_n}{D_n}\sinh\frac{\mathrm{w_{qnrP}}}{L_n} + \cosh\frac{\mathrm{w_{qnrP}}}{L_n}} + \alpha L_n e^{-\alpha \mathrm{w_{qnrP}}}\right] \tag{5.29}$$

$$J_n(-\mathrm{W_p}) = \int_\lambda j_n(\lambda, -\mathrm{W_p})\,d\lambda \tag{5.30}$$

$$j_p(\lambda, \mathrm{W_n}) = \frac{q\Phi\alpha L_p}{\alpha^2 L_p^2 - 1} e^{-\alpha \mathrm{w_{qnrN}}}\left[\frac{\left(\frac{S_p L_p}{D_p}\cosh\frac{\mathrm{w_{qnrN}}}{L_p} + \sinh\frac{\mathrm{w_{qnrN}}}{L_p}\right) - \left(\frac{S_p L_p}{D_p} - \alpha L_p\right)e^{-\alpha \mathrm{w_{qnrN}}}}{\frac{S_p L_p}{D_p}\sinh\frac{\mathrm{w_{qnrN}}}{L_p} + \cosh\frac{\mathrm{w_{qnrN}}}{L_p}} + \alpha L_p\right] \tag{5.31}$$

$$J_p(\mathrm{W_n}) = \int_\lambda j_p(\lambda, \mathrm{W_n}) d\lambda \tag{5.32}$$

$$J_{dr} = \int_\lambda j_{dr}(\lambda) d\lambda \tag{5.33}$$

Short circuit current:

$$J_{\mathrm{sc}} = J_n(-W_p) + J_{dr} + J_p(W_n) \tag{5.34}$$

Combining equations (5.22 – 5.26) we can obtain expression for optimal current:

$$J_{opt} = J_{\mathrm{sc}} - J_{\mathrm{sat}} \left(e^{\frac{qV_{opt}}{k_\mathrm{B}T}} - 1 \right) \tag{5.35}$$

Writing this expression in a slightly different way, we can get the expression for optimal voltage:

$$V_{opt} = \frac{k_\mathrm{B}T}{q} \ln \left(\frac{J_{\mathrm{sc}} - J_{opt}}{J_{\mathrm{sat}}} + 1 \right) \tag{5.36}$$

Finally, efficiency:

$$\eta = \frac{J_{opt} V_{opt}}{P_{\mathrm{inc}}} \tag{5.37}$$

where P_{inc} is total irradiance illuminating the solar cell.

6

MULTI-JUNCTION SOLAR CELLS

Multi-junction solar cells (MJSC) are solar cells (SC) that consist of more than one p-n junction (subcell) made of semiconductors with different energy gaps. The topmost subcell has the highest energy gap. This way it will absorb higher energy photons whose energy would be dominantly converted to heat if absorbed by low band-gap material. On the other hand, it will not absorb photons with lower energies, which allows subcells with lower energy gaps to absorb them more efficiently. This way solar spectrum is divided and each part is absorbed by different subcell specially optimized for those energies.

Effort has been made lately in developing both concentrating and one-sun multi-junction solar cells and significant improvements have been made [119, 97, 120, 156, 30]. In terms of efficiency, the advantage is on multi-junction side comparing with single-junction, unlike price. Multi-junction solar cells are fabricated using less abundant materials in nature which are sparse and, therefore expensive. For that reason, MJSCs are often used in concentrated photovoltaic (CPV) configuration. Here MJSCs have small surface and use significantly cheaper optics for focusing sunlight.

In Fig. 6.1 a schematic of a typical multi-junction solar cell is presented. It consists of three junctions. Namely, top junction, middle junction, and bottom junction. And, tunnel junctions in between. The three junctions behave as three different devices which can be connected in series (series constrained) or can have independent contacts (unconstrained). In series constrained solar cells currents must match. If not, the device with the minimal current will define the output current. On the other hand,

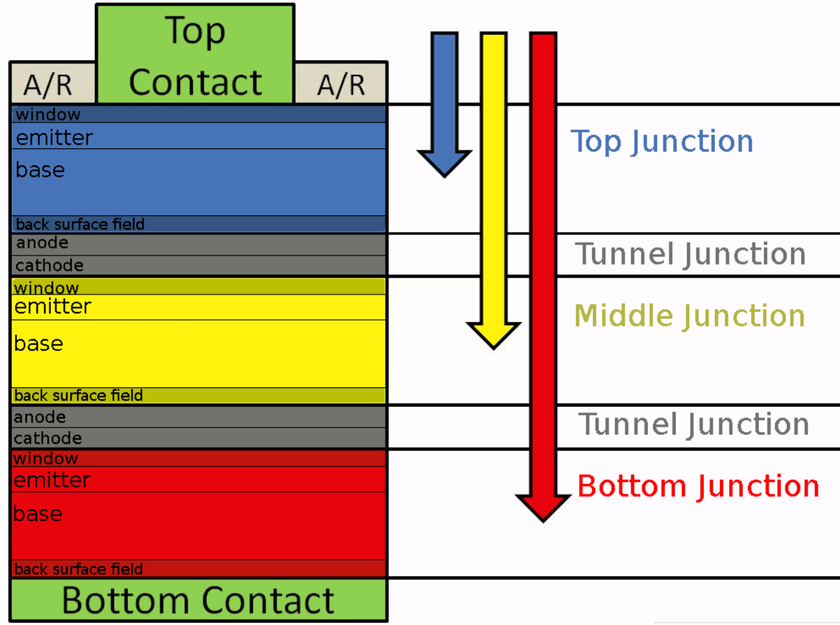

Figure 6.1: Schematic representation of a triple-junction solar cell. [119]

unconstrained solar cells have currents completely independent of each other. At the same time, voltages across the junctions are completely independent in both series constrained and unconstrained. The voltage independence in series constrained SCs gives us the possibility to optimize parameters of junctions in order to achieve the highest possible product of currents and voltages and thus, highest possible output power.

If we observe the middle subcell (Fig. 6.1) as a single SC, it will absorb photons with energies higher than its bandgap (Fig. 6.2), which will generate current $I^{(1)}_{middle}$. The voltage across this subcell will be $V^{(1)}_{middle}$. In a very rough estimation, it can be assumed $V^{(1)}_{middle} \approx E_{g,middle}/q$. Photons with energies larger than its bandgap will thermalize and all excess energy $E_{photon} - E_{g,middle}$ will be lost. This will be prevented by putting another subcell above. This subcell will have larger energy gap ($E_{g,top} > E_{g,middle}$) so the thermalization losses will be lower. If the energy gaps were chosen so in this tandem cell $I^{(2)}_{top} \approx I^{(2)}_{middle}$, their sum will approximately be equal to $I^{(1)}_{middle}$ (SC current from the previous case), therefore the increase in output power is going to be $\approx (E_{g,top} - E_{g,middle})/q \cdot I^{(2)}_{top}$. Hence, the advantage of the tandem cell over the single SC is obvious. Next, since photons with energies lower than $E_{g,middle}$ are transmitted, another subcell with lower energy gap can be added to the structure

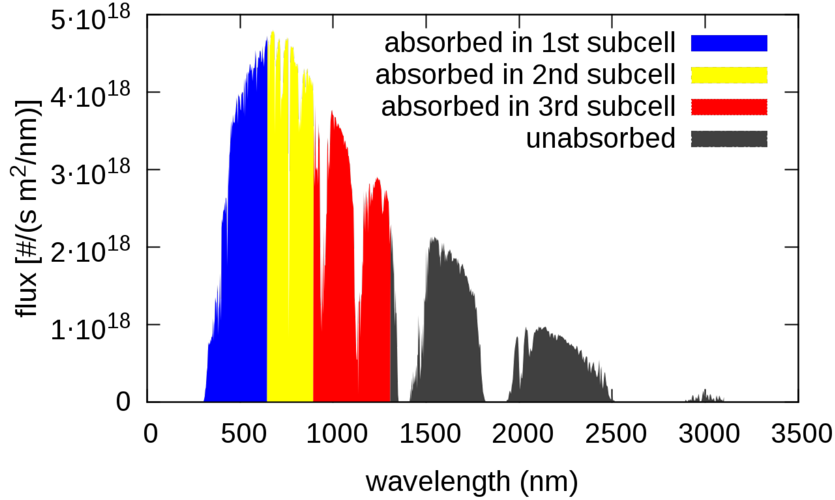

Figure 6.2: Absorption of different parts of solar spectrum in each subcell in a triple-junction solar cell; colors coincide with Fig. 6.1.

($E_{g,middle} > E_{g,bottom}$). The output power will be increased by $I_{bottom} \cdot V_{bottom}$. In the case of series constrained devices, energy gaps have to be chosen properly. Otherwise, the output power can even be decreased.

Thermalization and transmission losses have to be reduced in order to fabricate high efficiency devices, which can be achieved through spectrum splitting. One of the ways is to use advanced optics, such as prisms, beam splitters or holograms [31, 42, 38]. This way photons with certain energy ranges are directed to different appropriate solar cell [31, 42, 66]. Unfortunately, the complexity of the design makes this type of device difficult to reach a competitive price. Another, more convenient way, is to stack solar cells with different energy gaps, as already described, on top of each other. The advantage of multi-junction is well illustrated by comparing single-junction and multi-junction devices. While single junction record-setting device reaches (under one sun illumination) 28% [115], tandem cell (under one sun) reaches 32% [116]. The advantage is even more obvious when comparing to the three-junction device reaching (under one sun) 38% [181].

Above mentioned record-setting devices are based on III-V semiconductors, which are significantly more expensive compared to silicon SCs. Therefore, flat-plate silicon solar cells are more cost-effective. Due to its higher efficiency for the same mass, the III-V MJSCs are standard in space application. Other advantages are radiation

resistivity, which allows high end-of-life efficiency, small temperature coefficient and high reliability [142, 185]. It is interesting that solar cells in space have a slightly lower efficiency (record 35.1% [57, 82]) than on Earth (record 38.8% [57, 82]). It is a consequence of spectrum distribution. In space (AM0 spectrum) there are more high energy photons which are increasing thermalization losses, than on Earth (AM1.5g spectrum) since they are mainly attenuated by the atmosphere.

The main reason for the high prices in III-V SCs is the substrate, which is usually GaAs or Ge. They are fabricated by epitaxial growth on a thick substrate layer, which increases the price significantly. Since in case of space explorations, the price is not the main issue, it was for decades the main driver for MJSC research. Recently, the opportunity to compete in the market on Earth was gained through two concepts: concentrator photovoltaics and epitaxial lift-off. In the first case, optics, which are much cheaper than III-V materials, are used to focus sunlight on a very small area. That allowed very small MJSCs to absorb sunlight from a large area, produce high output power and, hence high efficiency. Currently, (1Q2018) the world record is held by a 4JSC reaching 46% efficiency at 508 suns concentration [15, 14].

The second method deals with the substrate. Since the substrate is unnecessarily thick, the lift-off technique lifts off only a thin solar cell of the substrate, whereas the substrate can be used again [40, 115, 220, 36, 133, 48, 110, 61]. This reduces the price of a newly fabricated thin-film SC. Thin-film SCs are very efficient and flexible, so photovoltaic integrated commercial products are already available or are announced [152, 147]. Another advantage of epitaxial lift-off is an increase in efficiency. Substrate often absorbs photons from luminescence and radiative recombination, which are now, in absence of substrate, being absorbed in the active part of the device and generate electron-hole pair, thus increasing the efficiency [214].

Lift-off can be done by creating a weakened layer in the place where we want to cut the substrate by implanting layer of H^+ ions. The device can now be separated by the substrate by simple tearing. On the other hand, it can be done by etching as well. First, before growing the device, a thin layer can be deposited on the substrate [216, 37]. At

the end, this layer can be etched without damaging the device. The Etching process is very fast, reaching 30mm/hr [182, 107]. This process was used for fabricating the world record single-junction GaAs solar cell [115] and GaInP/GaAs tandem [116].

6.1 multi-junction solar cell device structure

The main part of MJSC is a pn-junction. Due to different disadvantages, it requires additional layers when a photovoltaic device is fabricated (Fig. 6.1). First, it requires a window and back-surface field (BSF) layers which would reduce certain losses and adapt it for use in a device. Next, it requires antireflective coating (ARC) to increase the number of photons reaching the pn-junction. In many types of configuration, it requires tunnel junctions which separate subcells, while they are still electrically and optically connected. Finally, it requires metal contacts, so it can be used as a device. All these additional layers increase the complexity of the device and, hence the price, whereas they are at the same time crucial part in fabricating a photovoltaic device.

Window and BSF layers have passivation as their main role. Passivization reduces surface recombination velocity at interfaces, which has a huge influence on diffusion dark current and short-circuit current, by preventing minority carriers from reaching the surface. At the same time, majority carriers should not be affected. It should effectively be a barrier for the minority carriers. Window and BSF layers should have lattice constant equal as emitter and base and should be very thin in order to reduce the number of crystal defects. As already mentioned, their main role is passivation, therefore photon absorption should be reduced by using high bandgap materials, preferably indirect ones. Window layer should be transparent for light which is about to be absorbed in the observed pn-junction, whereas the BSF layer should be transparent for photons which should be absorbed in subsequent subcells.

Output power in SCs depends directly on the number of absorbed photons. One of the most important issues in all types of optical absorbers is reflection. Since reflection from SC's front surface can reach 30%, reducing it is a very important task

in the solar cell fabrication [195, 213]. This is a consequence of different refractive indices in semiconductors and surroundings medium, often air. The dielectric layer which can reduce the reflection is called anti-reflective coating (ARC). Its refractive index is between indices of the semiconductor and the medium and it's thickness should be equal to an odd multiple of a quarter of a wavelength of interest. This way the reflectance vanishes only for the narrow range of wavelengths, although it is significantly reduced for large part of the solar spectrum. It can be further reduced by introducing a multilayer ARC [213].

Since subcells are separated devices, in most of the configurations they should still be connected in series. The most common way to achieve this is to use tunnel junctions, commonly known as tunnel diodes or Esaki diodes. They are heavily doped pn-junctions where quantum tunneling is the main conduction mechanism. Their main trait is peak tunneling current I_p. While the current passing through them is lower than I_p, they behave as an ohmic contact, i.e. voltage drop across the tunnel junction is proportional to current. While they have high I_p and low equivalent resistance, they are the best solution for interconnections between neighboring subcells.

Electrical contacts (metal contacts) allow for the carriers to be extracted to the outside circuit and used in different applications. Since metal is opaque, it is necessary to make a metallic grid for the top contact which would cover only a part of the surface. If the grid surface is larger, carriers will be extracted more efficiently. At the same time, a smaller number of photons will be absorbed, therefore it is a trade-off which depends on each particular case. Bottom contact can cover the whole surface since it is not necessary to transmit light.

6.2 MULTI-JUNCTION SOLAR CELL DEVICE FABRICATION METHODS

As already mentioned, one of the most expensive parts of a MJSC is the substrate. The substrate is usually a semiconductor with a lower energy gap, since it is often used as a bottom subcell as well. Hence, the low energy gap is very important so

the MJSC would be able to absorb low energy photons as well. Other important characteristics are lattice constant, available impurities, price etc. The substrate defines crystal growth, i.e. lattice constant and crystal orientation. If the lattice constant of the growing material does not match the substrate lattice constant, it will be formed with strain and defects, which greatly lowers the performance. Some of the available materials are shown in Fig. 6.3. Silicon is the most abundant, which means cheap as well. Unfortunately, there are not many materials which could be grown on top of silicon, so it is not often used as a substrate. At the same time, its relatively high band gap prevents it from being used in MJSCs with more than three junctions.

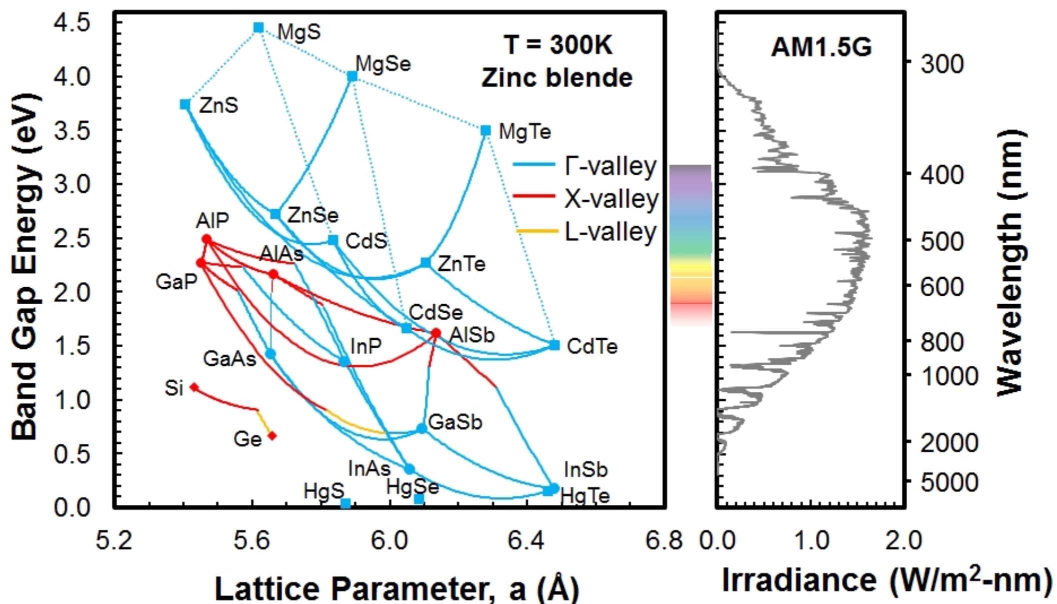

Figure 6.3: Semiconductors with respect to their lattice constant and energy gap (left) and solar irradiance as a function of photon energy (right). [24]

Another very important material is germanium. Due to its low band gap and lattice constant similar to the GaAs, Ge is the standard when it comes to commercial MJSCs [175, 67, 29]. Even more, this device held a world record with 41.6% efficiency (under AM1.5d spectrum and 364 suns concentration) for a while. As already explained, its high price is a limiting factor.

Other materials, such as GaAs can be used as substrate as well. Due to its very high band gap, GaAs can be used only for single-junction and dual-junction SCs [115, 127, 161, 160, 86]. Other promising materials are InP [208, 210, 207, 136, 135] and

GaSb [45, 144, 148, 80, 33]. They both allow growth of high-quality crystals and many different material combinations. Unfortunately, their high price is preventing them from being used more extensively.

Solar cells are fabricated by depositing layers of semiconductor material on the substrate. The process goes by introducing the substrate into an environment with liquid or gaseous materials, or single atoms or molecules, which are being deposited on the substrate layer after layer with the same crystal orientation as the substrate. This process is called epitaxy. There are many different epitaxial processes, such as liquid phase epitaxy (LPE), metal-organic vapor phase epitaxy (MOVPE), molecular beam epitaxy (MBE), etc.

As the name says, in LPE the material is deposited on the substrate from the liquid phase [124]. The required materials are dissolved in a melt of convenient material. When the melt is saturated at a certain temperature, lowering the temperature past the solubility limit causes the deposition. Clearly, this is happening well below the melting point of both the substrate and the deposited material. Materials such as Si, Ge and GaAs are usually grown using centrifugal LPE for thin film solar cell production [52, 76, 140], where temperature and spin are used to control growth speed and impurity concentrations [167, 76]. Unfortunately, it is not reliable enough in the case when the structure consists of a number of different materials.

In case of MOVPE the material is deposited from a gaseous metal-organic precursors [193]. Pressure, temperature and mixture of different gases in a reaction chamber lead to material deposition on the substrate. This way high precision structures can be created at a very high speed of about 10μm/h. Therefore, this is the standard method for III-V MJSC structures fabrication. The downside of this method is the inability to grow high-quality dilute nitride alloys [133].

Very high-quality structures can be grown using MBE [199, 159, 122], including dilute nitrides [172, 109, 180, 122], although at a lower rate than MOVPE (around 1μm/h). A beam of atoms or molecules is created and it reacts on the surface of the substrate, whereas layers of the material are being created. Obviously, a very high

vacuum is necessary for conduction of this type of process. Since the beam is easily controllable, this method is very convenient for different heterostructures, including nanostructure parts of III-V MJSCs [194].

6.3 MULTI-JUNCTION SOLAR CELL DEVICE REALIZATION APPROACHES

There are a number of different approaches in MJSC realization [142, 134, 84, 141, 174]. As already explained, different fabrication methods have different advantages and disadvantages. Next, there are semiconductors with different lattice-constants and energy gaps (Fig. 6.3), which requires creativity to overcome technological difficulties and fabricate high-efficiency multi-junction solar cells. The most common approaches were briefly described in the following.

6.3.1 *Monolithic Lattice-Matched MJSCs*

A straightforward way to fabricate a MJSC device is to grow subcells on top of each other. The main advantage of this approach is production simplicity. A complete device is produced in a single phase. The whole device is grown from the bottom to the top on the selected substrate.

The main disadvantage is that each semiconductor has to have the same or almost equal lattice constants. Otherwise, strain can cause defects, which negatively affects absorption and carrier transport. If the lattice constants are too different, monolithic growth becomes impossible. Materials used for this type of solar cells are semiconductors and/or alloys with similar lattice constants and different energy gaps. This limitation reduces the number of possible materials which could be used for MJSCs.

The most widely fabricated MJSC today is triple-junction GaInP/GaAs/Ge. In this case, Ge ($E_g \approx 0.7eV$) serves as a substrate on which GaAs ($E_g \approx 1.4eV$) and GaInP ($E_g = (1.8 - 1.88)eV$) subcells are grown. The growth is conducted using

MOCVD [106, 157, 158, 117]. Since there is slight lattice mismatch ($\approx 1\%$), a small amount of In can be added while the two upper subcells are grown.

The highest efficiency this device can achieve is 34.1% under one-sun illumination [46] and 41.6% under 364 suns [175]. The efficiency would be higher if the energy gaps could be chosen more optimally. In this configuration, the lowest subcell generates current around twice as high as the two upper subcells, due to low energy gap in Ge. The device is not optimally current matched due to restrictions in lattice constants and energy gaps (Fig. 6.3). Either way, Ge-based subcell increases V_{oc} by $\approx 250mV$.

6.3.2 *Metamorphic MJSCs*

The above-mentioned device should become current-matched with 17% [46] of In in the middle subcell [98, 169], converting it to $Ga_{0.83}In_{0.17}As$, while the top one should be $Ga_{0.35}In_{0.65}P$. Due to significant lattice mismatch in comparison to Ge, epitaxial growth would be very difficult, causing defects and dislocations, which reduce minority carrier lifetime and mobility [70]. Therefore, the buffer layer is introduced [43, 98] to gradually change the lattice constants. This concept is called upright metamorphic. This device can reach 41.1% efficiency at 454 suns illumination [46, 98]. This is lower than the lattice-matched current-mismatched device, although it is still a very good result. Based on theoretical predictions, the expected efficiency could be as high as 45% [169].

Different approaches are possible as well. For example, the efficiency of a MJSC can be increased if Ge bottom subcell ($E_g \approx 0.7eV$) is replaced by high-quality $Ga_{0.7}In_{0.3}As$ subcell [183] ($E_g \approx 1eV$). This device is grown upside down, hence is called inverted metamorphic [29, 87, 196, 81, 181]. First, on the GaAs substrate top subcell is grown, followed by the middle one. These subcells are lattice matched to GaAs substrate, which preserves the crystal quality. Next, the optically transparent buffer layer is grown, followed by the $Ga_{0.7}In_{0.3}As$ bottom subcell. Any crystal defects in the buffer layer affect only the bottom subcell, which is, luckily, very resistant to dislocations.

This type of device can reach efficiencies from 42.6% at 327 suns [89] to 44.4% at 302 suns [26], whereas it can achieve 37.9% at one-sun.

The internal structure of this approach allows different configurations which can exceed 40% efficiency [29, 87, 81, 181] and more than three subcells [175, 29, 166].

6.3.3 *Diluted Nitrogen MJSCs*

The ideal material for a subcell in a MJSCs would be a material with $E_g \approx 1eV$ and lattice matched to GaAs. This type of material can be realized as a dilute nitride alloy [129, 85]. It was noticed that small concentrations of N in GaAs can cause bowing in the band gap and, simultaneously, decrease the lattice constant [211]. Contrary to N, In increases the lattice constant. This means that adding both of them to GaAs the $Ga_{1-x}In_xAs_{1-y}N_y$ alloy can be created. If In and N are added in ratio $y/x = 0.35$, it can lower the energy gap, but at the same time keep lattice constant unaffected. This way a subcell with $E_g = 1eV$ and lattice matched to GaAs can be manufactured, which would make a metamorphic buffer layer unnecessary.

Unfortunately, this type of alloy grown by MOCVD has very poor quality [85, 125, 128, 126, 176, 113]. Fortunately, by adding Sb surfactant it is possible to grow satisfactory high-quality GaInAsNSb by MBE [109], while MOCVD is still not up to the task [118]. MJSC with dilute nitrogen can achieve 43.5% efficiency under 925 suns [63] and 44% under 942 suns [180], which was former world record for 3JSC [25].

Due to its lattice matching to GaAs and Ge, it is possible to fabricate MJSC with 4 or even 5 junctions.

6.3.4 *Mechanically Stacked and Wafer-Bonded MJSCs*

The simplest way to imagine MJSCs is just placing few single-junction SCs over each other. This concept is called mechanical stacking. Seemingly, it is simple but in reality, it is technologically very challenging. It requires perfect alignment of subcells. If

the device has more than two terminals, both top and bottom contacts of one subcell, which have to be grids, have to be aligned with contacts lower subcells to avoid shading. Next, both surfaces of each subcell have to have antireflection coating deposited on. Grid contacts have lower conductance due to its surface, which, again increases losses. Subcells in this configuration could be connected with some type of adhesive, so it might reduce heat dissipation.

If the SCs are connected using only heat and pressure, they are called "wafer-bonded". These devices are realized by bonding two different tandem or 3JSCs using usually only heat and pressure, without the use of any type of adhesive. The device fabricated this way behaves as ordinary two terminal lattice matched devices. The challenge is to create the bond with low resistance. This device can be sensitive to change in the light spectrum as well. MJSCs can be mechanically stacked using some type of adhesive [186] or by transfer printing [53] as well.

Besides previously mentioned disadvantages, there are many advantages to this type of devices. The main one is the independence of subcell. They do not have to be series constrained, therefore they can be optimized independently and operate in optimal regimes. Another huge advantage is in the wider range of possible materials. Since subcells do not need to be grown on top of each other, there are no constraints when it comes to materials, besides energy gaps. In this case, there is no voltage drop across the tunnel junctions since they are unnecessary. One of the first MJSCs was fabricated this way in the 1990s reaching 38% efficiency under 100 suns irradiation [79].

At the moment (2Q2018) the world record is held by the device fabricated by combining lattice matched epitaxial growth with wafer bonding, which has achieved 46% efficiency at 508 suns [65, 15, 14, 96]. Two lattice-matched dual junction solar cells, the first GaInP/GaAs, grown on GaAs substrate, and the second GaInAsP/GaInAs, grown on InP substrate, are mechanically stacked by wafer bonding and reach 44.7% efficiency at 297 suns [82]. Another device, 5JSC, has been reported with 37.8% effi-

ciency at one sun and AM1.5g spectrum [57]. Mechanically stacked SCs using transfer printing can reach up to 43.9% [53].

6.3.5 *III-V on Silicon MJSCs*

As already explained, most of lower energy gap subcells suffer from some type of flaw. Comparing to Ge substrates, Si substrates are much cheaper and have a higher energy gap. That leads to a reduction of current in the subcell, which is not a problem due to excess current in a Ge subcell, and an increase in voltage, which would lead to higher efficiency. In tandem configuration, the ideal match with Si would be subcell with $E_g \approx 1.7eV$, which could achieve 38% efficiency at 500 suns [209]. The the downside of Si is its low lattice constant. Only materials that have lattice matching with Si are GaP and GaPAsN. Due to the already mentioned problems related to diluted nitrogen, there has not been a significant success [88]. With the development of metamorphic growth, there were several attempts to grow GaAs on Si [179]. Direct growth of GaAs on Si leads to significant problems with the crystal structure [75].

Another approach is wafer bonding [220, 36, 64]. Dual junction device with a heterojunction GaInP ($E_g = 1.8eV$) as the upper subcell and Si as the lower one, in four-terminal configuration can reach 29.8% efficiency under one sun and AM1.5g spectrum [69]. Subcells in this device were fabricated separately and then connected by wafer bonding with optically transparent and electrically insulating interlayer. Another device, GaInP/GaAs//Si 3JSC realized in a similar fashion is worth mentioning. Tandem cell $Ga_{0.51}In_{0.49}P$/GaAs was manufactured inverted on a GaAs substrate. It was bonded with Si cell by fast atom beam activation, which leads to a transparent and electrically conductive interface. This device reached 30% efficiency under 112 suns illumination [68].

In the most general form, electron-hole pair generation in the mth subcell can be written as:

$$\begin{aligned} g^{(m)}(\lambda, x) &= \Phi(\lambda) \times \underbrace{[1 - R(\lambda)] \left(\prod_{k=1}^{m-1} [1 - R_k(\lambda)] \right)}_{\text{transmitted through the interfaces}} \\ &\times \underbrace{\left(\prod_{k=1}^{m-1} e^{[-\alpha_k(\lambda)(x_k - x_{k-1})]} \right)}_{\text{absorbed in the upper subcells}} \times \underbrace{e^{[-\alpha_m(\lambda)(x - x_m)]}}_{\text{absorbed in the observed subcell}} \end{aligned} \tag{6.1}$$

where $\Phi(\lambda)$ is the photon flux, $R(\lambda)$ is reflection coefficient on surface of the multi-junction solar cell device, $R_k(\lambda)$ reflection on the interface between the two upper subcells, $\alpha_k(\lambda)$ absorption in the upper subcell and $\alpha_m(\lambda)$ absorption in the mth subcell, x_k coordinate of the interface between k^{th} and $k + 1^{st}$ subcell, x_{k-1} coordinate of the interface between $k - 1^{st}$ and k^{th} subcell and x_m coordinate of the interface between m^{th} and $m + 1^{st}$ subcell.

Absorptions in individual subcells in a multi-junction solar cell are presented in Fig. 6.4, while absorption coefficients are presented in Fig. 6.5. Solar cells absorb photons of energies higher than their energy gap (shorter wavelengths) and are transparent for photons of energies lower than the energy gap (longer wavelengths), as shown on Fig. 6.5. The top subcell absorbs all photons higher than its energy gap (E_g). It is presented with blue color on Fig. 6.4.

However, if the subcell is not thick enough, not all photons are going to be absorbed and some of the higher energy photons will pass to the next solar cell. In this case, the second subcell absorbs photons with energies which are higher than its E_g and lower than upper subcell's E_g, plus all the photons with energies higher than the upper subcell's E_g that were not absorbed. This is presented with yellow color on the Fig. 6.4. The same analogy stands for any number of subcells in a multi-junction solar

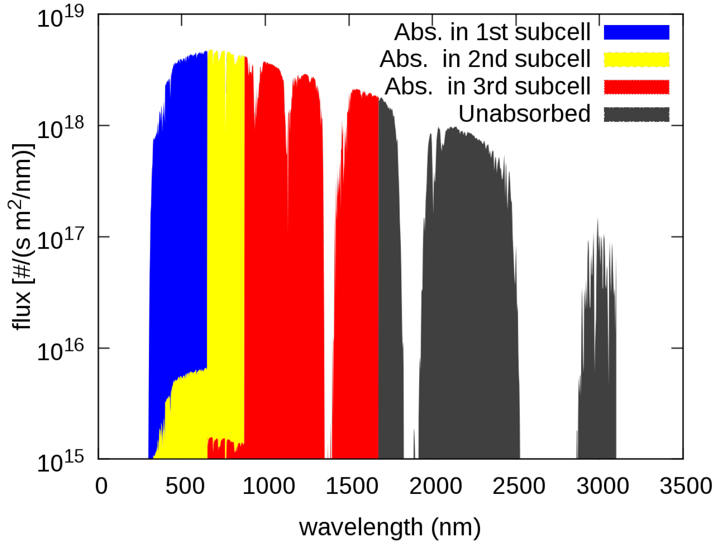

Figure 6.4: Absorption of different parts of solar spectrum in 4-junction solar cell.

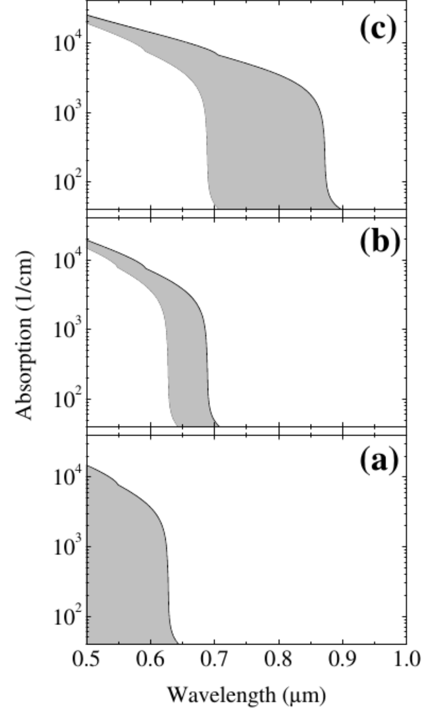

Figure 6.5: Absorption coefficients in the 1st subcells (a), the 2nd subcells (b) and the 3rd subcells (c).

cell. Absorptions are calculated using parallel implementation of the multi-band $\mathbf{k}\cdot\mathbf{p}$ code `kppw` [198]. The general expression for the current generated in the mth subcell is:

$$j^{(m)}(\lambda, x) = q \int_{x_{m1}}^{x_{m2}} \int_{\lambda_{g,l}}^{\lambda_{g,u}} g^{(m)}(\lambda, x) d\lambda dx \tag{6.2}$$

After calculation for a specific region in m^{th} solar cell, we obtain:

$$j_n^{(m)}(\lambda, -\mathrm{W_p}) = \frac{q\Phi^{(m)}\alpha_m L_n}{\alpha_m^2 L_n^2 - 1}\left[\frac{e^{-\alpha_m \mathrm{w_{qnrP}}}\left(\frac{S_n L_n}{D_n}\cosh\frac{\mathrm{w_{qnrP}}}{L_n} + \sinh\frac{\mathrm{w_{qnrP}}}{L_n}\right) - \left(\frac{S_n L_n}{D_n} - \alpha_m L_n\right)}{\frac{S_n L_n}{D_n}\sinh\frac{\mathrm{w_{qnrP}}}{L_n} + \cosh\frac{\mathrm{w_{qnrP}}}{L_n}} + \alpha_m L_n e^{-\alpha_m \mathrm{w_{qnrP}}}\right] \tag{6.3}$$

$$J_{dr}^{(m)}(\lambda) = q\Phi^{(m)}(\lambda)e^{-\alpha_m \mathrm{w}_{\mathrm{qnrP}}}\left(1 - e^{-\alpha_m \mathrm{w}_{\mathrm{dr}}}\right) \tag{6.4}$$

$$j_p^{(m)}(\lambda, \mathrm{W_n}) = \frac{q\Phi^{(m)}\alpha_m L_p}{\alpha_m^2 L_p^2 - 1} e^{-\alpha_m \mathrm{w}_{\mathrm{qnrN}}} \left[\frac{\left(\frac{S_p L_p}{D_p}\cosh\frac{\mathrm{w}_{\mathrm{qnrN}}}{L_p} + \sinh\frac{\mathrm{w}_{\mathrm{qnrN}}}{L_p}\right) - \left(\frac{S_p L_p}{D_p} - \alpha_m L_p\right)e^{-\alpha_m \mathrm{w}_{\mathrm{qnrN}}}}{\frac{S_p L_p}{D_p}\sinh\frac{\mathrm{w}_{\mathrm{qnrN}}}{L_p} + \cosh\frac{\mathrm{w}_{\mathrm{qnrN}}}{L_p}} + \alpha_m L_p \right] \tag{6.5}$$

where reduced flux $\Phi^{(m)}$ takes into account attenuations in previous subcells and $R(\lambda) = R_k(\lambda) = R_m(\lambda) = 0$ is assumed. Optimal current in the mth subcell is:

$$J_{opt}^{(m)} = J_{\mathrm{sc}}^{(m)} - J_{\mathrm{sat}}^{(m)}\left(e^{\frac{qV_{opt}^{(m)}}{k_{\mathrm{B}}T}} - 1\right) \tag{6.6}$$

Written differently, the optimal voltage in m^{th} subcell:

$$V_{opt}^{(m)} = \frac{k_{\mathrm{B}}T}{q}\ln\left(\frac{J_{\mathrm{sc}}^{(m)} - J_{opt}^{(m)}}{J_{\mathrm{sat}}^{(m)}} + 1\right) \tag{6.7}$$

In series constrained multi-junction solar cell with M solar cells $V_{opt} = \sum_{m=1}^{M} V_{opt}^{m}$ and $J_{opt}^{(1)} = J_{opt}^{(2)} = \cdots = J_{opt}^{(M)} = J_{opt}$, hence:

$$V_{opt} = \frac{k_{\mathrm{B}}T}{q}\ln\left[\left(\frac{J_{\mathrm{sc}}^{(1)} - J_{opt}}{J_{\mathrm{sat}}^{(1)}} + 1\right)\left(\frac{J_{\mathrm{sc}}^{(2)} - J_{opt}}{J_{\mathrm{sat}}^{(2)}} + 1\right)\cdots\left(\frac{J_{\mathrm{sc}}^{(m)} - J_{opt}}{J_{\mathrm{sat}}^{(m)}} + 1\right)\right] \tag{6.8}$$

In a slightly more compact form, Eq. 6.8 can be written as:

$$V_{opt} = \frac{k_{\mathrm{B}}T}{q}\sum_{m=1}^{M}\ln\left(\frac{J_{\mathrm{sc}}^{(m)} - J_{opt}}{J_{\mathrm{sat}}^{(m)}} + 1\right). \tag{6.9}$$

Now, power generated in the MJSC can be calculated as a product of optimal current and the voltage across the device:

$$P_{opt} = V_{opt} J_{opt} \tag{6.10}$$

In an unconstrained solar cells, since the currents are independent, the overall power is sum of powers in each subcell:

$$P_{opt} = \sum_{m=1}^{M} V_{opt}^{(m)} J_{opt}^{(m)} \tag{6.11}$$

7

LOSSES IN SOLAR CELLS

One of the most important aspects in fabricating efficient solar cells is keeping voltages across each subcell high. It can be done through losses minimization (Eq. 6.8). In order to do so, a detailed analysis is necessary for how they behave under different circumstances. Three different types of losses were observed. The most dominant in solar cells based on III-V semiconductors are radiative recombination, diffusion dark current, Shockley-Read-Hall recombination and Auger recombination.

Integrating recombination rate across the area of interest, we can calculate a number of carriers recombining per surface per unit of time. Multiplying it with electric charge q, we can obtain the recombination current density:

$$J = q \int_{w} U dz \tag{7.1}$$

7.1 DIFFUSION DARK CURRENT

Current in a solar cell has two contributions, solar irradiation, and voltage across the solar cell. These two contributions have opposite directions and therefore one of them lowers the other (Eqs. 5.19 – 5.20). Since we are producing energy from solar radiation, voltage-dependent part is accounted as a loss. It consists of minority carriers, as

well as solar-generated current. Voltage-dependent part of current equations in both $n-$type and $p-$type materials are [153], respectively:

$$j_{D,n} = \frac{qD_n n_0}{L_n}\left(e^{\frac{qV}{k_B T}} - 1\right)\left[\frac{\frac{S_n L_n}{D_n}\cosh\frac{w_{\mathrm{qnrP}}}{L_n} + \sinh\frac{w_{\mathrm{qnrP}}}{L_n}}{\frac{S_n L_n}{D_n}\sinh\frac{w_{\mathrm{qnrP}}}{L_n} + \cosh\frac{w_{\mathrm{qnrP}}}{L_n}}\right] \tag{7.2}$$

$$j_{D,p} = \frac{qD_p p_0}{L_p}\left(e^{\frac{qV}{k_B T}} - 1\right)\left[\frac{\frac{S_p L_p}{D_p}\cosh\frac{w_{\mathrm{qnrN}}}{L_p} + \sinh\frac{w_{\mathrm{qnrN}}}{L_p}}{\frac{S_p L_p}{D_p}\sinh\frac{w_{\mathrm{qnrN}}}{L_p} + \cosh\frac{w_{\mathrm{qnrN}}}{L_p}}\right] \tag{7.3}$$

In order to calculate diffusion dark current contribution, we need only the voltage independent part of the equations (7.2 – 7.3), which is obvious comparing to (5.23 – 5.25):

$$\begin{aligned} J_{DARK,0} &= \frac{qD_n n_0}{L_n}\left[\frac{\frac{S_n L_n}{D_n}\cosh\frac{w_{\mathrm{qnrP}}}{L_n} + \sinh\frac{w_{\mathrm{qnrP}}}{L_n}}{\frac{S_n L_n}{D_n}\sinh\frac{w_{\mathrm{qnrP}}}{L_n} + \cosh\frac{w_{\mathrm{qnrP}}}{L_n}}\right] \\ &+ \frac{qD_p p_0}{L_p}\left[\frac{\frac{S_p L_p}{D_p}\cosh\frac{w_{\mathrm{qnrN}}}{L_p} + \sinh\frac{w_{\mathrm{qnrN}}}{L_p}}{\frac{S_p L_p}{D_p}\sinh\frac{w_{\mathrm{qnrN}}}{L_p} + \cosh\frac{w_{\mathrm{qnrN}}}{L_p}}\right] \end{aligned} \tag{7.4}$$

7.2 RADIATIVE RECOMBINATION IN III-V SEMICONDUCTORS

One of the most dominant forms of recombination in direct III-V semiconductors is radiative recombination. It is energy radiated from solar cell which is observed as a gray body. Approach in calculations is macroscopic, using Planck law with absorptions calculated using $\mathbf{k} \cdot \mathbf{p}$ method. Derivations have been conducted with

help of [47]. According to Planck, number of photons radiated from a gray body Q_{eq} in frequency range $d\nu$ is:

$$Q_{eq} d\nu = \frac{8\pi \frac{\nu^2}{c'^3} d\nu}{e^{\frac{h\nu}{k_B T}} - 1} \tag{7.5}$$

In gray body, velocity of light is $c' = c/n_{ref}$, where c is velocity of light in vacuum and n refraction index. Radiatively generated electron-hole pairs in thermal equilibrium G_r is:

$$G_r = c' \int_0^\infty \alpha\left(h\nu\right) Q_{eq} d\nu \tag{7.6}$$

where $\alpha\left(h\nu\right)$ is absorption of photons (with energy $h\nu$) in material. Combining (7.5) with (7.6) we get:

$$G_r = \frac{8\pi n_{ref}^2}{h^3 c^2} \int_0^\infty \frac{\alpha(h\nu) \cdot (h\nu)^2}{e^{\frac{h\nu}{k_B T}}} d(h\nu) \tag{7.7}$$

In equilibrium, we have $R_{sp} = G_r$, where R_{sp} is spontaneous radiative recombination. Radiative recombination is the sum of spontaneous and stimulated recombination. Stimulated radiative recombination R_{st} can be calculated from the following relation:

$$\frac{dR_{sp}}{dR_{st}} = e^{\frac{h\nu}{k_B T}} - 1 \tag{7.8}$$

Therefore we have:

$$R_{sp} = \frac{8\pi n_{ref}^2}{h^3 c^2} \int_0^\infty \frac{\alpha \cdot (h\nu)^2}{e^{\frac{h\nu}{k_B T}}} d(h\nu) \tag{7.9}$$

$$R_{st} = \frac{8\pi n_{ref}^2}{h^3 c^2} \int_0^\infty \frac{\alpha \cdot (h\nu)^2}{e^{\frac{h\nu}{k_B T}} \left(e^{\frac{h\nu}{k_B T}} - 1 \right)} d(h\nu) \tag{7.10}$$

Symbols G_r, R_{sp} and R_{st} are values of generation and recombination in equilibrium. Out of equilibrium, symbols g_r, r_{sp} and r_{st} will be used. In the real solar cell, we will have voltage applied to the solar cell, which will disrupt the equilibrium. In that case, while the semiconductor is still non-degenerate:

$$\frac{r_{sp}}{R_{sp}} = \frac{np}{n_0 p_0} = \frac{np}{n_i^2} \tag{7.11}$$

$$\frac{r_{st}}{R_{st}} = \frac{np}{n_0 p_0} = \frac{np}{n_i^2} \tag{7.12}$$

$$r_r = r_{sp} + r_{st} \tag{7.13}$$

where n is electron concentration (Eq. 3.5), p hole concentration (Eq. 3.6) and n_i intrinsic carrier concentration (Eq. 3.10). From here radiative recombination rate is:

$$U_{\mathrm{RAD}} = r_r - g_r \tag{7.14}$$

Since we are dealing with solar cell devices, photon energies we are interested in are above 0.5eV and temperatures $\approx$ 300K, so $e^{\frac{h\nu}{k_B T}} >> 1$ and $r_{sp} >> r_{st}$. Therefore, and combining (7.11 – 7.14):

$$U_{\text{RAD}} = G_r \frac{np - n_i^2}{n_i^2} \tag{7.15}$$

From here we can calculate the radiative recombination coefficient:

$$B_{\text{RAD}} = \frac{U_{\text{RAD}}}{np - n_i^2} = \frac{8\pi n_{ref}^2}{n_i^2 h^3 c^2} \int_0^\infty \frac{\alpha(h\nu) \cdot (h\nu)^2}{e^{\frac{h\nu}{k_B T}}} d(h\nu) \tag{7.16}$$

which is important because it allows us to calculate the influence of radiative recombination on carrier lifetime in p-type (τ_p) and n-type (τ_n) semiconductor:

$$\tau_p = \frac{1}{B_{\text{RAD}} N_a} \tag{7.17}$$

$$\tau_n = \frac{1}{B_{\text{RAD}} N_d} \tag{7.18}$$

where N_a and N_d are acceptor and donor concentration, respectively. From Eq. 7.1 and Eq. 7.15 we can calculate radiative recombination current, using $np = n_i^2 e^{\frac{qV}{k_B T}}$:

$$J_{\text{RAD}} = qwG_r \left(e^{\frac{qV}{k_B T}} - 1 \right) \tag{7.19}$$

In more detailed form:

$$J_{\mathrm{RAD}} = q\mathrm{w}\frac{8\pi n_{ref}^2 n_i^2}{h^3 c^2}\left[\int_0^\infty \frac{\alpha \cdot (h\nu)^2}{e^{\frac{h\nu}{k_\mathrm{B}T}}} d(h\nu)\right]\left(e^{\frac{qV}{k_\mathrm{B}T}} - 1\right) \tag{7.20}$$

$$J_{\mathrm{RAD}} = J_{\mathrm{RAD,0}}\left(e^{\frac{qV}{k_\mathrm{B}T}} - 1\right) \tag{7.21}$$

where $J_{\mathrm{RAD,0}}$ is voltage independent part of radiative recombination current:

$$J_{\mathrm{RAD,0}} = q\mathrm{w}\frac{8\pi n_{ref}^2 n_i^2}{h^3 c^2}\left[\int_0^\infty \frac{\alpha \cdot (h\nu)^2}{e^{\frac{h\nu}{k_\mathrm{B}T}}} d(h\nu)\right] \tag{7.22}$$

Radiative recombination appears in both p-type and n-type semiconductor. In Eq. 7.22 thickness w can be either $\mathrm{w}_{\mathrm{qnrP}}$ or $\mathrm{w}_{\mathrm{qnrN}}$, depending in which region we are calculating it.

7.3 SHOCKLEY-READ-HALL RECOMBINATION

Except for direct radiative recombination, carriers can recombine via localized energy states in the forbidden energy gap. This type of recombination was first described by Shockley and Read [187] and Hall [99] , hence it is known as Shockley-Read-Hall recombination.

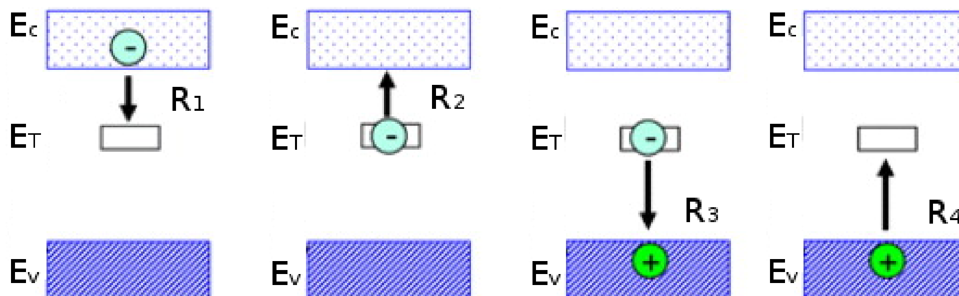

Figure 7.1: Schematic diagram for Shockley-Read-Hall recombination. [197]

There are four processes that take place in this type of recombination (Fig. 7.1): electron capture (R_1), electron emission (R_2), hole capture (R_3), hole emission (R_4). Hole capture is essentially electron emission and hole emission is actually electron capture. The difference between capture and emission $R_1 - R_2$ is electron recombination and $R_3 - R_4$ is hole recombination. Recombination centers (through which recombination takes place) can be either impurities either defects. If they are close to band edges, they are called shallow centers and, similarly, if they are near the middle of the forbidden zone, they are called deep centers. If the energy level of a recombination center is E_T, and if E_F is Fermi level, than the probability it is going to be occupied by an electron is described by Fermi-Dirac distribution:

$$f_T = \frac{1}{1 + e^{\frac{E_T - E_F}{k_B T}}} \tag{7.23}$$

Now, electron capture and emission rates can be written as:

$$R_1 = c_n n N_T (1 - f_T) \tag{7.24}$$

$$R_2 = e_n N_T f_T \tag{7.25}$$

Eq. 7.24 describes the probability of an electron being captured by a recombination center. It depends on electron concentration n, recombination center concentration N_T and probability the center is not already occupied $(1 - f_T)$. Capture probability constant $c_n = \sigma_n v_{th}$ is, essentially, the volume swept out per unit time by an electron with cross section σ_n and mean thermal velocity $v_{th} = \sqrt{3k_B T / m^*}$, where k_B is Boltzmann constant, T temperature and m^* electron mass. Eq. 7.25 describes the probability of an electron being emitted back to the conduction zone by a recombination center. It

depends on emission probability constant e_n, recombination center concentration N_T and probability the center is occupied by an electron f_T.

Next, hole capture and emission rates can be written as:

$$R_3 = c_p p N_T f_T \tag{7.26}$$

$$R_4 = e_p N_T (1 - f_T) \tag{7.27}$$

Eq. 7.26 describes the probability of a hole being captured by a recombination center. It depends on hole concentration p, recombination center concentration N_T and probability the center is not already occupied by a hole (i.e. is already occupied by an electron) f_T. Capture probability constant is $c_p = \sigma_p v_{th}$, σ_n capture cross section and v_{th} mean thermal velocity. Eq. 7.27 describes the probability of a hole being emitted back to the valence zone by a recombination center. It depends on emission probability constant e_n, recombination center concentration N_T and probability the center is occupied by a hole (i.e. not occupied by an electron) $(1 - f_T)$.

In thermal equilibrium the rates of capture and emission of electrons and holes are equal. It means $R_1 = R_2$ and $R_3 = R_4$. Combining with $n = n_i e^{\frac{E_F - E_i}{k_B T}}$ and $p = n_i e^{\frac{E_i - E_F}{k_B T}}$, we can obtain emission probability constants e_n and e_p:

$$e_n = c_n n_i e^{\frac{E_T - E_i}{k_B T}} \tag{7.28}$$

$$e_p = c_p n_i e^{\frac{E_i - E_T}{k_B T}} \tag{7.29}$$

In an nonequilibrium case when the semiconductor is illuminated and generates electron-hole pairs at rate G_L:

$$\frac{dn}{dt} = G_L - (R_1 - R_2) \tag{7.30}$$

$$\frac{dp}{dt} = G_L - (R_3 - R_4) \tag{7.31}$$

In steady state (detailed balance principle) the number of electrons leaving and returning to the conduction band has to be equal ($dn/dt = 0$). Vice versa, the number of holes leaving and returning to the valence band has to be equal as well ($dp/dt = 0$). Therefore:

$$G_L = R_1 - R_2 = R_3 - R_4 = U_{SRH} \tag{7.32}$$

where U_{SRH} is Shockley-Read-Hall recombination. Combining Eqs. 7.23 – 7.32:

$$U_{SRH} = v_{th}\sigma_n\sigma_p N_T \frac{pn - n_i^2}{\sigma_p[p + n_i e^{\frac{E_i - E_T}{k_B T}}] + \sigma_n[n + n_i e^{\frac{E_T - E_i}{k_B T}}]} \tag{7.33}$$

If we assume $\sigma_n \approx \sigma_p \approx \sigma$:

$$U_{SRH} = v_{th}\sigma N_T \frac{pn - n_i^2}{p + n_i e^{\frac{E_i - E_T}{k_B T}} + n + n_i e^{\frac{E_T - E_i}{k_B T}}} \tag{7.34}$$

In n-type semiconductor with low injection rate $n = n_0 + \Delta n \approx n_0$, $p = p_0 + \Delta p$ and $n = n_0 >> p$.

$$U_{SRH,n} = v_{th}\sigma N_T \frac{p - p_0}{n_i e^{\frac{E_i - E_T}{k_B T}} + 1 + n_i e^{\frac{E_T - E_i}{k_B T}}} \tag{7.35}$$

Using $e^{\frac{E_i - E_T}{k_B T}} + e^{\frac{E_T - E_i}{k_B T}} = 2cosh(\frac{E_T - E_i}{k_B T})$:

$$U_{SRH,n} = v_{th}\sigma N_T \frac{p - p_0}{1 + \frac{2n_i}{n_0} cosh(\frac{E_T - E_i}{k_B T})} = \frac{p - p_0}{\tau_p} \tag{7.36}$$

$$\tau_p = \frac{1 + \frac{2n_i}{n_0} cosh(\frac{E_T - E_i}{k_B T})}{v_{th}\sigma N_T} \tag{7.37}$$

Similarly, in a p-type semiconductor with low injection rate:

$$\tau_p = \frac{1 + \frac{2n_i}{p_0} cosh(\frac{E_i - E_T}{k_B T})}{v_{th}\sigma N_T} \tag{7.38}$$

where τ_p and τ_n are hole and electron excess minority carrier lifetimes, respectively. It is very difficult to obtain them analytically, so there are semi-empirical expressions fitted to experimental values for GaAs [138]:

$$\tau(N) = \frac{\tau_0}{1 + (\frac{N}{N_0})^{\gamma}} \tag{7.39}$$

N is doping concentration, fitting parameters for excess minority carriers in p-type material: $\tau_0 = 1877ns$, $N_0 = 5.32 \cdot 10^{15} cm^{-3}$, $\gamma = 1$ and fitting parameters for excess minority carriers in n-type material: $\tau_0 = 1877ns$, $N_0 = 1.67 \cdot 10^{17} cm^{-3}$, $\gamma = 1.89$.

In GaAs, with doping concentration above $10^{15}cm^{-3}$, $1 >> \frac{2n_i}{n_0}cosh(\frac{E_T-E_i}{k_BT})$ and we can assume $\tau = \frac{1}{v_{th}\sigma N_T}$. Now we can write Shockley-Read-Hall recombination rate in GaAs as:

$$U_{SRH} = \frac{pn - n_i^2}{\tau_n[p + n_i e^{\frac{E_i-E_T}{k_BT}}] + \tau_p[n + n_i e^{\frac{E_T-E_i}{k_BT}}]} \tag{7.40}$$

Recombination rate U_{SRH} is independent of dimensions. Multiplying it with electric charge q and material thickness w, we can obtain the Shockley-Read-Hall recombination current density:

$$J_{SRH} = qU_{SRH}w \tag{7.41}$$

Combining Eq. 7.41 with $pn = n_i^2 e^{\frac{qV}{k_BT}}$, more detailed expression can be written as:

$$J_{SRH} = qw\frac{n_i^2}{\tau_n[p + n_i e^{\frac{E_i-E_T}{k_BT}}] + \tau_p[n + n_i e^{\frac{E_T-E_i}{k_BT}}]}\left(e^{\frac{qV}{k_BT}} - 1\right) \tag{7.42}$$

Voltage- independent part of the Shockley-Read-Hall recombination current density is:

$$J_{SRH,0} = qw\frac{n_i^2}{\tau_n[p + n_i e^{\frac{E_i-E_T}{k_BT}}] + \tau_p[n + n_i e^{\frac{E_T-E_i}{k_BT}}]} \tag{7.43}$$

7.4 BAND-TO-BAND AUGER RECOMBINATION IN III-V SEMICONDUCTORS

At high carrier concentrations, collisions become inevitable. It is causing recombination of the first carrier and excitation of the second to a higher kinetic energy. Increase

in the energy of the second is equal to released energy by recombination. Finally, the second carrier will relax to the band edge and the extra energy will be lost as heat. In this type of recombination three particles are involved. One electron and one hole take part in recombination. Both electron and hole can be excited to different energy levels. We take that into account as different types of recombination. Auger recombination rates are: U_n for electrons and U_p for holes. Since in Auger processes three particles are involved (two in recombination and one in excitation), we can write Auger coefficients as:

$$U_n = C_n n^2 p \tag{7.44}$$

$$U_p = C_p p^2 n \tag{7.45}$$

where C_n and C_p represent coefficients of Auger recombination for electrons and holes, respectively. Opposite process is impact ionization with coefficients B_n and B_p. In a nonequilibrium case when the semiconductor is illuminated and generates electron-hole pairs at rate G_L:

$$\frac{dn}{dt} = G_L + (B_n n - C_n n^2 p) + (B_p p - C_p p^2 n) \tag{7.46}$$

In steady state ($dn/dt = 0$) when there is no external generation ($G_L = 0$) the number of carriers generated through impact ionization and recombined through Auger

recombination has to be equal for both electrons and holes, so $B_n n = C_n n^2 p$ and $B_p p = C_p p^2 n$. Now:

$$B_n = C_n np = C_n n_i^2 \tag{7.47}$$

$$B_p = C_p pn = C_p n_i^2 \tag{7.48}$$

where n_i is intrinsic carrier concentration. In steady state when there is external generation the number of overall carriers generated and recombined has to be equal ($G_L = U_{AUG}$). Combining Eqs. 7.46 – 7.48:

$$U_{AUG} = C_n n(np - n_i^2) + C_p p(pn - n_i^2) = (C_n n + C_p p)(pn - n_i^2) \tag{7.49}$$

where U_{AUG} is the overall Auger recombination in the device. Influence Auger recombination has on electron lifetimes (τ_n) and hole lifetimes (τ_p) can be expressed as:

$$\tau_n = \frac{1}{C_p N_a^2} \tag{7.50}$$

$$\tau_p = \frac{1}{C_n N_d^2} \tag{7.51}$$

where N_a and N_d are acceptor and donor concentration respectively.

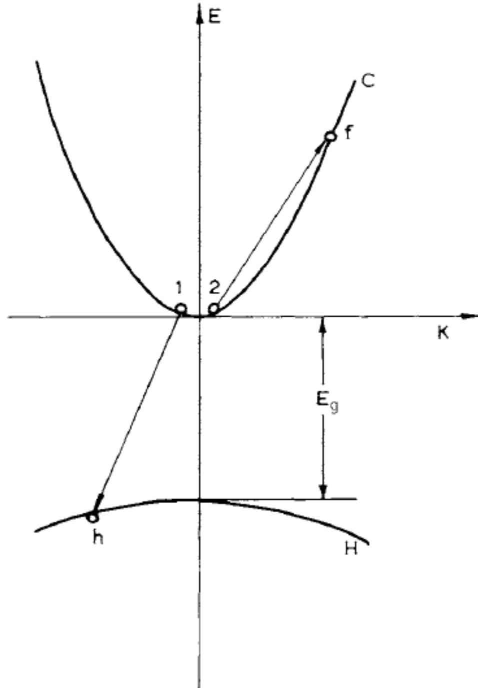

Figure 7.2: Auger CHCC recombination. [28]

There are many types of Auger recombination. Since we are interested in III-V alloys for solar cells device fabrication, there are three types of recombinations which are the most common, namely CHCC, CHHL and CHHS.

In CHCC recombination two electrons collide. An electron from position 1 in Fig. 7.2 collides with an electron on position 2 and recombines with a hole, position *h*. Electron 2 absorbs radiated energy and excites to position *f*, where it finally relaxes from to the band edge.

In the two types of recombination, CHHL and CHHS, two holes take part in the process. The first is more dominant in semiconductors where spin-orbit splitting Δ is larger than the energy gap E_g. This usually happens with materials with a small energy gap. The second is more common if energy gap is larger than the spin-orbit splitting. The main difference between these two processes is in fact that in materials with spin-orbit splitting larger than the energy gap, energy radiated during recombination in not large enough, so holes can not excite to the spin-orbit band.

In CHHL process (Fig. 7.3a) holes h_1 and h_2 collide in a heavy hole band. Hole h_1 recombines with electron 1. Energy radiated in the process is being absorbed by h_2 which excites to light holes band, and returns to the original band after relaxation.

When energy gap E_g of semiconductors is larger than spin-orbit splitting Δ, we have CHHS recombination. In this case (Fig. 7.3b), holes h_1 and h_2 collide in a heavy hole band. Hole h_1 recombines with electron 1. Energy radiated in the process is being absorbed by h_2 which excites to the spin-orbit band, position 2. Eventually, it returns to the original band after relaxation.

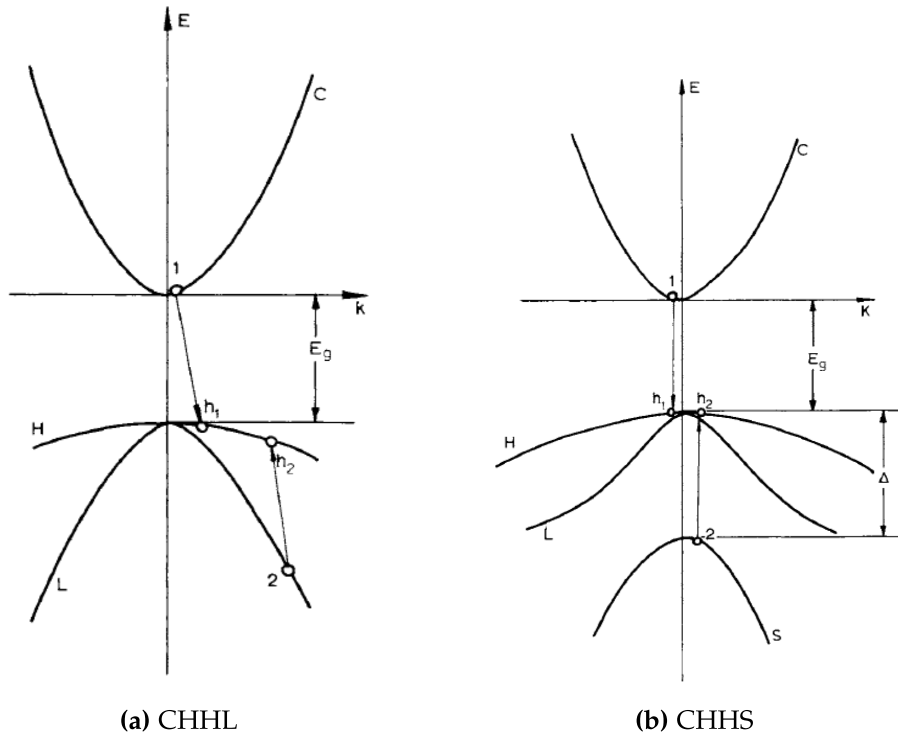

(a) CHHL **(b)** CHHS

Figure 7.3: Auger recombination in p-type materials. [28]

When each of collisions happens, there has to be enough energy in processes to trigger recombination. That minimum energy is called the threshold energy. In different material configuration each process will have different threshold energy and usually, one process will be more dominant than others.

The simplest way to understand the Auger recombination is by observing the simplest type of the recombination. It is a process in which two electons and one heavy hole take part, namely CHCC [41, 132] . During this process momentum and energy conservation have to be fulfilled:

$$\hbar\mathbf{k}_1 + \hbar\mathbf{k}_2 + \hbar\mathbf{k}_{hh} = \hbar\mathbf{k}_f \tag{7.52}$$

$$E_g + \frac{\hbar^2}{2m_e}(\mathbf{k}_1^2 + \mathbf{k}_2^2) + \frac{\hbar^2\mathbf{k}_{hh}^2}{2m_{hh}} = \frac{\hbar^2\mathbf{k}_f^2}{2m_e} \tag{7.53}$$

where $\hbar\mathbf{k}_1$, $\hbar\mathbf{k}_2$ and $\hbar\mathbf{k}_{hh}$ are momenta of the two electrons and one heavy hole at the beginning of the process, respectively, and $\hbar\mathbf{k}_f$ is momentum of the excited electron at the end of the process, while m_e is electron mass and m_{hh} heavy hole mass. Material's bandgap is E_g.

Now, the total kinetic energy of two electrons and one hole that take part in the recombination at the beginning of the process is:

$$\epsilon_k = \frac{\hbar^2}{2m_e}(\mathbf{k}_1^2 + \mathbf{k}_2^2) + \frac{\hbar^2\mathbf{k}_{hh}^2}{2m_{hh}} \tag{7.54}$$

Since the excited electron receives large energy from the collision, it gains huge momentum as well. Momentum conservation law (Eq. 7.52) requires large initial momenta at the beginning of the process as well. It means the colliding particles have to have large enough kinetic energy. The lowest energy required is called threshold energy ϵ_{th}. Since m_{hh}»m_e, it is more probable heavy hole will have larger momentum than electrons, hence $\mathbf{k}_{hh} \approx \mathbf{k}_f$. Now, taking this into account, together with Eqs. 7.52-7.54, the threshold momentum and energy can be estimated:

$$\hbar\mathbf{k}_h^{th} \simeq \sqrt{2m_eE_g} \tag{7.55}$$

$$\epsilon^{th} \simeq \frac{m_e}{m_h}E_g \tag{7.56}$$

Since in $n-$type materials concentration of electrons n is much larger than concentration of holes p, we will take into account only CHCC. On the other hand, in the $p-$type material, we have CHHL and CHHS. When energy gap E_g is wider than

spin-orbit splitting Δ, CHHS type is more dominant, whereas in opposite case CHHS does not exist. In solar cell, we have both $n-$type and $p-$type materials, so [153, 28]:

$$C_n = C_{\mathrm{CHCC}} \tag{7.57}$$

$$C_p = C_{\mathrm{CHHL}} + C_{\mathrm{CHHS}} \tag{7.58}$$

Auger recombination rate can be calculated from [28]:

$$\begin{aligned} U &= \frac{2\pi}{\hbar v} \sum |V_{if}|^2 \delta[\epsilon_c(k_1) + \epsilon_c(k_2) + E_g + \epsilon_h(k_h) - \epsilon_c(k_f)] \\ &\times \; f_c(\epsilon(k_1)) f_c(\epsilon(k_2)) f_h(\epsilon(k_h)) \end{aligned} \tag{7.59}$$

where v is normalization volume, $|V_{if}|^2$ is square of modulus of the Coulomb interaction operator matrix element between initial i and final state f, $f(\epsilon(k))$ distribution functions. Energy conservation is accounted using Dirac's δ- function.

Matrix element of the Coulomb interaction can be written in the following form [28]:

$$\begin{aligned} V_{if} &= \frac{1}{2} \int d^3\mathbf{r}_1 d^3\mathbf{r}_2 [\psi^*_{h\mu_h\mathbf{k}_h}(\mathbf{r}_1)\psi^*_{c\mu_f\mathbf{k}_f}(\mathbf{r}_2) - \psi^*_{h\mu_h\mathbf{k}_h}(\mathbf{r}_2)\psi^*_{c\mu_f\mathbf{k}_f}(\mathbf{r}_1)] \\ &\times \; \frac{e^2}{\kappa|\mathbf{r}_1 - \mathbf{r}_2|} [\psi_{c\mu_1\mathbf{k}_1}(\mathbf{r}_1)\psi_{c\mu_2\mathbf{k}_2}(\mathbf{r}_2) - \psi_{c\mu_1\mathbf{k}_1}(\mathbf{r}_2)\psi_{c\mu_2\mathbf{k}_2}(\mathbf{r}_1)] \end{aligned} \tag{7.60}$$

where $\psi_{\eta\mu\mathbf{k}}$ are wave functions of carrier-free band states, η denotes the band and μ is helicity index. The wave function can be determined from:

$$\psi_{\eta\mu\mathbf{k}} = \frac{e^{i\mathbf{kr}}}{\sqrt{v}} u_{\eta\mu\mathbf{k}}(\mathbf{r}) \tag{7.61}$$

where $u_{\eta\mu\mathbf{k}}(\mathbf{r})$ is Bloch periodic lattice function for arbitrary direction. Combining Eqs. 7.59 - 7.61 recombination rate can be obtained [28]:

$$\begin{aligned}
U &= \frac{2\pi}{\hbar}\left(\frac{4\pi e^2}{\kappa}\right)^2 \int \frac{d^3\mathbf{k}_1}{(2\pi)^3} \int \frac{d^3\mathbf{k}_2}{(2\pi)^3} \int \frac{d^3\mathbf{k}_f}{(2\pi)^3} \int d^3\mathbf{k}_h \\
&\times \delta[\mathbf{k}_1 + \mathbf{k}_2 + \mathbf{k}_h - \mathbf{k}_f] \\
&\times \delta[\epsilon_c(k_1) + \epsilon_c(k_2) + E_g + \epsilon_h(k_h) - \epsilon_c(k_f)] \\
&\times f_c[\epsilon(k_1)]\, f_c[\epsilon(k_2)]\, f_h[\epsilon(k_h)] \\
&\times \left(\frac{\mathbf{B}_{cc}(\mathbf{k}_f, \mathbf{k}_2)\mathbf{B}_{hc}(\mathbf{k}_h, \mathbf{k}_1)}{\kappa^2|\mathbf{k}_f - \mathbf{k}_2|^4} - \frac{\mathbf{B}(\mathbf{k}_1, \mathbf{k}_2, \mathbf{k}_h, \mathbf{k}_f)}{\kappa^2|\mathbf{k}_f - \mathbf{k}_2|^2|\mathbf{k}_f - \mathbf{k}_1|^2}\right)
\end{aligned} \tag{7.62}$$

where $\delta[\epsilon_c(k_1) + \epsilon_c(k_2) + E_g + \epsilon_h(k_h) - \epsilon_c(k_f)]$ takes care of energy conservation, $\delta[\mathbf{k}_1 + \mathbf{k}_2 + \mathbf{k}_h - \mathbf{k}_f]$ takes care of momentum conservation, the first term in brackets (containing $\mathbf{B}_{cc}$ and $\mathbf{B}_{hc}$) corresponds to Coulomb interaction, while the second (with $\mathbf{B}$) corresponds to exchange interaction. Quantities $\mathbf{B}_{cc}$, $\mathbf{B}_{hc}$ and $\mathbf{B}$ are overlap integrals of Bloch functions [28]:

$$\mathbf{B}_{cc}(\mathbf{k}_f, \mathbf{k}_2) = \sum_{\mu_2, \mu_f} |I_{c\mu_f\mathbf{k}_f, c\mu_2\mathbf{k}_2}|^2 \tag{7.63}$$

$$\mathbf{B}_{hc}(\mathbf{k}_h, \mathbf{k}_1) = \sum_{\mu_1, \mu_h} |I_{h\mu_h\mathbf{k}_h, c\mu_1\mathbf{k}_1}|^2 \tag{7.64}$$

$$\begin{aligned}
\mathbf{B}(\mathbf{k}_1, \mathbf{k}_2, \mathbf{k}_h, \mathbf{k}_f) &= \mathrm{Re} \sum_{\mu_1, \mu_2, \mu_h, \mu_f} I^*_{h\mu_h\mathbf{k}_h, c\mu_1\mathbf{k}_1} I^*_{c\mu_f\mathbf{k}_f, c\mu_2\mathbf{k}_2} \\
&\times I_{h\mu_h\mathbf{k}_h, c\mu_2\mathbf{k}_2} I_{c\mu_f\mathbf{k}_f, c\mu_1\mathbf{k}_1}
\end{aligned} \tag{7.65}$$

$$I_{\eta\mu\mathbf{k},\eta'\mu'\mathbf{k}'} = \frac{1}{\Omega}\int d^3\mathbf{r}\; u^*_{\eta\mu\mathbf{k}}(\mathbf{r})\; u_{\eta'\mu'\mathbf{k}'}(\mathbf{r}) \tag{7.66}$$

where Ω is integration area.

If arbitrary relationship between energy gap E_g and spin-orbit splitting Δ is assumed, Auger recombination coefficient in n-type semiconductor can be calculated by solving Eq. 7.62 using Eqs. 7.63 - 7.66, Eq. 7.44 and Eq. 7.57 in the four-band Kane model [111]. The same was already done in [91, 28]:

$$C_{\text{CHCC}} = a\left(\frac{m_e}{m_{hh}}\right)\frac{\hbar^3}{m_e^2\sqrt{E_g}}\frac{\langle\epsilon_c\rangle}{(k_\text{B}T)^{3/2}}\left(\frac{e^2}{\varepsilon_0\varepsilon_\text{r}E_g}\right)^2 e^{-\epsilon_{th}/k_\text{B}T} \tag{7.67}$$

$$\epsilon_{th} = \left(\frac{m_e}{m_{hh}}\right)E_g\frac{(\Delta+2E_g)(2\Delta+3E_g)}{(\Delta+3E_g)(\Delta+E_g)} \tag{7.68}$$

where m_e is the electron mass, m_{hh} the heavy hole mass, ε_0 the vacuum permittivity ε_r the relative permittivity (in preceiding expressions it was denoted as κ for simplicity, i.e. $\kappa = \varepsilon_0\varepsilon_\text{r}$) and a is a constant.

$$\langle\epsilon_c\rangle = \begin{cases} E_g & \text{for } E_g \ll \Delta \\ \frac{3}{2}k_\text{B}T & \text{for } E_g \gg \Delta \end{cases} \tag{7.69}$$

$$a = \begin{cases} 16\pi^{5/2}\left(\frac{E_g+\Delta}{3E_g+2\Delta}\right)^{3/2}\left(\frac{3E_g+\Delta}{2E_g+\Delta}\right)^{1/2} & \text{for } E_g \ll \Delta \\ (2\pi)^{5/2} & \text{for } E_g \gg \Delta \end{cases} \tag{7.70}$$

In case of a p-type semiconductor with a narrow band gap E_g (i.e. $E_g \ll \Delta$), the most favorable way of nonradiative Auger recombination is C_{CHHL}. It was first eval-

uated in [173], and later corrected by [90]. After solving Eq. 7.62 using Eqs. 7.63 - 7.66, Eq. 7.45 and Eq. 7.58 in the three-band Kane model [111], Auger recombination coefficient in the narrow gap p-type semiconductor can be obtained [90, 28]:

$$C_{\mathrm{CHHL}} = \frac{36\pi\hbar^3 e^4}{\varepsilon_0^2 \varepsilon_{\mathrm{r}}^2 m_{lh} m_{hh} E_g^2} \sqrt{\frac{k_{\mathrm{B}}T}{\epsilon_{th}}} g\left(\frac{\epsilon_{th}}{k_{\mathrm{B}}T}\right) e^{-\epsilon_{th}/k_{\mathrm{B}}T} \tag{7.71}$$

where m_{lh} is the light hole mass.

$$\epsilon_{th} = \left(\frac{m_e}{m_{hh}}\right) E_g \tag{7.72}$$

Since $m_{hh} \gg m_e$, $\epsilon_{th} \to 0$ and therefore:

$$g\left(\frac{\epsilon_{th}}{k_{\mathrm{B}}T}\right) = \frac{3\pi^2}{16}\left(\frac{\epsilon_{th}}{k_{\mathrm{B}}T}\right)^{5/2} \tag{7.73}$$

In the opposite case, when band gap E_g is similar or lower than the spin orbit splitting energy Δ, the most dominant channel of Auger recombination is C_{CHHs}. This process was studied in detail and presented in [92]. With hole transfer to split-off band, the expression for Auger recombination coefficient is slightly different since it includes different particles at different energy gaps. Therefore, combining Eqs. 7.59 - 7.61 expression for recombination rate,similar to 7.62, can be obtained with arbitrary relationship between E_g and Δ [28]:

$$\begin{aligned} U &= \frac{2\pi}{\hbar}\left(\frac{4\pi e^2}{\kappa}\right)^2 \int \frac{d^3\mathbf{k}_{1h}}{(2\pi)^3} \int \frac{d^3\mathbf{k}_{2h}}{(2\pi)^3} \int \frac{d^3\mathbf{k}_c}{(2\pi)^3} \int d^3\mathbf{k}_s \\ &\times \delta[\mathbf{k}_{1h} + \mathbf{k}_{2h} + \mathbf{k}_c - \mathbf{k}_s] \\ &\times \delta[\epsilon_h(k_{1h}) + \epsilon_h(k_{2h}) + \epsilon_c(k_c) + E_g - \epsilon_s(k_s) - \Delta] \\ &\times f_h[(\epsilon(k_{1h})]\, f_h[\epsilon(k_{2h})]\, f_c[\epsilon(k_c)] \\ &\times \left(\frac{\mathbf{B}_{hc}(\mathbf{k}_{2h}, \mathbf{k}_c)\mathbf{B}_{hs}(\mathbf{k}_{1h}, \mathbf{k}_s)}{|\mathbf{k}_{1h} - \mathbf{k}_s|^4} - \frac{\mathbf{B}(\mathbf{k}_c, \mathbf{k}_{2h}, \mathbf{k}_s, \mathbf{k}_{1h})}{|\mathbf{k}_{1h} - \mathbf{k}_s|^2 |\mathbf{k}_{2h} - \mathbf{k}_s|^2}\right) \end{aligned} \tag{7.74}$$

where $\delta[\epsilon_h(k_{1h}) + \epsilon_h(k_{2h}) + \epsilon_c(k_c) + E_g - \epsilon_s(k_s) - \Delta]$ takes care of energy conservation, $\delta[\mathbf{k}_{1h} + \mathbf{k}_{2h} + \mathbf{k}_c - \mathbf{k}_s]$ takes care of momentum conservation, the first term in brackets (containing $\mathbf{B}_{hc}$ and $\mathbf{B}_{hs}$) corresponds to Coulomb interaction, while the second (with $\mathbf{B}$) corresponds to exchange interaction. Quantities $\mathbf{B}_{cc}$, $\mathbf{B}_{hc}$ and $\mathbf{B}$ are overlap integrals of Bloch functions [90, 28]:

$$\mathbf{B}_{hc}(\mathbf{k}_{2h}, \mathbf{k}_c) = P^2(k_{2h})^{-2}[\mathbf{k}_{2h}, \mathbf{k}_c]^2 y_c(\mathbf{k}_c)[\Delta + E_c(k_c)] \tag{7.75}$$

$$\mathbf{B}_{hs}(\mathbf{k}_{1h}, \mathbf{k}_s) = \frac{3}{4}[\mathbf{k}_{1h}, \mathbf{k}_s]^2 k_s^2 k_{1h}^{-2} \hbar^4 m_s^{-2} \Delta^{-2} \tag{7.76}$$

$$\begin{aligned}
\mathbf{B}(\mathbf{k}_c, \mathbf{k}_{2h}, \mathbf{k}_s, \mathbf{k}_{1h}) &= \frac{1}{4} P^4 k_c^2 k_s^2 y_s(\mathbf{k}_s) y_c(\mathbf{k}_c)[\Delta - E_c][\Delta - E_s] \\
&\times \Bigg(1 + \frac{(\mathbf{k}_{1h}, \mathbf{k}_{2h})^2}{k_{1h}^2 k_{2h}^2} + \frac{(\mathbf{k}_c, \mathbf{k}_s)^2}{k_c^2 k_s^2} - \frac{(\mathbf{k}_{2h}, \mathbf{k}_s)^2}{k_{2h}^2 k_s^2} \\
&- \frac{(\mathbf{k}_{1h}, \mathbf{k}_s)^2}{k_{1h}^2 k_s^2} - \frac{(\mathbf{k}_{1h}, \mathbf{k}_c)^2}{k_{1h}^2 k_c^2} - \frac{(\mathbf{k}_{2h}, \mathbf{k}_c)^2}{k_{2h}^2 k_c^2} \\
&- [(\mathbf{k}_{2h}, \mathbf{k}_s)^2 (\mathbf{k}_{1h}, \mathbf{k}_c)^2 - (\mathbf{k}_{1h}, \mathbf{k}_s)^2 (\mathbf{k}_{2h}, \mathbf{k}_c)^2 \\
&- (\mathbf{k}_{1h}, \mathbf{k}_{2h})^2 (\mathbf{k}_c, \mathbf{k}_s)^2] k_{1h}^{-2} k_{2h}^{-2} k_s^{-2} k_c^{-2} \Bigg)
\end{aligned} \tag{7.77}$$

where P is Kane parameter ($P^2 = 3\hbar^2 E_g/(4m_e)$), $E_c = E_g + \epsilon_c(k_c)$ and $E_c = -\Delta - \epsilon_s(k_s)$ are roots of the dispersion equation in the Kane model [111]. Values $y_s(\mathbf{k}_s)$ and $y_c(\mathbf{k}_c)$ can be calculated from the expression:

$$y_x(\mathbf{k}_x) = [E_x^2(E_g - \Delta) + 2E_x(P^2|\mathbf{k}_x|^2 + E_g\Delta) + 2P^2|\mathbf{k}_x|^2\Delta]^{-1} \tag{7.78}$$

where index "x" can be either "c" or "s". Finally, solving 7.74 using Eqs. 7.75- 7.78, Eq. 7.45 and Eq. 7.58 in the four-band Kane model [111], Auger recombination coefficient in case $E_g - \Delta \gg k_B T$ is [90, 28]:

$$C_{\mathrm{CHHS}} = \frac{216\pi^{5/2}\hbar^3 e^4 m_e(\Delta + E_g)^2\sqrt{k_{\mathrm{B}}T}}{\varepsilon_0^2\varepsilon_{\mathrm{r}}^2 m_{hh} m_{so} E_g^2\sqrt{\epsilon_{th}}} e^{-\epsilon_{th}/k_{\mathrm{B}}T} \tag{7.79}$$

$$\epsilon_{th} = \left(\frac{m_{so}}{m_{hh}}\right) E_g \frac{(E_g - \Delta)}{(E_g + \Delta)(3E_g - 2\Delta)} \tag{7.80}$$

where m_{so} is spin-orbit interaction mass and $\kappa = \varepsilon_0\varepsilon_{\mathrm{r}}$ as well.

Now we can calculate Auger recombination current:

$$J_{\mathrm{AUG}} = q\int_w U dx \tag{7.81}$$

$$J_{\mathrm{AUG}} = q\left[(C_{\mathrm{CHHL}} n \mathrm{w_n} + (C_{\mathrm{CHHL}} + C_{\mathrm{CHHS}}) p \mathrm{w_p})\right](pn - n_i^2) \tag{7.82}$$

where $\mathrm{w_p}$ is width of quasi-neutral region in $p-$type semiconductor and $\mathrm{w_n}$ is width of quasi-neutral region in $n-$type semiconductor. In $n-$type $n \approx N_d$ and in $p-$type $p \approx N_a$. Since $pn = n_i^2 e^{\frac{qV}{k_B T}}$, we can write Eq. 7.82 as:

$$J_{\mathrm{AUG}} = q\left[C_{\mathrm{CHCC}} N_d \mathrm{w_n} + (C_{\mathrm{CHHL}} + C_{\mathrm{CHHS}}) N_a \mathrm{w_p}\right] n_i^2 \left(e^{\frac{qV}{k_B T}} - 1\right) \tag{7.83}$$

$$J_{\mathrm{AUG}} = J_{\mathrm{AUG,0}}\left(e^{\frac{qV}{k_{\mathrm{B}}T}} - 1\right) \tag{7.84}$$

where $J_{\mathrm{AUG},0}$ is voltage independent part of Auger recombination current:

$$J_{\mathrm{AUG},0} = q\left[C_{\mathrm{CHCC}} N_d \mathrm{w_n} + (C_{\mathrm{CHHL}} + C_{\mathrm{CHHS}}) N_a \mathrm{w_p}\right] n_i^2 \tag{7.85}$$

8

HEURISTIC MODELING OF MULTI-JUNCTION SOLAR CELLS

In case of very complex problems, classical approach becomes inefficient. Solving them might require too much time or computing power. Therefore, an alternative method might come in handy. One of such methods is heuristics. Heuristics creates a shortcut using available data, i.e. newly acquired knowledge, about the problem to make a choice between possible alternatives. Each iteration depends upon ranking of those alternatives in the previous iteration. Accuracy or precision might have to be sacrificed for speed. The main idea is obtaining sufficiently good results in available amount of time.

Due to its resemblance to human way of thinking and problem solving, it lies in a basis of artificial intelligence.

8.1 GENETIC ALGORITHMS

The idea of solving problems in engineering based on evolution traces back decades in history. In the 1950s and 1960s, scientists were trying to find an algorithm which would mimic biological systems and, starting with an unoptimal sets of solutions, find an optimal one. Evolution strategies were introduced by Rechenberg [177, 206] who tried to optimize the parameters of different devices. This idea was adopted and improved by Schwefel [184]. At the same time Fogel, Owens, and Walsh developed evolutionary programming [77]. Solutions were basically represented as a finite state

machine and they were evolving by randomly mutating state transitions and selecting the best solutions. These two methods, together with genetic algorithm are the foundation of modern evolutionary computation.

Genetic algorithms (GA) are a particular class of evolutionary algorithms. They were developed by John Holland [101] at the University of Michigan during the 1960s and 1970s. Unlike the most of scientist during that period, Holland was not trying to create an algorithm which would solve a particular problem, but rather to study the process of evolving. The GA he created was mimicking biological evolution. He laid the theoretical foundations for adaptation in evolutionary computation. Furthermore, he introduced population-based algorithms with operators such as natural selection, crossover, mutation and inversion. His schema theorem was for decades the foundation for all theoretical research on GAs.

Evolution is, naturally, an inspiration when it comes to problem-solving. It searches through a huge number of possible solutions, i.e. genetic sequences of living beings, to solve a problem of survival in a harsh and complex, constantly changing, environment. Over and above, it is highly parallelized. Hence, it creates very innovative and, very often, simple solutions to very complex problems. The most problems in science, engineering, biology... are very complex, with a huge number of constrained parameters which constantly change the environment and have many possible solutions. Therefore the algorithm has to be parallel, adaptive and to have an intelligent strategy for deciding which parameters provide the best results and how to move through the parameter space in order to find the optimal solution in the parameter space. Having said this, genetic algorithms are the logical choice for solving problems in many different fields.

GAs [55, 94, 93, 203, 212, 150] are adaptive heuristic searching methods based on natural selection. Even though they make use of random numbers, they are not random search methods, but based on previous iterations find the best solution within the search space. The heart of each genetic algorithm is selection, crossingover, muta-

tion and evaluation. Different genetic algorithms have these techniques implemented differently (Figs. 8.1 and 8.2).

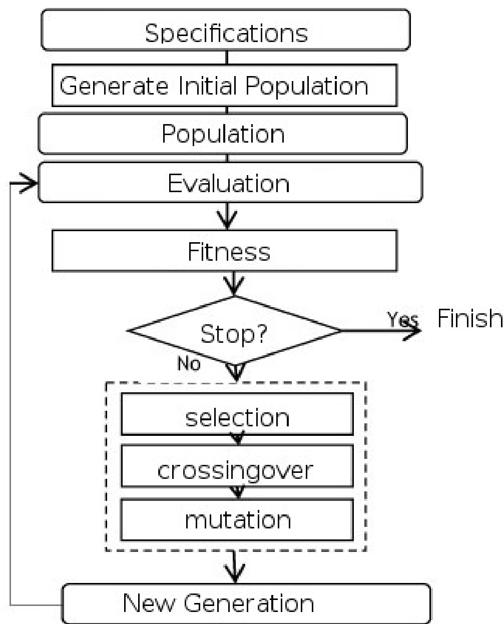

Figure 8.1: Genetic algorithm flow chart

Genetic algorithms basically need some specifications of the problem, such as population size, stopping criteria... Based on that, the initial population is created. Population consists of sets of parameters, i.e. individuals. Each individual is now being evaluated and generation sorted based on the fitnesses of individuals. This evaluation process can be parallelized and is being calculated on the compute nodes. Everything else is being done on the head node. If the stopping criterion is met, GA is finished. If the stopping criterion is not met, GA starts creating the new generation. Based on the fitness order and optimization options, selects the individuals which will take place in crossingover. After crossing over, individuals mutate to prevent quick convergence to a local maximum. This way the new generation is created. Individuals of the new generation are now being evaluated and the process repeats until a stopping criterion is met.

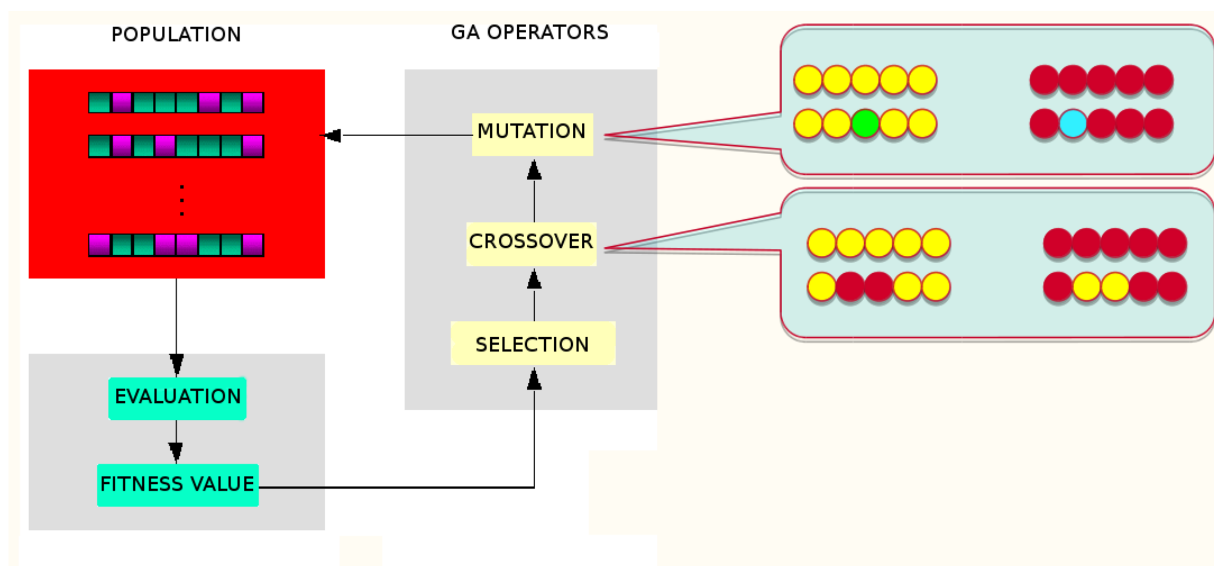

Figure 8.2: Schematic representation genetic algorithm

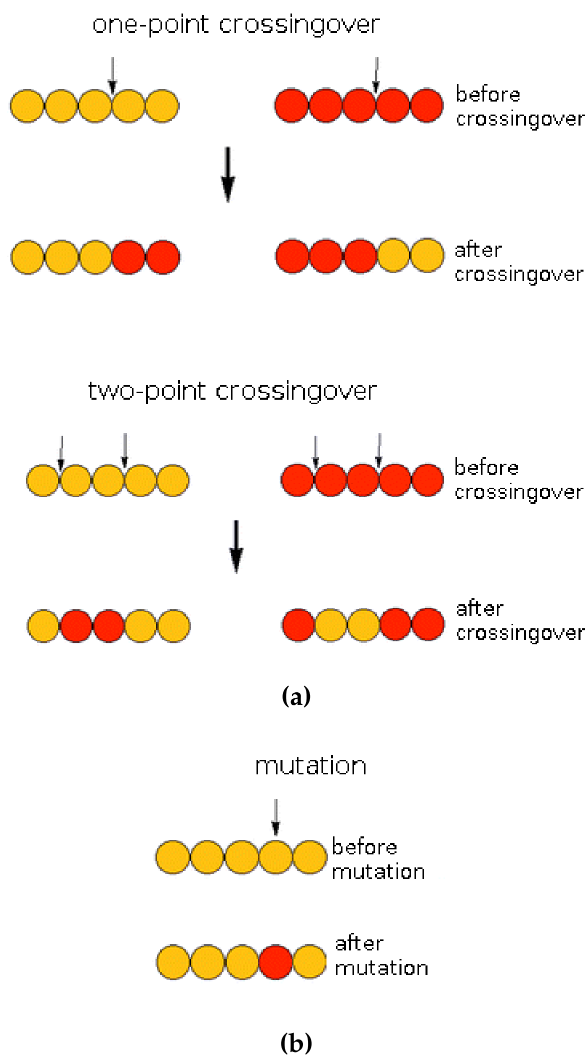

Figure 8.3: Schematic representation of one-point and two-point crossover and mutation

Selection, crossingover and mutation are called breeding. Those processes combine individuals in the current generation and create the next generation. Selection selects two individuals which are going to breed and is based on natural selection. It is being done using a roulette wheel algorithm with the relative fitnesses obtained in the evaluation. In other words, those individuals that provide better fitnesses will have more probability to breed. Before crossingover, encoding takes place, which converts parameters in an individual into strings of integer numbers. It is done by creating strings from each optimizing parameter with predetermined lengths. Each element in those strings, i.e. integer number, is called gene. In other words, each string is set of genes which represent one device parameter. By merging those strings, chromosomes are obtained. Chromosomes are string representation of each individual. Crossingover can be one-point or two-point crossingover. In one-point crossingover two chromosomes exchange two fragments, which are on either end. On the other hand, two-point crossingover allows exchange segments from the middle of the chromosome (Figs. 8.2 and 8.3a). Circles in Figs. 8.2 and 8.3 represent genes, whereas arrays of circles represent chromosomes.

The next step in the breeding process is a mutation. For each gene in each chromosome a random number is generated and if it is larger than the mutation threshold, that gene will be randomly altered. If the mutation happens on a more significant

digit in the gene, it can cause a significant jump in the parameter space, and vice versa. Therefore, mutation can be uniform or nonuniform, have upper or lower boundaries, can be variable depending on the fitness of the individual or the position of the digit in the gene (Figs. 8.2 and 8.3b). In the end, the chromosomes are decoded and converted to individuals, i.e. sets of solar cell parameters. The decoding is just a reverse process from the encoding.

Genetic algorithms rely on a single scalar quantity, therefore they are suitable for the wide range of problems. They do not make any assumptions about the objective function, so problems for which derivatives are very hard, or even impossible if they are undefined, to evaluate in closed form are solvable for genetic algorithms. It makes them robust and stable. For that reason, they are used when the objective function is discontinuous, stochastic, highly nonlinear or described by integral equations. Furthermore, they are being used when the search space is highly complex and large, poorly understood, multimodal or n-dimensional surface. The advantage of the GAs over other methods is the ease with which it can handle arbitrary kinds of constraints. It can be handled as weighted components of the fitness function, making them easy to adapt to the particular requirements of a very wide range of possible overall objectives. Some of the fields they have found use are optimization, automatic programming, machine and robot learning, economic modeling, immune system modeling, ecological modeling, modeling of social systems, etc.

Genetic algorithms are quick in locating the area where the optimal solution is, while, unlike more field-specific algorithms, it takes them more time to find the exact solution within the located area. There is a fast increase in fitness in the early stage of the optimization, which is followed by a long period of slow change in the fitness. If they are able to converge to the optimal solution, traditional simplex methods are significantly faster in locating it. Genetic algorithms are slower, but global search methods. It is a repercussion of a large number of individuals, typically required in dealing with complex problems, which have to be evaluated. On the other hand,

the evaluations are being conducted simultaneously, which allows a high degree of parallelization.

8.2 SHEMA THEOREM

Genetic algorithms are simple to understand and program, but extremely difficult to describe mathematically as their behavior is very complicated. The theoretical foundations were laid by Holland [101], whereas many sicentists made a significant contributions [95, 59, 155, 103, 204]. Holland's schema theorem was the traditional theory of GAs for decades, so it will be sketched briefly, based on [94, 150]. It assumes that, in a very general level of description, GAs work by discovering and recombining good building blocks of solutions. The assumption is that good building blocks are actually parameter sets whose combination build the optimal solution. Those parameter sets have to have a certain similarity. A schema [101] is a similarity template describing a subset of strings with similarities at certain string positions.

The simplest way to analyze the behavior of a genetic algorithm is to observe a binary system. Since strings are similar, not identical, we need a meta-symbol $'' * ''$ as a wild card, or the "don't care" bits. Schema matches a particular string if at every location particular bits of $1's$ and $0's$ match. The $*$ can match either. If we observe a byte long schemata ($l = 8$), one schema can be $H = *1111111$. This schema matches only two strings, namely $A_1 = 01111111$ and $A_2 = 11111111$. Another example of the schema can be $H = * * 1001 * *$, $H = 1 * 0 * 100*$... The first schema matches 16 different strings and the second one 8.

Since we use three signs to represent schemata of length l, there are 3^l possible schemata. If number system (or the alphabet) is of a cardinality k, there are $(k+1)^l$ possible schemata. Each particular string has to be represented with $1's$ and $0's$, therefore there are 2^l possible strings. If a generation contains n individuals, there are between 2^l (if all of them are equal) and $n \cdot 2^l$ (if all of them are different) schemata,

because each one of the bits can be represented either with its actual value or with a meta-symbol "$*$".

Since there are different schemata of the same length, they can be classified according to order and length. The order of schema ($o(H)$) is the number of defined bits. As an example, $o(*******1) = 1$, $o(1*0*100*) = 5$. Defining the length of a schema ($\delta(H)$) is the distance between the first and last defined bit. As an example, $\delta(*******1) = 0$, $\delta(1*0*100*) = 6$.

We are mainly interested in the effect of genetic algorithm operators (selection, crossover and mutation) on the number of schemata. Suppose there are $m(H,t)$ schemata within the population $\mathbf{A(t)}$ at the moment (generation) t. The probability a string A_i will be selected for reproduction is:

$$p_i = f_i/\bar{f} \tag{8.1}$$

where f_i is the fitness of a string A_i and $\bar{f}$ the average fitness of the entire population. Now, if $f(H,t)$ is the average fitness of the strings representing schema H at generation t, the probability the schema will be selected for the next generation (will survive selection) is:

$$p(H,t) = f(H,t)/\bar{f} \tag{8.2}$$

The expected number of schemata, if the only selection is taken into account, in the next generation can be written as:

$$E(m(H,t+1)) = m(H,t)\frac{f(H,t)}{\bar{f}} \tag{8.3}$$

Particular schema grows as a ratio of the average fitness of the schema to the average fitness of the entire population. In other words, a schema with higher average fitness will receive a higher number of samples in the next generation. Simply, above average schemata increases while the below average ones die off. If we assume a certain schema grows with a rate of $c\bar{f}$ from generation to generation, where c is a constant, we can write:

$$m(H,t+1) = m(H,t)\frac{\bar{f}+c\bar{f}}{\bar{f}} = m(H,t)(1+c) \tag{8.4}$$

If the schema grows at this rate from the beginning:

$$m(H,t) = m(H,0)(1+c)^t \tag{8.5}$$

which is a geometric progression. If the schema decays constantly, then $c < 0$ and we have geometric decay. If the population contains the optimal solution, the algorithm can find it quickly. Otherwise, we have to introduce new operators which can help explore other regions where the optimal solution might be. Crossover will be introduced through S_c and mutation through S_m.

Crossover allows expansion through information exchange between strings. If we observe two schemata $H_1 = *1*****0$ and $H_2 = ****10**$, we can see how crossingover affects particular schemata. In crossover two strings, that match the observed schemata, are chosen based on their fitness, sliced at random place and recombined. If they are sliced in the middle, we have $H_1 = *1**|***0$ and $H_2 = ****|10**$. In a case like this, information about the similarity of that string with other strings which match the schema H_1 will be destroyed because the specified bits are going to become parts of different offspring. This is destroying schemata H_1. In a case like this, the only way the schemata survives is if the string is recombined with an identical one, but the probability for that is low, therefore will be ignored. On

the other hand, schema H_2 will survive. If the string length is l, it can be sliced in $l-1$ places. It will be destroyed if the slicing happens somewhere between first and last defined bits, hence in one of $\delta(H)$ places. Decaying probability will be $p_d(H) = \delta(H)/(l-1)$ and surviving probability $p_s(H) = 1 - p_d(H)$. In case of observed schemata, $p_d(H_1) = 0.86$ and $p_s(H_1) = 0.14$, while $p_d(H_2) = 0.14$ and $p_s(H_2) = 0.86$. If the crossingover probability is p_c, lower bound of crossover survival is:

$$S_c(H) \geq 1 - p_c \frac{\delta(H)}{l-1} \tag{8.6}$$

Obviously, the shorter defining length schemata will have a higher probability to survive.

The downside of crossingover is that one good schema can become dominant and, if it does not contain the best solution, can lead to a local maximum. This is the place where mutation steps in. It provides enough diversity to ensure the reached maximum is global. The schema can be destroyed only if one of the defined bits is altered. Probability any bit will be mutated is p_m. Any single bit will be intact with probability $1 - p_m$. The number of defined bits is the order of schema $o(H)$. Since the mutations are independent, the lower bound of mutation survival is:

$$S_m(H) \geq (1 - p_m)^{o(H)} \tag{8.7}$$

Schema survives only if each one of $o(H)$ defined bits survive. Hence, if the $o(H)$ is lower, there is higher probability the schema will survive.

Finally, the expected number of schemata H in the next generation, if selection, crossingover and mutation are taken into account, can be written as:

$$E(m(H,t+1)) \geq m(H,t) \frac{f(H,t)}{\bar{f}} \left(1 - p_c \frac{\delta(H)}{l-1}\right) \left((1 - p_m)^{o(H)}\right) \tag{8.8}$$

Expression 8.8 is the schema theorem. It is the fundamental theorem of the genetic algorithm. It implies that short, low-order, above-average schemata increase exponentially in subsequent generations. It is a roadmap for how to conduct optimizations.

8.3 A MATEMATICAL MODEL OF THE SIMPLE GENETIC ALGORITHM

Well known schema theorem [102] predicts only the expected change in frequencies in schemas from one generation to another. Unfortunately, it does not say anything about population composition, distribution of fitnesses or speed of population convergence. Model presented here [203] is based on [150].

After encoding each individual is converted to a binary string of length l and can be presented with integer number i, where $i \in (0, 2^l - 1)$. In real code (Fig. 8.1) individuals are evaluated, selected based on their fitness and then encoded. In order to simplify the mathematics, we will assume that individuals are encoded first since the mathematical operations are more easily understood if applied on binary strings than real numbers. The population at generation t is represented by two real-valued vectors $\mathbf{p}(t)$ and $\mathbf{s}(t)$ with lengths 2^l. Vector $\mathbf{p}(t)$ is the proportion of each individual string in the population at generation t and vector $\mathbf{s}(t)$ is the probability that individual is going to be selected. The probability is determined based on its fitness value. In other words, $i-$th component of vector $\mathbf{p}(t)$, $p_i(t)$, is the proportion of the population at generation t consisting of string i and $i-$th component of vector $\mathbf{s}(t)$, $s_i(t)$, is the probability that the individual represented with i is going to be selected to be a parent for the next generation, based on its fitness. Shortly, $\mathbf{p}(t)$ defines the composition of the population and $\mathbf{s}(t)$ defines its quality. The fitness function $f(i)$ values for each individual will be components of the matrix F, where:

$$F_{i,j} = \begin{cases} f(i) & \text{for } i = j \\ 0 & \text{for } i \neq j \end{cases} \tag{8.9}$$

$i \in (0, 2^l - 1)$ and $j \in (0, 2^l - 1)$. Proportional selection $\mathbf{s}(t)$ can be defined as:

$$\mathbf{s}(t) = \frac{F\mathbf{p}(t)}{\sum_{j=0}^{2^l-1} F_{jj} p_j(t)} \tag{8.10}$$

The idea is to define a single operator G which, applied to $\mathbf{s}(t)$, would mimic the effects of running the genetic algorithm and creating the population in generation $t+1$ from the population in generation t, i.e.:

$$\mathbf{s}(t+1) = G\mathbf{s}(t) \tag{8.11}$$

This way iterating G on $\mathbf{s}(t)$ from the first generation would give an exact description of the expected behavior of the genetic algorithm. For now, we will take into account only selection. If we define expectation of x as $E(x)$:

$$E\left(\mathbf{p}(t+1)\right) = \mathbf{s}(t) \tag{8.12}$$

This means that the expected proportion of each individual in the next generation equals the quality in this generation. If we allow $\mathbf{x} \sim \mathbf{y}$ mean $\mathbf{x}$ and $\mathbf{y}$ differ only by a scalar factor and combining (8.10) and (8.12) we can obtain:

$$E\left(\mathbf{s}(t+1)\right) \sim F\mathbf{s}(t) \tag{8.13}$$

Now we have an expression in the form of (8.11). In case of only selection taken into account, we have $G = F$. This is expectation value and is exact only in case of an infinite population. In the case of finite population, sampling errors will cause deviation from the exact value.

Let's take into account crossingover and mutation, in one word recombination, using operator M. Now operator G will be a composition of operators F and M. Probability that individual k will be produced by recombination of i and j is $r_{i,j}(k)$, and therefore:

$$E\left(p_k(t+1)\right) = \sum_{i,j} s_i(t)s_j(t)r_{i,j}(k) \tag{8.14}$$

Since defining $r_{i,j}(k)$ and M is a bit tricky, we will define a simpler matrix M^0 whose elements $M^0_{i,j}$ give the probability $r_{i,j}(0)$ that individual containing all zeros is going to be produced in recombination of strings i and j. The expression for $r_{i,j}(0)$ equals the sum of two terms. The first term T_1 is the probability that crossingover will not happen between i and j and that either of them mutates to all zeros. The other term T_2 is the probability that crossingover will happen between i and j and that either of them mutates to all zeros. Number of ones in an individual is $|i|$, p_c is crossingover probability and p_m is mutation probability.

$$T_1 = \frac{1}{2}\left(1 - p_c\right)\left[p_m^{|i|}\left(1 - p_m\right)^{l-|i|} + p_m^{|j|}\left(1 - p_m\right)^{l-|j|}\right] \tag{8.15}$$

Individuals are of length l, number of possible crossingover points is $l - 1$ and the probability of choosing point c is $1/(l-1)$. Point c is a number which, counted from the right decides where the individual is going to be sliced. It produces two sub-individuals of lengths c (the right one) and $l - c$ (the left one). The individual i will be converted into i_2 (the right one) and i_1 (the left one). Similar with the individual j. After crossingover two new individuals will be produced: h from i_1 and j_2 and

k from j_1 and i_2. Number of ones in these new individuals is $|h| = |i_1| + |j_2|$ and $|k| = |j_1| + |i_2|$.

$$T_2 = \frac{1}{2}\frac{p_c}{1-l}\sum_{c=1}^{l-1}\left[p_m^{|h|}\left(1-p_m\right)^{l-|h|} + p_m^{|k|}\left(1-p_m\right)^{l-|k|}\right] \tag{8.16}$$

Next, we can write the expression for $r_{i,j}(0) = T_1 + T_2$. To make the expression a bit simpler: $\Delta_{i,j,k} = |i_2| - |j_2|$ and $\eta = p_m/(1-p_m)$.

$$r_{i,j}(0) = \frac{(1-p_m)^l}{2}\left[\eta^{|i|}\left(1-p_c+\frac{p_c}{l-1}\sum_{c=1}^{l-1}\eta^{-\Delta_{i,j,c}}\right) + \eta^{|j|}\left(1-p_c+\frac{p_c}{l-1}\sum_{c=1}^{l-1}\eta^{\Delta_{i,j,c}}\right)\right] \tag{8.17}$$

As already said, $r_{i,j}(0)$ are elements of matrix M^0. We can define permutations σ_i as:

$$\sigma_i\langle s_0, ..., s_{2^l-1}\rangle^T = \langle s_{i\oplus 0}, ..., s_{i\oplus(2^l-1)}\rangle^T \tag{8.18}$$

where $\oplus$ is exclusive-or. Now, we will define M as:

$$M(s) = \langle(\sigma_0 s)^T M^0 \sigma_0 s, ..., (\sigma_{2^l-1}s)^T M^0 \sigma_{2^l-1}s\rangle^T \tag{8.19}$$

In the end, we can write the expression for genetic algorithm operator G:

$$G\left(\mathbf{x}\right) = F \circ M\left(\mathbf{x}\right) \tag{8.20}$$

where $\circ$ is the composition operator. Combining (8.20) with (8.13) we obtain:

$$G(\mathbf{s}(t)) \sim \mathbf{s}(t+1) \tag{8.21}$$

Finaly, combining (8.21) with (8.10) we obtain:

$$G_p(\mathbf{p}(t)) \sim \mathbf{p}(t+1) \tag{8.22}$$

Results (8.21) and (8.22) represent genetic algorithm operators and are exact results in the case of an infinite population.

Operator F describes selection while operator M describes recombination, i.e. crossingover and mutation. As a consequence, operator G describes the main operations in genetic algorithm, selection, crossingover and mutation. Operator G applied to the population in the first generation produces the population in the next generation. It can be iterated until any stopping criteria are met and, therefore, provide the individual with the desired fitness. In MJSC optimization there are many parameters to be optimized, which does not create an infinite population, but sufficiently large for approximation to be reasonable.

8.4 GENETIC ALGORITHM IMPLEMENTATION USING PARALLEL COMPUTING

The genetic algorithm implementation was based on the PIKAIA genetic algorithm. PIKAIA was developed by Paul Charbonneau and Barry Knapp [55, 56] at the High Altitude Observatory of the National Center fo Atmospheric Research in 1995. MPI version was developed by Travis Metcalfe during a postdoctoral fellowship at the Harward-Smithsonian Center for Astrophysics [12]. MPI stands for **m**essage **p**assing **p**rotocol, which allows parallel computation. The version used in this thesis is MPI version which had to be converted from Fortran 77 to Fortran 90 and significantly alter

to comply with the needs of the problem, such as being able to solve n-dimensional problems.

Despite the changes, the core of the PIKAIA has been preserved, so the user guide written by the original creators can be found in Ref. [56].

The goal of the algorithm is to maximize the function provided in the $n-$dimensional space, where n is the number of optimizing parameters with values in range $[0.0, 1.0]$. This means the user has to scale the input parameters of the function. Optimization options have default values, while the user can provide a control vector with defined options for the optimization. The default number of individuals is $n_p = 100$, whereas the default number of generations is $n_g = 500$. The stopping criterion is the number of generations, unlike the most of the other algorithms.

The first step in the optimization is creating n_p individuals by a uniform random number generator. These individuals can be evaluated both sequentially and parallel, which can be defined by the user. After obtaining the fitness values for each individual, the algorithm starts creating a new generation. First, probabilities for selection have to be determined stochastically. All individuals within the population are ranked accordingly to their fitness. It is being done through the Roulette Wheel Algorithm. The ranking is equivalent to creating a roulette wheel with sectors with sizes linearly proportional to the fitness of each individual. The larger the size of each sector, larger the probability the individual will be selected for reproduction. Fitness differential is proportionality constant between fitness-based rank and selection probability. It can be specified by the user, while the default value is `fdiff` $= 1.0$. In case `fdiff=1` the selection is based on the fitness, whereas in case of `fdiff=0`, each individual can be selected with the equal probability. Throughout these optimizations the default value was used.

After two individuals are selected, encoding takes place. Individuals are encoded using decade system with the number of significant digits can be set by the user. The default value is $n_d = 5$. Encoding creates $n \cdot n_d$ long chromosome, i.e. concatenates n_d significant digits from n individuals.

Crossingover is the main advantage of genetic algorithms. It combines chromosomes from two individuals called parents and creates two new individuals called offspring. First, a random number is generated. If that number is lower than the crossingover probability, the crossingover takes place. The crossingover probability can be set by the user, although its default value is `pcross` = 0.85, which was used in the calculations.

Mutation operator allows diversity of the population. Again, a random number is generated for every gene (digit) in a chromosome of an offspring, and if it is lower than mutation probability `pmut`, mutation takes place. In the mutation process, the selected gene is replaced by randomly selected single digit number. The mutation probability can be constant or can vary depending on fitness. Default value is `pmut` = 0.005, if mutation mode is `imut` = 1. The default value is `imut` = 2, which allows mutation rate to vary between `pmutmn` = 0.0005 and `pmutmx` = 0.25. This is achieved by tracking the convergence of the population. Based on the convergence degree, the mutation rate is increased or decreased in order to keep the variability of the population and prevent the premature convergence. In the case when more than one gene has to mutate simultaneously in order to achieve desired value, the probability of that happening is called Hamming wall. An example for this is when 19 has to mutate to 20, or 20 to 19. The creep mutation option allows exactly this. If selected, it can add or subtract 1 if needed.

After creating new individuals, there are three reproduction plans for incorporating them into the population. If `irep` = 1 (default value) reproduction plan is set to full generational replacement, which was kept in the optimisation. In case `irep` = 2 or `irep` = 3, steady-state replacement takes place. The new individual is introduced only if its fitness is higher than the lowest in the current population and there are no identical individuals already. In case of `irep` = 2 the new individual replaces random individual from the population, while in case of `irep` = 3 it replaces the least fit one. In case of a large number of individuals and generations, even the lowest probability phenomenon can occur, so it can happen that the fittest individual from the current

generation is less fit than the fittest one from the previous generation. This is where the elitism comes in handy. It allows the fittest individuals to be preserved and passed on to the next generation. It is turned on by default (`ielite` $= 1$), but can be turned off as well (`ielite` $= 0$).

After the new generation is created, the process of evaluation can start again. It is the most time consuming, therefore parallelization speeds up the process significantly, especially for a large number of individuals. The same code can be used on both single core and multi-core machines. It can be specified by the user in program options.

In the begining, before the program is started, the user has to specify what type of structure is going to be optimised. There are two options: multi-junction solar cells (MJSC) and laser power converter in vertical epitaxial heterostructure architecture (VEHSA). The device can be optimised either by parallel of sequential PIKAIA, which can be chosen by the user. Next, number of subcells and the device thickness has to be provided. In case of MJSC, there are different spectra available: ASTM G173-03 extratrrestrial irradiation, ASTM G173-03 global tilt irradiation, ASTM G173-03 direct+circumsolar irradiation, blackbody at 6000K temperature and blackbody at 6000K temperature scaled to simulate air mass. On the other hand, in case of VEHSA device, only laser power and wavelength can be chosen.

The device parameters which can be optimised are current, voltage, thicknesses, impurity levels and energy gap. Current and voltage can not be choosen at the same time, since one can be calculated using the other. If current is choosen, there are options for series-constrained device or unconstrained. If the device is VEHSA, energy gap is not optimised. It has to be specified. Finally, type of losses can be selected. The implemented options are radiative recombination, diffusion dark current, Auger recombination and Shockley-Read-Hall recombination. Shockley-Read-Hall calculation depends on coefficients fitted for GaAs, therefore it is not applicable for the other III-V materials.

At the end of setup, depending on the complexity of the problem, the optimization parameters for the PIKAIA have to be choosen. All except for the numbers of individ-

uals and generations are left as their default values. Number of individuals, in case of M subcells choosen to be $M * 640$, since each node contains 64 cores, whereas the number of generations is $250 + M * 150$, which was choosen based on testing which values provide sufficient accuracy without sacrificing time.

When all the initial conditions are determined, the program calls PIKAIA and provides it with all the necessary instructions. After finishing the optimisation process, PIKAIA returns results of the optimization, including the fittest individual (optimal parameters vector) and its fitness (the expected efficiency).

Typical results of optimization are presented in Figs. 8.4 and 8.5. The first graph shows the fitnesses of each individual in each generation. The second graph shows the distribution of the individuals during the optimization process.

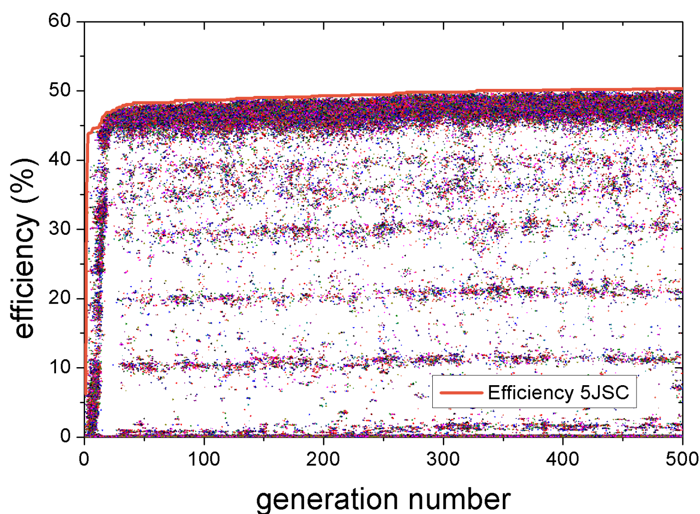

Figure 8.4: Illustration of the optimization progress for the 5-junction solar cell, where signs represent fitnesses of each individual while line represent fitness of the fittest individual in each generation during the optimization process.

The majority of individuals are grouped in range between 45% and 50%. Since the selection operator chooses individuals for reproduction according to their fitness, this is expected. The first generations are created randomly, so they tend to have lower fitnesses. Some of them have higher values, which depends on pure chance.

After 20 or 30 generations there has already been enough reproduction cycles, i.e. crossingovers, which creates clusters of individuals.

The second graph (i.e. Fig. 8.5) shows the distribution of individuals according to their fitness. Clusters can be clearly seen here. If we neglect very low values, which were dominantly discarded for different reasons, we can see clusters appearing

around 10%, 20% and one between 30% and 40%, with few peaks. These are all local maximums.

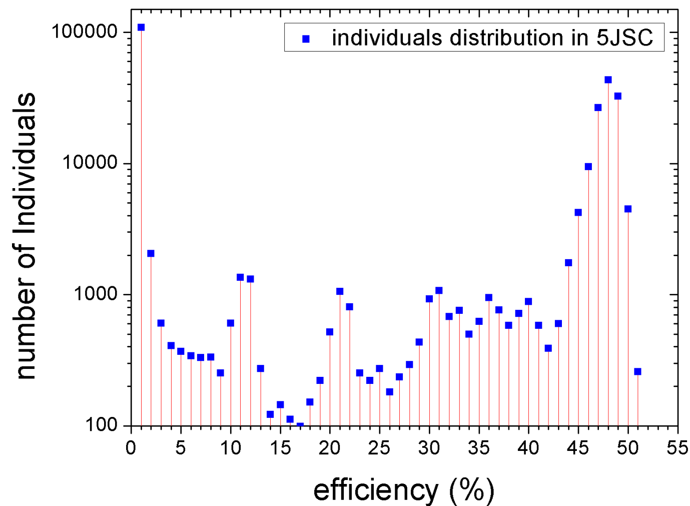

Figure 8.5: Illustration of the optimization procedure for 5-junction solar cell: individuals distribution during the optimization procedure.

The most of other optimizing algorithms would be stuck here, whereas the genetic algorithm has few mechanisms to avoid this. Two individuals in local maximums can produce an individual with much higher fitness, which would reproduce more often in next generations. This way algorithm gets out a local maximum. Another way is mutation. The individual in a local maximum can mutate and achieve higher fitness. On graph Fig. 8.4 it can be seen that in the first generations while the most of individuals have low fitnesses, some of them exceed 40%. In later generations happens that the highest fitness is slightly above the main cluster. This could be crossingover, although it could be attributed to mutation as well.

Overall, the genetic algorithm has shown it can reach the highest fitnesses very quickly, while the distribution of individuals is a proof of algorithm successfully avoids local maxima.

It is of utmost importance to understand how different levels of crossingover and mutation probabilities affect the optimization progress. Figures 8.6a– 8.6d show the distribution of individuals in case of a single-junction device. In case when crossingover probability is fixed (Figs. 8.6a and 8.6b) the distribution depends mainly on mutation. Therefore we can see individuals widely distributed over different efficiencies. The fact that they tend to localize near higher efficiencies is due to selection of the fittest individuals. When each individual is being mutated ($p_{mut} = 1$) the distribution

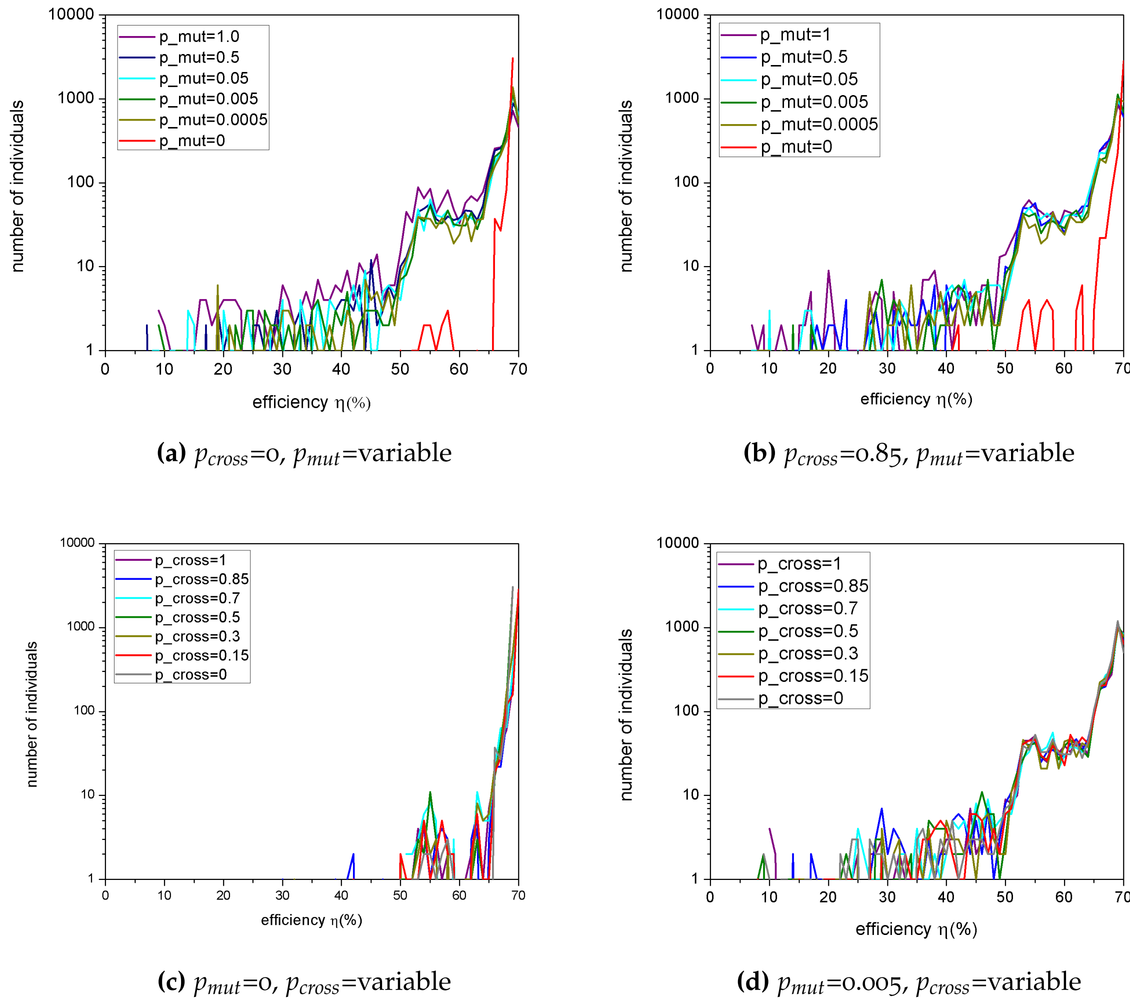

(a) p_{cross}=0, p_{mut}=variable

(b) p_{cross}=0.85, p_{mut}=variable

(c) p_{mut}=0, p_{cross}=variable

(d) p_{mut}=0.005, p_{cross}=variable

Figure 8.6: Distribution of individuals during the optimization process of single-junction device using genetic algorithm for different values of crossingover and mutation probability.

is more equal, than in comparison when there is no mutation ($p_{mut} = 0$). In Fig. 8.6a, in case of $p_{mut} = 0$, the only reproduction operator is selection, the main driving engine of the genetic algorithm. In case of simple problem as this one (single-junction device, 5 parameters optimized) the selection operator is enough to find the optimal solution quickly. Another difference is that almost all individuals are distributed near the highest possible value, although non of them reaches it. Despite all of it's abilities, selection alone is not enough to find the global maximum, which makes crossingover and mutation operators crucial. In case of no mutation (Fig. 8.6c), there is no wide distribution of individuals at lower efficiencies. Except for one, all of them are located at 50% or above. Again, when there is no crossingover ($p_{cross} = 0$) we get the same result as in the previously discussed case, which was expected. Even low crossingover

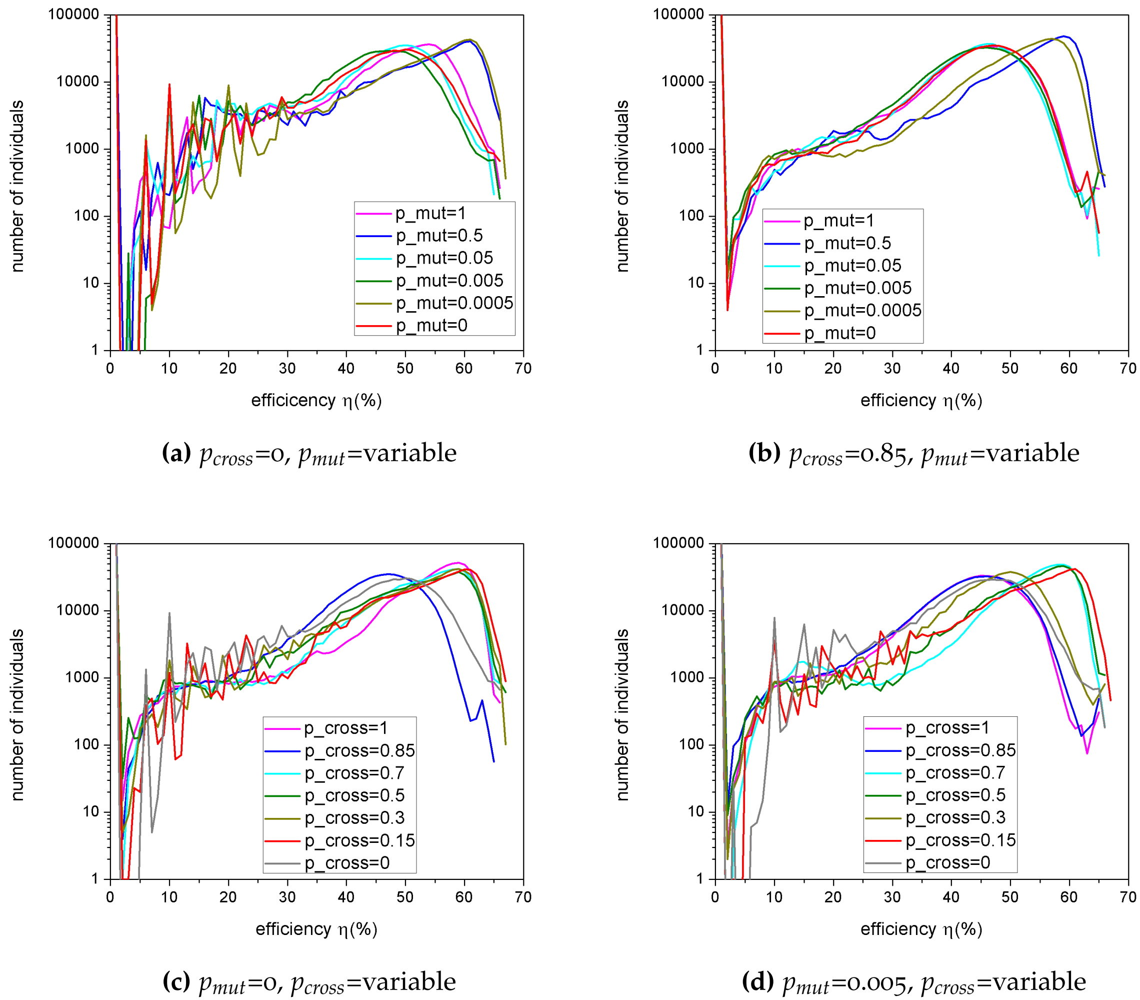

(a) p_{cross}=0, p_{mut}=variable

(b) p_{cross}=0.85, p_{mut}=variable

(c) p_{mut}=0, p_{cross}=variable

(d) p_{mut}=0.005, p_{cross}=variable

Figure 8.7: Distribution of individuals during the optimization process of 15-junction device using genetic algorithm for different values of crossingover and mutation probability.

and mutation probabilities, in combination with selection, lead to a global maximum for simple problems.

In case of complex problems (15-junction device), things are a bit different (Figs. 8.7a–8.7d). Due to complexity of the problem, we can see there is a wide distribution of individuals. In case of no crossingover (Fig. 8.7a), selection, in combination with low mutation probabilities, leads to large number of local maximums. Higher mutation probabilities reduce the number of local maximums, while they still exist to a certain level. High crossingover probabilities (Fig. 8.7b) manage to smooth the graph regardless of mutation, showing the true importance of crossingover operator in very complex problems. Important fact to notice is that high crossingover without mutation can not lead to the global maximum. It definitely does not allow less fit individuals

to become dominant and create local maximums, whereas allows few very fit individuals the same. Unfortunately, this is not enough to reach rhe global maximum (Fig. 8.7b, $p_{mut} = 0$ and Fig. 8.7c, $p_{cross} = 0.85$). Mutation seem to destroy the effect of the crossingover in certain situations (Fig. 8.7b). It looks like high levels of crossingover benefits from low mutation levels, which does not change it's genetic material significantly. On the other hand, looks like very high mutation levels help it find the global maximum as well. Only moderate mutations tend to keep it stuck in the area with lower efficiencies.

Based on the analysis of the results, looks like there is no definite recipe which combinations of mutations and crossingover probabilities are the most optimal. It depends on the problem complexity. For simpler problems selection operator, together with any levels of mutations and crossingover is sufficient to locate the global maximum. For complex problems, it is slightly different. It takes fine tuning of the operator combinations for the optimal solution. Since the crossingover smooths the graphs and tend to group the individuals around few very fit individuals, it is probably the best to go with a high crossingover probability and low mutation, which would help the algorithm create slightly more fit individuals, without destroying their genetic material. This solution might require more time and computing power, but will almost definitely lead to a global maximum.

The results provided in this paper were obtained using the crossingover probability $p_{cross} = 0.85$ and variable mutation rate with $p_{mut,min} = 0.0005$ and $p_{mut,max} = 0.25$.

9

RESULTS AND DISCUSSION

Following the growing demand for electricity, we quickly have to find another source of energy. Most of the energy today comes from fossil fuels. Problems emerging with this type of energy sources are pollution and climate change. We have released tremendous amounts of carbon dioxide and other pollutants, such as nitride and sulfuric compounds into the environment and it has a negative effect on ecosystems across the planet. Another huge problem with this is in fact that fossil fuels are not renewable and we are running out of them.

Solar cells (SCs) are devices with the potential to solve significant number of above-mentioned problems. Single junction solar cells (1JSC) cannot exceed the Shockley-Queisser limit [189] of around 30% in efficiency (Fig. 9.1). If we want them to become the main energy source in the future we need to overcome that limit. Multi-junction solar cells (MJSC) have proven they can increase the efficiency of solar energy conversion [201, 49, 120].

Another important type of device is laser power converters [218] (LPC). These devices allow optical power to be transmitted through optical fibers or directly through free space and they convert it to electricity. This is especially useful in environments sensitive to electromagnetic noise, power-over-fiber systems or remote power delivery, such as power delivery from space.

Both MJSCs and LPCs convert photon energy into electrical energy. The difference is in their structure and the type of irradiation they are converting. MJSCs

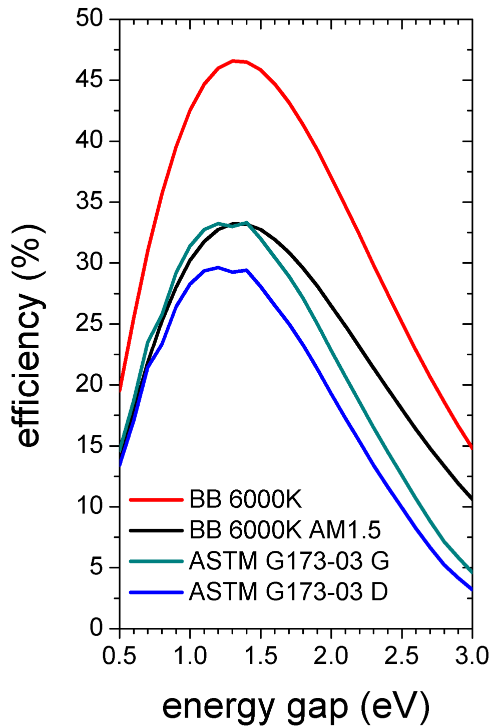

Figure 9.1: Shockley-Queisser limit for: 6000K blackbody radiation (red), 6000K blackbody radiation scaled to be comparable with AM1.5 spectrum (black), real global (green) and direct (blue) irradiation

are intended to convert solar energy into electricity. Solar irradiation consists of photons with a broad energy spectrum. Semiconductors optimally absorb very narrow part of the spectrum. Therefore, in order to achieve high conversion efficiency, we have to fabricate the device using many different semiconductors. They should have different energy gaps specifically chosen to match the Sun's spectrum. LPCs, on the other hand, convert laser irradiation to electricity. They are basically MJSCs as well, with a different structure. Namely, since laser light consists of photons with very narrow energy spectrum, it takes only one type of semiconductor. The problem is in high intensity of laser radiation.

Being very complex devices, they require optimization for high conversion efficiency. For the fabrication of these devices, we need to know which materials we need, their thickness and impurity concentration. Therefore, these parameters were chosen to be optimized. For the most efficient operation, we need to find the optimal combination of current and voltage (i.e. optimal load) so the device would operate in optimal conditions and produce the highest possible output power. Since the voltage can be calculated if we know the current, it is computationally less expensive to optimize current as well.

Number of optimizing parameters for MJSC is $5M + 1$ if series constrained and $6M$ if unconstrained, where M is the number of subcells. Since each subcell is a pn-junction, we need to know the material's energy gap E_g, thickness of p-type semiconductor $\mathrm{w_p}$, thickness of n-type semiconductor $\mathrm{w_n}$, impurity concentration in p-type semiconductor N_a, impurity concentration in n-type semiconductor N_d and optimal

current J_{opt}. The difference between series constrained and unconstrained is in the optimal current. Series constrained SCs are connected in series and, thus, have the same current. Therefore, there is only one parameter for optimization. Unconstrained SCs, on the other hand, are electrically independent. They can be connected to the external circuit separately since each subcell has its own terminals (wires). This means each subcell has its own optimal currents, so there is M parameters for optimization instead of only one. LPCs consist only on one type of semiconductors and the E_g is known from the beginning, while the rest of the parameters are the same as in series constrained MJSC. The number of optimizing parameters has to be $4M + 1$.

For single-junction solar cells there are 6 optimizing parameters for both series constrained and unconstrained, whereas for 5JSC there are 26 if series constrained and 30 if unconstrained. If we try to optimize series constrained MJSC with 10 subcells, there are 51 parameter for optimization. When it comes to LPCs, in case of single-junction there are 5 parameters. If the device has 15 subcells, there are 61 parameter to be optimized. Device parameters create a vast parameter space with many local maxima, making it difficult for the most of search methods to find the solution. Clearly, these optimizations are very complex. Adding to that the constraints between the parameters and conflicting requirements, it is obvious that the optimizing algorithm has to be fast and to be able to solve the problem without any deeper knowledge about it. Heuristic algorithms are the most appropriate for the task. Especially, parallel genetic algorithm.

Each series constrained MJSC is 5μm thick, which allows the most photons to be absorbed. At the same time, it is thin enough for efficient carrier collection at the contacts. Unconstrained ones, on the other hand, had their subcells optimized separately with overall thickness around 10μm. Diffusion lengths were assumed to be $L_n = 3\mu$m and $L_p = 10\mu$m.

Diffusion lengths are very important parameter as they describe carrier collection in the device, so they have to be chosen as close to reality as possible. In cases when it is possible to calculate carrier lifetimes and mobilities with high accuracy, it is simple

to determine diffusion lengths as well. Since there are not enough accurate data and models for wide range of materials, it was necessary do assume the values of the diffusion lengths. The assumed values are chosen in a way so its inaccuracy should not affect the overall results in a too negative way. In case of LPCs the diffusion lengths can be calculated as this device was assumed to be fabricated using GaAs, which will be explained in the folowing chapters.

LPCs are assumed to be made of GaAs. The thickness is 10μm, which allows almost 97% of irradiation to be absorbed when laser wavelength is $\lambda_{laser} = 855n$m. Diffusion lengths were calculated for this type of device. Mobilities [143] in both devices were calculated as a function of impurity concentration: $\log \mu_n = 0.16(\log N_a)^2 - 5.93 \log N_a + 58$ and $\log \mu_p = -0.0575 \log N_d + 3.416$. Having carrier mobilities, it is easy to calculate diffusion constants from Einstein's relation. Surface recombination velocities were assumed $S_p = S_n = 10^3$cm/s. MJSCs were illuminated with ASTM $G173 - 03$ Global tilted solar spectra, while LPCs were illuminated with laser light with energy $E_{laser} = 1.45$eV ($\lambda_{laser} = 855n$m) and intensity 5W/cm^2. All results are obtained at temperature 300K.

In order to test the model and optimization algorithm, results were compared with experimental values whenever possible.

In the begining of the optimization the genetic algorithm provides a set of device parameters, i.e. individual, which has to be evaluated. It means in the beginning there are thicknesses, impurity concentrations, material energy gap and optimal current for each subcell. The fitness value of the individual has to be obtained.

In the first step, only basic material parameters can be calculated. Effective masses can be calculated based on Eqs. 4.4- 4.7, carrier concentrations based on Eqs. 4.8-4.10 and refractive index based on Eq. 4.11. Relative dielectric permittivity can be calculated as refractive index squared. Next, built-in voltage and depletion region widths can be calculated (Eq. 5.1 and Eqs. 5.7– 5.9, respectively).

After all material and structure parameters were obtained, losses can be calculated. First, radiative recombination can be calculated using Eq. 7.22. Next, diffusion dark

current can be calculated from Eq. 7.4. In case of LPCs, Shockley-Read-Hall recombination can be calculated as Eq. 7.43. Finally, Auger recombination can be calculated using Eq. 7.85. The overall losses can be calculated as the sum of individual losses caused by different types of recombinations, as already explained, using the expression Eq. 5.25. When all losses and material parameters are determined, short-circuit current can be calculated as the sum of current in solar cell regions using expressions Eqs. 5.29– 5.34.

Finally, optimal current, optimal voltage and efficiency can be calculated from Eqs. 5.35– 5.37.

9.1 OVERALL SATURATION CURRENT

Radiative recombination (Eq. 7.22) depends mainly on the energy gap. It is one of the most dominant types of losses in direct energy gap semiconductors and can be kept low with increasing the energy gap, as can be seen from Fig. 9.2. The doping does not affect it as much as the energy gap.

Next, the diffusion dark current (Eq. 7.4) depends on energy gap as well. Unlike the radiative recombination, its dependence on doping levels is significant. It has the highest influence on efficiency in case of low impurity concentrations and low energy gaps. The influence of diffusion dark current is reduced by either an increase in energy gap or an increase in impurity levels.

Auger recombination (Eq. 7.85) depends on both energy gap and doping levels as well. Unlike the diffusion dark current, an increase of impurity levels increases the Auger recombination.

For devices with low energy gaps and low impurity levels (Fig. 9.2a), the diffusion dark current will be the most dominant type of loss, although it will only be slightly higher than the radiative recombination. As the energy gap increases, they both decrease at the same rate. At the same time, Auger recombination can be neglected, especially in case when the energy gap is larger.

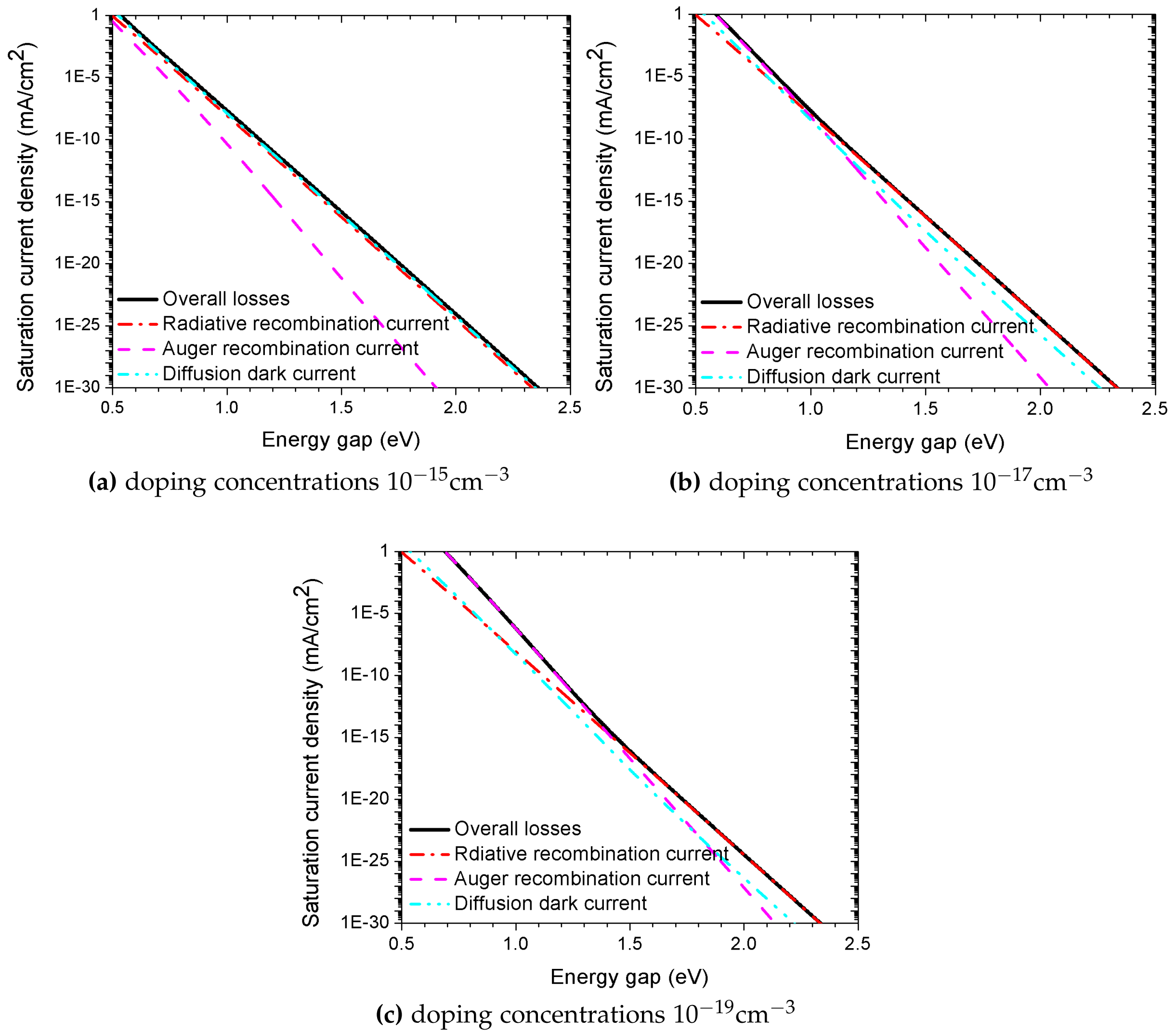

(a) doping concentrations 10^{-15}cm^{-3}

(b) doping concentrations 10^{-17}cm^{-3}

(c) doping concentrations 10^{-19}cm^{-3}

Figure 9.2: Saturation current density as a function of energy gap in a pn junction in case of: (i) overall losses accounted, (ii) only radiative recombination, (iii) only Auger recombination, and (iv) only diffusion dark current.

At moderate impurity levels (Fig. 9.2b), the diffusion dark current is still very high, although not as dominant any more. Now, for lower energy gaps the most dominant is Auger recombination. As the energy gap is becoming higher, radiative recombination takes over, which happens around $E_g \approx 1\text{eV}$. At a structure like this, the diffusion dark current is always an order of magnitude lower than the overall loss.

If the doping is high (Fig. 9.2c), the value of Auger recombination is few orders of magnitude higher than the other two types of losses for lower energy gaps. If the energy gap reaches around $E_g \approx 1.3\text{eV}$, radiative recombinations becomes the most dominant. This time, the diffusion dark current is few orders of magnitude lower than the overall loss.

Taking into account previous analysis, it is obvious that Auger recombination depends on energy gap more than other types of losses, hence it could be reduced with the higher energy gaps. This solution allows higher doping levels which keep diffusion dark current low. As already mentioned, this strategy is reducing the short circuit current as well, but this trade-off is necessary.

9.2 UNCONSTRAINED MULTI-JUNCTION SOLAR CELLS

In order to achieve the highest possible performance, parameters of solar cells have to be optimally selected. Example of such optimization is presented in (Fig. 9.3). Energy gaps of materials were taken from [49] where authors calculated the ideal energy gaps and efficiencies in case of detailed balance limit for the series constrained and unconstrained MJSC. Energy gaps were not optimized in this case in order to test the model since fabrication of unconstrained MJSCs is not common and there are not enough devices to compare results. It was assumed that detailed balance approach is equivalent to an optimized device when only the radiative radiation is taken into account. Next, in detailed balance approach infinite thickness was assumed, whereas widths of each stack in our optimization were set to around 10μm. One more difference is in fact that we are taking into account transport processes in the devices. Diffusion lengths were assumed to be $L_n = 3\mu$m and $L_p = 10\mu$m since they are long enough to provide good carrier collection, so the results can be compared to detailed balance, whereas at the same time they are not too different from the realistic ones, so we can get realistic results when the devices are optimized. Absorption was assumed $\alpha = 10^4\text{cm}^{-1}$ for similar reasons as diffusion lengths. Other parameters, i.e. widths, impurity concentrations and optimal current and voltage, were optimized using a genetic algorithm. The spectrum used for optimization is ASTM $G173 - 03$ Global tilt [22]. The goal of this optimization was to test our model by comparing with results presented in [49].

We can assume our model is correct since there is very low discrepancy between our results in the case of only radiative recombination being taken into account with detailed balance results (Fig. 9.3).

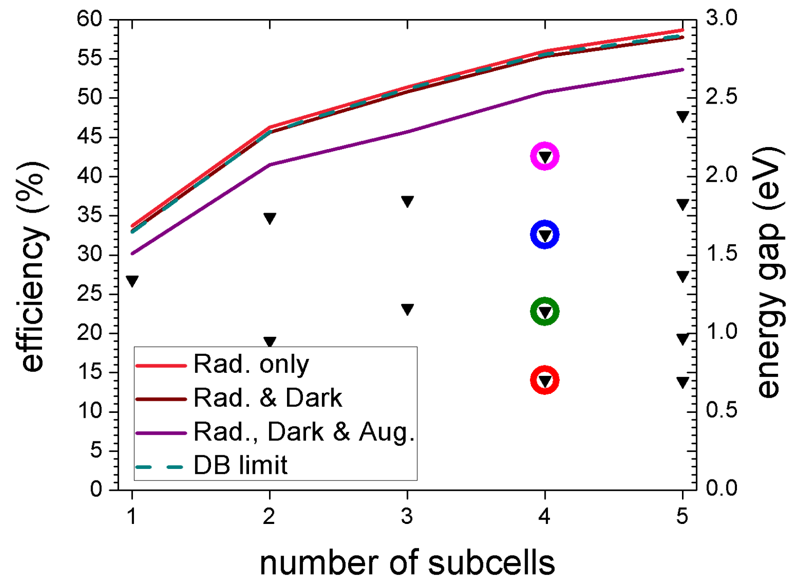

Figure 9.3: Maximum efficiency of unconstrained MJSC as a function of the number of subcells (lines, left axes) and the optimal arrangement of the E_g (signs, right axes): (i) for radiative recombination, (ii) for radiative recombination and diffusion dark current, (iii) for the radiative recombination, diffusion dark current and Auger recombination (iv) detailed balance limit [49].

Parameters were optimized in three different cases. Firstly, with only the radiative recombination. In this case, the highest efficiencies were achieved. Next, diffusion dark current was taken into account. As expected, efficiency reduced slightly. The reduction was between 0.2% and 0.6%. The most significant effect on efficiency Auger recombination has. In this case, efficiency drop was from around 3.2% for a small number of cells in stack up to 4.8% as the number of cells increased. The optimized structure was not series constrained, which means that optimal currents in each cell in MJSC are independent. It allowed efficiencies higher than 50%. The downside of a structure like this is the necessity for contacts for each junction in MJSC. This increases the complexity of the device and, as expected, price.

The optimization was conducted using genetic algorithm [150, 94]. As an example, 4JSC is presented with the evolution of optimization for each individual solar cell

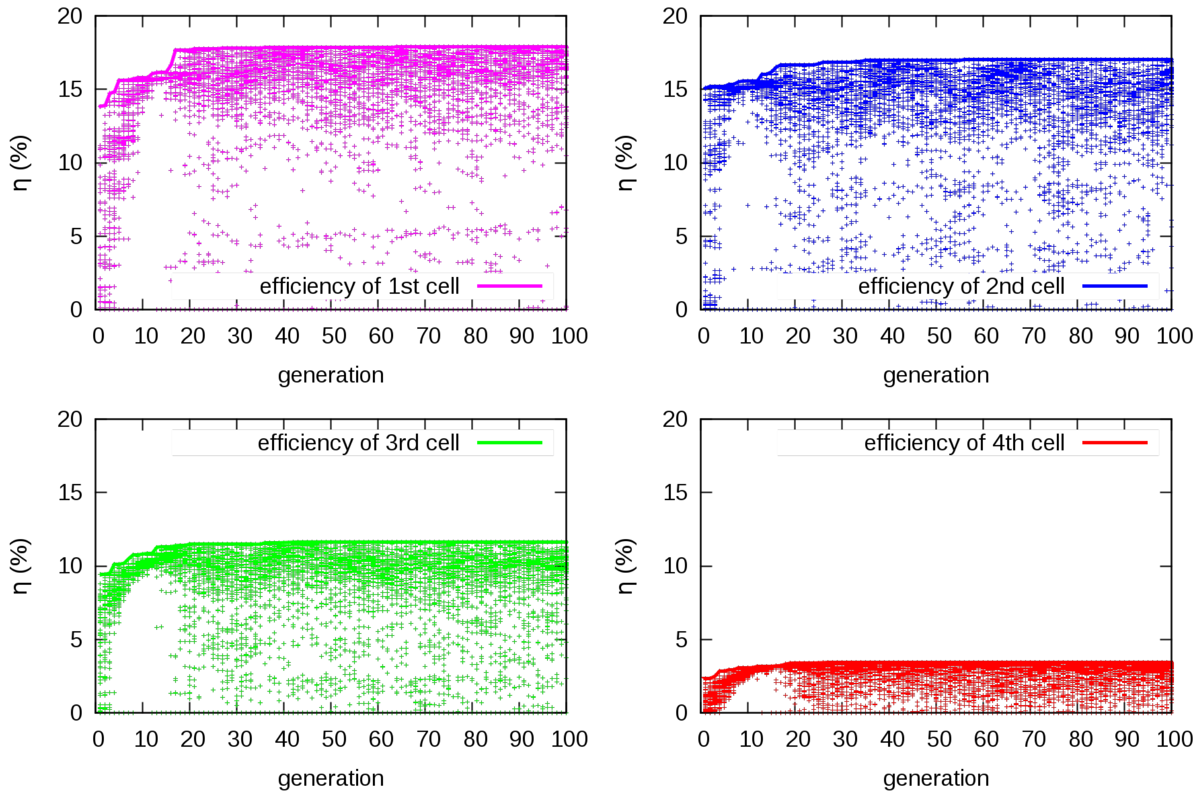

Figure 9.4: Optimization progress for individual SCs in unconstrained 4JSC under ASTMG173 Global tilt spectrum; signs represent fitnesses of each individual; lines represent fitness of the fittest individual in each generation during the optimization process.

(subcell) on Fig. 9.4. Colors on graphs correspond to colors of circles around optimal energy gaps for 4JSC in Fig. 9.3. Each point is the value of efficiency for a tested set of parameters, i.e. individuals. Each individual consists of solar cell parameters which are being optimized. In this case, parameters are dimensions, impurity concentrations and optimal current.

The number of optimizing parameters is $6M$, where M is the number of individual SCs in MJSC. For the first few generations we get low values of efficiencies. The best values are saved and used for creating a new set of individuals. With the new generations, values increase and converge to the best possible value of efficiency. During optimization progress there are still individuals that are far away from optimal value. That is the consequence of diversity, which assures algorithm does not converge to a local maximum. Overall optimization progress of the structure is presented in (Fig. 9.5).

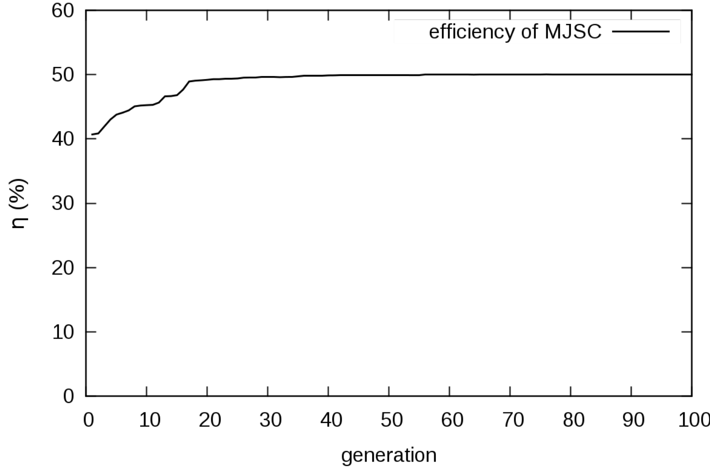

Figure 9.5: Overall optimization progress for unconstrained 4JSC under ASTMG173 Global tilt spectrum

Each subcell is 2.5μm tick, giving the device thickness of 10μm. This thickness was chosen because it is long enough to absorb the most of photons and at the same time shorter than diffusion lengths, which will not negatively affect carrier collection. Since it is very difficult to model dependency of minority carrier mobilities and diffusion lengths on energy gap, minority carrier diffusion lengths were assumed constant, as already explained. These values are slightly lower than the ones for GaAs and similar materials and slightly higher than the ones for AlGaAs and similar materials. Surface recombination velocity is taken as $S = 10^3$cm/s, which is, as well, a value a bit higher than the best values achievable in laboratories, but at the same time low enough not to negatively affect results. Other parameters are depended on the energy gap, as already shown.

Materials in 4JSC, which is taken as an example, should have energy gaps $E_{g,1} =$ 2.23eV, $E_{g,2} =$ 1.63eV, $E_{g,3} =$ 1.14eV and $E_{g,4} =$ 0.702eV, according to detailed balance approach. The model shows how certain types of losses decrease efficiency and offers the optimal parameters for which losses are minimized and efficiency, therefore, maximized. Model takes into account absorption of Sun radiation in the atmosphere and chooses the best parameters accordingly. Each solar cell absorbs in a different part of the spectrum (Fig. 9.6) and cell parameters were specially optimized in that manner. The top solar cell with energy gap of $E_{g,1} =$ 2.23eV absorbs radiation with wavelengths shorter than $\lambda_1 =$ 556nm. It is represented by magenta and is absorbed by a solar cell with energy gap marked with the same color on Fig. 9.3. Second solar cell absorbs wavelengths longer than λ_1 and shorter than $\lambda_2 =$ 760nm, third longer than λ_2 and shorter than $\lambda_3 =$ 1088nm and fourth longer than λ_3 and shorter than

$\lambda_4 = 1776$nm. The color correspondence still holds. When combined in the multi-junction solar cell, each cell absorbs light with wavelengths shorter than its boundary wavelength and longer than boundary wavelengths from the upper cell. This way if one subcell does not absorb a certain number of photons, they can not be accounted in subsequent subcells.

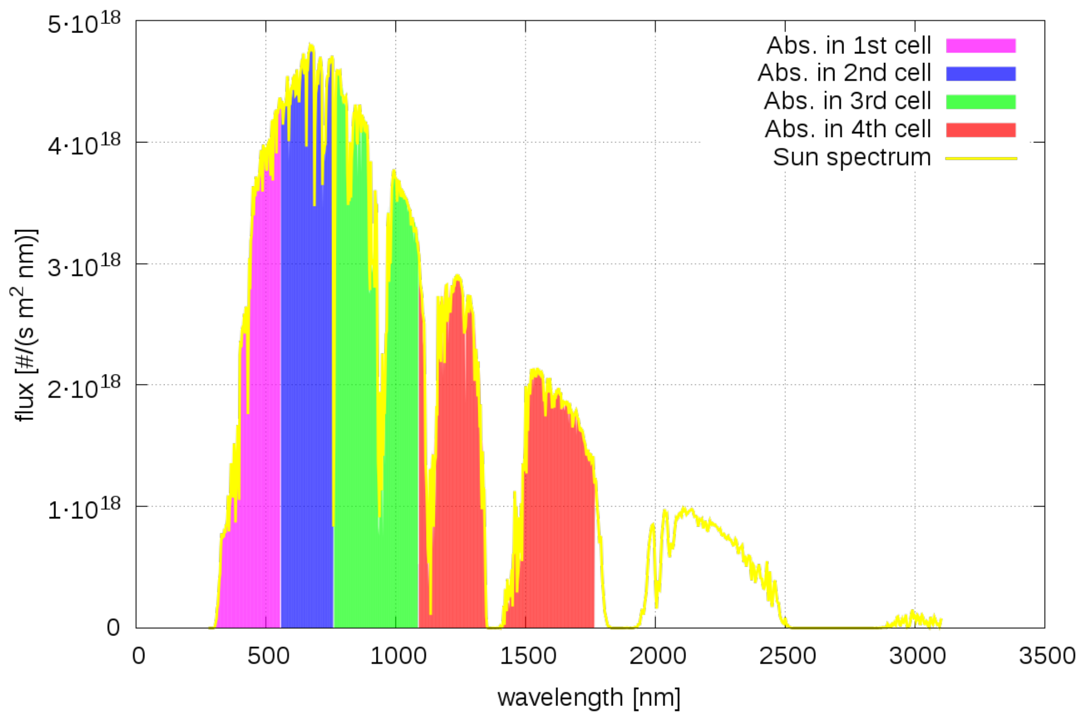

Figure 9.6: ASTM G173-03 Global tilted solar spectra and attenuated portion of this spectra absorbed by each of 4 subcells in unconstrained 4JSC

Since there are plenty of difficulties in the monolithic growth of solar cells, advances were made recently in wafer-bonding and mechanical stacking of solar cells. In order to grow crystals without any defects, which reduce efficiency, materials with an equal lattice constant are required. This limitation reduces the number of possible materials which could be used for multi-junction solar cells.

Wafer-bonding and mechanical stacking as methods for solar cell fabrication are led by Dimroth et. al. [65, 64], and Essig et. al. [69, 68]. The advantage of this approach is in fact that it allows manufacturing of solar cells with a wider range of materials and, thus, more efficient use of solar spectrum. Another important advantage is multi-terminal solar cell realization. This means that each individual solar cell in the multi-junction solar cell will have its own two terminals, i.e. connections. They

are optically coupled and electrically isolated with a material that has to be optically transparent. It allows us to observe them as different devices which do not have to be series connected and can have different optimal currents. Individual solar cells are optimized separately which increases the probability of reaching the highest possible efficiencies. Solar cells presented in Fig. 9.3 were optimized taking advantage of this fact exceed 40% in efficiency for two-junction solar cell and 50% in efficiency for the four-junction solar cell.

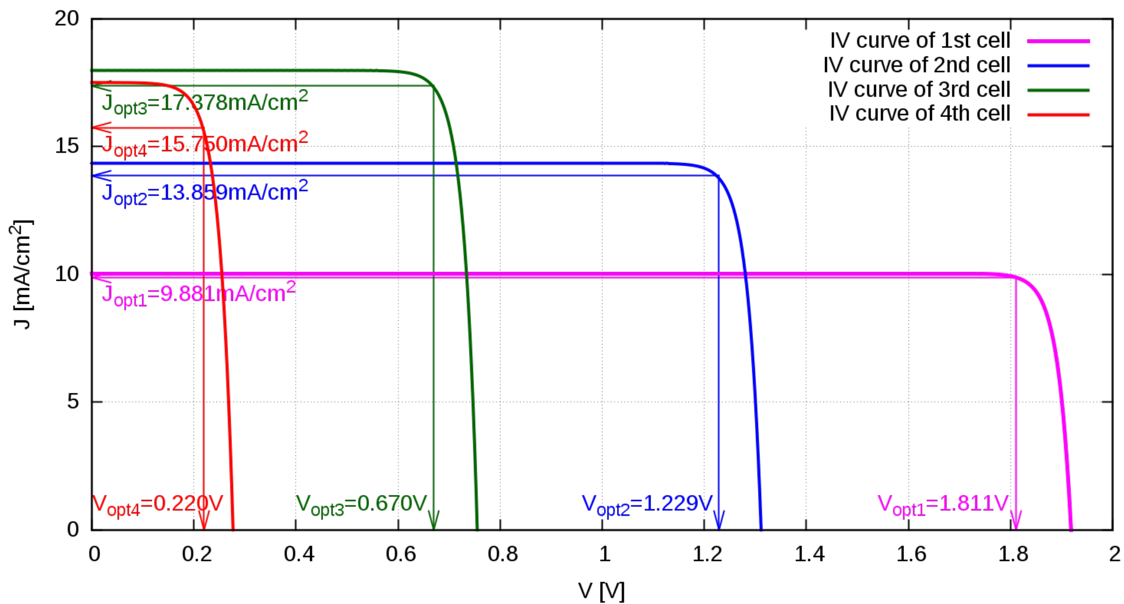

Figure 9.7: *JV* characteristics for individual subcells in unconstrained 4JSC

Current-voltage characteristics of unconstrained four-junction solar cell are presented in Fig. 9.7. It reaches 50.4% (Figs. 9.3 and 9.5). In this case, the solar cell has eight terminals. Subcells have their own optimal currents and voltages, namely optimal working points (J_{opt}, V_{opt}) which can be seen in Fig. 9.7. When this solar cell is used as a two-terminal device (Fig. 9.8), i.e. when individual solar cells are series connected, the top cell, which has the lowest current, defines the overall output current. Working points change (Eq. 6.7) in all subcells except for the top one since its current is not changing. The voltage is equal to the sum of individual voltages. This reduces efficiency to 38.83%. This is obviously a huge drop caused mainly because only part of generated carriers are extracted. The rest recombine and further reduce

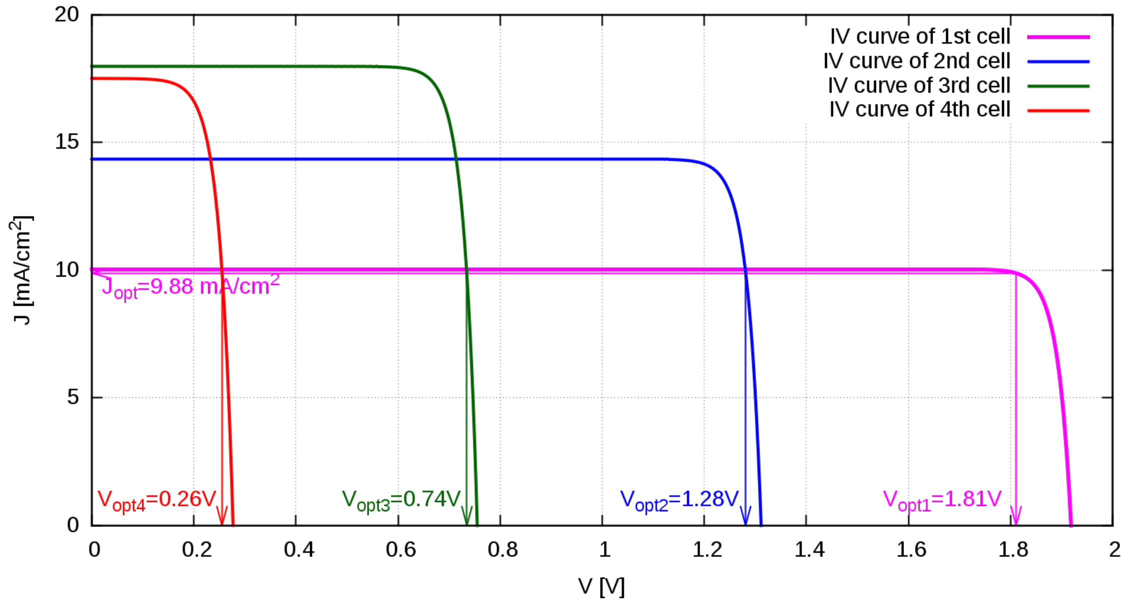

Figure 9.8: JV characteristics for individual subcells in unconstrained 4JSC when subcells are connected in series, i.e. when working as a two-terminal device

the efficiency. From this, it is obvious that we have to optimize parameters for series constrained solar cells separately.

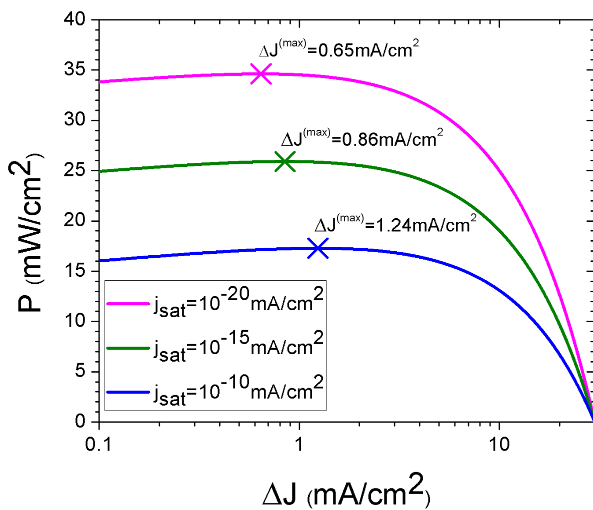

Figure 9.9: Solar cell output power as a function of difference (ΔJ) between short-circuit (J_{sc}) and optimal current (J_{opt}) in case of low, moderate and high losses levels.

The current in the 3rd subcell is larger than the one in 4th subcell simply because more photons fall on that cell. Generally speaking, there is no rule which says which current should be larger. It is just a balance between different conflicting requirements. Using the black body spectrum [49] the currents in multi-junction solar cell are in the descending order $J_{opt,4} > J_{opt,3} > J_{opt,2} > J_{opt,1}$. However if one uses that realistic ASTM $G173 - 03$ spectra which has a large attenuation in the atmosphere around 1400nm, the arrangement of the optimal current could be dif-

ferent. In our optimized multi-junction solar cell $J_{opt,4} < J_{opt,3}$, as it can be seen from (Fig. 9.7). Another interesting fact to notice is that the difference between short-circuit and optimal current ($\Delta J = J_{sc} - J_{opt}$) is larger for lower energy gaps, i.e. $\Delta J_1 > \Delta J_2 > \Delta J_3 > \Delta J_4$. Since optimal voltage (Eq. 5.36) is a function of ΔJ, it is more efficient to reduce optimal current slightly since it leads to a more significant increase of optimal voltage, which is clear from Fig. 9.9. Obviously, the higher the losses, the higher the difference between short-circuit and optimal current needed. Their dependence is not abrupt, which allows more possibilities for optimization algorithms to find the optimal combination of these parameters.

Table 9.1: Optimal parameters of an unconstrained MJSC in case when all types of losses are taken into account

M	m	$E_g[eV]$	w$[\mu m]$	w$_p[\mu m]$	w$_n[\mu m]$	$N_a[cm^{-3}]$	$N_d[cm^{-3}]$
1	1	1.340	10.000	0.016	9.984	1.131×10^{18}	2.076×10^{17}
2	1	1.740	5.000	0.009	4.991	9.417×10^{18}	8.646×10^{18}
	2	0.950	5.000	0.033	4.967	1.771×10^{17}	2.280×10^{16}
3	1	1.850	3.000	0.018	2.982	7.194×10^{18}	9.722×10^{18}
	2	1.160	3.000	0.056	2.944	2.492×10^{17}	1.111×10^{17}
	3	0.703	3.000	0.030	2.970	9.196×10^{16}	9.890×10^{15}
4	1	2.230	2.500	0.011	2.489	8.895×10^{18}	9.771×10^{18}
	2	1.630	2.500	0.011	2.489	7.753×10^{18}	3.802×10^{18}
	3	1.140	2.500	0.021	2.479	5.569×10^{17}	1.013×10^{17}
	4	0.702	2.500	0.005	2.495	5.211×10^{17}	9.416×10^{15}
5	1	2.390	2.500	0.023	2.477	9.183×10^{18}	8.932×10^{18}
	2	1.830	2.500	0.018	2.482	9.046×10^{18}	9.078×10^{18}
	3	1.370	2.500	0.010	2.490	2.220×10^{18}	4.433×10^{17}
	4	0.970	2.500	0.007	2.493	7.924×10^{17}	2.977×10^{16}
	5	0.695	2.500	0.002	2.498	1.832×10^{18}	9.063×10^{15}

Detailed solar cell parameters are presented in Table 9.1. The table presents parameters of subcells in an unconstrained MJSC when dark current, radiative and Auger recombination are taken into account. Energy gaps are taken from detailed balance [49], while other parameters were optimized. As already explained, radiative recombination will be reduced by the increase of energy gap (Eq. 7.22, Fig. 9.2). Diffusion dark current can be minimized by maximization of impurity concentrations and maximization of energy gaps (Eq. 7.22, Fig. 9.2). We will minimize Auger recombination if we maximize energy gap and, unlike diffusion dark current, minimize impurity

concentrations (Eq. 7.85, Fig. 9.2). From (Table 9.1) and already mentioned equations it can be seen that for higher energy gaps we have low Auger recombination since it depends on energy gap more strongly than dark current. Therefore, in order to minimize losses, the optimization algorithm found that best choice is to dope more heavily subcells with higher energy gaps and reduce diffusion dark current as well. Subcells with lower energy gaps should be doped lightly. The exception is when we have dimensions different than usually. When width of the $p-$type semiconductor is significantly thinner than others and we can even have heavy doping in combination with lower energy gaps. Even though this combination leads to higher losses, it leads to higher gains as well since it allows better carrier collection due to high ratio of diffusion length to the thickness. When we have lower doping, depletion region will be wider, which sets the lower limit for emitter thickness, w_p in the table.

Table 9.2: Maximum efficiencies of an unconstrained MJSC in with different combinations of losses

M	η[%] Rad.	η[%] Rad.& Dark.	η[%] Rad., Dark & Aug.
1	33.698	33.065	30.158
2	46.298	45.612	41.479
3	51.403	50.816	45.669
4	56.010	55.341	50.775
5	58.676	57.778	53.653

Efficiencies of MJSCs with different types of losses taken are presented in Table 9.2. These results are plotted in Fig. 9.2 as well. Examining the numbers themselves, it is obvious how difficult it is to suppress the Auger recombination, as oppose to diffusion dark current, which is something that should not be neglected when designing real devices.

9.3 SERIES CONSTRAINED MULTI-JUNCTION SOLAR CELLS

From equations (Eq. 5.22– 5.28) and Fig. 5.3 it is obvious that solar cell efficiency can be increased by increasing short circuit current, open circuit voltage and fill factor. Short

circuit current depends on the number of absorbed photons which create electron-hole pairs, i.e. carrier creation, and carrier collection at the contacts.

If E_g is lower, the number of absorbed photons is higher. At the same time, it is increasing carrier recombination, which reduces lifetimes. If lifetimes are lower it means carriers will not have enough time to reach contacts. Instead, they will recombine. This is reducing short circuit current only slightly. It still benefits significantly from lowering E_g (Fig. 9.10). On the other hand, E_g is the boundary for open circuit voltage. In the ideal case, if the losses were suppressed completely, open circuit voltage would still not be able to reach the E_g due to thermodynamic reasons, e.g. Carnot factor. Anyway, for high open circuit voltage high energy gap is crucial. This is only one of the conflicting requirements which makes the optimization necessary.

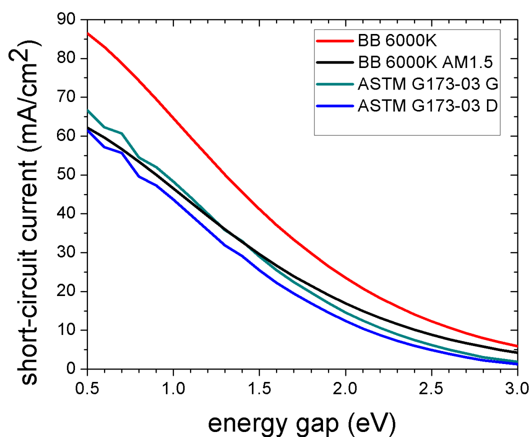

Figure 9.10: Short circuit current as a function of energy gap under 6000K blackbody radiation (red), 6000K blackbody radiation scaled to be comparable with AM1.5 air mass (black), real global (green) and direct (blue) irradiation.

There are different types of losses in solar cells. The most dominant in solar cells based on $III-V$ semiconductors are radiative recombination (Eq. 7.22), diffusion dark current (Eq. 7.4) and Auger recombination (Eq. 7.85). They all behave differently in different circumstances. Auger recombination is the most dominant type of recombination in semiconductors with lower energy gap (Fig. 9.2). As the energy gap increases, the diffusion dark current becomes the most dominant, while impurity concentration is still low. Therefore, the way to suppress this type of losses is by increasing impurity concentration. At the same time, higher impurity concentration elevates Auger recombination. This is another huge conflicting requirement. This all proves the necessity of heuristic optimization.

Maximum efficiency values achieved in optimization are presented in Fig. 9.11 together with the optimal arrangement of energy gaps. The device parameters were op-

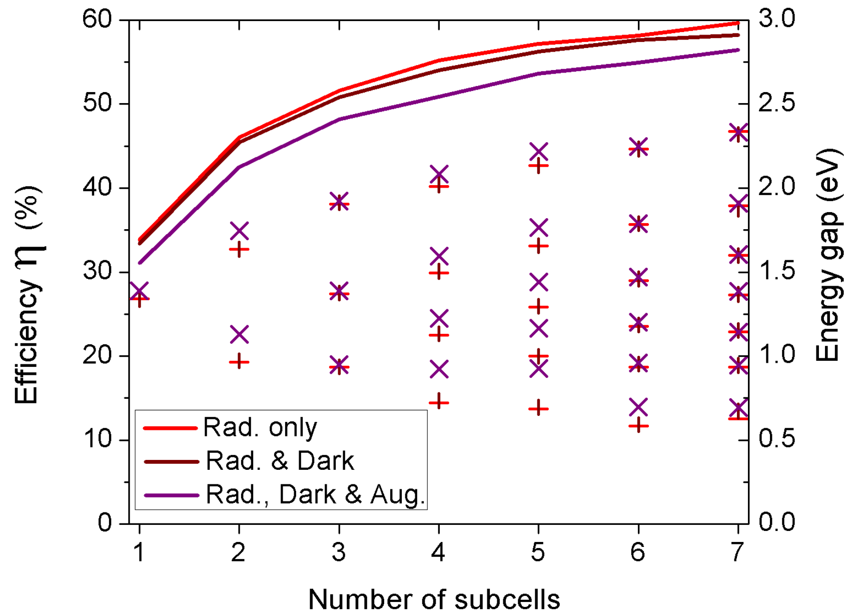

Figure 9.11: Maximum efficiency of series constrained MJSC as a function of the number of junctions (lines, left axes) and the optimal arrangement of the E_g (signs, right axes): (i) for radiative recombination, (ii) for radiative recombination and diffusion dark current, and (iii) for the radiative recombination, diffusion dark current and Auger recombination [201].

timized for up to 7 junctions. Detailed results are presented in Table 9.3. Optimized parameters are thickness of p-type semiconductor w_p, thickness of n-type semiconductor w_n, impurity concentration in p-type semiconductor N_a, impurity concentration in n-type semiconductor N_d, optimal current J_{opt} and energy gaps E_g, which was optimized as well, unlike in case of unconstrained MJSC. Similar discussion stands here as the one related to data in Table 9.1. The device was optimized in three different regimes:

1. only radiative recombination
2. radiative recombination and diffusion dark current
3. radiative recombination, diffusion dark current and Auger recombination

The idea behind this is to see how different types of losses affect the efficiency. It is evident that the Auger recombination has the highest impact. It is reducing the efficiency for $\approx 5\%$ comparing to when this type of recombination is not taken into account. This is something that should not be neglected in the actual device design.

Table 9.3: Optimal parameters of a series constrained MJSC in case when all types of losses are taken into account [201]

M	m	E_g[eV]	$w^{(m)}[\mu m]$	$w_p[\mu m]$	$w_n[\mu m]$	$N_a[cm^{-3}]$	$N_d[cm^{-3}]$
1	1	1.389	5.000	0.004	4.996	6.192×10^{18}	4.232×10^{17}
2	1	1.746	3.578	0.019	3.559	7.784×10^{18}	7.967×10^{18}
	2	1.128	1.422	0.026	1.396	4.546×10^{17}	9.645×10^{16}
3	1	1.922	1.727	0.023	1.703	6.138×10^{18}	7.884×10^{18}
	2	1.387	1.993	0.032	1.961	7.667×10^{17}	6.540×10^{17}
	3	0.949	1.280	0.044	1.236	1.679×10^{17}	6.340×10^{16}
4	1	2.010	1.427	0.016	1.411	9.356×10^{18}	5.951×10^{18}
	2	1.502	1.119	0.097	1.022	6.884×10^{17}	5.094×10^{17}
	3	1.120	1.524	0.056	1.468	1.987×10^{17}	6.718×10^{16}
	4	0.713	0.930	0.044	0.887	8.544×10^{16}	8.544×10^{16}
5	1	2.217	1.414	0.148	1.266	9.056×10^{18}	8.985×10^{18}
	2	1.767	1.120	0.025	1.095	8.342×10^{18}	9.346×10^{18}
	3	1.441	0.785	0.016	0.769	2.736×10^{18}	1.194×10^{18}
	4	1.167	0.832	0.020	0.812	7.102×10^{17}	1.342×10^{17}
	5	0.928	0.849	0.019	0.830	3.368×10^{17}	3.294×10^{16}
6	1	2.246	0.892	0.063	0.829	9.994×10^{18}	9.774×10^{18}
	2	1.789	0.735	0.015	0.720	9.539×10^{18}	9.206×10^{18}
	3	1.472	0.725	0.186	0.539	5.252×10^{17}	9.213×10^{17}
	4	1.201	0.866	0.120	0.746	7.179×10^{17}	2.594×10^{16}
	5	0.959	0.823	0.070	0.753	1.094×10^{17}	3.503×10^{16}
	6	0.698	0.958	0.035	0.924	9.172×10^{16}	1.137×10^{15}
7	1	2.352	1.002	0.399	0.603	7.024×10^{18}	5.851×10^{18}
	2	1.915	0.817	0.226	0.591	5.192×10^{18}	6.776×10^{18}
	3	1.612	0.588	0.169	0.419	2.193×10^{18}	2.140×10^{18}
	4	1.390	0.688	0.167	0.521	5.429×10^{17}	7.477×10^{17}
	5	1.159	0.670	0.066	0.604	2.296×10^{17}	3.802×10^{17}
	6	0.949	0.459	0.094	0.365	2.176×10^{17}	9.160×10^{15}
	7	0.727	0.776	0.082	0.693	5.609×10^{16}	1.533×10^{16}

As already explained, Auger recombination depends on energy gap more than other types of losses, hence it could be reduced with the higher energy gaps. As already mentioned, this solution is reducing the short circuit current as well, but this trade-off is necessary. In fact, this is exactly the way to go (Fig. 9.11,Table 9.3), according to the genetic algorithm used in the optimization. In almost all devices, when Auger recombination is taken into account the values of E_g are higher. The reason for this is $J^{(m)}_{\mathrm{AUG},0} \propto e^{-E_g^2/k_BT}$. Large E_g is reducing the contribution of the Auger losses to the overall losses faster than it does with the other types of losses in the device. By

Table 9.4: Maximum efficiencies of a series constrained MJSC in with different combinations of losses [201]

M	η[%] Rad.	η[%] Rad.& Dark	η[%] Rad., Dark & Aug.
1	33.852	33.382	31.080
2	46.025	45.424	42.467
3	51.624	50.797	48.276
4	55.221	54.006	50.777
5	57.205	56.232	53.653
6	58.150	57.634	54.917
7	59.637	58.204	55.317

detailed inspection of Table 9.3, we can see that higher E_gs are followed by higher doping levels, which reduces diffusion dark current even further. The reason for the dominance of the Auger recombination on the Fig. 9.11 is only a trade-off by the algorithm in order to maximize the efficiency.

Table 9.4 shows maximum efficiencies of a series constrained MJSC in three cases. First, when only radiative recombination is taken into account (η[%] Rad.). Second, when both radiative recombination and diffusion dark current are taken into account (η[%] Rad.& Dark.). Third, when all three types of losses are accounted (η[%] Rad., Dark & Aug.). The same results were presented graphically on Fig. 9.11.

Series constrained MJSCs have a constrain in optimization procedure as a consequence of current matching, hence it is expected to have lower efficiencies in comparison to unconstrained MJSCs. If we compare Tables 9.4 and 9.2, we will see that is correct for higher number of subcells, when only radiative recombination is accounted for, which is expected. On the other hand, results in case of all losses are completely different. These results are very similar, or series constrained device has higher efficiencies. Unconstrained MJSC is, as already explained, optimized in case of detailed balance, whereas series constrained MJSC is optimized for each case separately. Therefore results from the fourth column in Table 9.2 have slightly lower values than it would be the case if the device was optimized for all types of losses. This can be confirmed by comparing the values of energy gaps, especially in lower subcells. In case of unconstrained MJSCs they are very low, which are vulnerable recombinations, particularly to Auger recombination.

In order to test the results, we have compared our predicted efficiencies for series constrained MJSCs [201] with experimental results of the record setting MJSCs [96, 116, 181]. The results are summarized in Table 9.5, with equal number of junctions and without light concentration. There is a significant difference between the maximally predicted and the efficiency of actual solar cells devices, which points out the importance of the spectrum matching. Our optimization procedure can predict exactly the optimal energy gaps and also the optimal thickness of each subcell in order to achieve almost identical short-circuit currents through the device (Fig. 9.12a,b,Fig. 9.13).

Table 9.5: Comparison of 2-junction, 3-junction and 4-junction SCs with experimental results [96, 201]

η [%]	Rad. only	Rad. & Dark	Rad., Dark & Aug.	Exp. III-V
$2JSC$	46.0	45.4	42.5	31.6 ± 1.5 [116]
$3JSC$	51.6	50.8	48.3	37.9 ± 1.2 [181]
$4JSC$	55.2	54.0	50.8	/

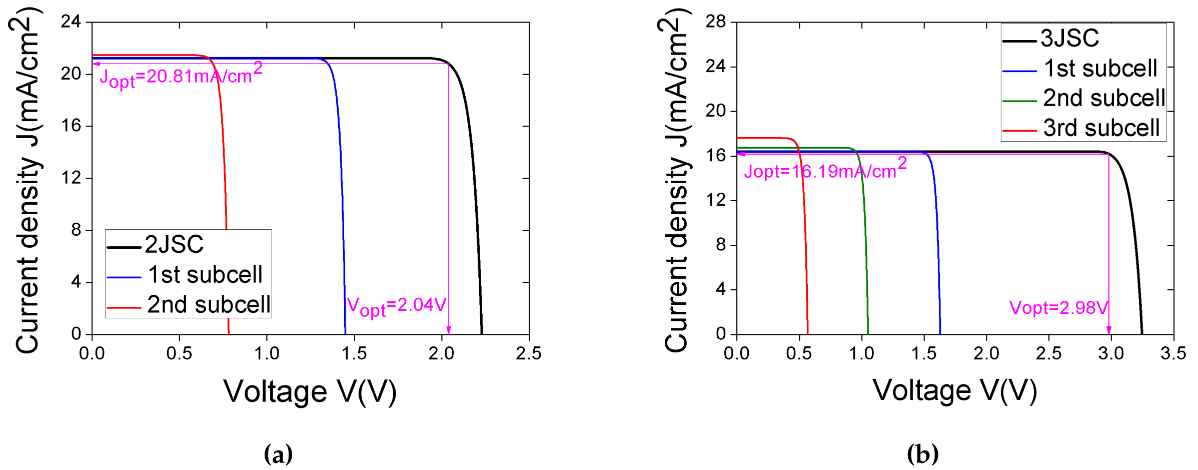

Figure 9.12: Optimal JV curve for: (a) 2-junction solar cell, (b) 3-junction solar cell [201].

We have achieved very small differences in our short circuit currents between subcells; in 2- junctions SC $J_{sc1} = 21.253$ mA/cm^2 vs. $J_{sc2} = 21.484$ mA/cm^2 (Fig. 9.12a [201]); in 3- junctions SC $J_{sc1} = 16.407$ mA/cm^2 vs. $J_{sc2} = 16.761$ mA/cm^2 vs. $J_{sc3} = 17.625$ mA/cm^2 (Fig. 9.12b [201]); in 4- junctions SC $J_{sc1} = 14.362$ mA/cm^2 vs. $J_{sc2} = 14.357$ mA/cm^2 vs. $J_{sc3} = 14.883$ mA/cm^2 vs. $J_{sc4} = 16.046$ mA/cm^2 (Fig. 9.13 [201]).

Such small deviations between J_{sc}'s and between J_{sc}'s and J_{opt} suggest efficient use of photo created carriers and its maximized collection. That proves the efficiency of the optimization algorithm as well.

It is interesting to notice how short-circuit currents in different subcells are in the descending order $J_{opt,4} > J_{opt,3} > J_{opt,2} > J_{opt,1}$, unlike the unconstrained device. The reason for this is that the constraint demands optimal currents to be equal, which further demands short-circuit currents to be similar. Since algorithm intelligently found a way to keep losses low, there was no need for a large difference between short-circuit and optimal currents.

On the other hand, in the actually fabricated devices subcells short circuit currents differ significantly (Fig. 9.14). The reason for that could be either material availability which defines E_gs and, thus, absorbed portions of the spectrum, or it could be due to approximated thicknesses of subcells. For the record efficiency devices [96, 116, 181] the measured short-circuit currents are: $J_{sc} = 14.30$ mA cm^{-2} for 2- junctions MJSC reported in [116] and $J_{sc} = 15.25$ mA cm^{-2} in 3- junctions MJSC reported in [181]. The overall short circuit current in series constrained MJSC is limited by the lowest J_{sc_i} of individual subcells. The reason for the low overall short circuit current could be in one under-performing subcell and below optimal spectral matching.

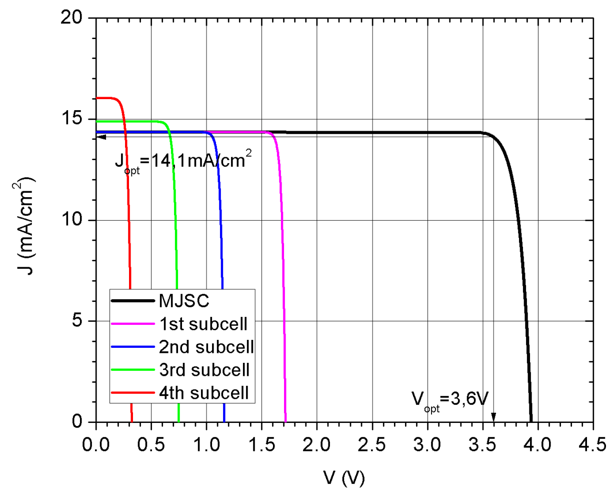

Figure 9.13: Optimal JV curve for 4-junction solar cell [201].

In Alta Devices' 2- junction MJSC the $V_{oc} = 2.547$ V [116] is higher in comparisons to our predicted, $V_{oc} = 2.229$ V. This is due to photon recycling [215, 149], which increases short-circuit currents and allows higher voltages. At the moment it is not taken into account in our model. However, in their device based on InGaP/GaAs

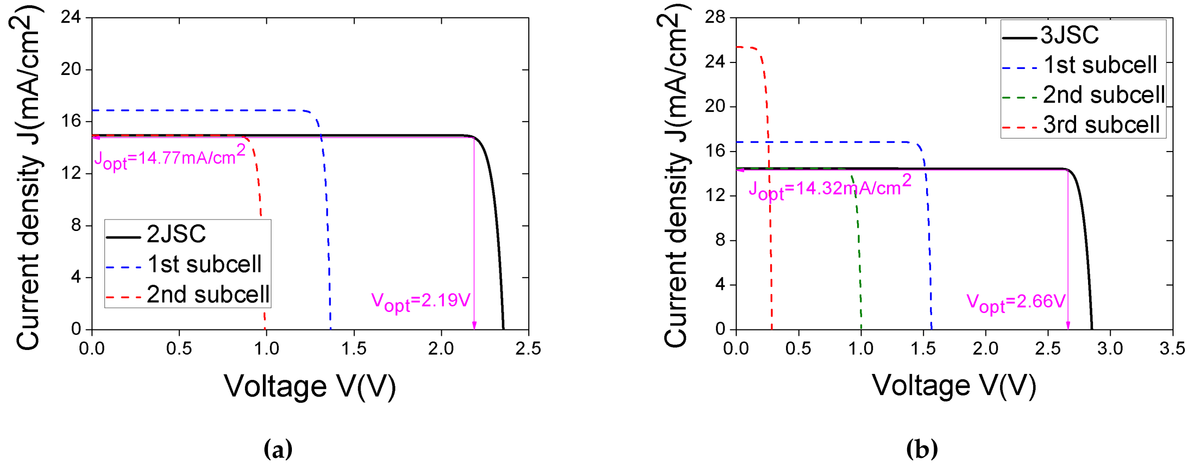

Figure 9.14: Predicted *JV* curve of our optimization based on extracted experimental parameters of record setting devices [201]: (a) Alta Devices® 2-junction solar cell [116], (b) Sharp® 3-junction solar cell [181].

tandem, the short circuit is low due to relatively high E_g in subcells. Relatively high E_g is another reason for the above mentioned high V_{oc} in the actual device.

In Sharp's 3- junction MJSC the $V_{oc} = 3.014$ V [181] is lower in comparison to our predicted $V_{oc} = 3.245$ V. With the increase of the number of subcells, the availability of materials and tuning between relevant parameters in actual devices becomes more demanding. That suggests that our algorithm successfully suppressed major losses during the optimization procedure and opened room for further improvements in MJSC design.

The validity of our method was tested by performing the optimization with parameters of the actual devices [116, 181]. In Alta Device® 2-junction SC [116] the upper subcell is made of $In_{0.49}Ga_{0.51}P$, lattice matched to GaAs, with $E_g = 1.9$ eV [205] and the lower subcell is GaAs, with $E_g = 1.42$ eV. The values of energy gaps were the only data available, so we had to fixate them in our model and let the rest of the MJSC parameters to be optimized by genetic algorithm. The predicted efficiency was 32.34% [201], which almost coincide with the measured, $31.6 \pm 1.5\%$ [116]. If we compare values of V_{oc} between the real device and the one from our model ($V_{oc} = 2.547$ V [116] versus $V_{oc} = 2.355$ V), we can see that there is only a small difference. Such

a small difference can be attributed to the photon recycling effect existing in the real device.

The Sharp® 3-junction SC [181], has the configuration of two upper subcells the same as in Alta Device® followed with $In_{0.53}Ga_{0.47}As$ as the lowest subcell with $E_g = 0.74$ eV [205]. The efficiency predicted by our optimization is 38.1% [201], which is again very close to measured, $37.9 \pm 1.2\%$ [181]. The JV characteristics are presented in Fig. 9.14. Comparing results on MJSCs optimized with fixed E_g's, dictated by actual material combinations in existing devices with those fully unconstrained, (Fig. 9.12a,b), the advantage of heuristic optimization is obvious.

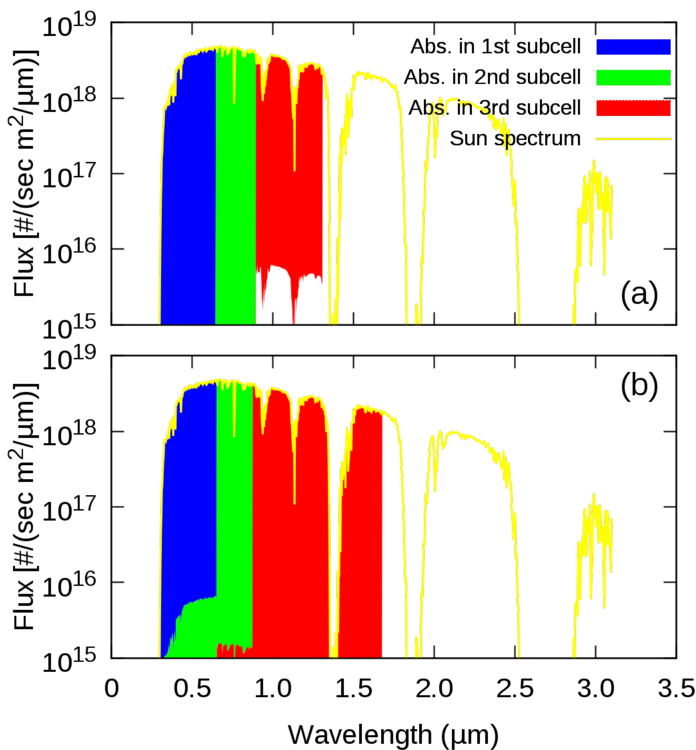

Figure 9.15: ASTM G173 – 03 Global tilted solar spectra and attenuated portion of this spectra absorbed by each of 3 subcells in 3-junction SC: (a) optimization based on our model [201] and (b) optimization based on extracted experimental parameters of record setting device [181].

When all parameters are freely optimized the optimal efficiency is dramatically increased, for $\sim$ 10%, due to much better adjustment of subcells absorption to the solar spectrum. If all subcells in the MJSC are properly optimized, the differences between their short-circuit currents should be very small.

In series constrained solar cells the lowest subcell's current defines the output current. A significant difference in short circuit currents leads to non-optimal carrier extraction from individual subcells in the MJSC. Those carriers that are not extracted recombine and increase losses, which decreases the voltage across the device.

Absorbing more photons does not necessarily lead to the higher efficiency (Fig. 9.15). For example, the 2nd subcell in Sharp® device happens to absorb the smallest portion of the solar spectra (Fig. 9.15b), hence has the lowest short- circuit current (Fig. 9.14b). That subcell defines the overall current of the device.

On the other hand the 3rd subcell absorbs the unnecessarily large portion of sun spectra (Fig. 9.15b) and produces too large short circuit current (Fig. 9.14b) in comparison with the one that defines the overall output current. The excess number of photons only contributes to losses and reduces voltage. To correct this, our model reveals that the 3rd subcell should be made of a material with a larger energy gap (Fig. 9.15a). Such larger gap material will prevent unnecessary absorption of the excess number of photons. This will lead to lower short-circuit current in the 3rd subcell and, in turn, will lower losses. This discussion is supported by results listed in Table 9.5.

Despite these results, there are certain drawbacks in the model. First and foremost, not all the losses were taken into account. Only radiative recombination, diffusion dark current and band to band Auger recombination were. The model would be more complete if other types of recombinations could be accounted. There are not enough reliable models for those losses which could be incorporated. At the same time, it is not easy to measure all the losses individualy, which leads to uncertanty in modeling such as this. Nevertheless, all material and device parameters were compared to experimental results where possible.

Furthermore, in this model, reflections were not taken into account, which could cause higher eficiencies estimated comparing to reality. With good antireflective coating, it can be kept very low. The same applies to tunnel junctions. It was assumed the record setting devices would have minimal reflection losses and minimal losses across the tunnel junctions, especially taking into account the low curents.

As already pointed out, certain parameters were fixed, which can cause inaccurate optimization. Deffinitely the most significant assumption are the diffusion lengths. They were taken as could be expected for GaAs, which means the assumption is pretty good for subcells with energy gap around 1.4eV. From the Table 9.3 it can be seen that

those subcells are doped moderately, which means the impurity levels should not increase the inaccuracy. The problem can be in different subcells. Subcells with lower energy gaps tend to have longer diffusion lengths, which leads to underestimated carrier collection and lower currents then it would be in real devices. On the other hand, subcells with higher energy gaps usually have shorter diffusion lengths, so we can assume the obtained currents are slightly higher than they would be in reality. The value was fixed for surface recombination velocity as well. The taken value is higher than it would be expected in a record setting device, which leads to underestimated carrier collection. Since the short-circuit currents predicted by the model are similar to the measured ones in case of record setting devices, it can be assumed that there is certain inaccuracy, although not too large.

Another important parameter is solar spectrum. It has already been described how important is it to match the subcells' energy gaps to the incoming photons. Different solar spectra have different spectral composition, which affects the efficiency significantly. The spectra choosen in this optimisation is ASTM $G173-03$ Global tilted solar spectra, which takes into account the absorption in the atmosphere. Different weather conditions and time of the day change the spectra significantly, so these results can not be compared to each measurement conducted outdoors. It would depend on test conditions. When it comes to laboratory measurements, the test conditions are standardized, so the comparison can be direct.

Another difference in comparison to optimization of unconstrained MJSCs can be observed here. In this case, it is possible for the subcells to absorb photons with higher energy which were not absorbed in the preceding subcell. This is a consequence of absorptions which are now calculated using the parallel `kppw` code [198]. The top subcell can potentially absorb photons from the whole solar spectrum. The only constraint is the absorption coefficient for photons with different energies. The subsequent subcell can absorb all photons transmitted by the upper subcell, again with absorption coefficient as the only constraint.

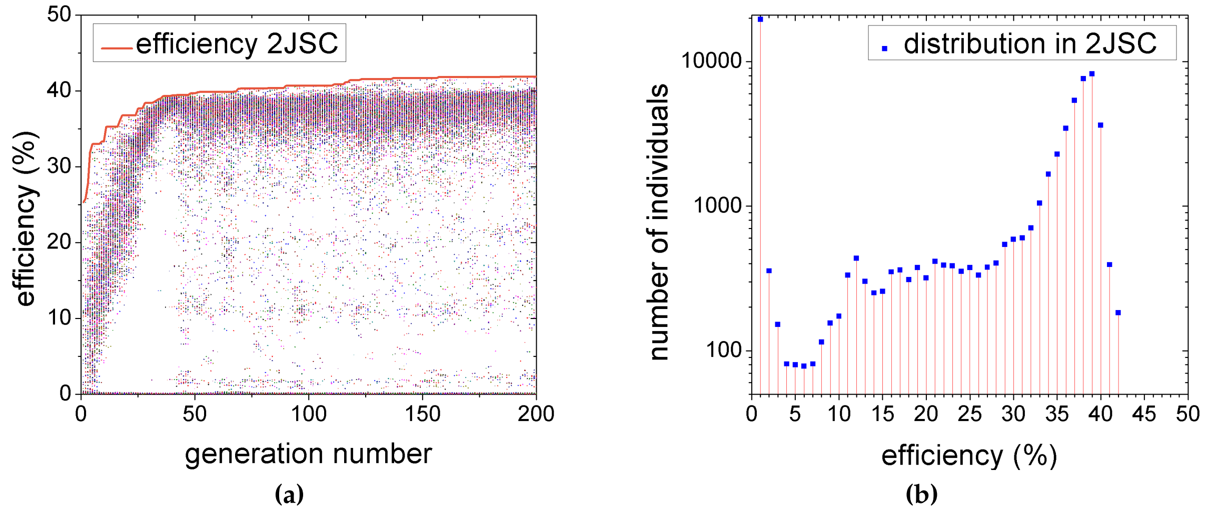

Figure 9.16: Illustration of the optimization procedure for series constrained 2JSC under ASTMG173 Global tilt spectrum: (a) signs represent fitnesses of each individual while line represent fitness of the fittest individual in each generation during the optimization process, (b) individuals distribution during the optimization procedure

As already explained, the optimization was conducted using a genetic algorithm. As an illustration of this procedure, optimization progress of 2JSC was presented in Fig. 9.16. Each point on Fig. 9.16a is the value of efficiency for a tested set of parameters, i.e. individuals. Each individual consists of solar cell parameters which are being optimized. In this case, parameters are energy gaps, dimensions, impurity concentrations and optimal current. The line connects the highest efficiency reached in each generation. The number of individuals with each efficiency value was presented in Fig. 9.16b. It is easy to see how most of the parameter sets provide the efficiency between 30% and 40%. This is the consequence of crossingover. Fitter individuals get to reproduce more, so they pull the whole generation towards the maximum. The downside of this is that they can be stuck in a local maximum. The highest number of parameter sets is around 39%, while the highest efficiency found is 41.6%. This is where another of the advantages, mutation, steps in. Mutated individuals can sometimes reach higher values than the others and share their genetic material with other individuals in subsequent generations. This operator makes sure the highest efficiency is always reached.

The full set of the results of our optimization procedure, i.e., the optimal E_g, the optimal thicknesses of subcells, the optimal thicknesses of p- and n- regions, $w_{p(n)}$,

as well as the optimal acceptor and donor concentrations $N_{a(d)}$ in each subcell, are summarized in Table 9.3. Those data can guide the future experiment and indicate how much more efficiency can be achieved with MJSC, which materials to target and how to correctly the balance between various contradicting requirements imposed by our model for losses. The validity of the data is confirmed by supporting graphs and comparison with real, fabricated, devices.

9.5 PHOTON ENERGY CONVERTERS

Solar cells have maximum conversion efficiency for monochromatic light or narrow spectrum with photon energies close to material energy gap [44]. Proof for that is in the fact that multi-junction solar cells (MJSC) have efficiencies significantly higher in comparison with single junction solar cells. Plus, single junction silicon SC has achieved efficiency of around 45% under 1W illumination and 1020nm wavelength. Therefore, the effort has been made in recent years in developing laser power converters (LPC) [108, 44, 114, 105, 34]. This way optical power can be transmitted through optical fibers or directly through free space and can be converted into electricity.

Vertical epitaxial heterostructure architecture (VEHSA) [73, 62, 51, 72, 74] (Fig. 9.17) has had a crucial influence on the development of LPCs. Since the monochromatic light source is not in thermal equilibrium, neither the Carnot limit nor Shockley-Queisser [189] limit applies to LPCs and therefore it is (theoretically) possible to asymptotically approach 100% efficiency [218].

There is another advantage, comparing to MJSC. Since there is a monochromatic light source, all subcells in LPC have the same bandgap E_g and they are made of the same material. Therefore, there are no problems with lattice mismatch. An important property of VEHSA LPCs is strong photon coupling [171]. Since the fabrication process is not ideal, there will always be a small discrepancy between subcells. With strong photon coupling, it is possible to slightly detune light source and still have high conversion efficiency. Like any other type of SCs, LPCs are very complex struc-

tures with a large number of parameters which have to be optimally selected in order to achieve these high efficiencies. Therefore, optimization is crucial.

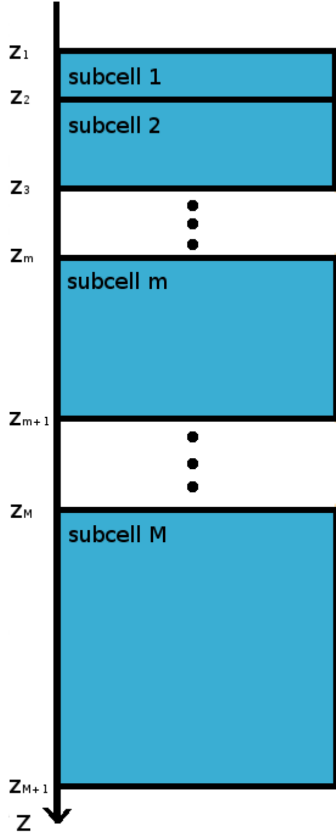

Figure 9.17: Schematic representation of LPC VEHSA device

In our analysis, we have optimized the pn junctions only. We assume the sufficiently good antireflective coating with neglected reflection. In order to find the optimal efficiency in such a multi-dimensional phase space, the global optimization was conducted using genetic algorithm [150, 94]. As already mentioned, subcells have the same E_g, so parameters which were optimized are thicknesses and impurity concentrations in both junctions in each subcell and the optimal current under current matching conditions. These parameters were chosen for optimization because those are the parameters needed in order to fabricate the device. If M is the number of subcells, the number of optimization parameters is $4M + 1$.

Since LPC VEHSA devices are slightly different than standard MJSCs (Fig. 9.17), there are small changes in the model. First, expression for generation (Eq. 6.1) can be simplified:

$$g^{(m)}(\lambda, z) = \Phi(\lambda)\alpha(\lambda)\exp[-\alpha(\lambda)(z - z_1)] \tag{9.1}$$

where $z \epsilon [z_\mathrm{m}, z_\mathrm{m+1}]$ and absorptions are calculated using the parallel `kppw` code [198]. Next, photon recycling and SRH recombination were introduced. Thanks to more detailed losses modeling, it became possible to analytically calculate carrier lifetimes:

$$\frac{1}{\tau} = \frac{1-\phi}{\tau_\mathrm{r}} + \frac{1}{\tau_\mathrm{srh}} + \frac{1}{\tau_\mathrm{a}} \tag{9.2}$$

where τ is a minority carrier lifetime. Particular lifetimes are radiative lifetime τ_{r} (Eqs. 7.17 and 7.18), Shockley-Read-Hall lifetime τ_{srh} (Eqs. 7.37–7.39) and Auger lifetime τ_{a} (Eqs. 7.50 and 7.51). It allows calculation of diffusion constant as $D = \mu \cdot (k_B T/q)$ and diffusion length:

$$L_{\mathrm{diff}} = \sqrt{\tau D} \tag{9.3}$$

Losses taken into account are diffusion dark current $J_{0,\mathrm{D}}$ (Eq. 7.4), radiative recombination $J_{0,\mathrm{R}}$ (Eq. 7.22), Shockley-Read-Hall $J_{0,\mathrm{S}}$ (Eq. 7.43) recombination and Auger recombination $J_{0,\mathrm{A}}$ (Eq. 7.85). Now, losses in the mth subcell are:

$$J_{\mathrm{sat}}^{(m)} = J_{0,\mathrm{D}}^{(m)} + J_{0,\mathrm{R}}^{(m)} + J_{0,\mathrm{S}}^{(m)} + J_{0,\mathrm{A}}^{(m)} \tag{9.4}$$

Since in direct III-V semiconductors absorption is high and, therefore, self-absorption, photon recycling is taken into account through ϕ [171, 138, 149, 192, 215]. Photon recycling is essentially reabsorption of photons after spontaneous emission. We calculate the spontaneous emission rate $S(\hbar\omega)$ and photon current $I_{em}(\hbar\omega)$ leaving the absorber. Now, recycled photons are all the photons reabsorbed before they had the opportunity to escape. Therefore:

$$\phi = 1 - \frac{S(\hbar\omega)}{I_{em}(\hbar\omega)} \tag{9.5}$$

Parameters affect the device performance in a similar way like in the discussion about MJSC. Except, there is no E_g to be optimized. Both short-circuit current and losses in an LPC device depend on laser wavelength, material type, doping levels and dimensions. Short-circuit currents can be enlarged by absorbing more photons, which can be achieved by increasing the thicknesses in different regions of the device. On

the other hand, however, larger thicknesses, especially comparable to or larger than diffusion lengths, lead to higher recombinations rate, hence losses. At the same time, higher doping levels allow higher open-circuit voltages while elevating recombination rates. Each of these parameters affects current, voltages and losses in a different way, it is very difficult to find the optimal combination of the device parameters. The LPC device was optimized using parallel genetic algorithm.

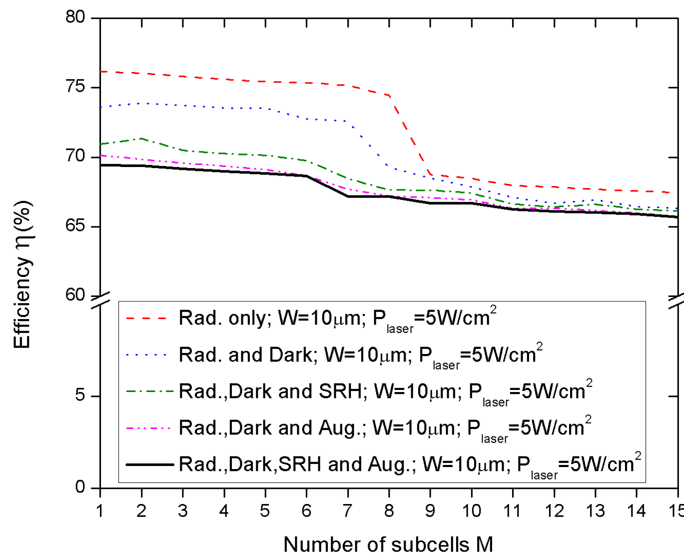

Figure 9.18: Maximum efficiency of LPC VEHSA device as a function of number of subcells, with $10\mu m$ thickness, $5W/cm^2$ laser irradiation and recombinations taken into account in different combinations

Results of optimization were presented in Fig. 9.18 ($10\mu m$ thick LPC device). Optimization was carried out with different combinations of losses, i.e. in different regimes:

1. only radiative recombination
2. radiative recombination and diffusion dark current
3. radiative recombination, diffusion dark current and Shockley-Read-Hall recombination
4. radiative recombination, diffusion dark current and Auger recombination

5. radiative recombination, diffusion dark current, Shockley-Read-Hall recombination and Auger recombination

First, only radiative recombination was taken into account, which is comparable with the detailed balance limit. In this case, very high efficiencies have been achieved, especially for smaller number of subcells. Since the most dominant types of losses are Shockley-Read-Hall and Auger recombinations, it was useful to compare them. The third optimization was conducted with diffusion dark current, radiative and Shockley-Read-Hall recombination. In the fourth, the Shockley-Read-Hall recombination was replaced with the Auger recombination. For a lower number of subcells, Auger recombination is more dominant. As the number of subcells is rising, the dominance of Auger recombination reduces. Finally, all types of losses were taken into account. In this case, the efficiencies are not significantly lower in comparison to the previous regime. It is telling us how significant Auger recombination is. This is especially important at high laser intensities, beacuse Auger recombination becomes very dependent on the carrier the concentration.

In order to test the model, the results were compared with experimental data [71] and presented in Fig. 9.19. The trends in slow decrease and sudden drops in efficiency are similar. The difference between theoretical and experimental results is between 3% and 5%, which is expected since we have neglected reflections and losses across the tunnel junctions. Next, we have optimized only pn-junctions and not the complete device.

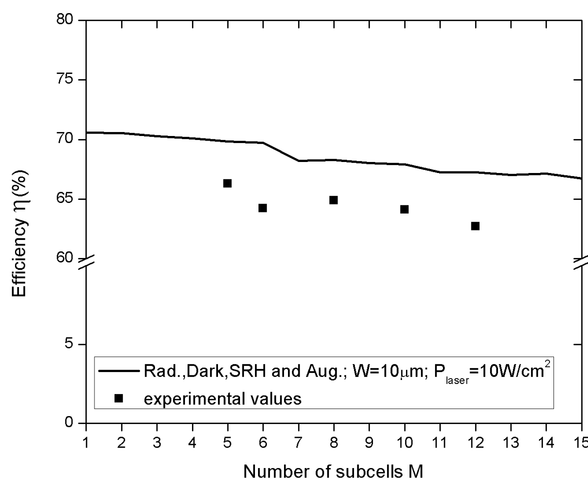

Figure 9.19: Maximum efficiency of LPC VEHSA device as a function of number of subcells ($10 \mu m$ thickness; $10 W/cm^2$ laser irradiation) and experimental data obtained in [71]

As the number of subcells in the device is increasing, the efficiency is slowly decreasing. And an interesting thing can be seen here. Between the cases when the device consists of 5 and 8 subcells there is a sudden drop in efficiency when experimental data is observed. This coincides with the optimized results. This drop exists when the device is optimized in any regime. Although, it is the most significant when only radiative recombination is accounted and appears between 8 and 10 subcells. The reason for this could be in the ratio between dimensions and diffusion lengths. It would explain why it happens later in case of only radiative recombination. When other types of losses are accounted for, it reduces the diffusion lengths.

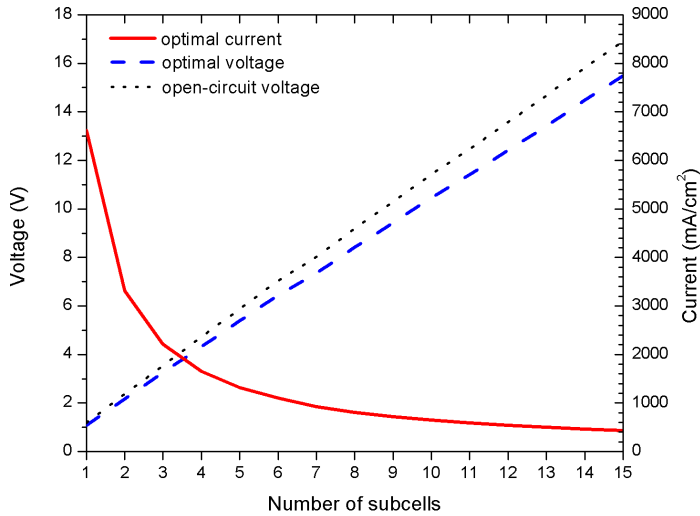

Figure 9.20: Optimal currents, optimal and open-circuit voltages in LPC VEHSA devices as a function of number of subcells, with $10\mu m$ thickness, $5W/cm^2$ laser irradiation and all types of losses taken into account

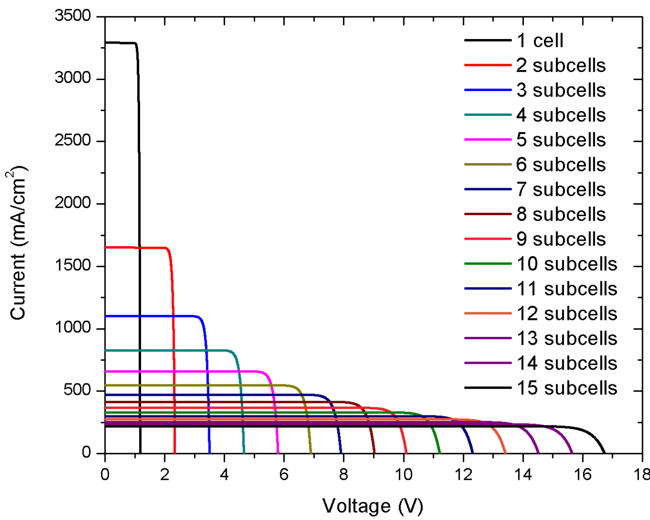

Figure 9.21: Current-voltage characteristics of LPC VEHSA device as a function of number of subcells, with $10\mu m$ thickness, $5W/cm^2$ laser irradiation and all types of losses taken into account

Efficiencies (Fig. 9.18) reduce with an increase in the number of subcells. Devices with higher a number of subcells have significantly lower output current and higher output voltages (Figs. 9.20 and 9.21) which leads to lower I^2R losses. The efficiency

drops only slightly with the increase in the number of subcells, which, consequently, makes them much more convenient for use in real-world applications than devices with smaller number of subcells. For instance, devices with 5 subcells have optimal voltage around 5V, which makes them perfect for use in electronics, whereas in automotive industry devices with 12 subcells and optimal voltage around 12V would be more applicable.

The advantage of heuristic modeling is that it can give us important insight into the device which would not be possible to see just observing the equations. This way we see that the algorithm found that the best way to fabricate the device is by higher doping concentration in thinner subcells. Since the thickness of each subcell is constrained by the overall thickness, laser wavelength and absorption, doping is the only unconstrained parameter. Higher doping levels lead to higher recombination rates, therefore is better to have it lower. On the other hand, higher doping allows higher voltages. Since in thin devices losses are lower, the algorithm found that the middle ground is higher impurity concentrations in upper subcells, which have to be thiner.

Table 9.6: Parameters of 15-subcell LPC 10 μm tick with 5 W/cm^2 laser power with Shockley-Read-Hall, radiative and Auger recombination taken into account

m	w$[\mu m]$	w$_p[\mu m]$	w$_n[\mu m]$	$N_a[cm^{-3}]$	$N_d[cm^{-3}]$
1	0.199	0.074	0.124	1.787×10^{18}	3.971×10^{18}
2	0.212	0.073	0.139	4.978×10^{17}	3.727×10^{18}
3	0.227	0.127	0.100	8.861×10^{17}	2.898×10^{18}
4	0.246	0.139	0.107	8.238×10^{17}	2.629×10^{18}
5	0.278	0.115	0.163	1.527×10^{18}	5.104×10^{18}
6	0.297	0.117	0.180	9.189×10^{17}	3.288×10^{18}
7	0.330	0.206	0.123	7.081×10^{17}	2.091×10^{18}
8	0.371	0.168	0.203	4.855×10^{17}	1.375×10^{18}
9	0.424	0.249	0.175	5.309×10^{17}	1.540×10^{18}
10	0.494	0.319	0.175	3.908×10^{17}	1.125×10^{18}
11	0.592	0.430	0.162	1.842×10^{17}	1.851×10^{17}
12	0.741	0.534	0.207	2.663×10^{17}	4.770×10^{17}
13	0.992	0.496	0.496	5.898×10^{16}	1.402×10^{16}
14	1.491	0.986	0.505	2.048×10^{15}	2.596×10^{17}
15	3.106	1.545	1.562	1.023×10^{15}	1.000×10^{15}

The results for 15 subcells PEC VEHSA device are presented in the Table 9.6 and Figures 9.20 and 9.21. This way voltages are maintained pretty much constant (Fig. 9.22). For thicker subcells we have to reduce the impurity levels, which leads to lower open-circuit and optimal voltages (Fig. 9.22).

Another trade-off is visible here. In order to prevent lower subcells to limit the overall device optimal current, lower subcells have higher currents on expense of their voltages (Fig. 9.22).

In order to quickly determine the thicknesses of different subcells for given device thickness and absorption, it is usually calculated as:

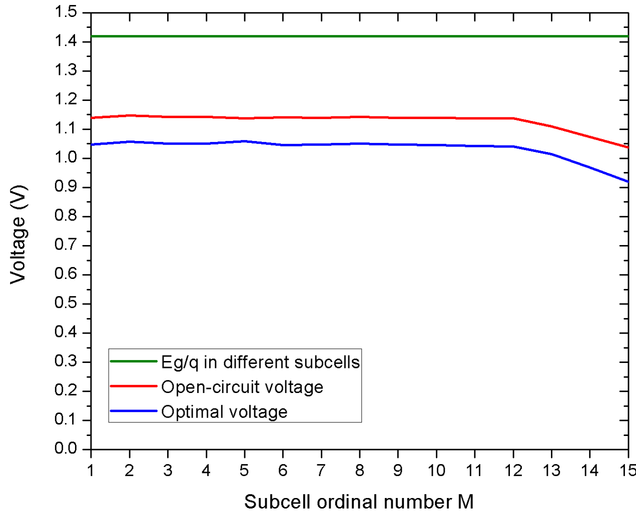

Figure 9.22: Optimal and open-circuit voltages compared with energy gap (with $10\mu m$ thickness, $5W/cm^2$ laser irradiation and all losses taken into account) for each subcell in 15-subcell PEC VEHSA device

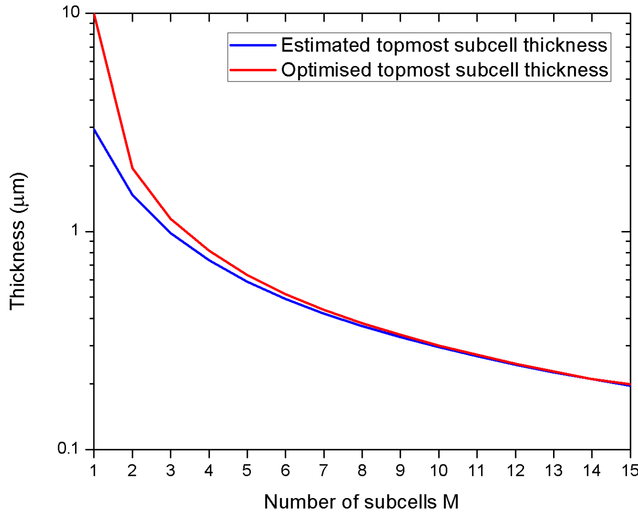

Figure 9.23: Estimated topmost subcell thickness compared with results from the optimization (with $10\mu m$ thickness, $5W/cm^2$ laser irradiation and all losses taken into account)

$$w_{top} = \frac{1}{\alpha M} \quad (9.6)$$

where α is the absorption coefficient and M number of subcells. Since the penetration depth is:

$$\delta = \frac{1}{\alpha} \tag{9.7}$$

and denotes the thickness of a material where, according to Beer-Lambert law, only 63% of the radiation is going to be absorbed Eq. 9.6. That leads to inaccurately estimated thicknesses, lower radiation absorption and, consequently, lower efficiencies. The above claim is confirmed in Fig. 9.23. With thickness less than 3μm, the device can absorb only around 60% laser radiation. In our optimization the algorithm suggested larger thicknesses which lead to absorption above 95%. In case when the device consists of only one pn junction, the thickness of the optimized device is 10μm, whereas the thickness of a device fabricated following the Beer-Lambert law would be less than 3μm.

10

CONCLUSIONS

The goal of any theoretical study is to propose new or improve existing design of a device. When it comes to solar cells, many milestones in design have already been passed, although there are many more to reach. With efficiency as the main property, it is easy to measure the value of different design ideas for solar cells. At the moment, the most promising seem to be multi-junction solar cells. This type of solar cells is setting records in efficiency. Since they are very complex devices, improvement in one aspect of the design can increase the efficiency. At the same time, if one aspect is not properly taken care of, it can lead to an underperforming device. Therefore, optimal matching of parameters is crucial in designing the device with the highest possible efficiency.

When designing a MJSC, it is of utmost importance to chose properly the materials for each subcell, to determine how thick each p- and n- type material is going to be, and, finally, to work out the optimal impurity concentration. Accordingly, effort has been made to calculate all material parameters, and consequently device parameters, using only these parameters. Optimization was conducted using heuristic modeling, namely genetic algorithm, since it is very reliable in locating global maximum. One sun and realistic ASTM G173 − 03 Global tilted solar spectra were assumed, while absorptions were calculated using the parallel `kppw` code.

Maximal efficiency can be reached only by maximizing gains and minimizing losses. Gains can be maximized by maximizing the number of absorbed photons and, in case of MJSC, properly distributing them in different subcells according to the material

they were made of and solar spectrum. Special attention was dedicated to losses. Their understanding is very important to draw proper conclusions from the data provided by the algorithm. It was found that the highest influence on solar cell efficiency is radiative recombination. At the same time, since it depends mostly on the material's energy gap, it is very difficult to minimize it without reducing gains. Diffusion dark current depends highly on impurity concentration, so it has high influence only at low energy gaps and low impurity levels. Auger recombination, on the other hand, rises with high doping, therefore, it has high influence only at high doping levels. Since Auger recombination reduces with increase in energy gaps more swiftly than diffusion dark current, the best solution is to dope subcells with higher energy gaps more heavily than subcells with lower energy gaps. This way both types of losses can be suppressed as much as possible.

The first device which was analyzed was unconstrained multi-junction solar cell. Since there are not many devices against which the results could be compared, optimal energy gaps were taken from detailed balance limit results. In this case only thicknesses and impurity levels were optimized. Efficiencies for MJSC with up to five subcells were presented on a graph with three different levels of sophistication together with detailed balance efficiencies and optimal energy gaps in this case. Three levels of sophistication mean in the first case only radiative recombination was accounted for; in the second radiative recombination and diffusion dark current; in the third Auger recombination together with the first two types of losses. The case when only radiative recombination was taken into account was used to test the model by comparing it against the detailed balance limit. When all losses are taken into account, a significant drop in efficiency was observed, unlike the case when Auger recombination was neglected. This means the device is not designed properly for real life conditions, meaning it does not suppress all losses completely. Detailed results were presented in a table.

Another important conclusion can be made by observing JV curve of these devices. In case of subcells with high energy gaps, the difference between short-circuit and

optimal currents is very small, unlike the subcells with low energy gaps. This is the consequence of higher losses in lower subcells. Voltages across the device are different between p- and n- type parts of the junction. By extracting smaller number of created carriers, the output current is lower, while the voltage across the device increases, which leads to higher output power. Luckily, high output power can be achieved for broad range of differences between short-circuit and optimal currents.

Next device is series constrained MJSC. In this case all parameters were optimized. Efficiencies and optimal energy gaps for up to seven subcells, again in three levels of sophistication, were presented on a graph while detailed results were presented in a table. The first conclusion that we can make is that energy gaps, when Auger recombination is taken into account, are slightly higher than in the other two cases. That is obvious considering the discussion related to losses.

This time, the results were compared with record setting devices. Optimizations were repeated with parameters of those devices and obtained efficiencies match perfectly, which is confirmation of the model reliability. Record setting devices have significantly lower efficiencies compared with the devices proposed by the algorithm. The reason for that can be seen by observing JV curves. In the case of the real devices short-currents in different subcells differ notably, while in case of the optimized devices they are almost equal. One underperforming subcell limits the output current, hence limits the device efficiency. Therefore, each aspect of the device has to be optimized carefully.

Another important conclusion can be made by observing absorbed portions of spectra in each subcell in both real and optimized devices. A real device absorbs significantly more photons, while at the same time has lower efficiency. The reason is that while the underperforming subcell limits the output current, all the excess carriers recombine and increase losses. Therefore, more absorbed photons does not automatically mean higher efficiency.

The third optimized device is photon energy converter. Since semiconductors optimally absorb photons with energies equal to their energy gap, the logical conclusion

is that the conversion efficiency will be the highest in case of illumination with laser light. PEC are actually MJSCs with subcells made of the same material. Therefore they have equal energy gaps. Ordinary MJSCs have subcells which are supposed to absorb photons with different energies. Subcells in PEC, on the other hand, absorb laser light where photons have very narrow energy spectrum, which makes the design of this type of devices extremely challenging. Each subcell has to absorb exactly the number of photons to generate current equal to all the other subcells. Small deviation affects all the other subcells more severely than in case of MJSC. In case of optimizing this type of devices, Shockley-Read-Hall recombination, as well as photon recycling, were taken into account.

Results for up to fifteen subcells were presented on a graph with different combinations of losses. Detailed results were presented in a table only for PEC with fifteen subcells. The reliability of the model was confirmed by comparing with fabricated devices with different number of subcells.

Devices with higher number of subcells have higher output voltage, so PEC can be used for, e.g. power-over-fiber systems optimized to deliver power at voltage optimal for different uses. This requires optimal design and it is very important to determine the thickness of each subcell properly in order to achieve the highest conversion efficiency. If the thicknesses are not calculated properly, the percentage of absorbed photons can drop significantly, which was especially pointed out.

Due to the complexity of solar cells and their uses in different configurations and different conditions, it is very difficult to fabricate them properly. It takes detailed analysis and careful tuning of each parameter in order to reach the highest possible efficiency. This careful tuning seems to be impossible without heuristic optimization.

11

FUTURE WORK

Regardless of the attempt to make this model as detailed as possible, there are still phenomena in MJSC and parts of MJSC which were not taken into account. As already mentioned, only pn-junctions were optimized. Next step would be to model window and BSF layers. These areas have a major influence on diffusion lengths and, consequently, on carrier collection. This would affect both short-circuit currents and open-circuit voltages. They can be modeled in similar fashion as p- and n- part on pn junction, although mere heavily doped. They have certain, although small, contribution in carrier generation.

Next, as already explained, individual subcells in MJSC are separated devices. They are connected via tunnel junctions and optically and electrically constrained. Therefore, tunnel junctions have to be good conductors and transparent for photons which a subcell below is supposed to absorb. Tunnel junctions are actually tunnel diodes which consist of haevily doped pn junctions. The main conduction mechanism is quantum tunneling. One of the main parameters of tunnel junctions is their peak current (J_p). For currents lower than, say, 90% of J_p there is pretty high linearity in JV characteristics of the tunnel diode. Therefore, in case of $J_{sc} < 0.9 \cdot J_p$ tunnel junction can be modeled as a simple voltage drop:

$$V = r_{TJ} J \tag{11.1}$$

where V is voltage drop across the tunnel junction, J solar cell current and r_{TJ} equivalent resistance of the tunnel junction.

Reflectivity and antireflective coating could be introduced into the model using only dependence of the reflectance of ARC as a function of wavelength. Grid is opaque, so in terms of light absorption its influence can be accounted by reducing the top surface through which photons penetrate into the MJSC. In terms of conductivity, carrier extraction and series resistance, its influence becomes very complicated.

When it comes to pn-junction, few more improvements can be made. Firstly, SRH recombination is taken into account only in case of PEC, since it can be calculated only for GaAs. If modeled for wide range of energy gaps, it could be accounted for MJSC as well. Secondly, radiative recombination is calculated the same way in all three regions. If there modeled better for different regions, it might improve the MJSC model and results as well. Finally, surface recombination is not taken into account at all. It could give us important insight in how surface processes affect the device if modeled properly, especially in combination with window and BSF layer.

The devices were optimized using one diode model (Fig. 5.2). This means losses are represented with only one diode. In general case, different losses have different influence, which is changing in different circumstances. In general case:

$$J = J_{\text{sc}} - J_{\text{sat}} \left(e^{\frac{qV}{mk_BT}} \right) \tag{11.2}$$

where J and V are the device current and voltage, respectively, J_{sc} short-circuit current, k_B Boltzmann constant, T temperature, q electric charge and m diode ideality factor. Ideality factor usually varies between 1 and 2, although it can be even higher in case of significant surface recombination. If modeled with more than one diode:

$$J = J_{\text{sc}} - J_{\text{sat}_1} \left(e^{\frac{qV}{m_1k_BT}} \right) - J_{\text{sat}_2} \left(e^{\frac{qV}{m_2k_BT}} \right) - \cdots - J_{sat_n} \left(e^{\frac{qV}{m_nk_BT}} \right) \tag{11.3}$$

Different ideality factors describe how and in which circumstances different types of losses dominate in the device. If, for example, loss i is the most significant, the overall ideality factor will be m_i. In other words, ideality factor describes the deviation of the device in comparison to the ideal diode.

Losses minimization has already been discussed. Another way to minimize losses is by photon recycling. Recombinations which have photons as a product do not necessarily need to be losses, as those photons can be reabsorbed, as already described in Chapter 9.5.

BIBLIOGRAPHY

[1] Affordability of solar pv - grow solar. https://www.growsolar.org/power-pack/homeowners-small-businesses-farmers/power-hour/virtual-power-hour/affordability-of-solar-pv/. Accessed: 2019-1-31.

[2] Best research-cell efficiencies - nrel. https://www.nrel.gov/pv/assets/images/efficiency-chart.png. Accessed: 2019-1-31.

[3] Bp statistical review of world energy 2017. https://www.bp.com/content/dam/bp/en/corporate/pdf/energy-economics/statistical-review-2017/bp-statistical-review-of-world-energy-2017-full-report.pdf. Accessed: 2018-3-3.

[4] Chemistry for non-majors - lumen. https://courses.lumenlearning.com/cheminter/chapter/unit-cells/. Accessed: 2019-1-31.

[5] Earth overshoot day. http://www.overshootday.org/. Accessed: 2018-3-3.

[6] Earth overshoot day on wikipedia. https://en.wikipedia.org/wiki/Earth_Overshoot_Day. Accessed: 2018-3-3.

[7] Ecological footprint - econation. https://econation.co.nz/ecological-footprint/. Accessed: 2019-1-31.

[8] The environmental impacts of transportation, author: Dr. jean-paul rodrigue. https://transportgeography.org/?page_id=5711. Accessed: 2018-3-3.

[9] Food and agriculture organization of the united nations, 29 november 2006. http://www.fao.org/docrep/010/a0701e/a0701e00.htm. Accessed: 2018-3-3.

[10] Food's carbon footprint. http://www.greeneatz.com/foods-carbon-footprint.html. Accessed: 2018-3-3.

[11] Footprint network. https://www.footprintnetwork.org/our-work/earth-overshoot-day/. Accessed: 2018-3-3.

[12] Footprint network. http://whitedwarf.org/parallel/. Accessed: 2019-1-9.

[13] Footprint network data. http://data.footprintnetwork.org/. Accessed: 2018-3-3.

[14] Fraunhofer institute for solar energy systems, photovoltaics report, february 2018. https://www.ise.fraunhofer.de/content/dam/ise/de/documents/publications/studies/Photovoltaics-Report.pdf. Accessed: 2018-3-3.

[15] Fraunhofer institute for solar energy systems, press release 26/14, new world record for solar cell efficiency at 46% french-german cooperation confirms competitive advantage of european photovoltaic industry. https://www.ise.fraunhofer.de/en/press-and-media/press-releases/press-releases-2014/new-world-record-for-solar-cell-efficiency-at-46-percent. Accessed: 2016-11-19.

[16] Gaas band structure and carrier concentration - ioffe institute. http://www.ioffe.ru/SVA/NSM/Semicond/GaAs/bandstr.html. Accessed: 2019-1-31.

[17] Global manmade greenhouse gas emissions by sector, 2013. https://www.c2es.org/content/international-emissions/. Accessed: 2018-3-3.

[18] Ioffe institute, semiconductors database.

[19] Microquanta certificate for the record of perovskite module efficiency.

[20] Photovoltaics report - fraunhofer ise. https://www.ise.fraunhofer.de/en/publications/studies/photovoltaics-report.html. Accessed: 2019-1-31.

[21] Pn junction - wikipedia. https://en.wikipedia.org/wiki/PâĂŞn_junction. Accessed: 2019-1-31.

[22] Reference solar spectral irradiance: ASTM G173 − 03.

[23] United nations development programme - world energy assessment: Energy and the challenge of sustainability. http://www.undp.org/content/undp/en/home/librarypage/environment-energy/sustainable_energy/world_energy_assessmentenergyandthechallengeofsustainability.html. Accessed: 2018-3-3.

[24] Woodall research lab - uc davis. https://woodall.ece.ucdavis.edu/resources/. Accessed: 2019-1-31.

[25] Green Martin A., Emery Keith, Hishikawa Yoshihiro, Warta Wilhelm, and Dunlop Ewan D. Solar cell efficiency tables (version 41). Progress in Photovoltaics: Research and Applications, 21(1):1–11.

[26] Green Martin A., Emery Keith, Hishikawa Yoshihiro, Warta Wilhelm, and Dunlop Ewan D. Solar cell efficiency tables (version 43). Progress in Photovoltaics: Research and Applications, 22(1):1–9.

[27] A. A. de Vos and H. Pauwels. On the thermodynamic limit of photovoltaic energy conversion. Applied Physics, 25:119–125, June 1981.

[28] V.N. Abakumov, V.I. Perel, and I.N. Yassievich. Modern problems in condensed matter sciences, V33 - Nonradiative recombination in semiconductors. Elsevier, 1991.

[29] D. Aiken, E. Dons, S. S. Je, N. Miller, F. Newman, P. Patel, and J. Spann. Lattice-matched solar cells with 40% average efficiency in pilot production and a roadmap to 50%. IEEE Journal of Photovoltaics, 3(1):542–547, Jan 2013.

[30] C Algora and Ignacio Rey-Stolle. Handbook of Concentrator Photovoltaic Technology. 04 2016.

[31] Barnett Allen, Kirkpatrick Douglas, Honsberg Christiana, Moore Duncan, Wanlass Mark, Emery Keith, Schwartz Richard, Carlson Dave, Bowden Stuart, Aiken Dan, Gray Allen, Kurtz Sarah, Kazmerski Larry, Steiner Myles, Gray Jeffery, Davenport Tom, Buelow Roger, Takacs Laszlo, Shatz Narkis, Bortz John, Jani Omkar, Goossen Keith, Kiamilev Fouad, Doolittle Alan, Ferguson Ian, Unger Blair, Schmidt Greg, Christensen Eric, and Salzman David. Very high efficiency solar cell modules. Progress in Photovoltaics: Research and Applications, 17(1):75–83.

[32] E. A. Alsema, M. J. de Wild-Scholten, and V. M. Fthenakis. Environmental impacts of PV electricity generation - a critical comparison of energy supply options. 21st European Photovoltaic Solar Energy Conference and Exhibition, 2006. Dresden, Germany.

[33] S.V. Timoshina N.K. Andreev, V.M. Sorokina. Solar cells based on gallium antimonide. Semiconductors, 43(5):668–671, 2009.

[34] V. Andreev, V. Khvostikov, V. Kalinovsky, V. Lantratov, V. Grilikhes, V. Rumyantsev, M. Shvarts, V. Fokanov, and A. Pavlov. High current density GaAs and GaSb photovoltaic cells for laser power beaming. In 3rd World Conference on Photovoltaic Energy Conversion, 2003. Proceedings of, volume 1, pages 761–764 Vol.1, May 2003.

[35] Gerardo L. Arauo and Antonio Marti. Absolute limiting efficiencies for photovoltaic energy conversion. Solar Energy Materials and Solar Cells, 33(2):213–240, 1994.

[36] Melissa J. Archer, Daniel C. Law, Shoghig Mesropian, Moran Haddad, Christopher M. Fetzer, Arthur C. Ackerman, Corinne Ladous, Richard R. King, and Harry A. Atwater. GaInP/GaAs dual junction solar cells on Ge/Si epitaxial templates. Applied Physics Letters, 92(10):103–503, 2008.

[37] B Aspar, Hubert Moriceau, E Jalaguier, Chrystelle Lagahe, A Soubie, B Biasse, A.-M Papon, Alain Claverie, J Grisolia, G Benassayag, F Letertre, O Rayssac, Thierry Barge, Christophe Maleville, and Bruno Ghyselen. The generic nature of the Smart-Cut(R) process for thin film transfer. 30:834–840, 07 2001.

[38] H. A. Atwater, M. D. Escarra, C. N. Eisler, E. D. Kosten, E. C. Warmann, S. Darbe, J. Lloyd, and C. Flowers. Full spectrum ultrahigh efficiency photovoltaics. In 2013 IEEE 39th Photovoltaic Specialists Conference (PVSC), pages 1631–1634, June 2013.

[39] P. Baruch. A two level system as a model for a photovoltaic solar cell. Journal of Applied Physics, 57(4):1347–1355, 1985.

[40] G.J. Bauhuis, P. Mulder, E.J. Haverkamp, J.C.C.M. Huijben, and J.J. Schermer. 26.1% thin-film GaAs solar cell using epitaxial lift-off. Solar Energy Materials and Solar Cells, 93(9):1488 – 1491, 2009.

[41] A.R. Beattie and P.T. Landsberg. Auger effect in semiconductors. Proceedings of the Royal Society of London A: Mathematical, Physical and Engineering Sciences, 249(1256):16–29, 1959.

[42] Mitchell Bernhard, Peharz Gerhard, Siefer Gerald, Peters Marius, Gandy Tobias, Goldschmidt Jan Christoph, Benick Jan, Glunz Stefan W., Bett Andreas W., and Dimroth Frank. Four-junction spectral beam-splitting photovoltaic receiver with high optical efficiency. Progress in Photovoltaics: Research and Applications, 19(1):61–72.

[43] A. W. Bett, C. Baur, F. Dimroth, and J. Schöne. Metamorphic GaInP-GaInAs layers for photovoltaic applications. MRS Proceedings, 836:L6.4, 2004.

[44] A. W. Bett, F. Dimroth, R. Löckenhoff, E. Oliva, and J. Schubert. III-V solar cells under monochromatic illumination. In 2008 33rd IEEE Photovoltaic Specialists Conference, pages 1–5, May 2008.

[45] A W Bett and O V Sulima. GaSb photovoltaic cells for applications in TPV generators. Semiconductor Science and Technology, 18(5):S184, 2003.

[46] Andreas Bett, Dimroth Frank, Wolfgang Guter, Raymond Hoheisel, Eduard Oliva, Simon P Philipps, Jan Schöne, Gerald Siefer, Marc Steiner, Alexander Wekkeli, Elke Welser, Matthias Meusel, Wolfgang Köstler, and Gerhard Strobl. Highest efficiency multi-junction solar cell for terrestrial and space applications. 01 2009.

[47] J.S. Blackmore. Semiconductor Statistics. Elsevier Science B.V., 1962.

[48] J. Boisvert, D. Law, R. King, D. Bhusari, X. Liu, A. Zakaria, W. Hong, S. Mesropian, D. Larrabee, R. Woo, A. Boca, K. Edmondson, D. Krut, D. Peterson, K. Rouhani, B. Benedikt, and N. H. Karam. Development of advanced space solar cells at Spectrolab. In 2010 35th IEEE Photovoltaic Specialists Conference, pages 123–127, June 2010.

[49] Andrew S Brown and Martin A Green. Detailed balance limit for the series constrained two terminal tandem solar cell. Physica E: Low-dimensional Systems and Nanostructures, 14:96 – 100, 2002.

[50] A.S. Brown and M.A. Green. Limiting efficiency for current-constrained two-terminal tandem cell stacks. Progress in Photovoltaics: Research and Applications, 10(5):299–307, 2002.

[51] Mark C. A. York, Francine Proulx, Denis P. Masson, Abdelatif Jaouad, Boussairi Bouzazi, Richard Arès, Vincent Aimez, and S Fafard. Enhanced photocarrier extraction mechanisms in ultra-thin photovoltaic GaAs n/p junctions. Proc.SPIE, 9743:9743 – 9743 – 7, 2016.

[52] P. Capper and M. Mauk. Liquid Phase Epitaxy of Electronic, Optical and Optoelectronic Materials. Wiley Series in Materials for Electronic & Optoelectronic Applications. Wiley, 2007.

[53] Andrew Carlson, Hyun-Joon Kim-Lee, Jian Wu, Paulius Elvikis, Huanyu Cheng, Anton Kovalsky, Steven Elgan, Qingmin Yu, Placid M. Ferreira, Yonggang Huang, Kevin T. Turner, and John A. Rogers. Shear-enhanced adhesiveless transfer printing for use in deterministic materials assembly. Applied Physics Letters, 98(26):264104, 2011.

[54] D.M. Chapin, C.S. Fuller, and G.L. Pearson. A new silicon p-n junction photocell for converting solar radiation into electrical power. Journal of Applied Physics, 25:676–677, 1954.

[55] P. Charbonneau. Genetic algorithms in astronomy and astrophysics. Astrophysical Journal Supplement, 101:309, 1995.

[56] P. Charbonneau and B. Knapp. A User's Guide to PIKAIA 1.0, 1995.

[57] P. T. Chiu, D. C. Law, R. L. Woo, S. B. Singer, D. Bhusari, W. D. Hong, A. Zakaria, J. Boisvert, S. Mesropian, R. R. King, and N. H. Karam. Direct semiconductor bonded 5J cell for space and terrestrial applications. IEEE Journal of Photovoltaics, 4(1):493–497, Jan 2014.

[58] Silvia Collavini, Sebastian F. Völker, and Juan Luis Delgado. Understanding the outstanding power conversion efficiency of perovskite-based solar cells. Angewandte Chemie International Edition, 54(34):9757–9759, 2015.

[59] Thomas E. Davis and Josh Carlos Principe. A simulated annealing like convergence theory for the simple genetic algorithm. In Richard K. Belew and Lashon B. Booker, editors, ICGA, pages 174–181. Morgan Kaufmann, 1991.

[60] A. de Vos. Detailed balance limit of the efficiency of tandem solar cells. Journal of Physics D Applied Physics, 13:839–846, 1980.

[61] P Demeester, I Pollentier, P De Dobbelaere, C Brys, and P Van Daele. Epitaxial lift-off and its applications. Semiconductor Science and Technology, 8(6):1124, 1993.

[62] Masson Denis, Proulx Francine, and Fafard Simon. Pushing the limits of concentrated photovoltaic solar cell tunnel junctions in novel high-efficiency GaAs phototransducers based on a vertical epitaxial heterostructure architecture. Progress in Photovoltaics: Research and Applications, 23(12):1687–1696.

[63] Daniel Derkacs, Rebecca Jones-Albertus, Ferran Suarez, and Onur Fidaner. Lattice-matched multijunction solar cells employing a 1eV GaInNAsSb bottom cell. pages 1805–, 10 2012.

[64] F. Dimroth, T. Roesener, S. Essig, C. Weuffen, A. Wekkeli, E. Oliva, G. Siefer, K. Volz, T. Hannappel, D. Häussler, W. Jäger, and A. W. Bett. Comparison of direct growth and wafer bonding for the fabrication of GaInP/GaAs dual-junction solar cells on silicon. IEEE Journal of Photovoltaics, 4(2):620–625, March 2014.

[65] F. Dimroth, T. N. D. Tibbits, M. Niemeyer, F. Predan, P. Beutel, C. Karcher, E. Oliva, G. Siefer, D. Lackner, P. Fuß-Kailuweit, A. W. Bett, R. Krause, C. Drazek, E. Guiot, J. Wasselin, A. Tauzin, and T. Signamarcheix. Four-junction wafer-bonded concentrator solar cells. IEEE Journal of Photovoltaics, 6(1):343–349, Jan 2016.

[66] Vincenzi Donato, Busato Alessandro, Stefancich Marco, and Martinelli Giuliano. Concentrating PV system based on spectral separation of solar radiation. physica status solidi (a), 206(2):375–378.

[67] J. H. Ermer, R. K. Jones, P. Hebert, P. Pien, R. R. King, D. Bhusari, R. Brandt, O. Al-Taher, C. Fetzer, G. S. Kinsey, and N. Karam. Status of C3MJ+ and C4MJ production concentrator solar cells at spectrolab. IEEE Journal of Photovoltaics, 2(2):209–213, April 2012.

[68] S. Essig, J. Benick, M. Schachtner, A. Wekkeli, M. Hermle, and F. Dimroth. Wafer-bonded GaInP/GaAs//Si solar cells with 30% efficiency under concentrated sunlight. IEEE Journal of Photovoltaics, 5(3):977–981, May 2015.

[69] S. Essig, M. A. Steiner, C. Allebe, J. F. Geisz, B. Paviet-Salomon, S. Ward, A. Descoeudres, V. LaSalvia, L. Barraud, N. Badel, A. Faes, J. Levrat, M. Despeisse, C. Ballif, P. Stradins, and D. L. Young. Realization of GaInP/Si dual-junction solar cells with 29.8% 1-sun efficiency. IEEE Journal of Photovoltaics, 6(4):1012–1019, July 2016.

[70] Stephanie Essig, Oussama Moutanabbir, A Wekkeli, H Nahme, E Oliva, Andreas Bett, and Dimroth Frank. Fast atom beam-activated n-Si/n-GaAs wafer bonding with high interfacial transparency and electrical conductivity. 113, 05 2013.

[71] S. Fafard, F. Proulx, M. C. A. York, L. S. Richard, P. O. Provost, R. Arès, V. Aimez, and D. P. Masson. High-photovoltage GaAs vertical epitaxial monolithic heterostructures with 20 thin p/n junctions and a conversion efficiency of 60%. Applied Physics Letters, 109(13):131107, 2016.

[72] S Fafard, f proulx, m.c.a York, Matthew Wilkins, Christopher Valdivia, Michal Bajcsy, D Ban, Abdelatif Jaouad, Boussairi Bouzazi, Richard Arès, V Aimez, Karin Hinzer, and D.P. Masson. Advances with vertical epitaxial heterostructure architecture (VEHSA) phototransducers for optical to electrical power conversion efficiencies exceeding 50 percent. 9743:974304, 03 2016.

[73] S. Fafard, M. C. A. York, F. Proulx, C. E. Valdivia, M. M. Wilkins, R. Arès, V. Aimez, K. Hinzer, and D. P. Masson. Ultrahigh efficiencies in vertical epitaxial heterostructure architectures. Applied Physics Letters, 108(7):071101, 2016.

[74] S. Fafard, M. C. A. York, F. Proulx, M. Wilkins, C. E. Valdivia, M. Bajcsy, D. Ban, R. Arès, V. Aimez, K. Hinzer, M. Ishigaki, and D. P. Masson. Ultra-efficient n-junction photovoltaic cells with VOC>14v at high optical input powers. In 2016 IEEE 43rd Photovoltaic Specialists Conference (PVSC), pages 2374–2378, June 2016.

[75] S. F. Fang, K. Adomi, S. Iyer, H. Morkoç, H. Zabel, C. Choi, and N. Otsuka. Gallium arsenide and other compound semiconductors on silicon. Journal of Applied Physics, 68(7):R31–R58, 1990.

[76] R.F.C. Farrow, S.S.P. Parkin, P.J. Dobson, J.H. Neave, and A.S. Arrott. Thin Film Growth Techniques for Low-Dimensional Structures. Nato Science Series B:. Springer US, 2013.

[77] L.J. Fogel, A.J. Owens, and M.J. Walsh. Artificial Intelligence Through Simulated Evolution. John Wiley & Sons, 1966.

[78] Stephen J. Fonash. Homojunction solar cells. In Solar Cell Device Physics, chapter 4, pages 133 – 186. Academic Press, 1st edition, 1981.

[79] L. M. Fraas, J. E. Avery, J. Martin, V. S. Sundaram, G. Girard, V. T. Dinh, T. M. Davenport, J. W. Yerkes, and M. J. O'Neil. Over 35-percent efficient GaAs/GaSb tandem solar cells. IEEE Transactions on Electron Devices, 37(2):443–449, Feb 1990.

[80] L. M. Fraas, G. R. Girard, J. E. Avery, B. A. Arau, V. S. Sundaram, A. G. Thompson, and J. M. Gee. GaSb booster cells for over 30% efficient solar cell stacks. Journal of Applied Physics, 66(8):3866–3870, 1989.

[81] R. M. France, J. F. Geisz, M. A. Steiner, D. J. Friedman, J. S. Ward, J. M. Olson, W. Olavarria, M. Young, and A. Duda. Pushing inverted metamorphic multijunction solar cells toward higher efficiency at realistic operating conditions. IEEE Journal of Photovoltaics, 3(2):893–898, April 2013.

[82] Dimroth Frank, Grave Matthias, Beutel Paul, Fiedeler Ulrich, Karcher Christian, Tibbits Thomas N. D., Oliva Eduard, Siefer Gerald, Schachtner Michael, Wekkeli Alexander, Bett Andreas W., Krause Rainer, Piccin Matteo, Blanc Nicolas, Drazek Charlotte, Guiot Eric, Ghyselen Bruno, Salvetat Thierry, Tauzin Aurélie, Signamarcheix Thomas, Dobrich Anja, Hannappel Thomas, and Schwarzburg

Klaus. Wafer bonded four-junction GaInP/GaAs//GaInAsP/GaInAs concentrator solar cells with 44.7% efficiency. Progress in Photovoltaics: Research and Applications, 22(3):277–282.

[83] I. B. Fridleifsson, R. Bertani, E. Huenges, J. Lund, A. Ragnarsson, L. Rybach, O. Hohmeyer, and T. Trittin. The possible role and contribution of geothermal energy to the mitigation of climate change. IPCC Scoping Meeting on Renewable Energy Sources, pages 59–80, 2008. Luebeck, Germany.

[84] D.J. Friedman. Progress and challenges for next-generation high-efficiency multijunction solar cells. Current Opinion in Solid State and Materials Science, 14(6):131 – 138, 2010.

[85] D.J. Friedman, J.F. Geisz, S.R. Kurtz, and J.M. Olson. 1-eV solar cells with GaInNAs active layer. Journal of Crystal Growth, 195(1):409 – 415, 1998.

[86] I. García, I. Rey-Stolle, B. Galiana, and C. Algora. A 32.6% efficient lattice-matched dual-junction solar cell working at 1000 suns. Applied Physics Letters, 94(5):053509, 2009.

[87] J. F. Geisz, D. J. Friedman, J. S. Ward, A. Duda, W. J. Olavarria, T. E. Moriarty, J. T. Kiehl, M. J. Romero, A. G. Norman, and K. M. Jones. 40.8% efficient inverted triple-junction solar cell with two independently metamorphic junctions. Applied Physics Letters, 93(12):123505, 2008.

[88] J. F. Geisz, J. M. Olson, D. J. Friedman, K. M. Jones, R. C. Reedy, and M. J. Romero. Lattice-matched GaNPAs-on-silicon tandem solar cells. In Conference Record of the Thirty-first IEEE Photovoltaic Specialists Conference, 2005., pages 695–698, Jan 2005.

[89] John F. Geisz, Anna Duda, Ryan M. France, Daniel J. Friedman, Ivan Garcia, Waldo Olavarria, Jerry M. Olson, Myles A. Steiner, J. Scott Ward, and Michelle Young. Optimization of 3-junction inverted metamorphic solar cells for high-

temperature and high-concentration operation. AIP Conference Proceedings, 1477(1):44–48, 2012.

[90] B.L. Gelmont and Sokolova Z.N. N/a. Tekh. Poluprovodn. [Sov. Phys.-Semicond.]., 15:1316, 1981.

[91] B.L. Gelmont and Sokolova Z.N. N/a. Tekh. Poluprovodn. [Sov. Phys.-Semicond.]., 16:1670, 1982.

[92] B.L. Gelmont and Sokolova Z.N. N/a. Tekh. Poluprovodn. [Sov. Phys.-Semicond.]., 16:582, 1982.

[93] David E. Goldberg. Simple genetic algorithms and the minimal, deceptive problem. In Lawrence Davis, editor, Genetic algorithms and simulated annealing, Research Notes in Artificial Intelligence, pages 74–88. Pitman, London, 1987.

[94] D.E. Goldberg. Genetic Algorithms in Search, Optimization, and Machine Learning. Addison-Wesley, Reading, Massachusetts, 1989.

[95] D.E. Goldberg and P. Segrest. Finite Markov chain analysis of genetic algorithms. Proceedings of the Second International Conference on Genetic Algorithms, pages 1–8, 1987.

[96] Martin A. Green, Yoshihiro Hishikawa, Ewan D. Dunlop, Dean H. Levi, Jochen Hohl-Ebinger, and Anita W.Y. Ho-Baillie. Solar cell efficiency tables (version 51). Progress in Photovoltaics: Research and Applications, 26(1):3–12, 2018. PIP-17-216.

[97] Martin A. Green, Mark J. Keevers, Ian Thomas, John B. Lasich, Keith Emery, and Richard R. King. 40% efficient sunlight to electricity conversion. Progress in Photovoltaics: Research and Applications, 23(6):685–691, 6 2015.

[98] Wolfgang Guter, Jan Schöne, Simon P. Philipps, Marc Steiner, Gerald Siefer, Alexander Wekkeli, Elke Welser, Eduard Oliva, Andreas W. Bett, and Frank Dimroth. Current-matched triple-junction solar cell reaching 41.1% conversion

efficiency under concentrated sunlight. Applied Physics Letters, 94(22):223504, 2009.

[99] R.N. Hall. Germanium rectifier characteristics. Phys. Rev., 83:228, 1951.

[100] L.C. Hirst and N.J Ekins-Daukes. Fundamental losses in solar cells. Progress in Photovoltaics: Research and Applications, 19(3):286–293, 2011.

[101] John H. Holland. Adaptation in Natural and Artificial Systems. University of Michigan Press, Ann Arbor, MI, 1975. second edition, 1992.

[102] John H. Holland. Adaptation in Natural and Artificial Systems: An Introductory Analysis with Applications to Biology, Control and Artificial Intelligence. MIT Press, Cambridge, MA, USA, 1992.

[103] Jeffrey Horn. Finite markov chain analysis of genetic algorithms with niching. In Proceedings of the 5th International Conference on Genetic Algorithms, pages 110–117, San Francisco, CA, USA, 1993. Morgan Kaufmann Publishers Inc.

[104] H.J. Hovel. Semiconductors and semimetals. volume 11. solar cells. 1 1975.

[105] Jie Huang, Yurun Sun, Yongming Zhao, Shuzhen Yu, Jianrong Dong, Jiping Xue, Chi Xue, Jin Wang, Yunqing Lu, and Yanwen Ding. Four-junction AlGaAs/GaAs laser power converter. Journal of Semiconductors, 39(4):044003, 2018.

[106] M. Ikeda, K. Nakano, Y. Mori, K. Kaneko, and N. Watanabe. MOCVD growth of AlGaInP at atmospheric pressure using triethylmetals and phosphine. Journal of Crystal Growth, 77(1):380 – 385, 1986.

[107] Schermer J. J., Mulder P., Bauhuis G. J., Voncken M. M. A. J., van Deelen J., Haverkamp E., and Larsen P. K. Epitaxial lift-off for large area thin film III/V devices. physica status solidi (a), 202(4):501–508.

[108] T.-C. Wu J. Liu J.-G. Werthen, S. Widjaja. Power over fiber: a review of replacing copper by fiber in critical applications, 2005.

[109] David B. Jackrel, Seth R. Bank, Homan B. Yuen, Mark A. Wistey, James S. Harris, Aaron J. Ptak, Steven W. Johnston, Daniel J. Friedman, and Sarah R. Kurtz. Dilute nitride GaInNAs and GaInNAsSb solar cells by molecular beam epitaxy. Journal of Applied Physics, 101(11):114916, 2007.

[110] Kelly M. K., Ambacher O., Dimitrov R., Handschuh R., and Stutzmann M. Optical process for liftoff of group III-Nitride films. physica status solidi (a), 159(1):R3–R4.

[111] E. O. Kane. The k·p method. Semiconduct. Semimetal., 1:75–100, 1966.

[112] Evan O. Kane. Band structure of indium antimonide. Journal of Physics and Chemistry of Solids, 1(4):249 – 261, 1957.

[113] R.J. Kaplar, D. Kwon, S.A. Ringel, A.A. Allerman, Steven R. Kurtz, E.D. Jones, and R.M. Sieg. Deep levels in p- and n-type InGaAsN for high-efficiency multi-junction III-V solar cells. Solar Energy Materials and Solar Cells, 69(1):85 – 91, 2001.

[114] Reichmuth S. Kasimir, Helmers Henning, Philipps Simon P., Schachtner Michael, Siefer Gerald, and Bett Andreas W. On the temperature dependence of dual-junction laser power converters. Progress in Photovoltaics: Research and Applications, 25(1):67–75.

[115] B. M. Kayes, H. Nie, R. Twist, S. G. Spruytte, F. Reinhardt, I. C. Kizilyalli, and G. S. Higashi. 27.6% conversion efficiency, a new record for single-junction solar cells under 1 sun illumination. In 2011 37th IEEE Photovoltaic Specialists Conference, pages 004–008, June 2011.

[116] B. M. Kayes, L. Zhang, R. Twist, I. K. Ding, and G. S. Higashi. Flexible thin-film tandem solar cells with >30% efficiency. IEEE Journal of Photovoltaics, 4(2):729–733, 2014.

[117] A.E. Kibbler, Sarah R. Kurtz, and J.M. Olson. Carbon doping and etching of MOCVD-grown GaAs, InP, and related ternaries using CC14. Journal of Crystal Growth, 109(1):258 – 263, 1991.

[118] T. W. Kim, T. J. Garrod, K. Kim, J. J. Lee, S. D. LaLumondiere, Y. Sin, W. T. Lotshaw, S. C. Moss, T. F. Kuech, Rao Tatavarti, and L. J. Mawst. Narrow band gap (1eV) InGaAsSbN solar cells grown by metalorganic vapor phase epitaxy. Applied Physics Letters, 100(12):121120, 2012.

[119] R. R. King, D. C. Law, K. M. Edmondson, C. M. Fetzer, G. S. Kinsey, H. Yoon, R. A. Sherif, and N. H. Karam. 40% efficient metamorphic GaInP/GaInAs/Ge multijunction solar cells. Applied Physics Letters, 90(18), 2007.

[120] Richard R. King. Multijunction cells: Record breakers. Nature Photonics, 2(5):284–286, 5 2008.

[121] Akihiro Kojima, Kenjiro Teshima, Yasuo Shirai, and Tsutomu Miyasaka. Organometal halide perovskites as visible-light sensitizers for photovoltaic cells. Journal of the American Chemical Society, 131(17):6050–6051, 2009. PMID: 19366264.

[122] Gitanjali Kolhatkar, Abderraouf Boucherif, Christopher E. Valdivia, Steven G. Wallace, Simon Fafard, Vincent Aimez, and Richard Arès. Al-enhanced N incorporation in GaNAs alloys grown by chemical beam epitaxy. Journal of Crystal Growth, 380:256 – 260, 2013.

[123] V Kumar and Jitendra Singh. Model for calculating the refractive index of different materials. Indian Journal of Pure and Applied Physics, 48, 08 2010.

[124] E Kuphal. Liquid phase epitaxy. 52:380–409, 06 1991.

[125] S. Kurtz, J. F. Geisz, D. J. Friedman, J. M. Olson, A. Duda, N. H. Karam, R. R. King, J. H. Ermer, and D. E. Joslin. Modeling of electron diffusion length in GaInAsN solar cells. In Conference Record of the Twenty-Eighth IEEE

Photovoltaic Specialists Conference - 2000 (Cat. No.00CH37036), pages 1210–1213, 2000.

[126] S. Kurtz, S. W. Johnston, J. F. Geisz, D. J. Friedman, and A. J. Ptak. Effect of nitrogen concentration on the performance of $Ga_{1-x}In_xN_yAs_{1-y}$ solar cells. In Conference Record of the Thirty-first IEEE Photovoltaic Specialists Conference, 2005., pages 595–598, Jan 2005.

[127] S. R. Kurtz, J. M. Olson, and A. Kibbler. High efficiency GaAs solar cells using GaInP2 window layers. In IEEE Conference on Photovoltaic Specialists, pages 138–140 vol.1, May 1990.

[128] Sarah Kurtz, Steve Johnston, and Howard M. Branz. Capacitance-spectroscopy identification of a key defect in N-degraded GalnNAs solar cells. Applied Physics Letters, 86(11):113506, 2005.

[129] Steven R. Kurtz, A. A. Allerman, E. D. Jones, J. M. Gee, J. J. Banas, and B. E. Hammons. InGaAsN solar cells with 1.0 eV band gap, lattice matched to GaAs. Applied Physics Letters, 74(5):729–731, 1999.

[130] P. T. Landsberg and P. Baruch. The thermodynamics of the conversion of radiation energy for photovoltaics. Journal of Physics A: Mathematical and General, 22(11):1911, 1989.

[131] P. T. Landsberg and G. Tonge. Thermodynamic energy conversion efficiencies. Journal of Applied Physics, 51(7):R1–R20, 1980.

[132] P.T. Landsberg and A.R. Beattie. Auger effect in semiconductors. Journal of Physics and Chemistry of Solids, 8:73 – 75, 1959.

[133] D. C. Law, D. M. Bhusari, S. Mesropian, J. C. Boisvert, W. D. Hong, A. Boca, D. C. Larrabee, C. M. Fetzer, R. R. King, and N. H. Karam. Semiconductor-bonded III-V multijunction space solar cells. In 2009 34th IEEE Photovoltaic Specialists Conference (PVSC), pages 2237–2239, June 2009.

[134] Daniel C. Law, R.R. King, H. Yoon, M.J. Archer, A. Boca, C.M. Fetzer, S. Mesropian, T. Isshiki, M. Haddad, K.M. Edmondson, D. Bhusari, J. Yen, R.A. Sherif, H.A. Atwater, and N.H. Karam. Future technology pathways of terrestrial III-V multijunction solar cells for concentrator photovoltaic systems. Solar Energy Materials and Solar Cells, 94(8):1314 – 1318, 2010. National Conference on the Emerging Trends in the Photovoltaic Energy and Utilization.

[135] Marina S. Leite, Robyn L. Woo, Jeremy N. Munday, William D. Hong, Shoghig Mesropian, Daniel C. Law, and Harry A. Atwater. Towards an optimized all lattice-matched InAlAs/InGaAsP/InGaAs multijunction solar cell with efficiency >50%. Applied Physics Letters, 102(3):033901, 2013.

[136] C. T. Lin, W. E. McMahon, J. S. Ward, J. F. Geisz, M. W. Wanlass, J. J. Carapella, W. Olavarria, M. Young, M. A. Steiner, R. M. Frances, A. E. Kibbler, A. Duda, J. M. Olson, E. E. Perl, D. J. Friedman, and J. E. Bowers. Fabrication of two-terminal metal-interconnected multijunction III-V solar cells. In 2012 38th IEEE Photovoltaic Specialists Conference, pages 944–948, June 2012.

[137] Joseph J. Loferski. Theoretical considerations governing the choice of the optimum semiconductor for photovoltaic solar energy conversion. Journal of Applied Physics, 27(7):777–784, 1956.

[138] Matthew P. Lumb, Myles A. Steiner, John F. Geisz, and Robert J. Walters. Incorporating photon recycling into the analytical drift-diffusion model of high efficiency solar cells. Journal of Applied Physics, 116(19):194504, 2014.

[139] J. W. Lund. Characteristics, development and utilization of geothermal resources. Geo-Heat Centre Quarterly Bulletin, Oregon Institute of Technology, 28(2):1–9, June 2007.

[140] A. Luque, G. Sala, W. Palz, G. dos Santos, and P. Helm. Tenth E.C. Photovoltaic Solar Energy Conference: Proceedings of the International Conference, held at Lisbon, Portugal, 8–12 April 1991. Springer Netherlands, 2012.

[141] Antonio Luque. Will we exceed 50% efficiency in photovoltaics? Journal of Applied Physics, 110(3):031301, 2011.

[142] Olson J. M., Friedman D. J., and Kurtz Sarah. High-Efficiency III-V Multijunction Solar Cells, chapter 9, pages 359–411. Wiley-Blackwell, 2005.

[143] Tom Markvart and Luis Castañer. Chapter ia-2 - semiconductor materials and modelling. In L. Castañer A. McEvoy, T. Markvart, editor, Practical Handbook of Photovoltaics (Second Edition), pages 33–62. Academic Press, Boston, second edition edition, 2012.

[144] I Ye Maronchuk, V V Kurak, E V Andronova, and Ye A Baganov. Obtaining GaSb/InAs heterostructures by liquid phase epitaxy. Semiconductor Science and Technology, 19(6):747, 2004.

[145] A. Martí and G. L. Araújo. Limiting efficiencies for photovoltaic energy conversion in multigap systems. Solar Energy Materials and Solar Cells, 43(2):203–222, 1996.

[146] C. D. Mathers. Upper limit of efficiency for photovoltaic solar cells. Journal of Applied Physics, 48(7):3181–3182, 1977.

[147] L. S. Mattos, S. R. Scully, M. Syfu, E. Olson, L. Yang, C. Ling, B. M. Kayes, and G. He. New module efficiency record: 23.5% under 1-sun illumination using thin-film single-junction GaAs solar cells. In 2012 38th IEEE Photovoltaic Specialists Conference, pages 3187–3190, June 2012.

[148] M G Mauk and V M Andreev. GaSb-related materials for TPV cells. Semiconductor Science and Technology, 18(5):S191, 2003.

[149] O. D. Miller, E. Yablonovitch, and S. R. Kurtz. Strong internal and external luminescence as solar cells approach the shockley-queisser limit. IEEE Journal of Photovoltaics, 2(3):303–311, July 2012.

[150] Melanie Mitchell. An Introduction to Genetic Algorithms. MIT Press, Cambridge, MA, USA, 1998.

[151] Shigehiko Mori, Haruhi Oh-oka, Hideyuki Nakao, Takeshi Gotanda, Yoshihiko Nakano, Hyangmi Jung, Atsuko Iida, Rumiko Hayase, Naomi Shida, Mitsunaga Saito, Kenji Todori, Taro Asakura, Akihiro Matsui, and Masahiro Hosoya. Organic photovoltaic module development with inverted device structure. 1737, 01 2015.

[152] J. N. Munday, D. M. Callahan, C. Chen, and H. A. Atwater. Three efficiency benefits from thin film plasmonic solar cells. In 2011 37th IEEE Photovoltaic Specialists Conference, pages 907–910, June 2011.

[153] J. Nelson. The Physics of Solar Cells. Imperial College Press, 2003.

[154] Jenny Nelson. Analysis of the p-n junction. In The Physics of Solar Cells, chapter 6, pages 145 – 176. Imperial College Press, 1st edition, 2003.

[155] A. Nix and M. Vose. Modeling genetic algorithms with markov chains. Annals of Mathematics and Artificial Intelligence, 5:79–88, 1992.

[156] Arthur J. Nozik, Gavin Conibeer, and Matthew C Beard, editors. Advanced Concepts in Photovoltaics. Energy and Environment Series. The Royal Society of Chemistry, 2014.

[157] Y. Ohba, M. Ishikawa, H. Sugawara, M. Yamamoto, and T. Nakanisi. Growth of high-quality InGaAlP epilayers by MOCVD using methyl metalorganics and their application to visible semiconductors lasers. Journal of Crystal Growth, 77(1):374 – 379, 1986.

[158] Y. Ohba, Y. Nishikawa, C. Nozaki, H. Sugawara, and T. Nakanisi. A study of p-type doping for AlGaInP grown by low-pressure MOCVD. Journal of Crystal Growth, 93(1):613 – 617, 1988. Special Issue of Journal of Crystals Growth.

[159] Y. Ohshita, H. Suzuki, N. Kojima, T. Tanaka, T. Honda, M. Inagaki, and M. Yamaguchi. Novel material for super high efficiency multi-junction solar cells. Journal of Crystal Growth, 318(1):328 – 331, 2011. The 16th International Conference on Crystal Growth (ICCG16)/The 14th International Conference on Vapor Growth and Epitaxy (ICVGE14).

[160] J. M. Olson, S. R. Kurtz, A. E. Kibbler, and P. Faine. A 27.3% efficient $Ga_{0.5}In_{0.5}P$/GaAs tandem solar cell. Applied Physics Letters, 56(7):623–625, 1990.

[161] J. M. Olson, S. R. Kurtz, A. E. Kibbler, and P. Faine. Recent advances in high efficiency GaInP2/GaAs tandem solar cells. In IEEE Conference on Photovoltaic Specialists, pages 24–29 vol.1, May 1990.

[162] Brian O'Regan and Michael Grätzel. A low-cost, high-efficiency solar cell based on dye-sensitized colloidal tio2 films. Nature, 353:737 EP –, Oct 1991.

[163] Giles Parkinson. Graph of the day: The plunging cost of solar pv. `http://reneweconomy.com.au/graph-of-the-day-the-plunging-cost-of-solar-pv-41843/`. Accessed: 2016-11-19.

[164] J. E. Parrott. The limiting efficiency of an edge-illuminated multigap solar cell. Journal of Physics D: Applied Physics, 12(3):441, 1979.

[165] J.E. Parrott. Thermodynamics of solar cell efficiency. Solar Energy Materials and Solar Cells, 25(1):73–85, 1992.

[166] P. Patel, D. Aiken, A. Boca, B. Cho, D. Chumney, M. B. Clevenger, A. Cornfeld, N. Fatemi, Y. Lin, J. McCarty, F. Newman, P. Sharps, J. Spann, M. Stan, J. Steinfeldt, C. Strautin, and T. Varghese. Experimental results from performance improvement and radiation hardening of inverted metamorphic multijunction solar cells. IEEE Journal of Photovoltaics, 2(3):377–381, July 2012.

[167] Y. Pauleau. Chemical Physics of Thin Film Deposition Processes for Micro- and Nano-Technologies. Nato Science Series II:. Springer Netherlands, 2012.

[168] W. G. Pfann and W. Van Roosbroeck. Radioactive and photoelectric pn junction power sources. Journal of Applied Physics, 25(11):1422–1434, 1954.

[169] S.P. Philipps, G. Peharz, R. Hoheisel, T. Hornung, N.M. Al-Abbadi, F. Dimroth, and A.W. Bett. Energy harvesting efficiency of III-V triple-junction concentrator solar cells under realistic spectral conditions. Solar Energy Materials and Solar Cells, 94(5):869 – 877, 2010.

[170] M. B. Prince. Silicon solar energy converters. Journal of Applied Physics, 26(5):534–540, 1955.

[171] F. Proulx, M. C. A. York, P. O. Provost, R. Arès, V. Aimez, D. P. Masson, and S. Fafard. Measurement of strong photon recycling in ultra-thin GaAs n/p junctions monolithically integrated in high-photovoltage vertical epitaxial heterostructure architectures with conversion efficiencies exceeding 60%. physica status solidi (RRL) Rapid Research Letters, 11(2):1600385–n/a, 2017. 1600385.

[172] A. J. Ptak, D. J. Friedman, Sarah Kurtz, and R. C. Reedy. Low-acceptor-concentration GaInNAs grown by molecular-beam epitaxy for high-current p-i-n solar cell applications. Journal of Applied Physics, 98(9):094501, 2005.

[173] Beattie A. R. and Smith G. Recombination in semiconductors by a light hole auger transition. physica status solidi (b), 19(2):577–586.

[174] King R. R., Bhusari D., Larrabee D., Liu X.-Q., Rehder E., Edmondson K., Cotal H., Jones R. K., Ermer J. H., Fetzer C. M., Law D. C., and Karam N. H. Solar cell generations over 40% efficiency. Progress in Photovoltaics: Research and Applications, 20(6):801–815.

[175] R R King, Andreea Boca, Hong WP, X.-Q Liu, D Bhusari, D Larrabee, K M Edmondson, D C Law, Chris Fetzer, S Mesropian, and N.H. Karam. Band-gap-

engineered architectures for high-efficiency multijunction concentrator solar cells. 01 2009.

[176] Steven R. Kurtz, A A. Allerman, and E D. Jones. InGaAsN solar cells and minority carrier properties. 10 1999.

[177] I. Rechenberg. Cybernetic solution path of an experimental problem. In Royal Aircraft Establishment Translation No. 1122, B. F. Toms, Trans. Ministry of Aviation, Royal Aircraft Establishment, Farnborough Hants, August 1965.

[178] B K Ridley. Quantum processes in semiconductors; 4th ed. Clarendon Press, Oxford, 1999.

[179] T Roesener, Henning Döscher, Andreas Beyer, Sebastian Brückner, Vera Klinger, Wekkeli , P Kleinschmidt, C Jurecka, J Ohlmann, K Volz, W Stolz, Thomas Hannappel, Andreas Bett, and Dimroth Frank. MOVPE growth of III-V solar cells on silicon in 300 mm closed coupled showerhead reactor. 01 2010.

[180] Vijit Sabnis, Homan Yuen, and Mike Wiemer. High-efficiency multijunction solar cells employing dilute nitrides. AIP Conference Proceedings, 1477(1):14–19, 2012.

[181] Kazuaki Sasaki, Takaaki Agui, Katsuya Nakaido, Naoki Takahashi, Ryusuke Onitsuka, and Tatsuya Takamoto. Development of InGaP/GaAs/InGaAs inverted triple junction concentrator solar cells. AIP Conference Proceedings, 1556(1):22–25, 2013.

[182] J. J. Schermer, G. J. Bauhuis, P. Mulder, W. J. Meulemeesters, E. Haverkamp, M. M. A. J. Voncken, and P. K. Larsen. High rate epitaxial lift-off of InGaP films from GaAs substrates. Applied Physics Letters, 76(15):2131–2133, 2000.

[183] J. C. Schultz, M. E. Klausmeier-Brown, M. L. Ristow, L. D. Partain, M. M. Al-Jassim, and K. M. Jones. Development of high-quantum-efficiency, lattice-mismatched, 1.0-eV GaInAs solar cells. Journal of Electronic Materials, 22:755–761, July 1993.

[184] Hans-Paul Schwefel. Evolutionsstrategie und numerische optimierung, 01 1975.

[185] Bailey Sheila and Raffaelle Ryne. Space Solar Cells and Arrays, chapter 10, pages 413–448. Wiley-Blackwell, 2005.

[186] Xing Sheng, Christopher A Bower, Salvatore Bonafede, John W Wilson, Brent Fisher, Matthew Meitl, Homan Yuen, Shuodao Wang, Ling Shen, Anthony Banks, Christopher J Corcoran, Ralph G Nuzzo, Scott Burroughs, and John A Rogers. Printing-based assembly of quadruple-junction four-terminal microscale solar cells and their use in high-efficiency modules. 13, 04 2014.

[187] W. Shockley and W. T. Read. Statistics of the recombinations of holes and electrons. Phys. Rev., 87:835–842, Sep 1952.

[188] William Shockley and Hans J. Queisser. Detailed balance limit of efficiency of p-n junction solar cells. Journal of Applied Physics, 32(3):510–519, 1961.

[189] William Shockley and Hans J. Queisser. Detailed balance limit of efficiency of pn junction solar cells. Journal of Applied Physics, 32(3):510–519, 1961.

[190] G. Smestad and H. Ries. Luminescence and current-voltage characteristics of solar cells and optoelectronic devices. Solar Energy Materials and Solar Cells, 25(1):51 – 71, 1992.

[191] Tomah Sogabe, Yasushi Shoji, Mitsuyoshi Ohba, Katsuhisa Yoshida, Ryo Tamaki, Hwen-Fen Hong, Chih-Hung Wu, Cherng-Tsong Kuo, Stanko Tomić, and Yoshitaka Okada. Intermediate-band dynamics of quantum dots solar cell in concentrator photovoltaic modules. Scientific Reports, 4(4792), 2014.

[192] Myles A. Steiner, John F. Geisz, J. Scott Ward, Ivan Garcia, Daniel J. Friedman, Richard R. King, Philip T. Chiu, Ryan M. France, Anna Duda, Waldo J. Olavarria, Michelle Young, and Sarah R. Kurtz. Optically enhanced photon recycling in mechanically stacked multijunction solar cells. IEEE Journal of Photovoltaics, 6(1):358–365, 1 2016.

[193] G.B. Stringfellow. Organometallic Vapor-Phase Epitaxy: Theory and Practice. Elsevier Science, 1999.

[194] T. Sugaya, A. Takeda, R. Oshima, K. Matsubara, S. Niki, and Y. Okano. InGaP-based InGaAs quantum dot solar cells with GaAs spacer layer fabricated using solid-source molecular beam epitaxy. Applied Physics Letters, 101(13):133110, 2012.

[195] Barbara Swatowska, T Stapinski, Kazimierz Drabczyk, and Piotr Panek. The role of antireflection coatings in silicon solar cells - the influence on their electrical parameters. XLI:487, 01 2011.

[196] T. Takamoto, T. Agui, A. Yoshida, K. Nakaido, H. Juso, K. Sasaki, K. Nakamora, H. Yamaguchi, T. Kodama, H. Washio, M. Imaizumi, and M. Takahashi. World's highest efficiency triple-junction solar cells fabricated by inverted layers transfer process. In 2010 35th IEEE Photovoltaic Specialists Conference, pages 412–417, June 2010.

[197] Tracy L. Thompson and John T. Yates. Surface science studies of the photoactivation of tio2new photochemical processes. Chemical Reviews, 106(10):4428–4453, 2006. PMID: 17031993.

[198] Stanko Tomić, Andrew G. Sunderland, and Ian J. Bush. Parallel multi-band k center dot p code for electronic structure of zinc blend semiconductor quantum dots. J. Mater. Chem., 16(20):1963–1972, 2006.

[199] W. T. Tsang. Chemical beam epitaxy of InP and GaAs. Applied Physics Letters, 45:1234–1236, December 1984.

[200] Franz Urbach. The long-wavelength edge of photographic sensitivity and of the electronic absorption of solids. Phys. Rev., 92:1324–1324, Dec 1953.

[201] Slobodan Čičić and Stanko Tomić. Automated design of multi junction solar cells by genetic approach: Reaching the >50% efficiency target. Solar Energy

Materials and Solar Cells, 181:30 – 37, 2018. Thin film solar cells and applications.

[202] Alexis De Vos. Is a solar cell an endoreversible engine. Solar Cells, 31(2):181–196, 1991.

[203] M.D. Vose and G. Liepins. Punctuated equilibria in genetic search. Complex Systems, 5:31–44, 1991.

[204] Michael D. Vose. Modeling simple genetic algorithms. In L. Darrell Whitley, editor, FOGA, pages 63–73. Morgan Kaufmann, 1992.

[205] I. Vurgaftman and J. R. Meyer. Band parameters for nitrogen-containing semiconductors. J. Appl. Phys., 94:3675–3696, 2003.

[206] Vent W. Rechenberg, ingo, evolutionsstrategie - optimierung technischer systeme nach prinzipien der biologischen evolution. 170 s. mit 36 abb. frommann-holzboog-verlag. stuttgart 1973. broschiert. Feddes Repertorium, 86(5):337–337.

[207] R. J. Walters, M. González, J. G. Tischler, M. P. Lumb, J. R. Meyer, I. Vurgaftman, J. Abell, M. K. Yakes, N. Ekins-Daukes, J. G. J. Adams, N. Chan, P. Stavrinou, and P. P. Jenkins. Design of an achievable, all lattice-matched multijunction solar cell using InGaAlAsSb. In 2011 37th IEEE Photovoltaic Specialists Conference, pages 000122–000126, June 2011.

[208] M. W. Wanlass, T. J. Coutts, J. S. Ward, and K. A. Emery. High-efficiency heteroepitaxial InP solar cells. In The Conference Record of the Twenty-Second IEEE Photovoltaic Specialists Conference - 1991, pages 159–165 vol.1, Oct 1991.

[209] M. W. Wanlass, T. J. Coutts, J. S. Ward, K. A. Emery, T. A. Gessert, and C. R. Osterwald. Advanced high-efficiency concentrator tandem solar cells. In The Conference Record of the Twenty-Second IEEE Photovoltaic Specialists Conference - 1991, pages 38–45 vol.1, Oct 1991.

[210] J. S. Ward, M. W. Wanlass, T. J. Coutts, K. A. Emery, and C. R. Osterwald. InP concentrator solar cells. In The Conference Record of the Twenty-Second IEEE Photovoltaic Specialists Conference - 1991, pages 365–370 vol.1, Oct 1991.

[211] Markus Weyers, Michio Sato, and Hiroaki Ando. Red shift of photoluminescence and absorption in dilute GaAsN alloy layers. 31:L853–L855, 06 1992.

[212] Darrell Whitley. An executable model of a simple genetic algorithm. In L. Darrell Whitley, editor, FOGA, pages 45–62. Morgan Kaufmann, 1992.

[213] D. N. Wright, E. S. Marstein, and A. Holt. Double layer anti-reflective coatings for silicon solar cells. In Conference Record of the Thirty-first IEEE Photovoltaic Specialists Conference, 2005., pages 1237–1240, Jan 2005.

[214] Sheng Xing, Yun Myoung Hee, Zhang Chen, Al-Okaily Ala'a M., Masouraki Maria, Shen Ling, Wang Shuodao, Wilson William L., Kim Jin Young, Ferreira Placid, Li Xiuling, Yablonovitch Eli, and Rogers John A. Device architectures for enhanced photon recycling in thin-film multijunction solar cells. Advanced Energy Materials, 5(1):1400919.

[215] Eli Yablonovitch. Lead halides join the top optoelectronic league. Science, 351(6280):1401–1401, 2016.

[216] Eli Yablonovitch, T. Gmitter, J. P. Harbison, and R. Bhat. Extreme selectivity in the lift-off of epitaxial GaAs films. Applied Physics Letters, 51(26):2222–2224, 1987.

[217] Woon Seok Yang, Jun Hong Noh, Nam Joong Jeon, Young Chan Kim, Seungchan Ryu, Jangwon Seo, and Sang Il Seok. High-performance photovoltaic perovskite layers fabricated through intramolecular exchange. Science, 348(6240):1234–1237, 2015.

[218] Mark C A York and Simon Fafard. High efficiency phototransducers based on a novel vertical epitaxial heterostructure architecture (VEHSA) with thin p/n junctions. Journal of Physics D: Applied Physics, 50(17):173003, 2017.

[219] P. YU and M. Cardona. Fundamentals of Semiconductors: Physics and Materials Properties. Graduate Texts in Physics. Springer Berlin Heidelberg, 2010.

[220] James M. Zahler, Katsuaki Tanabe, Corinne Ladous, Tom Pinnington, Frederick D. Newman, and Harry A. Atwater. High efficiency InGaAs solar cells on Si by InP layer transfer. Applied Physics Letters, 91(1):012108, 2007.